AN INVESTIGATION OF POSSIBLE TRIGGERED STAR FORMATION IN BRIGHT RIMMED CLOUDS

A THESIS SUBMITTED TO
THE UNIVERSITY OF KENT AT CANTERBURY
IN THE SUBJECT OF ASTROPHYSICS
FOR THE DEGREE
OF DOCTOR OF PHILOSOPHY.

By
Lawrence K. Morgan
April 2006

Contents

Abstract **vi**

Acknowledgements **1**

1 Introduction **2**

1.1 Molecular Material In The Interstellar Medium 2

1.2 The Formation Of Dense Clumps Within Molecular Clouds 3

1.3 The Formation Of Protostellar Cores 3

1.3.1 The Role Of Turbulence And The Magnetic Field 4

1.4 Chemical Evolution Of Star Forming Cores 4

1.5 Optically Thick Phases 5

1.6 Photon Dominated Regions 5

1.7 Radiation-Driven Implosion 6

1.7.1 Pressure Balances 8

1.8 The Sugitani Catalogue 9

1.9 Archival Data 10

1.9.1 IRAS 10

1.9.2 HIRES Processing 10

1.9.3 The NVSS 11

1.9.4 MSX 12

1.9.5 2MASS 12

1.10 Aims 13

2 Instrumentation **14**

2.1 The JCMT 14

2.2 The SCUBA 14

2.2.1 Jiggle-Mapping Mode 15

2.2.2 Atmospheric Effects 15

2.3 SCUBA Data Reduction . . . 16
2.3.1 Calibration . . . 17
2.4 JCMT Spectrometry . . . 21
2.4.1 Frequency-switching . . . 22
2.4.2 Position-switching . . . 22
2.4.3 Calibration Of Spectral Line Data . . . 22
2.4.4 Data Reduction . . . 23

3 Theory **24**
3.1 Ionisation And Recombination . . . 24
3.1.1 The Strömgren Sphere . . . 24
3.2 Thermal Emission . . . 25
3.2.1 Evidence For Dust . . . 26
3.3 Greybody Modelling . . . 28
3.4 Emission Processes . . . 30
3.5 Temperature Scales . . . 32
3.6 Molecular Levels . . . 33
3.7 Conditions For Gravitational Collapse . . . 36
3.7.1 Virial Theorem . . . 36
3.7.2 Jeans Mass . . . 39
3.8 Signatures Of Star Formation . . . 40
3.8.1 Infall . . . 40
3.8.2 Outflow . . . 43

4 Radio And Mid-Infrared Emission From BRCs **44**
4.1 Introduction . . . 44
4.2 Survey Procedure . . . 45
4.2.1 The NVSS . . . 45
4.2.2 MSX Data . . . 45
4.3 Results And Analysis . . . 45
4.3.1 Source Identification And Classification . . . 45
4.3.2 Confusing Sources . . . 47
4.3.3 Ionised Rims Associated With SFO Objects . . . 48
4.3.4 Identification Of Ionising Stars . . . 49
4.3.5 Flux Comparison . . . 50
4.3.6 Upper Limits To The Ionising Flux For Non-Detections . . . 52
4.3.7 Candidate Ultra-Compact HII Regions . . . 54

4.3.8 Previous Observations . . . 56
4.4 Discussion . . . 57
4.4.1 IBL Pressure . . . 58
4.5 Summary . . . 58
4.6 Conclusions . . . 59

5 A SCUBA Survey Of Bright-Rimmed Clouds 60
5.1 Introduction . . . 60
5.2 Observations . . . 61
5.2.1 IRAS HIRES Observations . . . 61
5.3 Results . . . 63
5.3.1 Core Positions, Fluxes And Sizes . . . 64
5.4 Correlation With Radio Free-Free Emission . . . 64
5.5 Associated Infrared Objects-2MASS Data . . . 65
5.6 Observational Summary . . . 67
5.7 Temperature, Mass And Density . . . 67
5.7.1 Dust Continuum . . . 67
5.8 Analysis . . . 75
5.8.1 Cloud Classification . . . 75
5.8.2 Cloud Morphology . . . 75
5.8.3 Morphological Analysis . . . 81
5.8.4 Core Internal Sources . . . 83
5.8.5 Classification of the Internal Sources . . . 85
5.8.6 The Mass Function Of The SFO Catalogue . . . 86
5.9 Has The Star Formation In The Sample Been Induced? . . . 90
5.10 Discussion . . . 91
5.10.1 Cloud Morphology And Physical Properties . . . 91
5.10.2 The Mass Function Of The Sample . . . 93
5.10.3 Infrared Sources . . . 93
5.10.4 Internal Sources . . . 93
5.10.5 Aging The Star Formation . . . 94
5.11 Conclusions . . . 94

6 Outflow And Infall 96
6.1 Introduction . . . 96
6.2 Observations . . . 96
6.3 Results . . . 97

6.4 Individual Sources . . . 97
6.4.1 Notes On Individual Sources . . . 97
6.5 Outflow Summary . . . 101
6.6 Infall . . . 101
6.7 CO Observational Analysis . . . 103
6.8 Pressure Balances . . . 106
6.9 Mass Analysis . . . 111
6.10 Temperature Ratios . . . 111
6.11 Virial Mass . . . 112
6.11.1 Pressurised Virial Mass . . . 114
6.12 Discussion . . . 115
6.12.1 Outflow . . . 115
6.12.2 Infall . . . 115
6.12.3 Pressure Balance . . . 116
6.12.4 CO Masses And Temperatures . . . 117
6.12.5 Virial Masses . . . 117
6.13 Summary And Conclusions . . . 118

7 Summary And Conclusions **120**
7.1 Observational Summary . . . 120
7.2 Discussion . . . 121
7.2.1 Triggered Or Inhibited Star Formation? . . . 121
7.2.2 Star Formation Time Scales . . . 123
7.3 Conclusions . . . 124
7.4 Further Work . . . 126
7.4.1 Modelling . . . 127

A Images **128**
A.1 Description Of Plots And Images . . . 128

B Further Acknowledgements **167**

Bibliography **167**

Abstract

A survey of bright-rimmed clouds has been undertaken to determine the state of star formation within them. This predominantly northern sky survey has utilised data from the NVSS, MSX and DSS surveys to identify ionisation at the rim of these clouds, the physical properties of these ionised boundary layers have been determined from the NVSS observations. SCUBA observations of submillimetre cores embedded within the clouds show sources that are commonly high in mass and luminosity. These sources are shown to be consistent with criteria for Class 0 protostars. Molecular line observations of the clouds show the presence of outflow and low level infall associated with the clouds. This supports the conclusion that these clouds are star forming. The pressure found for the internal molecular material of the clouds from molecular line observations, combined with the external pressures derived from the NVSS 20cm snapshots, show that, invariably, there is a large pressure gradient at the rim of the clouds, causing the propagation of photoionisation induced shocks into the interior of the clouds.

The results are discussed in the light of radiatively driven implosion models which suggest that the induced shocks may trigger the collapse of dust 'clumps' within the molecular clouds to form protostellar objects. The association of high pressure gradients with protostellar cores supports this hypothesis, though some evidence is presented that star formation within the clouds may actually be hindered by the presence of the ionisation front.

Acknowledgements

I would like to thank my mother for supporting me through my education, I would not have gotten to this point without her help.

Hannah has been my most ardent supporter, she has helped me through the worst crises, both personal and thesis-related, and has put up with my whining all the way.

I want to thank all of the friends who have endured the discussions of subjects they have no part in. Pub physics has been foisted upon many. In particular I acknowledge the support of Chris, Justine, Bob and Barbara, all of whom have supported me both in spirit and in food and lodging.

I do not think I would have ever finished this thesis without the help of Dr. Mark Price. He has never failed to offer me the comfort of his settee or spare room without ever mentioning rent or complaining about the inconvenience.

Dr. Mark Thompson deserves special thanks for effectively being my supervisor, he has taught me a great deal about astronomy and has usually been the one to give me the one piece of advice I needed in order to progress.

Dr. James Urquhart has been a good friend throughout my PhD and has always helped me to produce the work I might otherwise have given up on. He has always been ready to offer support and advice with any aspect of my life, whether work-related or personal, and is another person I have to name as being responsible for my current position (that's a good thing!).

I offer my thanks to Christine Westen for giving me food and lodging for a good few years whenever I felt like turning up. I also have to thank Simon for giving a different perspective on my work and sharing his weekends with me.

To everyone I have forgotten to name, I'm sorry, send me a donation at my current address and I will insert your name.xx

Chapter 1

Introduction

1.1 Molecular Material In The Interstellar Medium

The spectroscopist F.W.Adams first observed molecules in the interstellar medium in 1937 when he detected absorption lines from the radicals CN, CH^+ and CH near 400 nm in the spectra of several bright stars. The lines he detected were very narrow, supporting the idea that the absorbing radicals are at very low temperatures and not associated with the envelope of the observed stars. Since this first detection of the molecular content of the interstellar medium, and especially with the advent of infrared and radio wavelength astronomy, research into interstellar molecules has intensified manyfold. The most complex molecules so far detected in interstellar space (among which are included alcohols, acids, aldehydes, amides and amines) are much less complicated than those involved in living material. However, their discovery in a medium previously judged to be very unfavourable to their synthesis came as a surprise.

Present estimates place approximately half the mass of interstellar gas in the galaxy in molecular form. The majority of this molecular material is in huge interstellar clouds throughout the Galaxy. The most abundant molecule found in the interstellar medium is, of course, the hydrogen molecule as this is the most widespread element in space. The molecule has no permanent dipole and is thus not easily detectable, pure rotation lines are observable. However, because of the low mass of the hydrogen atom, its rotational levels are widely spaced and require relatively high temperatures (T>70 K) to excite even the lowest levels appreciably.

In order to detect and observe interstellar molecular clouds it is necessary to use molecules with abundances far less than that of H_2 as neither H_2 nor He is usually sufficiently excited in the bulk of molecular clouds to emit. Although the asymmetric molecule carbon monoxide (CO) is 100 000 times less abundant than the H_2 molecule, it is the molecule which most easily allows detection of interstellar molecular material as it is the most abundant molecule after H_2. Molecular clouds are characterised by very strong emission from the CO molecule; theoretical arguments have shown that its presence is linked with that of molecular hydrogen in an abundance ratio of $CO/H_2 \sim 8 \times 10^{-6}$.

1.2 The Formation Of Dense Clumps Within Molecular Clouds

The notion that stars form as a result of the gravitational condensation of diffuse matter dates back almost as far as the theory of universal gravitation itself, having been suggested by Newton himself in 1692 (Jeans 1928; Larson 2003). On galactic scales the associated tidal forces counteract the self-gravity of the interstellar material and the formation of individual dense regions can occur only where the molecular gas is dense enough to become unstable to its own self-gravity, i.e. in galactic spiral arms where gas has been swept up by density waves, or in large complexes which may contain several giant molecular clouds.

1.3 The Formation Of Protostellar Cores

In a typical molecular cloud the emission of far infrared radiation from molecules such as CO cools the material. The high densities of the material within molecular clouds mean that collisional atomic processes (such as stimulated emission) and molecular emission are highly effective in removing thermal energy from the cloud. The clouds are generally transparent to this emission while the high opacity of the material at Far UltraViolet (FUV) wavelengths keeps the heating rate by external sources low. This means that molecular clouds are, in general, very cold ($\sim$ 10-20 K). While newly formed stars may locally heat regions to around 100 K, the gas within dense collapsing cores becomes thermally coupled to the dust. This then controls the temperature by its strongly temperature-dependent thermal emission, maintaining a low and almost constant temperature of about 10 K over a wide range of densities (Larson 2003 and references within).

On the small scale of individual protostellar cores the predominant force opposing self gravitational collapse is the thermal pressure (though turbulence is expected to play a significant role, see Section 1.3.1). The balance of these two opposing processes is described by the Jeans analysis (see Section 3.7) which defines the minimum mass of a molecular cloud which may be expected to collapse under its own gravity, assuming a specific isothermal temperature and density for the cloud. The removal of thermal energy from within the cloud is what allows the collapse of protostellar cores of one solar mass or less.

The Jeans analysis is, of course, a simplification of the processes occuring during the formation of protostellar cores. If thermal pressure were truly the only force opposing gravity then one might expect molecular clouds to collapse rapidly and efficiently into star forming cores. However, while the majority of molecular clouds are in fact observed to be forming stars, they appear to be doing so inefficiently, typically turning only a few percent of their mass into stars before being dispersed (Larson 2003). The inefficiency of these molecular clouds in producing stars has long been considered evidence of the importance of additional effects in the formation of stars. Magnetic fields, or the poorly defined effect of 'turbulence', have both been suggested as possible methods of support in molecular clouds, holding the clouds in near-equilibrium. However, observations of the structure of molecular clouds suggest, rather than an equilibrium configuration, a highly irregular, filamentary and rapidly changing appearance. Molecular clouds therefore appear to be highly dynamic structures.

1.3.1 The Role Of Turbulence And The Magnetic Field

The broad line profiles observed towards molecular clouds indicate mostly small-scale random motions. These motions are often referred to as 'turbulence' even though their detailed nature remains unclear and they may not closely resemble classical eddy turbulence. However, the velocity dispersions inferred from observed linewidths increase with region size in a way that resembles the classical Kolmogorov law, $v_\lambda \sim U\left(\frac{\lambda}{L}\right)$, where v_λ is the velocity at a scale λ, U is the energy per unit mass and L is the scale of the largest unstable region(Larson 2003 and references within). The turbulent motions present within observed molecular clouds are roughly equivalent to the degree of self-gravity; this suggests that gravity and turbulence are equally important in controlling the structure and evolution of these clouds. The lack of accurate measurements of magnetic field strength makes it difficult to truly test models of star formation which assume important levels of magnetic field strengths.

1.4 Chemical Evolution Of Star Forming Cores

The low temperatures in protostellar cores caused by the cooling processes mentioned previously mean that the chemistry within star formation regions is dominated by low temperature gas-phase reactions (Langer et al. 2000). These lead to the formation of small radicals and unsaturated molecules, with the formation of small amounts of long carbon chains if the material is initially atomic carbon rich. There is observational evidence that ices form in cold molecular cores prior to the onset of star formation (e.g Bacmann et al. (2003); Walmsley et al. (2004)). Once Young Stellar Objects (YSO) have formed they provide a bright continuum against which the ices in the colder outer envelope may be seen in absorption (e.g Chiar et al. (1998); Keane et al.

(2001); Gibb et al. (2000)). These ices form as a result of the increasing density during the collapse phase, the density becomes sufficiently high that molecules may accrete onto dust grains and are incorporated into an icy mantle. Organic species such as CS and C_2S deplete readily onto grains, while nitrogen species such as N_2H^+ and NH_3 (in addition to HCO^+) are much less prone to depletion. For this reason C_2S/NH_3 and C_2S/N_2H^+ abundance ratios have been proposed as indicators of the time that has passed since the gas was atomic-carbon rich (Langer et al. 2000), this may provide a timescale for star formation. However, it should be noted that this can only be an indication of the amount of time that has passed since the cloud was subject to a large dynamical event, not necessarily the actual age of the cloud.

The formation of a new star within the cloud radiates heat into the circumstellar envelope causing the molecules to evaporate back into the gas-phase, while shocks and turbulence result from the outflows emanating from the newly-formed star. The increasing densities and decreasing temperatures during protostellar collapse cause the enhanced depletion of many gas-phase molecules in the protostellar envelopes. The outer, more diffuse, parts of the collapse envelopes still show chemical differentiation. HCO^+ is found to be an excellent tracer of the inner envelope structure and mass, whereas N_2H^+ appears to trace preferentially the quiescent outer envelope. N_2H^+ may be destroyed by proton transfer to CO and H_2O in regions where these molecules are not significantly condensed onto grains (Langer et al. 2000).

1.5 Optically Thick Phases

As the density within the protostellar core increases to around 10^{-13} g cm^{-3} (2×10^{10}n(H_2)cm^{-3}) the central dense region becomes opaque to the thermal radiation emitted from the dust grains. The central temperature then begins to rise above $\sim$ 10K. The density continues to rise through accretion, pressure forces increase faster than gravity and the collapse halts with a central density of $\sim 2 \times 10^{-10}$gcm^{-3}. A central region (approximately in hydrostatic equilibrium) then forms and continues to grow in mass as matter falls into it via accretion. This first core is only a transient feature and a second phase of collapse begins when the central temperature rises above 2000K, causing hydrogen molecules to dissociate (Larson 2003).

1.6 Photon Dominated Regions

A large amount of the energy output from massive stars is absorbed and reprocessed by the surrounding molecular material. High energy (UltraViolet (UV)) photons dissociate this molecular material and ionise atoms. The transition region between ionised and molecular material is known as a Photon Dominated Region (PDR). Photoelectric heating and UV pumping can heat the external layers of PDRs to temperatures in excess of 1000 K while the inner material is cooled via infrared lines to temperatures of ~ 10 K. PDRs surrounding young massive stars are ideal laboratories to study second generation star formation in which the effects of massive stars upon their surroundings have caused sequential or 'triggered' star formation.

1.7 Radiation-Driven Implosion

When a star first 'turns on' it begins to ionise its surroundings. The initial expansion of this ionised region is rapid up to the Strömgren sphere equilibrium radius, which ranges from 0.01 to 4 pc dependent upon the spectral type of the ionising star. Following this rapid expansion the ionisation front moves outward much more slowly, at approximately the sound speed of the ionised gas (~ 11.4 km s^{-1}) following a shock front propagating into the surrounding neutral gas.

The ionisation front moves slowly (subsonically (Bertoldi 1989)) into the globule, creating a dense outer shell of ionised gas (the Ionised Boundary Layer, or IBL), which streams radially away from the cloud surface. The increased density in the shell leads to a higher recombination rate which shields the globule from quickly evaporating (Reipurth 1983). The increased pressure due to ionisation heating in the ionised gas causes an expansion of the IBL into the intercloud medium and an ionisation front preceded by a shock in the neutral gas propagates into the cloud (Lefloch & Lazareff 1994; White et al. 1997). The UV radiation from the OB star(s) sweeps the molecular material of the cloud radially away from the ionising source. Overdensities in the surrounding medium are less readily dispersed than the diffuse surrounding material and may thus shield this material, forming a cometary morphology with a dense core located at the 'head' of the cometary globule (see Fig. 1).

Bertoldi (1989) found that for a wide range of parameters, the ionised gas expands supersonically into the intercloud medium with approximately D-critical conditions at the ionisation front (D- and R-type fronts are classified as 'Dense' and 'Rarefied', which refer to the density of the material the ionisation front is expanding into). The two main parameters defining the initial cloud in his analysis are the cloud's column density and an ionisation parameter relating the strength of the ionising radiation field to the density of the cloud. These parameters separate clouds into objects with different evolutions;

1. Clouds with small column densities, or those very close to the ionising source, are rapidly ionised and expand into the intercloud medium.

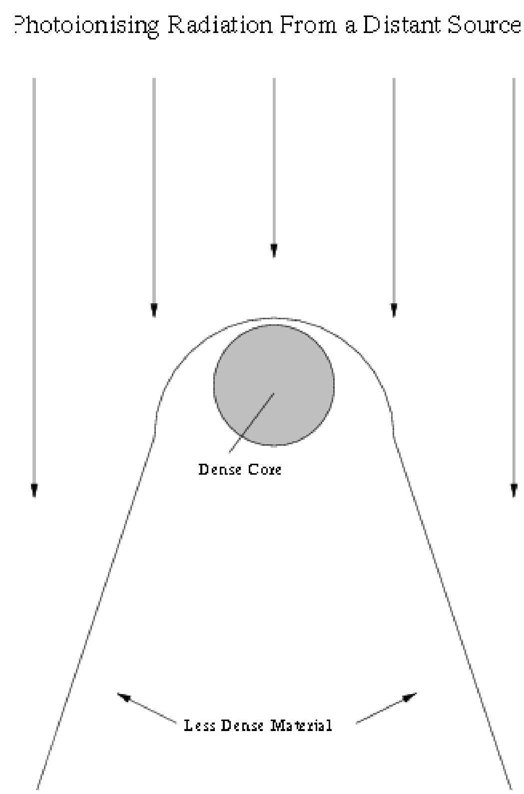

Figure 1: The cometary morphology created by ionising radiation impinging upon a molecular cloud.

2. Clouds that have higher column densities (are more opaque to the ionising radiation) in which the penetrating ionisation front slows down to develop a shock front before it ionises the entire cloud, lose only part of their initial mass during the subsequent ionisation-driven implosion. The remaining gas becomes highly compressed as the ionisation shock front focuses the neutral shocked gas onto the symmetry axis of the initial cloud. Because of the large compression of the gas in the post-implosion material clouds that were initially gravitationally stable can become supercritical and collapse to form stars.

1.7.1 Pressure Balances

The ratio of the internal pressure of the molecular cloud (mostly due to turbulent motions, but with a small thermal contribution) to the external pressure of the IBL is predicted by Radiatively Driven Implosion (RDI) models to be key to the evolution of the cloud. Bertoldi (1989) specified five different scenarios of varying cloud and IBL parameters to describe the UV radiation effects on the evolution of molecular clouds.

1. Clouds Unaffected. In this scenario, the ionisation front pressure is significantly less than the internal molecular pressure of the cloud. Thus, the ionisation front cannot even confine the cloud. A steady state is not achievable in this scenario as photoionised gas is unable to uniformly expand away from the cloud. Overall, there will be no dynamical effect of the ionisation front upon such a cloud. These conditions are usually not found in HII regions.

2. Cloud Implosion. These clouds will be compressed by an ionisation shock front. An IBL is established which absorbs a fraction of the incident ionising flux. The ionised gas streams off the neutral shocked gas layer with a steady flow pattern.

3. Strong Ionisation Shock Fronts. Here, the velocity of the ionisation shock front would exceed the sound speed in the ionised interclump gas. This situation quickly leads to a buildup of a dense, ionised, recombining layer which shields the ionisation front from the ionising flux that drives it. This limits the maximum possible velocity of the ionisation shock front to the sound speed in the ionised interclump gas.

4. 'Zapped Clouds'. Clouds with low column densities and/or in regions of very high ionising flux will be completely ionised by the initial rapid ionisation front. These clouds will be rapidly dispersed into the intercloud medium.

5. Nonequilibrium Evaporation Fronts. In this case, either the ionising flux is too high, or the initial cloud mass is too low to support the prolonged existence of an ionisation front. Therefore, equilibrium can not be established.

These five scenarios may, effectively, be sorted into three evolutionary types. If the ionisation front has a pressure less than that of the cloud then the cloud will be dynamically unaffected by that front.

If, conversely the front is at a greater pressure than that of the cloud then two ultimate scenarios are possible. In the first case, the cloud will be compressed by the shock front and will implode along the symmetry axis of the cloud. In the second possibility, the cloud will be unable to support the ionisation front in equilibrium and will be totally dispersed.

1.8 The Sugitani Catalogue

Sugitani et al. (1991) performed a search for Bright Rimmed Clouds (BRC) in the northern hemisphere using the Sharpless (1959) catalogue, followed by a similar search in the southern hemisphere (Sugitani & Ogura 1994). Their criteria for selection were clouds that had IRAS point sources surrounded by curved bright rims, as identified through Palomar Sky Survey red prints. BRCs that had IRAS sources located just upon their rims were excluded as such IRAS sources are possibly not stellar objects but emission from dusty clumps. They claim an accuracy in the position of their IRAS identifications of better than 0.25 arcminutes. Additional criteria were imposed upon the observed IRAS fluxes in order to exclude emission from diffuse dust. Detection in at least two IRAS bands, one of which was required to be the 25 μm band, was necessary for inclusion with point source correlation coefficients of F or better at 25 μm (IRAS points have correlation coefficients between 87%-100% classified as A=100%, B=99%, ... , N=87%).
The ratio of the IRAS flux values of these sources indicate that they have Far InfraRed (FIR) colours consistent with YSOs. This makes them ideal sources with which to investigate triggered star formation.

From a search towards 65 H II regions, 44 BRCs associated with IRAS point sources in/around 18 HII regions were selected by Sugitani et al. (1991). A further 45 BRCs were identified by Sugitani & Ogura (1994). The combination of these two catalogues shall hereafter be referred to as the SFO catalogue and shall provide sources which are the subject of further searches for triggered star formation regions. A portion of the SFO catalogue was known to be associated with molecular outflows and/or Herbig-Haro objects (highly collimated jets of partially ionized plasma moving away from young stars at supersonic speeds) so at least some of the SFO catalogue is known to contain star forming regions. The identification of these YSOs as *triggered* star formation regions is the primary aim of this study.

1.9 Archival Data

Much worthwhile astronomy may be achieved simply using the data available in publicly accessible archives. The Archives that have proved useful in writing this thesis are described here.

1.9.1 IRAS

The Infrared Astronomical Satellite (IRAS) was a joint project of the US, UK and the Netherlands and performed an, unbiased, sensitive, all sky survey at 12, 25, 60 and 100 μm. Launched in January 1983, IRAS ceased operations in November 1983 after having successfully surveyed more than 96% of the sky (The IRAS Explanatory Supplement[1], hereafter IRAS ES). The primary instrument of the IRAS was a 60 cm diameter liquid helium cooled, infrared telescope.

The IRAS catalogue consists primarily of a catalogue of infrared point sources and an atlas of absolute surface brightness images of the entire infrared sky. The limiting sensitivity of the IRAS catalogues, away from confused regions of the sky, is about 0.5 Jy at 12, 25 and 60 μm and about 1.5 Jy at 100 μm for point sources, and about a factor of three brighter than this for small extended sources (IRAS ES).

The IRAS Sky Survey Atlas (ISSA) is a set of FITS images of the infrared sky at 12, 25, 60 and 100 μm. The ISSA images were made from coadded IRAS survey data at moderate resolution. Full details of the ISSA images and their construction are given in the Explanatory Supplement to the IRAS Sky Survey Atlas.

1.9.2 HIRES Processing

The advantage of HIRES processing is that higher (near diffraction-limited) images may be obtained from the original IRAS images. HIRES employs the Maximum Correlation Method (MCM) (Aumann et al. 1990) to construct (resolution-enhanced) coadded images from the original IRAS images and is a three-step process summarised at the IRSA website[2]. In short,

1. Raw survey data in the format of CRDD (Calibrated, Reconstructed Detector Data) are retrieved. The full set of survey CRDD is stored in a FITS table format merged with the pointing (boresight) information.

2. A program called LAUNDR is used to clean up the CRDD. It removes 'glitches' from the scans, these are non-source-like signals usually caused by radiation hits on individual detectors. LAUNDR was also used here to remove a linear baseline from each individual detector scan, bringing all scans to a flat background.

[1] available at:http://irsa.ipac.caltech.edu/IRASdocs/exp.sup
[2] http://irsa.ipac.caltech.edu/IRASdocs/hires_over.html

3. A program called YORIC iteratively applies the MCM algorithm to the LAUNDR'd data. The default processing applies YORIC for 20 iterations.

The MCM algorithm is based upon the fact that when the IRAS was constructed data rate considerations forced the detector sizes to be much larger than the diffraction limit of the telescope itself ($\sim 22''$). The MCM algorithm is capable of producing near diffraction limited images from the original IRAS scans. YORIC creates a modelled flat sky observation from detector response functions, this simulated data is then used to correct the actual detector flux. In this way the effective point spread function at every point in the image can be used to enhance the resolution of the image.

HIRES Processing Defaults

These defaults are those chosen by the Infrared Processing and Analysis Centre (IPAC) to provide the best performance (highest resolution, freedom from artifacts) for the majority of targets, these defaults are not necessarily the best choice for any given specific target and data should be analysed for possible improvement in the reduction process parameters. The important default parameters are:

∗The image size is 1 degree by 1 degree.

∗The pixel size is $15''$.

∗All four bands are processed.

∗The data are de-striped with detector baseline removal and flux bias is applied.

∗The algorithm is iterated 20 times, with maps produced at the 1st, 5th, 10th and 20th iterations.

1.9.3 The NVSS

The compact D and DnC configurations of the Very Large Array (VLA) were utilised to create 1.4 GHz continuum and linear polarisation images. These configurations have a largest baseline of 0.59 km and a HPBW of $\sim 45\,''$. The full National Radio Astronomy Observatory (NRAO) VLA Sky Survey (NVSS) is based on 217,446 'snapshot' observations of partially overlapping primary-beam areas (Condon et al. 1998). The NVSS covered the area of sky north of J2000 δ = -40° and all the results obtained during the survey are available from the NVSS postage stamp server[3] to the entire astronomical community.

The resolution of the NVSS is $45''$ FWHM, the r.m.s. noise in unconfused regions is $\sigma \approx 0.45$ mJy beam^{-1}. The images are insensitive to smooth radio structures much larger than

[3]http://www.cv.nrao.edu/nvss/postage.shtml

several arcminutes in both coordinates (diffuse synchrotron emission from the Galaxy and the 3 K cosmic microwave background, for example) (Condon et al. 1998).

1.9.4 MSX

The Midcourse Space eXperiment (MSX) was a space mission designed and flown by the Ballistic Missile Defense Organisation (BMDO) and had multiple mission objectives, including infrared observations of the Earth itself. The main application of the MSX to astronomy was to complete a census of the Galactic plane in the mid-infrared regime, filling in areas missed by the IRAS survey and the COsmic Background Explorer/Diffuse InfraRed Background Experiment (COBE/DIRBE), or where the sensitivity of the IRAS was degraded by confusion noise arising in areas of high source densities or structured extended emission (Egan et al. 1999). The infrared instrument aboard the MSX (SPIRIT III) provided Nyquist sampling in the cross scan direction.

The MSX surveyed the entire galactic plane within the range $|b| \leq 5°$ (b = Galactic latitude) in four mid-infrared spectral bands between 6 and 25 μm at a spatial resolution of $\sim 18.3''$ (Price et al. 2001). The A band of the MSX is the most sensitive and ranges from 6.8 - 10.8 μm and includes the broad silicate band at 9.7 μm and the PAH emission features at 7.7 μm and 8.6 μm. Images were downloaded from the NASA/IPAC Infrared Science Archive[4] and were analysed using GAIA, part of the Starlink Software Collection. The MSX 8.3 μm images were smoothed to a resolution of $45''$, to match that of the NVSS images and improve the signal-to-noise ratio. The r.m.s. noise of each individual image was determined from off-source sky measurements and ranged from 1.5 - 39.1 $\times 10^5$ W m^{-2} sr^{-1}.

1.9.5 2MASS

The Two Micron All Sky Survey (2MASS) project made simultaneous observations in the J(1.24 μm), H(1.66 μm) and Ks(2.16 μm) near-infrared bands and used two 1.3 m telescopes, one at Mt. Hopkins, Arizona, and one at Cerro Tololo, Chile. The 2MASS covered 99.998% of the sky.

Point Source Catalog

The 2MASS All-Sky Release Point Source Catalogue (Cutri et al. 2003) contains astrometry and photometry in the three survey bandpasses for 470,992,970 sources. Positions, magnitudes, astrometric and photometric uncertainties and flags indicating the quality of the source characterizations are presented for each source. The photometric sensitivities of the 2MASS point source catalog are generally better than 15.8, 15.1 and 14.3 magnitudes at J,H and K_s bands respectively (sensitivities represent a signal to noise ratio of 10).

[4] http://irsa.ipac.caltech.edu

1.10 Aims

The main aim of this thesis is to determine the state of star formation within the northern SFO catalogue and to determine the effect that the ionisation of the BRCs has had upon any identified star formation. This aim will be achieved in the following ways,

1. Characterising the physical properties of IBLs; i.e. determining the properties of the IBLs at the edge of the clouds in the sample. Utilising the 20cm data available from the NVSS the pressure within the exterior boundary of the clouds maybe determined. This data will also assist the identification of the stars responsible for ionising the clouds.

2. Identifying the existence of star forming cores. A SCUBA survey of the northern SFO catalogue will allow the identification of submillimetre cores within the BRCs, analysis of the submillimetre emission will allow a determination of the properties of any star-forming cores within the cloud sample.

3. Looking for the signals of star formation. Molecular line observations will allow the identification of star-forming indicators, such as infall signatures and outflow characteristics. In addition, molecular line observations will allow the determination of the internal pressure of the clouds. This, in comparison with the IBL pressures determined from NVSS data will allow an analysis to be made of the pressure balance of the clouds in order to determine whether photoionisation shocks are being driven into the clouds concerned.

Chapter 2

Instrumentation

2.1 The JCMT

The James Clerk Maxwell Telescope (JCMT[1]) is the largest astronomical telescope in the world designed specifically to operate in the submillimetre wavelength region of the spectrum. The dish has a diameter of 15 m and is situated close to the summit of Mauna Kea, Hawaii, at an altitude of 4092m. The JCMT operates spectral line receiver systems currently operating in four frequency bands, 'A', 'B', 'C' and 'D', respectively covering about 211-276, 315-370, 430-510 and 625-710 GHz.

2.2 The SCUBA

The Submillimetre Common-User Bolometer Array (SCUBA) (Holland et al. 1999) is a dual-camera system mounted on the JCMT. The SCUBA is comprised of two bolometer arrays which simultaneously sample a similar field of view ($2.3'$ in diameter), a 91 pixel short-wave array, optimised for operation at 450 μm, and a long-wave array of 37 pixels optimised for operation at 850 μm. The bolometer arrays are arranged in a hexagon pattern (see Fig.2) and both arrays sample the sky simultaneously utilising a dichroic beamsplitter. The telescope's secondary mirror is moved in a 64 point 'jiggle' pattern to fill in the gaps in spatial coverage resulting from the spacing between individual bolometers.

SCUBA is optimised for detection of thermal dust emission emitted at temperatures between 3 and 30 K and is thus ideally suited to observations of protostellar and prestellar cores which are generally dusty environments at approximately 10-20 K. A dual-bladed 'chopper' allows the bolometers to switch between sky emission, the emission from an ambient temperature blade, or

[1] The JCMT is operated by the Joint Astronomy Centre on behalf of PPARC for the United Kingdom, the Netherlands Organisation of Scientific Research and the National Research Council of Canada.

the reflection of the cold internal optics from the back of a polished blade. Thus, SCUBA may be calibrated via a hot and cold load calibration system similar to that used with heterodyne systems (see Section 2.4.3).

2.2.1 Jiggle-Mapping Mode

The SCUBA is essentially both a camera and a photometer. To maximise its performance under various observing parameters there are four observing modes for use with the instrument (photometry, scan-mapping, jiggle-mapping and polarimetry), for the work undertaken in this thesis only the jiggle-mapping mode has been used.

Jiggle-mapping is used when either, a source is extended but still smaller than the array field of view or, when searching for point-like sources in a blank field. As mentioned in Section 2.2 SCUBA must 'jiggle' around a pattern of offset positions in order to fully sample the sky. For an individual array this pattern need only consist of 16 points, however to simultaneously sample both the long-wave and short-wave arrays it is necessary to carry out a 64-point jiggle pattern with 3 arcsec sampling (Holland et al. 1999).

The jiggle pattern is designed to Nyquist sample the image plane, this requires that pixels in the map plane should be of a size so that the FWHM of the beam is no less than 2.355 pixels across corresponding to the standard deviation of a Gaussian source function.

'Chopping' is performed in order to subtract the thermal sky emission from the final image. The chop size is typically of order 120 arcsec in order to chop away from the main array position. However, since the chopped beam travels through a different path length to the on-source beam the effects of short-term sky variability are not completely removed. For this reason the telescope is also 'nodded', the telescope is physically moved off-source, normally the primary mirror is moved to a new position where the source is now in the 'off' chop position and a new region of sky is observed. Any linear gradients in the sky emission may now be identified. The reason that both nodding and chopping is needed is that sky variability occurs over very small scales and thus only one technique is not sufficient. If a point source is the subject of the image, then chop throws may be reduced to only 30-40 arcsec. Increasing the chop throw to 120 arcsec for an extended source may result in a signal-to-noise degradation of a factor of two.

2.2.2 Atmospheric Effects

Submillimetre observations are especially susceptible to atmospheric effects, the transmission of submillimetre wavelength radiation through water vapour is extremely low. The site of the JCMT is at an extremely dry, high, site. Despite only having to overcome three percent of the

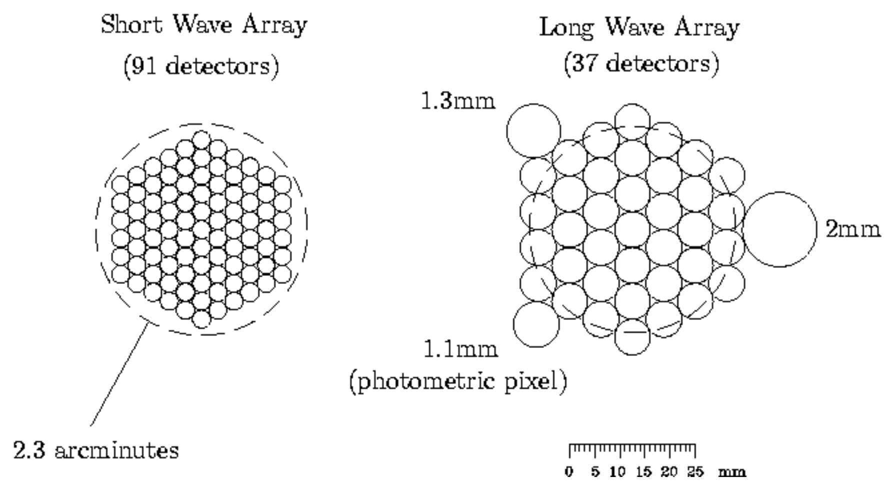

Figure 2: The layout of the SCUBA bolometers. Taken from Holland et al. (1999)

atmosphere's Precipitable Water Vapour (PWV), knowledge of the atmospheric attenuation of a source signal is vital for the correct calibration of SCUBA data. To measure the attenuation the telescope is dipped (usually between 80° and 15°, referred to as a 'skydip') and temperature reference measurements are taken from a hot load at ambient temperature and a cold load at 45 K. Knowing the transmission behaviour of the telescope it is then possible to derive the zenith sky opacity (Holland et al. 1999 and references therein). The Caltech Submillimetre Observatory (CSO) is situated near to the JCMT and operates a 225 GHz radiometer which performs a skydip in a fixed direction (azimuth = 316°) every ten minutes. The relationships between the SCUBA wavelengths and the CSO tau-meter are well established[2].

The JCMT Water Vapor Monitor (WVM) is situated in the receiver cabin and measures the sky opacity every 6 seconds. It is pointed just slightly off the main beam. The JCMT skydips, CSO and WVM tau measurements are well calibrated against each other. The WVM is generally the preffered measurement of the sky opacity as it has the highest resolution and is pointed in the direction of the main beam.

2.3 SCUBA Data Reduction

Data were edited and calibrated using the SCUBA User Reduction Facility (SURF) (Jenness & Lightfoot 2000) and the Starlink image analysis package KAPPA (Currie & Berry 2002). Initially, the sky emission measured during the 'nod' phase of the observations (in which the telescope is moved off-source) is subtracted from the on-source emission to remove the

[2]See the JCMT web pages at:http://www.jach.hawaii.edu/JACpublic/JCMT/Continuum_observing/SCUBA/astronomy/calibration/calib_atmosphere.html

contribution from general background radiation. Extinction values determined from one of the methods mentioned earlier (skydips or CSO-taumeter) are used to correct each pixel for the sky opacity at this point. Pixels that contain no emission from the source itself are selected manually in order to subtract the local sky emission from the image if they are readily apparent, pixels with spurious ‘spikes’ of noise are clipped to remove their emission from the total image and contributions from bolometers that have been overly noisy, malfunctioning or otherwise ‘bad’ during the observation period are removed from the data. The remaining flux values from each bolometer are now ‘binned’ into positions corresponding to their spatial distribution on the sky. The image is now complete, if uncalibrated.

2.3.1 Calibration

Two methods have been used in the calibration of the SCUBA data presented in this thesis, the method used for any particular map is dependant upon which calibration sources were available for observation at the time that sources were observed. The preferred method is primary calibration using Mars or Uranus.

Primary Calibration

A telescope’s response to sky emission is not generally spatially flat (i.e. the telescope will measure different levels of flux at two different points, even if the level of emission is in fact equal). Therefore, if an observed object is extended on the scale of the telescope’s beam, the pattern of the telescope response is convolved with the observed image. This is known as beam-, or flux-, coupling. Both Mars and Uranus are extended on the scale of the SCUBA beam, therefore flux coupling correction is required. In order to find the true HPBW of the telescope a simple deconvolution of the observed point spread function and the planetary disc contribution is performed using the formula

$$\theta_A = \sqrt{\theta_{obs}^2 - \frac{ln2}{2} W^2} \tag{1}$$

where θ_A is the Full-Width Half-Maximum (FWHM) of the telescope beam, θ_{obs} is the FWHM of the point spread function fitted to the convolved observation and W is the diameter of the planet given by the starlink program FLUXES (Privett et al. 1998).

The intensity response of a Gaussian beam to the planet’s flux is given by

$$I_p(r) = I_p(0) \int_0^{W/2} 2\pi r \; e^{-\frac{r^2}{2\sigma^2}} \mathrm{d}r \tag{2}$$

in which it is assumed that the telescope is centred upon the planet and that the planet is of area $\int_0^{W/2} 2\pi r \mathrm{d}r$ and has a peak intensity of $I_p(0)$. The solution of Eq.2 is

$$I_p(r) = I_p(0)\ 2\pi\sigma^2\big(1 - e^{-\frac{1}{2\sigma^2}\left(\frac{W}{2}\right)^2}\big) \tag{3}$$

dividing this quantity by the planet's area $(\pi\left(\frac{W}{2}\right)^2)$ gives the flux in one beam due to the planet's total flux S_{tot}. So, the flux density, S_{beam} is given by

$$S_{beam} = \frac{S_{tot}}{k} \tag{4}$$

where

$$k = \frac{x^2}{1 - e^{-x^2}} \tag{5}$$

and here

$$x = \frac{W}{1.2\theta_A} \tag{6}$$

The Flux Conversion Factor (FCF, the value by which the entire map is multiplied to convert it to units of Jy/beam) is then given by

$$FCF = \frac{S_{beam}}{V_{peak}} \tag{7}$$

where V_{peak} is the peak signal measured from the planetary map measured in volts.

Secondary Calibration

If a planetary source is not available for a calibration image then a secondary source is used, secondary sources are listed on the JCMT webpage[3] and the FCF in the case of a secondary calibrator being used is simply

$$FCF = \frac{S_{sec}}{V_{peak}} \tag{8}$$

where S_{sec} is the flux (in Jy) of the secondary calibrator (as quoted on the JCMT webpage) and V_{peak} is the peak flux of the map in volts.

For the sources observed in this thesis, absolute flux calibration was performed using calibration maps of the primary calibrators, Uranus and Mars, or the secondary calibrators CRL 618, CRL 12688, 16293-2422, IRC 10216 and OH 231.8 depending upon the observation date, time and sky position. Predicted fluxes for Uranus and Mars were estimated using the values given

[3]http://www.jach.hawaii.edu/JACpublic/JCMT/Continuum_observing/SCUBA/astronomy/calibration/secondary_2004.html

by the Starlink package FLUXES (Privett et al. 1998) and predicted fluxes for the secondary calibrators were taken from the JCMT calibrator webpage.

The JCMT Beam Shape

The JCMT has a well known error beam contribution to total flux measurements. Plots of typical beam shapes taken from maps of Uranus are shown in Figure 3 along with the fits to the beam shape. The total beam (primary beam + error beam) was modelled by fitting a combination of two circularly symmetric gaussian functions to azimuthally averaged beam maps of the primary calibrators. The gaussian fit parameters are given in Table 1. Calibrated images were converted to FITS format and deconvolved in order to remove the contribution from the error beam. The deconvolution was performed using the MIRIAD (Sault et al. 1995) *clean* task with a circularly symmetric representation of the double gaussian fit function. The maps were then restored to a resolution of $14''$ primarily to increase the signal-to-noise ratio of the 450 μm images. An example of the final cleaned and calibrated images is shown in Fig. 4

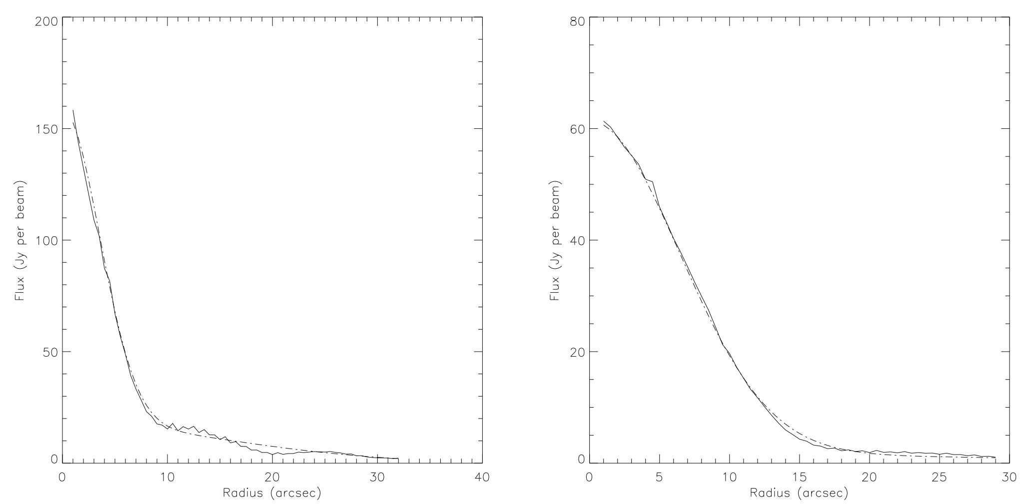

Figure 3: 450 μm (left) and 850 μm (right) beam shapes, the azimuthally averaged beams are shown as solid lines with modelled two-Gaussian fits to the beam shown as dashed lines.

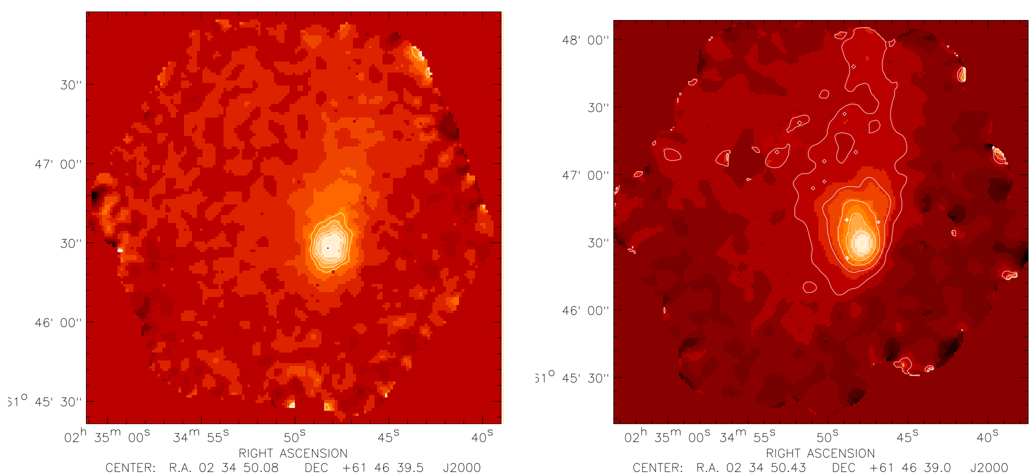

Figure 4: SFO 7 450 μm (left) and 850 μm (right) SCUBA images.

Table 1: Gaussian fit parameters for azimuthal averages of the primary calibrator beam maps.

Date	Wavelength (μm)	Main Beam FWHM($''$)	Main Beam Relative Peak	Error Beam FWHM($''$)	Error Beam Relative Peak
2^{nd} Nov 2001	450	8.0	0.962	32.2	0.038
	850	15.0	0.992	85.2	0.007
2^{nd} Dec 2001[a]	450	8.8	0.884	31.5	0.116
	850	15.3	0.949	56.8	0.051
7^{th} Jan 2002	450	9.2	0.952	40.9	0.048
	850	15.3	0.985	67.9	0.015
10^{th} Jan 2002[b]	450	9.2	0.952	40.9	0.048
	850	15.3	0.985	67.9	0.015
11^{th} Jan 2002[b]	450	9.2	0.952	40.9	0.048
	850	15.3	0.985	67.9	0.015
18^{th} Feb 2002[c]	450	9.0	0.913	29.7	0.087
	850	15.8	0.910	56.8	0.090
12^{th} Mar 2002[c]	450	8.1	0.943	32.9	0.057
	850	14.9	0.979	56.8	0.021
15^{th} Mar 2002[d]	450	9.7	0.822	31.6	0.178
	850	15.6	0.887	37.6	0.113
20^{th} Mar 2002	450	8.7	0.871	27.2	0.129
	850	14.9	0.960	48.1	0.040
21^{st} Mar 2002	450	9.7	0.822	31.6	0.178
	850	15.6	0.887	37.6	0.113
29^{th} Mar 2002	450	8.8	0.915	32.6	0.085
	850	15.5	0.983	82.9	0.017
30^{th} Mar 2002	450	9.7	0.822	31.6	0.178
	850	15.6	0.887	37.6	0.113
31^{st} Mar 2002	450	7.9	0.804	22.4	0.196
	850	14.9	0.959	46.6	0.041
19^{th} Apr 2002	450	9.4	0.878	31.0	0.122
	850	15.0	0.961	47.1	0.039
20^{th} Apr 2002	450	8.2	0.890	30.3	0.110
	850	15.3	0.981	70.1	0.019
21^{st} Apr 2002	450	8.3	0.890	36.3	0.110
	850	15.1	0.972	64.2	0.028

[a] No beam map data available, average beam assumed.
[b] No beam map data available. Beam shape of 7^{th} Jan 2002 assumed.
[c] 850 μm error beam unfittable, average 850 μm error beam assumed.
[d] No beam map data available. Beam shape of 20^{th} March 2002 assumed

2.4 JCMT Spectrometry

The spectral line observations covered in this thesis are that of ^{12}CO, ^{13}CO and C^{18}O observed in the $J = 2-1$ transition, along with HCO^{+} and H^{13}CO^{+} observed in the $J = 3-2$ transition. These lines have respective central frequencies of 230.538, 220.398, 219.560, 267.558 and 260.255 GHz.

'A' band spectral line observations at the JCMT cover the range of 211 - 276 GHz. This range includes the CO ($J = 2-1$) and HCO ($J = 3-2$) lines mentioned above. The spectrometer backend is the The 'Dutch' (or Digital) Autocorrelation Spectrometer (DAS).

Point-by-point spectral line observations can be made using either position-switching, or frequency-switching. Frequency-switching was used for all of the spectral line observations presented in this thesis apart from the ^{12}CO observations as this transition is expected to have a large width. Position-switching was used for the ^{12}CO observations, to avoid subtracting source emission from the overall line.

2.4.1 Frequency-switching

Frequency-switched observations consist of shifting the frequency of the local oscillator, in the case of the lines observed in this work by 8.1 MHz. The 'off' position gives a line-free reference so that the spectra may be calibrated. Frequency-switching is most useful for narrow lines so that source emission is not included at the switch frequency. Frequency-switching is also useful for spatially extended objects for which position-switching may not be a convenient option. An advantage of frequency switching, compared to position switching, is that less time is spent physically moving the telescope, so more time may be spent observing the target source.

2.4.2 Position-switching

In position-switched observations the telescope alternately observes the source and a reference position, this provides the observer with a pair of spectra from which a calibrated result may be obtained eliminating most instrumental and atmospheric effects.

2.4.3 Calibration Of Spectral Line Data

Noise cannot be completely eliminated from any receiver, and so it must be accounted for. To account for the noise in a receiver, a 'hot load' and a 'cold load' (typically at room temperature and $\sim$ 80K respectively) are physically placed in front of the receiver's input beam. In measuring the power of a load, the output is the power emitted by that load as well as the power due to the noise inherent in the receiver. In the Rayleigh-Jeans domain, power is directly proportional to temperature, so measurements of the hot and cold loads can be expressed as $T_m(H) = T_H + T_N$ and $T_m(C) = T_C + T_N$ respectively, where $T_m(H)$ and $T_m(C)$ are the temperatures measured when the hot and cold loads are placed in the beam respectively, T_H and T_C are the known temperatures of the hot and cold loads and T_N is the temperature added to the measurement by the noise of the receiver, assumed to be equal at both temperatures. The ratio of these two measurements can thus tell the observer the amount of noise added to the measurement.

During each observing run a 'standard source' is observed. This source will be a well-known, non-variable source that enables the response of the system to be determined at any particular time. Values for standard source spectra are well known and generally available on the JCMT web-page, calibrated to the standard T_A^* antenna temperature scale. The $antennatemperature$, T_A^* is the temperature of a (presumably distant) blackbody that would produce the observed power measurement, irrespective of whether or not the antenna is observing a thermal source or if that source actually fills the antenna's power pattern, or beam. Data from the observations are generally calibrated to the standard T_A^* antenna temperature scale at the telescope which accounts for the optical depth of the atmosphere, the radiation efficiency and rearward spillover. Rearward and forward spillover are contributions to the telescope's received radiation that do not come from the main beam. Rearward spillover is radiation that comes from behind the dish and is intercepted by the prime focus of the telescope. Forward spillover occurs in secondary focus antenna, it is radiation that is intercepted by the secondary focus that has not come via the prime focus path. Rearward and forward spillover are shown in Fig.5, the direction is shown in terms of transmission, which, by reciprocity also describes reception in reverse. In order to determine the actual brightness temperature of the source (the temperature resulting in the given brightness if inserted into Jeans' law, see chapter 3), the antenna temperature must be corrected for the forward spillover of the beam, η_{fss}, and the coupling efficiency of the beam, η_c. In practise, η_c is very difficult to measure and is considered to be of order unity, satisfactory as long as the source is extended relative to the beam. Here, a scale named the corrected receiver scale is used, in which,

$$T_R^* = \frac{T_A^*}{\eta_{fss}} \tag{9}$$

for the A3 receiver η_{fss} is 0.8.

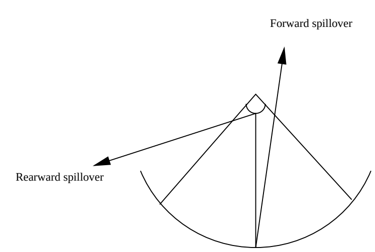

Figure 5: Secondary focus antenna with forward and rear spillover.

2.4.4 Data Reduction

Data were reduced using the Starlink software package SPECX. Polynomial baselines were fitted to the line-free emission and subtracted from the spectra as a whole. R.M.S. measurements were performed using line-free channels and the peak temperatures, line widths (at half-power) and line centre positions were measured.

Chapter 3

Theory

3.1 Ionisation And Recombination

3.1.1 The Strömgren Sphere

As a star ignites and begins emitting ionising radiation into its surroundings (ionising radiation being that with an energy, $h\nu$, greater than that required to ionise hydrogen, 13.6 eV) a sphere of ionised gas expands around it as the surrounding molecular material is dissociated and the atomic gas is ionised. This sphere of ionised gas is separated from the molecular material (unaffected by the fledgling star) by a partially ionised shell of gas of a radius defined by the mean free path length of an ionising photon, $1/n\sigma_\nu$ where n is the number density of atoms and σ_ν is the ionisation cross-section of the surrounding material for photons of frequency ν. This mean free path length is typically much less than the radius of the ionised sphere and the shell which it parameterises is known as the ionisation front.

For the sphere to reach equilibrium the total number of ionising photons emitted by the star must equal the total number of recombinations occuring within the surrounding material per unit time.

$$S_i = \int_0^V n^2 \alpha dV = \frac{4}{3} R_S^3 \pi n^2 \alpha \tag{10}$$

where S_i is the emitted flux of photons, V is the volume of the ionised region, α is the recombination coefficient and R_S is the radius of the (assumed uniformly dense) spherical ionised region. In this state of equilibrium the sphere is known as a Strömgren sphere. Rearranging,

$$R_S = \sqrt[3]{\frac{3S_i}{4\pi n^2 \alpha}} \tag{11}$$

The frequency of the radiation produced by recombinations within the ionised sphere is generally close to the ionisation frequency as most recombinations occur in slow moving material, adding little energy to the emitted photon. The ionised gas is also generally optically thick to these photons and so the mean free path of these photons is small, meaning that the assumption may be made that any photons produced by recombination processes instantly ionise another atom within the immediate vicinity. This is called the 'on the spot' approximation.

3.2 Thermal Emission

Continuum emission from YSOs in submillimetre and infrared regimes is thought to originate in several regions incorporating and surrounding the hot core of a star-forming cloud. The stellar photosphere is the 'visible surface' of the star, i.e. the region where the optical depth ≈ 1. Radiation resulting from the nuclear reactions in the core of a star travels outward through opaque layers until the opacity is low enough to allow the radiation to pass into interstellar space, thus preserving the image of the last layer that emitted it, this being the photosphere.

The star accretes material from the circumstellar disc, the point at which this occurs forms a boundary between the star itself and the more diffuse material surrounding it. The process of accretion releases energy at infrared and submillimetre wavelengths.

The radiation emitted by the photosphere is reprocessed by the circumstellar disc, this, along with energy arising from accretion within the disc results in the emission of submillimetre and infrared radiation. The contribution from the disc is a significant fraction of the total radiation observed in YSOs and has, in fact, been suggested as the principal source of submillimetre emission from T Tauri stars. The discs are usually cool, with a flat spectrum showing a near-independence of luminosity upon frequency over a wide range (Beckwith et al. 1990).

The consideration of what constitutes the 'edge' of a circumstellar disc is a contentious issue. A typical summary of the structure of a star forming cloud is a disc less than ~ 100 AU in radius, which is in turn surrounded by an 'envelope' of outer radius 10^2 - 10^3 AU. The definition of this envelope as a separate entity, or as a more diffuse, tenuous region of the circumstellar disc is still a matter of debate.

The cloud incorporating the star formation region is opaque to the radiation of the internal stellar source. At submillimetre and infrared wavelengths it is possible to observe the reprocessed radiation of the surrounding material. The emission that is observed is due to the dust grains that form the envelope and colder surrounding cloud. In 'prestellar' cores, prior to star formation, low temperature gas-phase reactions dominate the chemistry, leading to the formation of small radicals and unsaturated molecules (Langer et al. 2000). Higher temperatures may exist locally surrounding newly formed stars. YSOs heat their surrounding dust to a few hundred K providing a bright continuum.

The thermal emission observed toward star-forming cores then originates from dust grains, heated from within by an embedded YSO. The composition of these dust grains is an important area of study into the earliest stages of star formation.

3.2.1 Evidence For Dust

Extinction is a well-established and observed phenomenon (e.g. Gibson et al. (1997); Sartori & Lepine (1996); Lada et al. (1994)) in which light from distant sources (stars, star-forming regions, other galaxies etc.) is obscured by some process or agent. We can define extinction by an extinction coefficient α, such that the observed intensity of a distant source, I_ν, is the function of that source's emitted intensity, $I_{\nu o}$, α and the distance, l, through which the observed radiation has travelled through the interstellar medium, thus.

$$I_\nu = I_{\nu o} \exp(\, - \int_0^l \alpha \, \mathrm{d}l) \tag{12}$$

The coefficient α is not constant but is approximately proportional to the density of gas and dust in the interstellar medium and, in fact, is a sensitive function of the chemistry in regions of high chemical variability. Observations of the effects of extinction have been made at many wavelengths and is found to vary as a function of frequency, approximated by the curve shown in Fig. 6. The strongest feature in the interstellar extinction curve is the ultraviolet bump at 0.2 μm. Recent results point toward a carbonaceous molecule causing the UV bump (Ehrenfreund & Charnley 2000).

For a particular wavelength regime, in which it is implicitly assumed that extinction is due to dust grains in the observed star-forming cloud, Eq. 12 may be replaced with a more specific formulation. The assumption has been made that there is a common grain radius a in uniform cloud of number density n_g m^{-3}. Then,

$$I_\nu = I_{\nu o} \exp(\, - n_g \pi a^2 Q_{ext} l) \tag{13}$$

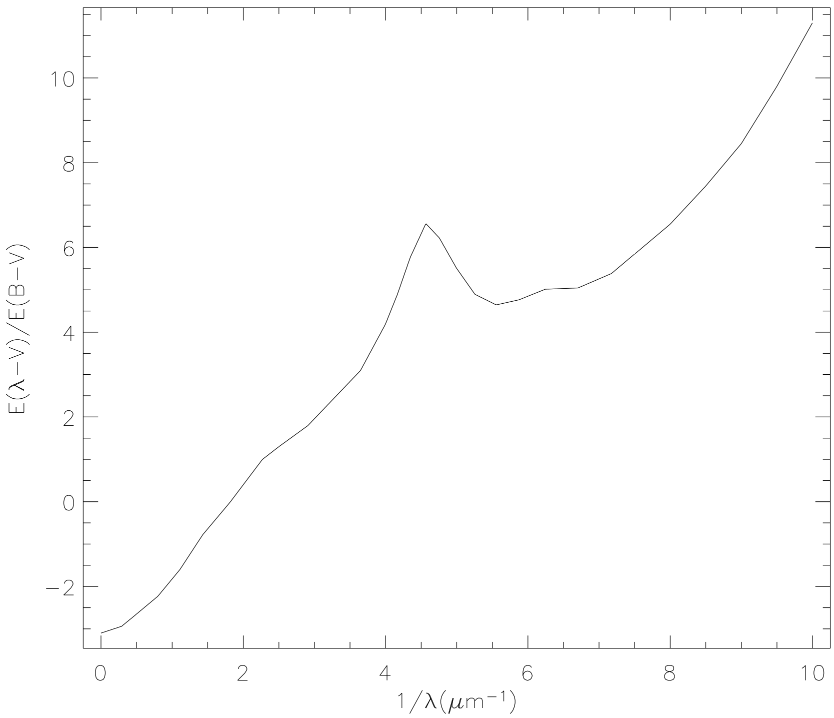

Figure 6: The interstellar extinction curve. Data points taken from Savage & Mathis (1979).

where Q_{ext} is called the efficiency factor for extinction and is made up of two parts,

$$Q_{ext} = Q_{abs} + Q_{sca} \tag{14}$$

in which both absorption (Q_{abs}) and scattering (Q_{sca}) by each grain are considered. The relative radiative losses due to each mechanism are dependant upon the refractive index of the grain material. By selecting appropriate values of the refractive index and of grain size it is a trivial task to fit any portion of the interstellar extinction curve with a combination of grain chemistries. The problem in this method is that because of the number of free parameters, the fits are not necessarily unique. Through spectral features, laboratory measurements, and the modelling of radiative transfer processes, a mixture of graphite and silicate grains appears to be the predominant component of the interstellar medium responsible for extinction, with a size distribution approximated by a power law with an exponent of n= -3.3 to -3.6 (Mathis et al. 1977) (i.e. $N(a) \propto a^n$).

3.3 Greybody Modelling

From the description of thermal emission above it is clear that the continuum emission from dust results from a complex combination of dust chemistry, dust grain size, as well as bulk properties such as temperature and density. While these properties may be assumed to be reasonably similar from object to object on a large scale, especially when comparing objects that are known to be similar in composition (e.g. YSOs), on a small scale these properties may change drastically. The chemical composition and size distribution of dust grains will change depending upon the physical conditions in their environment. In star forming clouds the chemical composition of dust grains surrounding the central protostellar object is dependent upon the opacity of local material, which shields molecules from radiative dissociation. The density of the material, which itself changes over relatively small scales, has an effect upon the rate at which collisional and surface processes occur. The chemical abundances will also change as a function of temperature due to the variation of sublimation temperatures between species.

Despite the difficulties in determining the actual composition and behaviour of each of these different chemical regimes, dust emission is still useful as an astronomical probe, if only because it is one of the few tools available with which astronomers are able to investigate star-forming regions.

Greybody analysis consists of a number of assumptions about the properties of the dust clouds. The greybody method is so called because of the variation from the behaviour of a blackbody in dust clouds. The photons that are observed originate from regions where the optical depth τ, < 1 and thus the observed radiation is a summation of all of the photons emitted by the dust grains along the line of sight to a depth of $\tau \simeq 1$. By assuming that these photons are representative of the physical conditions within the dust cloud, average densities and temperatures along the line of sight may be determined. However, this argument is not without flaw, star-forming regions are neither uniformly dense or isothermal.

To fully investigate the nature of the emission arising from star-forming regions a full treatment of the radiative transfer process is required. This is a complex and detailed procedure, especially in more than one dimension, and is beyond the scope of this thesis. Detailed radiative transfer solutions have been performed in a number of cases (e.g. Shirley et al. (2003); Steinacker et al. (2004); Stamatellos et al. (2004)) and, despite the fundamental flaws in performing a grey-body analysis, the results are often in close agreement, implying that such simple analyses may be effective in determining the bulk properties of a dust cloud at scales comparable to, or larger than, the angular resolution of FIR telescopes (Gordon 1995). This assumption must however be treated with caution as, in no cases, have the clouds in question been subjected to a full

radiative transfer solution. The greybody modelling procedure is as follows.
The averaged temperature of the dust cloud along the line of sight, and global optical depth of an object, is determined by a greybody fit (e.g. Dent et al. (1998)) of the form

$$F_\nu = \Omega B_\nu(T_d)(1 - e^{-\tau_\nu}), \tag{15}$$

where F_ν is the flux measured (in Janskys, i.e. 10^{-26}W Hz^{-1} m^{-2}) at a frequency ν (in Hz), Ω (in radians) is the solid angle subtended by the cloud in question, $B_\nu(T_d)$ is the Planck function (in Janskys) evaluated at a dust temperature, T$_d$, and frequency, ν, and τ_ν is the optical depth at frequency ν.

The approach has been adopted of parameterising the optical depth, τ_ν, in terms of the dust emissivity, β, so that τ may be evaluated at arbitrary ν from a known reference frequency, ν_{ref} and optical depth τ_{ref}, i.e. $\tau_\nu = \tau_{ref}\left(\frac{\nu}{\nu_{ref}}\right)^\beta$. β has been found to range from 0.7 up to ~ 2, with lower values generally being found for embedded star forming objects as opposed to the general extended cloud emission (Huard et al. 1999 and references therein). Greybody fitting here is performed at wavelengths at which the emission is extended (or unresolved in the case of IRAS fluxes). To maintain consistency with other works (e.g. Thompson et al. (2004b)) the value of $\beta = 2$ has been adopted.

The mass of the dust and gas present in the star-forming clouds for which greybody analyses have been carried out may be found by making certain assumptions. For an optically thin cloud with a uniform temperature the total ($M_{dust}+M_{gas}$) mass of the cloud M is given by Hildebrand (1983),

$$M = \frac{d^2 F_\nu C_\nu}{B_\nu(T_d)}, \tag{16}$$

where d is the distance to the cloud in parsecs, F_ν is the observed flux density in Janskys and $B_\nu(T_d)$ is the Planck function (in Janskys) evaluated at frequency, ν (Hz), and dust temperature, T_d (K). The parameter C_ν is a mass conversion factor combining both the dust-to-gas ratio and the frequency dependent dust opacity, κ_ν. Quoted values for C_ν range from 21.4 g cm^{-2} (Kruegel & Siebenmorgen 1994) to 286 g cm^{-2} (Draine & Lee 1984). A value of $C_\nu = 50$ g cm^{-2} at $\nu = 850$ μm has been adopted here following Thompson et al. (2004a), who observed submillimetre cores around the object SFO 11 taken from the SFO catalogue.

The uncertainties in the mass (and hence density) of the clouds are generally dominated by temperature effects in the non-linear Planck function in Eq.16. Typical values of observed 850 μm flux and SED determined dust temperature, have uncertainties of $\sim$ 10% and $\pm$ 1-2 K respectively leading to an factor of $\sim \sqrt{2}$ uncertainty in mass and density. However, in the case of low signal-to-noise ratios this uncertainty may rise to a factor of 10.

3.4 Emission Processes

The generic description of radiation is Planck's law,

$$B_\nu = \frac{2h\nu^3}{c^2}\frac{1}{e^{h\nu/k_BT}-1} \tag{17}$$

in which B_ν is the measured intensity of the radiation emitted at frequency ν by a blackbody at a temperature T, k_B represent Boltzmann's constant . For thermal sources for which $h\nu/k_BT \ll 1$ then the Rayleigh - Jeans' law becomes applicable which states that

$$B_\nu = \frac{2k_B\nu^2}{c^2}T \tag{18}$$

even where the criterion $h\nu/k_BT \ll 1$ does not hold the condition

$$T_B = \frac{c^2}{2k_B\nu^2}B_\nu \tag{19}$$

may still be applied though, in this case, the quantity T_B is not the thermodynamic temperature of a black-body. The quantity T_B will be covered in more detail later.

As radiation passes through a medium it is subject to various processes, the intensity of the radiation will change due to gains, $\mathrm{d}I_{\nu+}$, and losses, $\mathrm{d}I_{\nu-}$. thus,

$$\mathrm{d}I_{\nu+} = -\kappa I_\nu \mathrm{d}s \tag{20}$$

and

$$\mathrm{d}I_{\nu-} = \epsilon_\nu \mathrm{d}s \tag{21}$$

along a path length $\mathrm{d}s$.

So the change of intensity through a slab of thickness $\mathrm{d}s$ will be:

$$[I_\nu(s+\mathrm{d}s) - I_\nu(s)]\mathrm{d}\sigma\mathrm{d}\Omega\mathrm{d}\nu = [-\kappa_\nu I_\nu + \epsilon_\nu]\mathrm{d}\sigma\mathrm{d}\Omega\mathrm{d}\nu\mathrm{d}s \tag{22}$$

$$\Rightarrow \frac{\mathrm{d}I_\nu}{\mathrm{d}s} = -\kappa_\nu I_\nu + \epsilon_\nu \tag{23}$$

where κ_ν is the opacity or the material and ϵ_ν is the emissivity of the material. $\mathrm{d}\sigma$ $\mathrm{d}\Omega$ and $\mathrm{d}\nu$ here represents the intervals of cross-sectional area, solid angle and frequency respectively.

If there is equilibrium (i.e. the losses in the material match the gains) then $\kappa_\nu I_\nu = \epsilon_\nu$ and the brightness distribution will be described by a black-body function with the temperature of the medium, assuming that the medium is in Local Thermodynamic Equilibrium (LTE).

$$\frac{\epsilon_\nu}{\kappa_\nu} = B_\nu(T) \quad \text{(Kirchoff's law)}$$

Now define optical depth $\mathrm{d}\tau_\nu$,

$$\mathrm{d}\tau_\nu = \kappa_\nu \mathrm{d}s \tag{24}$$

then Eq. 23 can be written as

$$\frac{1}{\kappa_\nu}\frac{\mathrm{d}I_\nu}{\mathrm{d}s} = \frac{\mathrm{d}I_\nu}{\mathrm{d}\tau_\nu} = -I_\nu + B_\nu(T). \tag{25}$$

Multiply by $e^{-\tau_\nu}$ and integrate by $\mathrm{d}\tau_\nu$

$$\int_0^{\tau_\nu(0)} e^{-\tau_\nu}\frac{\mathrm{d}I_\nu}{\mathrm{d}\tau_\nu}\mathrm{d}\tau_\nu = \int_0^{\tau_\nu(0)} (-I_\nu + B_\nu(T))e^{-\tau_\nu}\mathrm{d}\tau_\nu \tag{26}$$

This integral is solvable through partial integration to give

$$I_\nu(s) = I_\nu(0)e^{-\tau_\nu} + \int_0^{\tau_\nu(0)} B_\nu(T)e^{-(\tau_\nu - \tau_\nu')}\mathrm{d}\tau_\nu' \tag{27}$$

If the medium is isothermal then

$$I_\nu(s) = I_\nu e^{-\tau_{\nu(0)}} - B_\nu(T)(1 - e^{-\tau_\nu}). \tag{28}$$

The brightness temperature, T_B, may be defined by the relation

$$I_\nu = B_\nu(T_B), \tag{29}$$

this is especially useful in situations in which the Rayleigh-Jeans' law may be applied so that Eq. 19 may be applied. So that

$$T_B = \frac{c^2}{2\nu^2 k_B} I_\nu. \tag{30}$$

Using the above relations along with Eq. 25 we can give the transfer equation the simple form of

$$\frac{\mathrm{d}T_B}{\mathrm{d}\tau_\nu} = -T_B(s) + T(s) \tag{31}$$

where $T(s)$ is the blackbody temperature of the medium at s.

So, for an isothermal medium

$$T_B(s) = T_B(0)e^{-\tau_\nu} + T(1 - e^{-\tau_\nu}) \tag{32}$$

3.5 Temperature Scales

Thus far, all analyses have been made assuming that the observed emission arises from a continuum spectrum. The following descriptions now treat the phenomena of molecular transition lines, in which the emission in question arises from photons of specific frequencies, emitted due to changes in energy levels in molecules located in the region under observation. These molecular processes will be subjected to more detailed scrutiny in section 3.6.

A useful quantity in the analysis of an astrophysical medium is the 'radiation temperature' found by equating the total Planck function to the approximation in the Rayleigh-Jeans limit,

$$B_\nu = \frac{2h\nu^3}{c^2}\frac{1}{e^{h\nu/k_BT}-1} = \frac{2\nu^2}{c^2}k_BT_B \tag{33}$$

$$J_\nu = \frac{c^2}{2k_B\nu^2}I = \frac{h\nu}{k_B}\frac{1}{e^{h\nu/k_BT}-1} \tag{34}$$

where J_ν is the observed temperature above the background level. So, assuming that $T_B(0) = 0$ (i.e. that the temperature required to produce a brightness of 0 is 0) and then correcting for background temperature (assumed equal to the cosmic microwave background radiation temperature $T_{bg} = 2.7K$) Eq. 33 becomes

$$T_B = \frac{h\nu}{k_B}\Big(\frac{1}{e^{h\nu/k_BT}-1} - \frac{1}{e^{h\nu/k_BT_{bg}}-1}\Big)\left(1-e^{-\tau_\nu}\right) \tag{35}$$

Some assumptions on the nature of the medium under scrutiny are necessary at this point:
- all of the molecules along the line of sight possess a uniform excitation temperature in the transition in question and that the excitation temperatures of the two isotopic species are equal and that the cloud is in at least local thermodynamic equilibrium (i.e. that the excitation temperatures of the species are equal to the kinetic temperature of the gas);
- that at least one of the isotopic species in question is optically thick. This means that the common excitation temperature may be obtained from the peak radiation temperature of this line.

Because of the assumption that the medium is optically thick to radiation at the frequency of at least one of the lines observed ($\tau_\nu \gg 1$) then the factor of $1 - e^{-\tau_\nu}$ in Eq. 35 $\rightarrow 1$ so,

$$T_B = \frac{h\nu}{k_B}\Big(\frac{1}{e^{h\nu/k_BT}-1} - \frac{1}{e^{h\nu/k_BT_{bg}}-1}\Big) \tag{36}$$

which gives,

$$T_{ex} = T_o\Big[ln\Big(\frac{T_o}{T_B + T_oJ(T_{bg})} + 1\Big)\Big]^{-1} \tag{37}$$

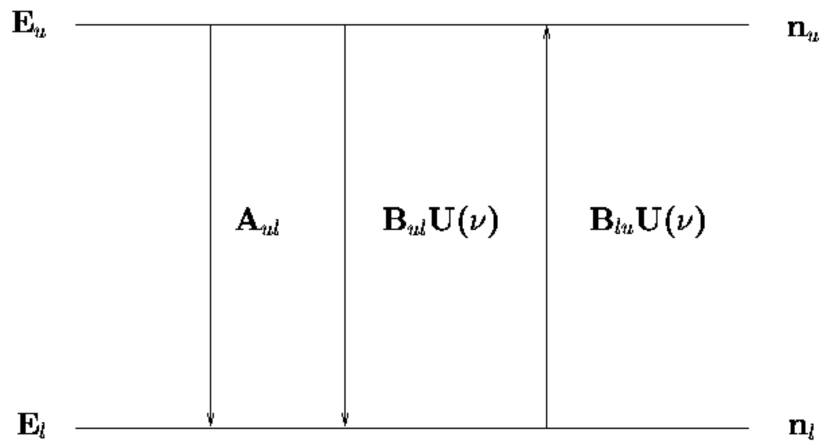

Figure 7: A simple two level molecule.

where T_o is equivalent to $\frac{h\nu}{k_B}$. Now knowing T_{ex} for all species one can solve Eq. 35 for τ_ν,

$$\tau_\nu = -ln\Big[1 - \frac{k_B T_B}{h\nu}\Big(\frac{1}{e^{T_o/T_{ex}} - 1} - \frac{1}{e^{T_o/T_{bg}} - 1}\Big)^{-1}\Big] \tag{38}$$

thus the optical depth of observed optically thin lines may be found using the excitation temperature found using the radiation of an optically thick line.

3.6 Molecular Levels

Changes in the energy levels of a molecule may be described using the Einstein coefficients A_{ul}, B_{ul} and B_{lu}. In the simple case of a two level molecule with level 1 (l) separated from level 2 (u) by an energy $h\nu$ (Fig.7) the coefficient A_{ul} describes the probability per unit time that a molecule will spontaneously drop from level 2 to level 1, emitting a photon of energy $h\nu$ in the process, $B_{ul}U(\nu)$ is the probability per unit time that a molecule will be stimulated into emitting a photon of energy $h\nu$ through the surrounding radiation field described by $U(\nu)$ (the average energy density of the radiation field) and $B_{lu}U(\nu)$ is the probability per unit time that the molecule will absorb a photon of energy $h\nu$, thereby increasing the energy of the molecule by $h\nu$, from the lower to upper level.

Assuming that collisional processes do not dominate the population levels of the molecule and that the gas is in thermal equilibrium then the number of molecules dropping from energy level 2 to 1 will be matched by the number of molecules jumping from energy level 1 to 2, i.e.

$$n_u \left(A_{ul} + B_{ul}U(\nu)\right) = n_l B_{lu} U(\nu) \tag{39}$$

In thermal equilibrium all available energy levels are populated according to the Boltzmann distribution

$$\frac{n_u}{n_l} = \frac{g_u}{g_l} e^{-h\nu/k_B T} \tag{40}$$

where g_u and g_l are the degeneracies of the upper and lower energy states respectively and T is the temperature of the gas.

From Eq. 39 and 40,

$$U(\nu) = \frac{A_{ul}}{B_{ul}} \Big(\frac{g_l}{g_u} \frac{B_{lu}}{B_{ul}} e^{h\nu/k_B T} - 1 \Big)^{-1}. \tag{41}$$

In thermal equilibrium

$$U(\nu) = \frac{8\pi h \nu^3}{c^3} \frac{1}{e^{h\nu/k_B T} - 1} \tag{42}$$

(i.e. radiation described by the Planck function) which can only be true given Eq.41 if $g_l B_{lu} = g_u B_{ul}$

so

$$U(\nu) = \frac{A_{ul}}{B_{ul}} \frac{1}{e^{h\nu/k_B T} - 1} = \frac{8\pi h \nu^3}{c^3} \frac{1}{e^{h\nu/k_B T} - 1} \tag{43}$$

$$\therefore B_{ul} = \frac{g_l}{g_u} B_{lu} = \frac{c^3}{8\pi h \nu^3} A_{ul} \tag{44}$$

Combining the three possible mechanisms for energy transitions in the 2-level molecule (ignoring collisional and lasing processes),

$$\mathrm{d}E_e(\nu) + \mathrm{d}E_s(\nu) - \mathrm{d}E_a(\nu) = \mathrm{d}I_\nu \mathrm{d}\Omega \mathrm{d}\sigma \mathrm{d}\nu \mathrm{d}t$$

$$= \frac{h\nu}{4\pi} \Big[n_u A_{ul} + n_u B_{ul} \frac{4\pi}{c} I_\nu - n_u B_{lu} \frac{4\pi}{c} I_\nu \Big] \phi(\nu) \mathrm{d}\Omega \mathrm{d}\sigma \mathrm{d}s \mathrm{d}\nu \mathrm{d}t \tag{45}$$

where

$$\mathrm{d}E_e(\nu) = h\nu n_u A_{ul} \phi_e(\nu) \mathrm{d}V \frac{\mathrm{d}\Omega}{4\pi} \mathrm{d}\nu \mathrm{d}t \tag{46}$$

$$\mathrm{d}E_a(\nu) = h\nu n_l B_{lu} \frac{4\pi}{c} I_\nu \phi_a(\nu) \mathrm{d}V \frac{\mathrm{d}\Omega}{4\pi} \mathrm{d}\nu \mathrm{d}t \tag{47}$$

and

$$\mathrm{d}E_s(\nu) = h\nu n_u B_{ul} \phi_e(\nu) \mathrm{d}V \frac{\mathrm{d}\Omega}{4\pi} \mathrm{d}\nu \mathrm{d}t \tag{48}$$

where $\phi_e(\nu)$ and $\phi_a(\nu)$ are the line profiles for emission and absorption respectively. The assumption has been made that $\phi_e(\nu) = \phi_a(\nu) = \phi(\nu)$

Rearranging Eq.45

$$\frac{\mathrm{d}I_\nu}{\mathrm{d}s} = -\frac{h\nu}{c}\left(n_l B_{lu} - n_u B_{ul}\right) I_\nu \phi(\nu) + \frac{h\nu}{4\pi} n_u A_{ul} \phi(\nu) \tag{49}$$

which, through comparison with Eq.23 (and remembering that $g_l B_{lu} = g_u B_{ul}$) gives

$$\kappa = \frac{h\nu}{c} n_l B_{lu} \Big(1 - \frac{g_l n_u}{g_u n_l}\Big) \phi(\nu) \tag{50}$$

and

$$\epsilon_\nu = \frac{h\nu}{4\pi} n_u A_{ul} \phi(\nu) \tag{51}$$

using Eq.44

$$B_{lu} = \frac{g_u}{g_l} A_{ul} \frac{c^3}{8\pi h \nu^3} \tag{52}$$

and utilising Eq.40

$$\kappa = \frac{c^2}{8\pi\nu^2} \frac{g_u}{g_l} n_l A_{ul} \left[1 - e^{-h\nu/k_B T}\right] \phi(\nu) \tag{53}$$

here, the expression $1 - e^{-h\nu/k_B T}$ is a correction for stimulated emission which ~ 1 even for $T \sim 10^4$K in the UV and visual regime, this is not necessarily the case in the radio regime however and must be included.

Remembering Eq.24 and rearranging again using Eq.40 gives,

$$\tau_\nu = \int \kappa_\nu \mathrm{d}s = \frac{c^2}{8\pi\nu^2} A_{ul} \left[e^{h\nu/k_B T} - 1\right] \phi(\nu) \int n_u \mathrm{d}s \tag{54}$$

we may now use the relation $\int n_u \mathrm{d}s = N_u$, here N_u is the *column* density of the source.

Integrating over all τ, using the more convenient variable of velocity using the conversion $\mathrm{d}v = \frac{c}{\nu}\mathrm{d}\nu$ and the fact that $e^{h\nu/k_B T} - 1 \rightarrow h\nu/k_B T$ for $h\nu \ll k_B T$

$$\int \tau_\nu \mathrm{d}v = \frac{h\nu}{k_B T} \frac{c^3}{8\pi\nu^3} N_u A_{ul} \tag{55}$$

noting that the term $\phi(\nu)\mathrm{d}\nu$ disappears as it is normalised such that $\int \phi(\nu)\mathrm{d}\nu = 1$.

For a linear molecule,

$$A_{ul} = \frac{1}{4\epsilon_0} \frac{64\pi^3}{3hc^3} \nu_{ul}^3 |\mu_{ul}|^2 \tag{56}$$

where ϵ_0 is the permittivity of free space, $|\mu_{ul}|^2 = \mu^2 \frac{J+1}{2J+3}$ and μ is the electric dipole moment in debyes.

For optically thin transitions $\int T_B \mathrm{d}v$ can be approximated to $[J_\nu(T) - J_\nu(T_{bg})] \int \tau_\nu \mathrm{d}v$ so

$$N_u = \frac{3\epsilon_0 T}{2h}\Big(\frac{k_B}{\pi\nu\mu}\Big)^2 \frac{(2J+3)}{(J+1)}\Big(\frac{1}{e^{h\nu/k_B T}-1} - \frac{1}{e^{h\nu/k_B T_{bg}}-1}\Big)^{-1} \int T_B \mathrm{d}v \tag{57}$$

This allows the calculation of the number of molecules in the upper energy state, in order to calculate the total number of molecules the fraction $\frac{N_u}{N_{Tot}}$ must be ascertained.

$$\frac{N_{J+1}}{N_{Tot}} = \frac{2J+1}{Z}\exp\Big(-\frac{hBJ(J+1)}{k_B T}\Big) \tag{58}$$

where N_{J+1} and N_{Tot} are the relative numbers of molecules in the upper and all levels respectively, B is the rotational constant and Z is the partition function.

$$Z = \sum_{J=0}^{\infty}(2J+1)e^{\frac{-hBJ(J+1)}{k_B T_{ex}}} \tag{59}$$

where B is the rotational constant of the molecule in question. If the temperature is large compared to the separation between energy levels then the partition function may be simplified to

$$Z \simeq \frac{k_B T_{ex}}{hB}, \tag{60}$$

for $C^{18}O$ the difference between using Eq. 59 and Eq. 60 becomes significant (>%10) at temperatures below 17 K. As the excitation temperatures found for the sources in question all exceed 24 K (Chapter 6) the use of Eq. 60 is justified. Many protostellar regions are found to be much colder than this, e.g. Bok globules have temperatures normally $\sim$ 10 K.

The total number of molecules along the line of sight is

$$N_{Tot} = \frac{3\epsilon_0 k_B^3}{2B}\Big(\frac{T_{ex}}{h\pi\nu\mu}\Big)^2 \frac{(2J+3)}{(J+1)} \frac{e^{hBJ(J+1)/k_B T}}{(2J+1)}\Big(\frac{1}{e^{h\nu/k_B T_{ex}}-1} - \frac{1}{e^{h\nu/k_B T_{bg}}-1}\Big)^{-1} \int T_B \mathrm{d}v \tag{61}$$

The integral $\int T_B \mathrm{d}v$ is the integrated line intensity and may be determined from Gaussian fits to the line profile. This equation will be used to determine masses and densities from molecular line observations in chapter 6.

3.7 Conditions For Gravitational Collapse

3.7.1 Virial Theorem

An isolated, uniformly dense molecular cloud may begin to collapse under its own gravity if the total mass of the cloud exceeds a certain value. This critical value may be ascertained through

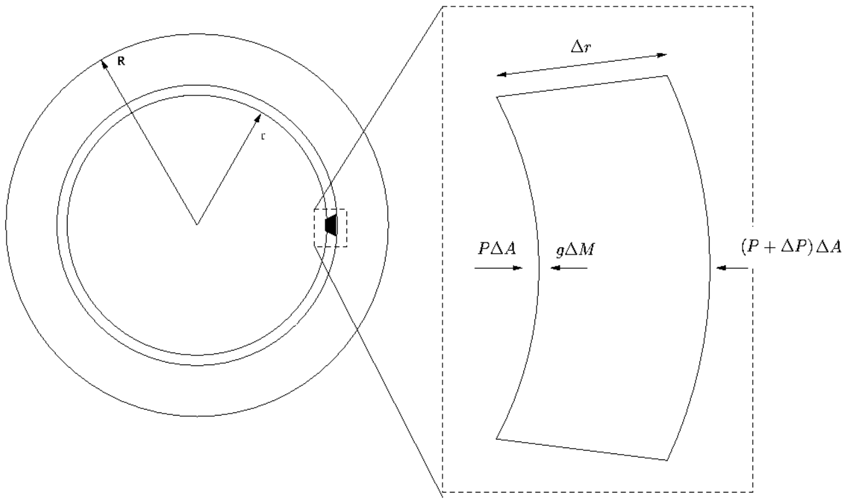

Figure 8: The forces acting on a radial element of a system of mass M and radius R.

equating the factors supporting the cloud against collapse with those acting to make the cloud collapse. In order to make the simplest analysis certain assumptions are made: that the cloud is of a mass, M_{cloud}, is spherical with a radius of R, has a density, $\rho(r)$, and is isothermal with a temperature, T. It is also assumed that the only forces acting on the cloud are those of its own self-gravity and the internal thermal pressure. The pressure acting on the cloud as a function of radial distance, r, is denoted by $P(r)$.

The mass within a spherical shell element a distance r from the centre of the cloud and dr wide is

$$m(r) = \int_0^r \rho(r) 4\pi r^2 \mathrm{d}r \tag{62}$$

This acts as a gravitational mass situated at the centre of the cloud, the acceleration upon an exterior mass is then given by

$$g(r) = -\frac{Gm(r)}{r^2} \tag{63}$$

Generally, there is a difference in pressure across the radial element. Consider a small volume element between radii r and $r + \Delta r$, with cross-sectional area ΔA and volume $\Delta r \Delta A$ (see Fig.8). If the pressure acting upon the innermost surface of the element is not equal to the pressure acting on the outer surface then a net force will result. The force (acting inwards, towards the centre of the sphere) is,

$$\left[P(r) + \frac{\mathrm{d}P}{\mathrm{d}r}\Delta r - P(r)\right]\Delta A = -\frac{\mathrm{d}P}{\mathrm{d}r}\Delta r \Delta A \tag{64}$$

Therefore, the total inward acceleration of a mass element at distance, r, from the centre of the sphere is given by,

$$\frac{\mathrm{d}^2 r}{\mathrm{d}t^2} = g(r) - \frac{1}{\rho(r)}\frac{\mathrm{d}P}{\mathrm{d}r} \tag{65}$$

(where $\rho(r) = \Delta M/\Delta r \Delta A$)

From this equation it can be seen that, for the cloud to be in hydrostatic equilibrium then,

$$\frac{\mathrm{d}P}{\mathrm{d}r} = -\frac{Gm(r)\rho(r)}{r^2} \tag{66}$$

at all radii. To solve for the entire cloud then,

$$\int_0^R 4\pi r^3 \frac{\mathrm{d}P}{\mathrm{d}r}\mathrm{d}r = -\int_0^R \frac{Gm(r)\rho(r)4\pi r^3}{r^2}\mathrm{d}r \tag{67}$$

this equation then neatly describes the action of forces upon the cloud, the right hand side of the equation is the gravitational potential energy of the system and the left hand side can be integrated to give

$$-3\int_0^R P(r)4\pi r^2 \mathrm{d}r. \tag{68}$$

The right hand side of Eq.67 can be solved to give

$$-\int_0^R \frac{Gm(r)\rho(r)4\pi r^3}{r^2}\mathrm{d}r = -\int_{m=0}^{m=M} \frac{Gm(r)}{r}\mathrm{d}m = E_G = -3\langle P\rangle V \tag{69}$$

where $\mathrm{d}m$ is the mass contained between r and $r + \mathrm{d}r$ and V is the volume of the system. Thus, the average pressure required to support a system of gravitational energy E_G and volume V is,

$$\langle P\rangle = -\frac{1}{3}\frac{E_G}{V}. \tag{70}$$

Consider a single particle of an ideal gas, contained within a cube of side L. The particle has velocity V=(V_x, V_y, V_z) and momentum P=(P_x, P_y, P_z). If we consider travel along one axis only (e.g. the z-axis) then we can describe the rate at which the particle will strike a side perpendicular to this axis as $V_z/2L$. The momentum transfer per strike is thus $2P_z$, spread over an area of L^2. So, the rate of momentum transfer per unit area of the single surface is $P_z V_z/L$. If we now consider all N particles in the cubical box then the pressure acting on one side of the box due to the momentum transfer of the particles is

$$P = \frac{N}{L^3}\langle P_z V_z\rangle \tag{71}$$

where $\langle P_z V_z \rangle$ is an average over all particles. If the gas is isotropic, all directions of motion are equally likely and $\langle P_x V_x \rangle = \langle P_y V_y \rangle = \langle P_z V_z \rangle = \frac{\langle \mathbf{P.V} \rangle}{3}$ where $\mathbf{P.V} = \mathrm{P_x V_x + P_y V_y + P_z V_z}$.

Thus the pressure on each side of the box is equal to

$$P = \frac{n}{3}\langle \mathbf{P.V} \rangle \tag{72}$$

where n is the number density of particles.

For a non-relativistic gas $P.V = mv^2$, the pressure may then be described as $P = \frac{2}{3}n\langle\frac{1}{2}mv^2\rangle = \frac{2}{3}$ of kinetic energy density, E_{KE}.

So, $\langle P \rangle = \frac{2}{3}\frac{E_{KE}}{V}$ and from Eq.70 $\langle P \rangle = -\frac{1}{3}\frac{E_G}{V}$. Therefore,

$$2E_{KE} + E_G = 0. \tag{73}$$

This is commonly known as the virial theorem, the time average of the kinetic energy of a closed system is equal to half the (negative) time averaged potential energy.

3.7.2 Jeans Mass

In the previous section the gravitational potential energy of a spherical cloud was defined as

$$E_G = -\int_{m=0}^{m=M} \frac{Gm(r)}{r}\mathrm{d}m \tag{74}$$

For a spherical cloud of radius R and mass M that is uniformly dense this becomes

$$E_G = -\frac{3}{5}\frac{GM^2}{R} \tag{75}$$

where the coefficient of $\frac{3}{5}$ relates specifically to the case of a spherical cloud of uniform density. If the density distribution of the cloud is higher toward the centre then this factor increases. By using the expression for thermal kinetic energy, i.e.

$$K.E. = \frac{3}{2}k_B T \tag{76}$$

where k_B is Boltzmanns constant and T is the temperature of the cloud (previously defined as isothermal) it is possible to define thermal kinetic energy of the cloud assuming that the cloud consists of N_T total particles, each of which provides an average energy of $\frac{3}{2}kT$ to the thermal energy of the system. If the gravitational potential energy of the system exceeds that provided by the thermal energy of the particles then the cloud will collapse inward. Therefore, the condition for the collapse of the cloud is,

$$-\frac{3}{5}\frac{GM^2}{R} > \frac{3}{2}N_T k_B T \tag{77}$$

and thus, a cloud of radius R can condense if its mass exceeds

$$M_J = \frac{5}{2}\frac{k_B T}{G\mu m_H}R \tag{78}$$

This critical mass is known as the Jeans mass and it, along with its derivatives for a particular cloud of ρ_J and R_J is a common and important quantity in the analysis of molecular condensations.

3.8 Signatures Of Star Formation

Observing the actual process of protostellar collapse is not necessarily an easy task. With many interpretations possible of a single piece of kinematic evidence, defining a unique signature of collapse has been an area of hotly contested debate.

3.8.1 Infall

Infall is classically indicated by an asymmetric molecular line profile, more intense in the blue end of the spectrum. In a gravitationally bound, spherically symetric cloud almost all theoretical models of cloud collapse predict an increasing collapse velocity toward the cloud centre, described by the relation of $v(r) \propto r^{-0.5}$ (Zhou & Evans 1994 and references within). In these models the density and excitation temperature of the clouds peak toward the centre of the clouds and decrease radially away from the centre. In the idealised case of a spherically symmetric, centrally condensed, gravitationally bound cloud the asymmetric line profile arises through the velocity gradients and optical depth of the line in question.

Fig. 9 shows a schematic diagram of infall occuring in a spherical cloud. The region of infall is surrounded by an envelope of material static with respect to the rest velocity of the cloud. This envelope will produce a self-absorption dip in the observed molecular line profile, given a sufficiently high opacity in the relevant transition (see Fig. 10).

The infalling cloud core is divided into the regions 1-4, region 1 being closest to the observer. The emission from regions 1 and 2 will appear red-shifted to the observer, while emission from regions 3 and 4 will appear blue-shifted. The emission from the near (red-shifted) side of the core is partially absorbed by the cooler outer static envelope. The emission from the far (blue-shifted) side of the core is absorbed to a lesser degree due to the higher temperature of the foreground material and the substantially different velocity of the foreground material.

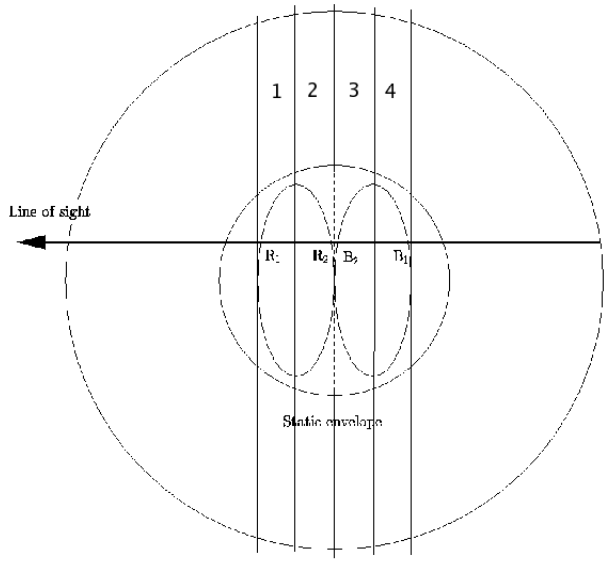

Figure 9: Collapse in a spherical cloud. An envelope of static material exists surrounding the infall region, the velocity of this infalling material is described by $v(r) \propto r^{-0.5}$ and the ovals represent lines of constant line-of-sight velocity.

Using molecular line emission emanating from this infall region, one can compare the observed temperatures of the blue-shifted and red-shifted infall regions. All collapse models predict that density will increase toward the centre of a region such as has been described. This type of cloud may be expected to be internally heated by an embedded source, if it is not then it may be assumed to be isothermal. In either case the excitation temperature of the molecular transition in question will increase toward the centre of the cloud.

Here it is necessary to define T_{blue} and T_{red} as the observed temperatures of the blue-shifted and red-shifted material respectively. The excitation temperatures and optical depths at B_1 and R_1 may be expected to be equal, as may the excitation temperatures and optical depths at B_2 and R_2, these will be denoted as T_1, τ_1, T_2 and τ_2 respectively. The difference between T_{blue} and T_{red} can then be defined as

$$T_{blue} - T_{red} = (T_2 - T_1)(1 - e^{-\tau_1})(1 - e^{-\tau_2}) \tag{79}$$

as the excitation temperature increases toward the centre of the cloud then $T_2 > T_1$. Thus the velocity profile will show $T_{blue} > T_{red}$ and this asymmetry should increase with the optical depth of the transition. It should be pointed out that if the kinematic temperature of the cloud *decreases* toward the centre then this observed asymmetry would indicate *expansion* of the cloud.

Fig. 10 shows the line profiles of HCO^+ and $H^{13}CO^+$ in the BRC SFO 44. The double peaked

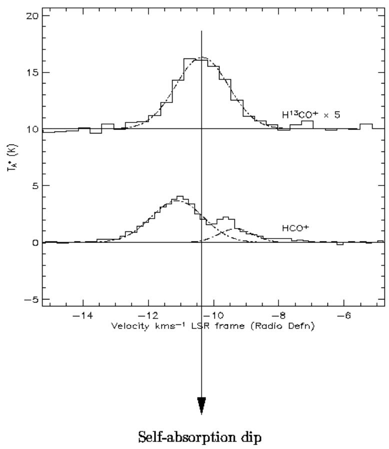

Figure 10: Observed molecular line emission observed for SFO 44 in HCO^+ and $H^{13}CO^+$. Best fit Gaussian line profiles are overlaid as dashed lines. The $H^{13}CO^+$ has been multiplied by a factor of 5 for clarity. The peak of the optically thin $H^{13}CO^+$ transition has been demarcated in order to highlight the self-absorption dip at the same velocity in the optically thick HCO^+ line profile.

structure that is visible in the HCO^+ line is due to a combination of the asymmetry previously described with the self-absorption of the outer envelope of the cloud. The asymmetry of the profile toward the blue end of the spectrum occurs because, as shown in Fig. 9, there will be two points along the line-of-sight that have the same Doppler shift. As explained, the excitation temperature rises toward the centre of the cloud, thus, in an optically thick line, the higher excitation temperature point will be obscured by the lower one in the red-shifted region. The converse will be true in the blue-shifted region. Thus, a signature of infall in a cloud is a double peaked structure with a high blue peak relative to the red one, or, an asymmetry of a single peaked line profile toward the blue end of the spectrum relative to an optically thin line.

This asymmetry may be quantified through the velocities of the chosen optically thin and thick lines. Mardones et al. (1997) introduced the line asymmetry as a collapse indicator

$$\delta V = \frac{V_{thick} - V_{thin}}{\Delta V_{thin}} \tag{80}$$

where, V_{thick} is the velocity of the thick line, V_{thin} is the velocity of the thin line and ΔV_{thin} is the linewidth of the thin line. A large value of δV relative to the statistical uncertainty in the linewidths indicates infall. The velocities are those measured at the intensity peaks of the lines, thus, in a double peaked asymmetric spectral line profile, V_{thick} will be the velocity measured at the blue-shifted peak.

3.8.2 Outflow

One of the earliest indicators of star-formation, especially in regions of massive star formation, is a high energy outflow of gas from the region. This gas is usually expelled bipolarly and has energies comparable to the energy involved in the accretion process (Bachiller 1996). The outflow process is observed to be coeval with the infall process at the early stages of star formation. No true consensus exists on the actual launching mechanism of bipolar outflows (Arce & Sargent 2005) though they are universally acknowledged to be associated with the early stages of star formation. The observation of molecular flow is through the velocity dispersion of molecular transitions in the gas associated with the outflow, usually a carbonaceous material. A high linewidth, and, especially non-Gaussian behaviour of the velocity dispersion are clear indicators of outflow activity in molecular clouds. An example of this behaviour is shown in Fig. 11.

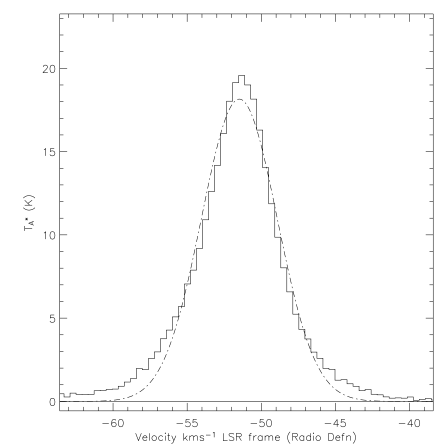

Figure 11: Observed molecular line emission observed for SFO 5 in ^{12}CO. A best fit Gaussian line profile is overlaid as a dashed line. Note the large velocity dispersion (*cf*. other molecular line transitions in Appendix A) and the excess ^{12}CO emission as compared to the Gaussian fit in the wings of the line profile.

Chapter 4

Radio And Mid-Infrared Emission From BRCs

4.1 Introduction

The general conditions prevalent within the IBLs of BRCs are not well known as most studies have, to date, accurately determined the conditions within only a few individual clouds (e.g. Lefloch & Lazareff 1995; Lefloch et al. 1997; Megeath & Wilson 1997; White et al. 1999; Thompson et al. 2004a). From observations of the free-free emission associated with BRCs identified in the SFO catalogue, the ionised gas pressure, the ionising photon flux impinging upon the cloud surface and the electron density of the IBL have been determined. This has been achieved using data obtained from the NRAO VLA 20 cm Sky Survey (NVSS) (Condon et al. 1998). MSX images at 8.3 μm have been used to trace the Photon Dominated Regions (PDRs) associated with the BRCs, confirming the identification of individual sources of 20 cm emission as IBLs. The identification of the primary ionising stars associated with each BRC has allowed a comparison of the 20 cm emission measured toward each BRC, with that predicted by the incident ionising flux. Through further quantification of these properties of IBLs at the edge of BRCs it is possible to clarify the role of the RDI scenario in global star formation. To this end information has been collated using a thorough literature search and the SIMBAD database of astronomical catalogues[1] as well as analysing optical, radio and infrared images to identify the stars responsible for ionising the clouds.

[1] http://simbad.u-strasbg.fr

4.2 Survey Procedure

4.2.1 The NVSS

20 cm radio images were obtained from the NVSS radio catalogue (Condon et al. 1998) downloaded using the postage stamp server[2] (see chapter 2). The sample presented here is comprised of 44 $15' \times 15'$ images centred upon the coordinates of each IRAS source associated with each BRC contained in the SFO catalogue.

4.2.2 MSX Data

MSX images were downloaded from the NASA/IPAC Infrared Science Archive[3] and were examined using GAIA, part of the Starlink Software Collection. Ionising (UV) radiation excites Polycyclic Aromatic Hydrocarbons (PAHs), which re-emit the absorbed energy at infrared wavelengths (Leger & Puget 1984). MSX 8.3 μm images incorporate the PAH spectral features at 7.7 μm and 8.6 μm, as well as very small dust grain continuum emission. Images of the sample of BRCs were acquired in order to trace any associated PAH emission and confirm that any observed 20 cm emission at the cloud rims may be free-free continuum emission from the IBL. The A band of the MSX includes the broad silicate band at 9.7 μm and the PAH emission features at 7.7 μm and 8.6 μm, which are of particular interest to this study as they trace the interface between molecular material and ionisation features associated with 20 cm emission.

4.3 Results And Analysis

4.3.1 Source Identification And Classification

Using NVSS data the BRCs from the survey of Sugitani et al. (1991) have been studied. Identification of bright rims is initially achieved by overlaying contours of the 20 cm emission onto the R-band images of the clouds obtained from the Digitised Sky Survey (DSS) and searching for 20 cm emission that is positionally coincident with the bright optical rims of the clouds. No 20 cm emission was detected (to a level of three times the r.m.s. noise, typically $\simeq$ 1.35 mJy beam^{-1}) associated with the rims of the clouds SFO 3, 8, 9, 19, 20, 22, 23, 24, 26, 33, 34 and 39. The images of SFO 16, 17 & 18 were disregarded due to their relatively low quality, which is due to the sidelobes of nearby confusing sources, combined with the low surface brightness of the 20 cm rim emission from these clouds. For the clouds SFO 2 & 44 there are no MSX data to assist with the identification, however, as the emission is clearly extended the inclusion of these

[2] http://www.cv.nrao.edu/nvss/postage.shtml
[3] http://irsa.ipac.caltech.edu

sources is justified. A total of 26 radio sources were determined to be positionally associated with the BRCs from the SFO catalogue. The coordinates of the peak emission, peak fluxes and integrated flux densities of these sources are presented in Table 2. DSS $15' \times 15'$ regions overlaid with NVSS and MSX 8.3 μm emission contours are presented in Appendix A, centred on the IRAS source position given in Sugitani et al. (1991).

Table 2: Properties of radio emission associated with the SFO objects.

SFO Object	Peak Emission $\alpha(2000)$	Peak Emission $\delta(2000)$	Peak Flux (mJy/beam)	Integrated Flux Flux (mJy)	Source Classification
1	23 59 33.7	+67 23 54	69.2	728.4	1
2	00 03 50.3	+68 32 09	4.4	13.2	1
4	00 58 60.0	+60 53 16	5.3	26.6	1
5	02 29 01.8	+61 33 17	11.5	21.4	1
6	02 34 45.0	+60 48 18	4.6	42.9	1^T
7	02 34 47.8	+61 49 14	11.7	86.3	1
10	02 48 07.3	+60 25 35	30.7	519.6	1
11	02 51 33.0	+60 03 43	4.0	10.1	1
12	02 55 00.9	+60 35 44	12.0	127.0	1
13	03 00 52.5	+60 40 19	3.7	6.3	1
14	03 01 24.2	+60 29 12	8.1	41.9	3
15	05 23 26.5	+33 11 54	3.3	3.0	1
16	05 20 00.9	-05 50 22	1.1	0.6	4
17	05 31 27.1	+12 04 54	1.9	7.7	4
18	05 44 28.7	+09 08 40	8.1	9.1	4
21	05 39 38.3	-03 36 25	1.3	1.3	4
25	06 41 06.3	+10 14 30	3.0	15.5	1
27	07 04 03.8	-11 23 19	3.6	39.0	1^T
28	07 04 41.4	-10 22 15	1.3	0.6	4
29	07 04 54.5	-12 09 42	2.2	0.6	4
30	18 18 46.1	-13 44 39	57.1	125.6	1
31	20 50 48.8	+44 21 29	12.8	345.5	1
32	21 32 34.9	+57 24 08	2.9	5.0	1
35	21 36 09.3	+58 31 53	1.8	12.1	1
36	21 36 10.6	+57 26 34	3.8	11.5	1
37	21 40 29.0	+56 36 13	3.5	11.0	1
38	21 40 44.3	+58 15 01	6.0	26.6	1
40	21 46 09.1	+57 09 59	4.9	14.6	1
41	21 46 29.0	+57 18 10	2.7	28.5	1
42	21 46 38.6	+57 11 39	4.9	1.2	1
43	22 47 50.3	+58 02 51	35.3	204.5	1
44	22 28 59.1	+64 12 11	37.0	95.8	1

^{T}Tentative classification, see Section 4.3.2 for details

The radii of the optical bright rims (taken from Sugitani et al. 1991) of the clouds toward which 20 cm emission has been detected, range from 13 - 133″, corresponding to a physical size of 0.04 - 0.83 pc. From the source counts of Condon et al. (1998), it has been determined that there is a probability of ∼0.2 of finding a background NVSS radio source within 133″ of the IRAS point (to the sensitivity of the NVSS catalogue $\sigma \sim 0.45$ mJy beam^{-1}). This implies that up to ∼5 sources may potentially be due to confused background radio galaxies. In order to rule out any possible confusion the NVSS archival data were compared with optical DSS images and mid-infrared MSX 8.3 μm images.

PAH emission is a tracer of UV-dominated PDRs (Leger & Puget 1984) as the PAHs are transiently heated by the absorption of UV photons, therefore MSX images of the northern SFO catalogue can help to identify PDRs that are associated with the detected radio emission. Comparing emission in the optical, radio and infrared regimes helps to eliminate chance associations and can identify true emission from the bright rim. The radio sources detected in the NVSS survey images were classified according to the scheme of Thompson et al. (2004b):

Type 1. Bright-rim emission clouds with 20 cm and 8.3 μm emission positionally coincident with their bright optical rims.

Type 2. Broken-rimmed clouds, in which the 20 cm and MSX 8.3 μm emission is positionally coincident with the rim of the cloud (as Type 1) but the rim has a reverse curvature with respect to the normal orientation, i.e. the rim is curved towards the molecular cloud, rather than the ionising star (e.g. the well known broken-rimmed globule CG4 in the Gum Nebula (Reipurth 1983)). No clouds of this type were identified in this survey, the classification has been retained to maintain consistency with Thompson et al. (2004b).

Type 3. Embedded objects with compact and coincident 20 cm and mid-infrared emission that is set back from the rim toward the centre of the cloud.

Type 4. 20 cm emission that is uncorrelated with either the bright optical rim or MSX 8.3 μm emission.

4.3.2 Confusing Sources

The sources SFO 6 & 27 have been tentatively labelled as Type 1 although there is some confusion as to their identification. These objects shall now be examined in more detail and justification for their nominal identifications given.

SFO 6

SFO 6 has strong ($\sim 9\sigma$) 20 cm emission associated with the optical rim which appears to follow the optical bright rim (Appendix A). There is a small region of 8.3 μm emission centred at the peak of the optical rim which, due to the confused nature of the emission, is not definitive enough to infer any clear association with the cloud rim, but does not contradict an identification of the source as Type 1. However, the 20 cm emission near the optical rim is confused by a stronger unassociated source that has no optical or infrared counterpart, and is thus likely to be an extra-galactic background source. It is suggested that this source may be NEK 135.2+00.3, identified in the Clark Lake 30.9 MHz galactic plane survey (Kassim 1988). The source is unresolved in the survey and only marginally resolved in the NVSS image.

SFO 27

SFO 27 has strong ($\sim 6\sigma$) 20 cm emission associated with the optical rim (Appendix A). There is widespread MSX 8.3 μm emission associated with the IRAS source and extending along the optical rim which supports an identification of the source as Type 1. However, the 20 cm emission near the optical rim is confused by a stronger unassociated source that has no obvious optical or infrared counterpart.

The analyses of SFO 6 and SFO 27 has been continued treating them as Type 1 objects. The emission from the background sources has been masked as much as is possible by discounting flux obviously associated with them.

4.3.3 Ionised Rims Associated With SFO Objects

For those objects that have been identified as Type 1 sources the ionising photon flux impinging upon the clouds, the electron densities and the pressures in the IBLs have been evaluated. These quantities were determined by using the general equations from Lefloch et al. (1997). Rearranging their Eq. (6), the ionising photon flux Φ arriving at the cloud rim may be written in units of cm^{-2} s^{-1} as

$$\Phi = 1.24 \times 10^{10} \left(\frac{S_\nu}{\mathrm{mJy}}\right) \left(\frac{T_e}{\mathrm{K}}\right)^{0.35} \left(\frac{\nu}{\mathrm{GHz}}\right)^{0.1} \left(\frac{\theta}{\mathrm{arcsec}}\right)^{-2} \tag{81}$$

The 20 cm flux measured at the ionised rim may be overestimated due to nebula emission from the HII regions in which the BRCs are embedded. This emission forms a background which may add to the actual rim brightness at 20 cm. However, due to the poor (u,v) coverage of the NVSS snapshot observations, any structure larger than $\sim 5'$ is filtered out (Condon et al. 1998). Therefore if any large scale nebula emission is present it may be expected to be at a low level. This is supported by comparing the DSS images, in which nebula emission shows up as large, diffuse, red regions, to the NVSS data in which no correlating 20 cm emission is found.

The electron density (n_e) of the IBL surrounding the cloud may also be derived from the integrated radio flux S_ν by substituting for the ionising photon flux in Eq.(6) of Lefloch et al. (1997). The electron density in cm^{-3} is given by:

$$n_e = 122.41 \sqrt{\frac{S_\nu T_e^{0.35} \nu^{0.1} \theta^{-2}}{\eta R}} \tag{82}$$

where those quantities common to both Eq. 81 and 82 are in the same units, R is the radius of the cloud in pc and η is the effective thickness of the IBL as a fraction of the cloud radius (typically $\eta \sim 0.2$, (Bertoldi 1989)).

As the ionised flow is sonic at the cloud surface (Lefloch & Lazareff 1994) the ram pressure of the flow must be taken into account, as well as the bulk pressure of the ionised layer. Assuming a totally ionised gas, the total pressure of the ionised layer (kg m^{-1} s^{-2}) with respect to the internal neutral gas is

$$P_T = P_i + \rho_i c_i^2 = 2\rho_i c_i^2 \tag{83}$$

where c_i is the isothermal sound speed in the ionised interclump gas (assumed to be 11.4×10^3 m s^{-1} Bertoldi (1989)) and ρ_i is the density within the IBL in units of kg m^{-3}.

Values for Φ, n_e and P_T were calculated using Eqs. 81 - 83, assuming a boundary layer thickness fraction of $\eta = 0.2$ (Bertoldi 1989) and an effective electron temperature, $T_e = 10^4$ K. As the relatively low angular resolution of the NVSS means that a number of BRCs are either unresolved, or marginally resolved, at 20 cm the cloud radii were taken from the original BRC survey paper of Sugitani et al. (1991)). Values for Φ, n_e and P_T are presented in Table 3.

In the derivation of the ionising fluxes of these clouds it has been implicitly assumed that the bright rims are resolved, this is not always the case (e.g. SFO 15, Fig. 12). A comparison of the ratio between predicted, and measured, ionising fluxes in the resolved (e.g. SFO 38 Fig. 12) and unresolved case does not reveal any consistent effect associated with this beam 'dilution'. The analysis of the cloud SFO 5 reveals an ionising flux of 7.5×10^8 cm^{-2} s^{-1}, whereas the (resolved) observations of Lefloch et al. (1997) find 4.8×10^9 cm^{-2} s^{-1} using the same analysis. This difference in results may possibly be attributed to the different frequencies of observation and total area of integrated emission. Lefloch et al. (2002) find a factor of ~ 6 between predicted and measured ionising flux in their resolved observations of the Trifid nebula. However, the (also resolved) observations of SFO 5 presented in Lefloch et al. (1997) find a small (0.8) fractional difference between their predicted and measured ionising fluxes. While the lack of resolution of the bright rims in some cases is certainly undesirable, and an important consideration in future observations, it does not appear to be a significant factor in the flux comparisons presented here.

4.3.4 Identification Of Ionising Stars

The SIMBAD astronomical database was searched in order to identify possible ionising stars of each BRC. All O or B type stars located within each HII region were considered as possible

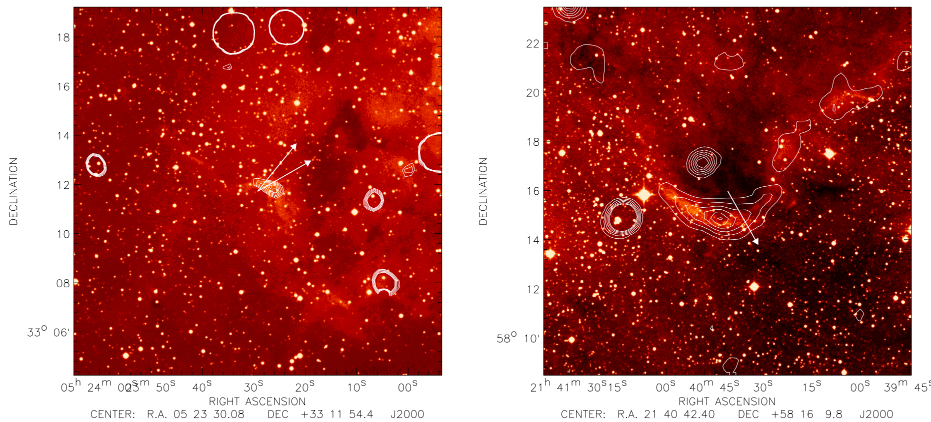

Figure 12: NVSS 20 cm emission contours overlaid on DSS images of SFO 15 (left) and SFO 38 (right). Arrows show the direction of the ionising source(s).

candidate ionising stars. For each star the predicted ionising fluxes incident on the rim of the relevant SFO object were determined using the tables of Panagia (1973) and the stellar spectral type. If there was disagreement in the literature as to the classification of a star, or it was simply not quoted, it has been assumed that the star in question is an evolved main sequence star (Type V). A list of stars with high predicted ionising fluxes (i.e. nearby OB stars) was drawn up. Stars that contributed less than 50% of the flux of the most dominant star were discounted. The stars that have been identified as the main ionising stars of each SFO object are listed in Table 4 along with their positions, the HII region with which they are associated and their spectral type.

4.3.5 Flux Comparison

From the tables of Panagia (1973) the fluxes of Lyman continuum photons associated with each star were determined and this allowed the calculation of the subsequent flux expected to impinge on the optical bright rims. It has been assumed that there are no losses due to absorption by intervening material between the star and cloud, also, the star-cloud distance used in these calculations is that seen in projection on the plane of the sky. Together, these assumptions lead to the predicted ionising flux being a strict upper limit. This limit assumes that the ionising star has been correctly classified, a misclassification of an ionising star may lead to large differences in the ionising flux than that predicted, a misclassification of half a spectral class may lead to an increase, or decrease, of a factor of two in the predicted Lyman photon flux. There are sometimes disagreements in the literature on the spectral classification of a particular star. Two examples of this are the stars HD 5394 and BD +60 502 that are believed to be ionising the surfaces of SFO 4 and SFO 5 respectively. The former has been identified as B0IV by Morgan et al. (1955), but as B3IV by Racine (1968), and the latter as 05 by Conti & Alschuler (1971) and B8

Table 3: Values for the measured ionising flux, predicted ionising flux, the measured electron density and ionised gas pressure for Type 1 radio sources detected in the survey.

SFO Object	Measured Ionising Flux Φ (10^8 cm^{-2} s^{-1})	Predicted Ionising Flux Φ_P (10^8 cm^{-2} s^{-1})	Electron Density n_e (cm^{-3})	Ionised Gas Pressure P_i/k_B (10^5 cm^{-3}K)
1	18.5	43.7	272	85.8
2	2.7	2.1	84	26.7
4	2.7	43.1	196	61.8
5	7.5	61.3	113	35.8
6	3.1	32.1	121	38.2
7	3.6	78.7	51	16.2
10	9.9	10.5	161	50.8
11	2.3	10.2	72	22.8
12	5.2	44.5	109	34.5
13	3.2	12.4	63	20.0
15	3.0	18.8	71	22.4
25	2.2	27.1	66	20.8
27	5.6	1.7	133	42.1
30	22.1	4065.9	142	44.7
31	8.7	3.5	151	47.5
32	2.2	11.4	124	39.0
35	1.2	6.9	63	20.1
36	2.4	59.6	54	17.2
37	2.0	10.2	111	35.1
38	2.8	13.3	77	24.4
40	2.5	8.1	108	34.3
41	1.5	8.0	77	24.4
42	1.3	7.3	78	24.6
43	4.8	145.8	86	27.3
44	2.1	4.6	84	26.5

by Boulon & Fehrenbach (1958). In these cases the type specified as the most reliable by the SIMBAD database has been used.

The predicted ionising fluxes are presented along with the measured ionising fluxes in Table 3. It can be seen in the majority of cases that $\Phi_P > \Phi$ as expected, however, the difference between Φ_P and Φ in some cases is much larger than expected. The disparity between Φ_P and Φ in these cases is most likely due to the assumption that there is negligible absorption between the ionising star and the bright rim. Lefloch et al. (2002) find an attenuation of a factor of ~ 6 over a distance of ~ 1 pc. The assumed distances in this sample range from 1 to 37 pc and it is thus expected that attenuation has a significant effect upon the ratio of predicted to measured ionising fluxes. It is worth noting that the projected star-cloud distance is an underestimate. The combination of these two facts illustrates that theoretical predictions of Φ based upon the spectral type and projected distance of the ionising star often overestimate the true ionising

Table 4: Ionising stars of the SFO objects, their relevant HII regions, positions and ionising fluxes.

SFO Object	HII Region	Ionising Star	α (2000)	δ (2000)	Spectral Type	Projected Distance to Bright Rim (Pc)
1	(S171/NGC 7822)	BD +66 1675[a]	00 02 10.3	+67 24 32	O7V	3.7
2	(S171/NGC 7822)	BD +66 1675	00 02 10.3	+67 24 32	O7V	16.9
3	(S171/NGC 7822)	BD +66 1675	00 02 10.3	+67 24 32	O7V	5.3
4	(S185)	HD 5394[b]	00 56 42.3	+60 43 00	B0IV	1.1
5	(S190/IC 1805)	BD +60 502[c]	02 32 42.5	+61 27 22	O5V	14.9
		BD +60 504[c]	02 32 49.4	+61 22 42	O4V	16.1
		BD +60 507[c]	02 33 20.6	+61 31 18	O5V	17.1
6	(S190/IC 1805)	BD +60 504	02 32 49.4	+61 22 42	O4V	20.5
7	(S190/IC 1805)	BD +60 502	02 32 42.5	+61 27 22	O5V	14.6
		BD +60 504	02 32 49.4	+61 22 42	O4V	16.6
		BD +60 507	02 33 20.6	+61 31 18	O5V	11.4
8	(S190/IC 1805)	BD +60 502	02 32 42.5	+61 27 22	O5V	12.4
		BD +60 504	02 32 49.4	+61 22 42	O4V	11.3
		BD +60 507	02 33 20.6	+61 31 18	O5V	11.1
9	(S190/IC 1805)	BD +60 502	02 32 42.5	+61 27 22	O5V	15.0
		BD +60 504	02 32 49.4	+61 22 42	O4V	14.4
		BD +60 507	02 33 20.6	+61 31 18	O5V	13.1
10	(S199/IC 1848)	HD 17505[d]	02 51 08.0	+60 25 04	O6V	12.3
11	(S199/IC 1848)	HD 17505	02 51 08.0	+60 25 04	O6V	11.9
12	(S199/IC 1848)	BD +60 586[d]	02 54 10.7	+60 39 03	O8III	3.9
13	(S199/IC 1848)	BD +59 578[d]	02 59 23.2	+60 33 59	O7V	7.0
14	(S199/IC 1848)	BD +59 578	02 59 23.2	+60 33 59	O7V	8.6
15	(S236/IC 410)	HD 242908[e]	05 22 29.3	+33 30 50	O5V	22.1
		HD 242926[e]	05 22 40.1	+33 19 10	O6V	12.0
16	(S276)	δ Ori[f]	05 32 04.1	+00 21 55	O9.5I	37.3
		θ^1 Ori[f]	05 35 15.5	-05 23 19	O7V	26.7
		ι Ori[f]	05 35 26.8	-05 54 31	O8.5II	26.9
17	(S264/λ Ori)	λ Ori[f]	05 35 08.2	+09 56 04	O5V	16.3
18	(S264/λ Ori)	λ Ori	05 35 08.2	+09 56 04	O5V	17.0
19	(S277/IC 434)	HD 37468[g]	05 38 44.8	-02 36 01	O9.5V	13.3
20	(S277/IC 434)	HD 37468	05 38 44.8	-02 36 01	O9.5V	8.3
21	(S277/IC 434)	HD 37468	05 38 44.8	-02 36 01	O9.5V	7.1
22	(S281)	θ^1 Ori[h]	05 35 15.5	-05 23 19	O7V	6.5
		ι Ori[h]	05 35 26.8	-05 54 31	O8.5II	8.1

photon flux illuminating these clouds. Another effect which may affect these results is that the 20 cm emission from the bright rims was measured using an interferometer, which acts as a high pass filter and may thus filter out flux from large scale structures. In two cases (SFO 27 and SFO 31) the flux that has been predicted is significantly less than the flux that is observed.

In the case of SFO 27 the 20 cm flux is confused with an unassociated source and so the measured 20 cm flux, and hence the calculated value of Φ, are highly uncertain. In the case of SFO 31 the direction of the suspected ionising star is not supported by the morphology of the cloud and no other possible ionising stars have been identified in the region.

4.3.6 Upper Limits To The Ionising Flux For Non-Detections

There are a total of 12 clouds in this survey where no 20 cm emission was detected to a level of 3σ. The upper limits of any possible 20 cm emission from these clouds have been checked for consistency with the flux predicted from the candidate ionising stars. The predicted ionising

Table 4: **(cont.)** Ionising stars of the SFO objects, their relevant HII regions, positions and ionising fluxes.

SFO Object	HII Region	Ionising Star	α (2000)	δ (2000)	Spectral Type	Projected Distance to Bright Rim (Pc)
23	(S249)	BD +22 1303[i]	06 22 58.2	+22 51 46	O9V	8.3
24	(S275/NGC 2244)	HD 46223[j]	06 32 09.3	+04 49 25	O5V	19.3
25	(S273/NGC 2264)	HD 47839[k]	06 40 58.6	+09 53 45	O7V	4.7
26	(S296/CMaOBI)	HD 54662[l]	07 09 20.2	-10 20 48	O7III	29.7
27	(S296/CMaOBI)	HD 53456[l]	07 04 38.3	-11 31 27	BOV	3.9
28	(S296/CMaOBI)	HD 53367[l]	07 04 25.5	-10 27 16	B0IV	2.1
29	(S296/CMaOBI)	HD 53975	07 06 36.0	-12 23 38	O7.5V	9.5
30	(S49)	BD -13 4927[e]	18 18 40.1	-13 45 18	O5V	1.0
31	(S117)	HD 199579[m]	20 56 34.7	+44 55 29	O6V	20.5
32	(S131/IC 1396)	HD 206267[n]	21 38 57.6	+57 29 21	O6V	11.3
33	(S131/IC 1396)	HD 206267	21 38 57.6	+57 29 21	O6V	10.5
34	(S131/IC 1396)	HD 206267	21 38 57.6	+57 29 21	O6V	12.1
35	(S131/IC 1396)	HD 206267	21 38 57.6	+57 29 21	O6V	14.5
36	(S131/IC 1396)	HD 206267	21 38 57.6	+57 29 21	O6V	4.9
37	(S131/IC 1396)	HD 206267	21 38 57.6	+57 29 21	O6V	11.9
38	(S131/IC 1396)	HD 206267	21 38 57.6	+57 29 21	O6V	10.4
39	(S131/IC 1396)	HD 206267	21 38 57.6	+57 29 21	O6V	12.6
40	(S131/IC 1396)	HD 206267	21 38 57.6	+57 29 21	O6V	13.4
41	(S131/IC 1396)	HD 206267	21 38 57.6	+57 29 21	O6V	13.5
42	(S131/IC 1396)	HD 206267	21 38 57.6	+57 29 21	O6V	14.1
43	(S142/NGC 7380)	HD 215835	22 46 54.2	+58 05 04	O5V	5.4
44	(S145)	HD 213023[o]	22 26 52.4	+63 43 05	O9V	8.5
		BD 62 2078[p]	22 25 33.6	+63 25 03	O7.5V	13.8

Stars found to be at similar distances to, formally declared to be associated with or described as 'probable members' of relevant HII regions in the following references: [a]Crampton & Fisher (1974); [b]Savage et al. (1977); [c]Ishida (1970); [d]Hughes et al. (1978); [e]Humphreys (1978); [f]Reynolds & Ogden (1979); [g]Kuiper (1975); [h]O'Dell & Doi (2003); [i]Hardie et al. (1960); [j]Ogura & Ishida (1981); [k]Gies et al. (1997); [l]Claria (1974); [m]Bally & Scoville (1980); [n]Matthews (1979); [o]Chavarria-K. et al. (1994); [p]Sugitani et al. (2000)

flux was determined as described in Section 4.3.3, using the stars and spectral types as laid out in Table 4. The 3σ upper limits, subsequent maximum possible observed (i.e 3σ) fluxes and predicted ionising fluxes are presented in Table 5. It can be seen that $\Phi_P > \Phi_{max}$ in all but one case and that $\Phi_P > 10\Phi_{max}$ in a large number ($\sim 40\%$) of cases. These predictions are obviously inconsistent with the NVSS observations. In these cases the reasons for the discrepancies between theoretical prediction and measurement may mean that the predicted ionising star may be misclassified or misidentified, that extinction between the suspected ionising star and bright rim is significant, or that the assumed distances between star and cloud are incorrect. One example of a large discrepancy between predicted and measured flux is SFO 30. The measured ionising flux for this object is 22.1×10^8 cm^{-2} s^{-1}, while the predicted flux is extremely high compared to the rest of the sample at 4065.9×10^8 cm^{-2} s^{-1}. This disparity may well reside in the short distance of SFO 30 to its identified ionising star. SFO 30 is much closer to its ionising star than most of the sample (1.0 pc compared to a mean of 12.6 $\sigma = 7.0$). This object presents a good case study for the investigation of projection effects upon the ionising flux. It is also possible that the ionising star has been misclassified. With such a low comparative measured ionising flux it is unlikely that the projected distance of 1.0 pc to an 05V star is a true measurement.

Table 5: Values for the 3σ levels, maximum possible measured ionising flux and predicted ionising flux, for radio sources not detected in the survey.

SFO Object	3σ flux upper limit (mJy)	Max. observed ionising flux Φ_{max} (10^8 cm^{-2} s^{-1})	Predicted ionising flux Φ_P (10^8 cm^{-2} s^{-1})
3	2.04	2.02	21.15
8	1.52	1.78	118.31
9	2.10	2.02	78.22
19	0.75	0.51	0.57
20	1.40	1.47	1.47
22	1.78	1.93	22.83
23	1.91	2.07	2.52
24	2.69	2.17	11.52
26	1.37	1.22	1.06
33	1.55	1.13	13.29
34	1.40	1.48	9.98
39	1.72	1.85	9.18

4.3.7 Candidate Ultra-Compact HII Regions

One 20 cm source in this survey has been identified as a Type 3 source, SFO 14. The 20 cm NVSS emission from SFO 14 follows a potential ionised cloud rim, although there is a localised peak coincident with the IRAS position which is clearly identifiable in the MSX image. The radio emission arising from this peak has been treated as a separated object. The total radio flux measured from SFO 14 is 41.9 mJy, a region of flux incorporating the infrared peak but discounting the radio emission apparently emitted by the bright optical rim contributes 3.9 mJy to this total. This region has the characteristics of a compact, or ultra-compact HII region: it is infrared-luminous ($L_{IR} \sim 10^3$ - 10^4 $L_\odot$) and its IRAS colours match the criteria suggested by Wood & Churchwell (1989) for ultra-compact HII regions (namely that log F_{60}/log $F_{12} \geq$ 1.3 and log F_{25}/log $F_{12} \geq 0.57$, where the subscripts of 12, 25 and 60 represent the wavelength of the observation in microns). To further investigate the possibility of this object being an embedded compact (or ultra-compact) HII region within the BRC, the Far InfraRed (FIR) and radio luminosity of the source have been used to estimate the spectral class of any YSO that may be present. The FIR luminosity of an embedded YSO is almost entirely due to the luminosity of the YSO itself, reprocessed by the circumstellar dust in the region and re-emitted in the FIR.

In addition to HIRES IRAS fluxes taken from images obtained from the NASA/IPAC Infrared Science Archive[4] 450 μm and 850 μm fluxes presented in chapter 5 have been used as well as the 2 mm flux presented in Sugitani et al. (2000) to estimate the FIR luminosities of SFO 14. The luminosity was estimated by integrating under a greybody fit using the IRAS 60 μm flux together with the 450 μm, 850 μm and 2 mm flux measurements, the distance (1.9 kpc) was

[4]http://irsa.ipac.caltech.edu

taken from Sugitani et al. (1991). Further details about the SCUBA observations may be found in chapter 5, while details of the greybody modelling may be found in chapter 3. The assumption has been made that all of the luminosity arises from a single embedded YSO. This assumption may be rather crude but enables an initial estimate. Wood & Churchwell (1989) showed that, for a realistic initial mass function, the spectral type of the most massive member in a cluster is only 1.5 - 2 spectral classes lower than that derived for the single embedded star case.

In a compact or ultra-compact HII region, the 20 cm flux is predominantly due to thermal free-free emission. If this emission is assumed to be optically thin, and the assumption is made that the region is in photoionisation equilibrium, then it is possible to relate the integrated radio flux of the region to the total number of ionising photons from the embedded YSO via Eq. (7) of Carpenter et al. (1990).

$$N_i = 7.7 \times 10^{43}\ S_\nu\ D^2\ \nu^{0.1} \tag{84}$$

where N_i is the total number of photons per second ionising the cloud material, S_ν is the integrated radio flux density in mJy, D is the distance to the source in kpc and ν is the frequency of the observation in GHz. Note that the 5 GHz term of Eq. (7) of Carpenter et al. (1990) has been removed and the equation coefficient adjusted accordingly. Using the results of this equation the tables of Panagia (1973) can be used to find the spectral type of any central YSO. The results of the above analyses are presented in Table 6. There is good agreement between the spectral type predicted through the different methods, suggesting that there is a B0.5 - B1.5 YSO embedded within the molecular material of the clouds.

A literature search was carried out in order to identify the nature of the candidate ultra-compact HII region. SFO 14 is a well studied region within the W3/W4/W5 molecular cloud complex and is associated with the infrared stellar cluster AFGL 4029 (Deharveng et al. 1997). Snell et al. (1988) report the presence of a strong molecular outflow and Carpenter et al. (2000) find that the region contains an embedded cluster containing 240 ± 10 stars. The region has been found to contain a luminous red YSO invisible in the optical, associated with a cluster of massive red stars; an optical and IR reflection nebula; a high velocity ionised stellar wind; an optical jet and a bright H_2 emission knot (Deharveng et al. 1997). The spectral type of the most massive star in this cluster (inferred from the NVSS 20 cm flux) is consistent with that derived by Deharveng et al. (1997) from infrared observations.

The BRC identified as a potential high mass star-forming site has therefore been confirmed as containing an embedded cluster. The spectral class of the star within this cluster has been determined as being early B type and thus relatively young with a main sequence lifetime of $\sim 10^6$ years. A molecular outflow is also present (Snell et al. 1988) and so star formation is still occurring in this region. The region of emission is larger than the NVSS 45″ beam (corresponding to 0.4 pc at the assumed distance) at the 3σ level and so is not an ultra-compact HII region, the main sequence lifetime for the most massive predicted YSO is $\sim 10^6$ years and so we can assume an age of the embedded cluster that is younger than this. The radii of the 3σ contours of the embedded cluster is 1.1 pc. Given a propagation speed of 0.903 pc Myr^{-1} (Lefloch & Lazareff 1994) it is found that the radio region would have taken $\sim$1.2$\times$ 10^6 years (similar to the main sequence lifetime of a B0.5 star) to have formed as a consequence of the embedded clusters' influence. Using conservative estimates, the cluster is sufficiently old that it may have been influenced by the propagation of photoionisation shocks into the cloud. The distance of the core from the optical bright rim is 0.56 pc, assuming a shock velocity of 1 km s^{-1} (Thompson et al. 2004a; White et al. 1999) a shock crossing time of $\sim$ 5$\times$ 10^5 years is found. This is not conclusive evidence that the star exciting the bright rim of this cloud has affected the star-forming processes within the cloud, however, neither can the possible influence of this star be ruled out.

Accurate ages are needed for the star embedded within the cluster and for the star(s) that are ionising the region. This will allow a more certain link between the development of the embedded cluster and the ionising star(s) to be drawn. These ages may be determined through better spectral classifications of the stars, future infrared and optical spectral line observations will help to determine the information necessary in order to classify these stars.

Table 6: Infrared and radio-derived spectral types for the Type 3 radio source detected in the survey.

SFO Object	14
IRAS PSC ID	02575+6017
IR Luminosity ($L_{IR}/L_\odot$)	8321
Spectral Type (IR)	B0.5
Flux S_ν (mJy)	3.9
Ionising Photon Flux Log(N_i)(s^{-1})	45.0
Spectral Type (Radio)	B1.5

4.3.8 Previous Observations

Many of the clouds within the sample have outflows, indicating ongoing star formation within the regions. Table 7 summarises previous observations of outflow within the sample.

Table 7: Summary Of Previous Observations Of The SFO Catalogue.

SFO Object	Notes	Reference
5	Outflow detected, absence of UCHII region, star cluster formed in core	Lefloch et al. (1997)
11NE SMM1	Outflow detected.	Thompson et al. (2004a)
11E SMM1	Outflow detected.	Thompson et al. (2004a)
13	Embedded stellar cluster. Older sources distributed toward rim suggesting small-scale sequential star formation.	Carpenter et al. (2000)
16	Outflow detected.	De Vries et al. (2002)
18	Outflow detected.	De Vries et al. (2002)
20	Outflow detected.	Sugitani et al. (1989)
25	Outflow detected. Classified as Class I protostar. Compact CO outflow, Giant Herbig-Haro flow and its bow-shock pairs, an infrared reflection nebula and a near-infrared source	De Vries et al. (2002) Margulis et al. (1989) Wolf-Chase et al. (2003) and references therein
37	Outflow detected.	De Vries et al. (2002)

4.4 Discussion

25 clouds from this survey were classified as Type 1 radio sources, i.e. with 20 cm emission clearly associated with their photoionised cloud rims. The pressures from their IBLs were estimated in Section 4.3.3 and, together with data on the molecular interior of the clouds, these may allow the determination of the pressure balance between the IBL and the internal molecular material of the clouds. In the RDI scenario a photoionisation driven shock propagates into the molecular cloud. However, if the internal pressure of the cloud is greater than or equal to the pressure in the developing IBL, the shock stalls at the surface of the cloud (Lefloch & Lazareff 1994). Evaporation of the cloud ensures that eventually (provided that the source of ionisation is maintained) the surface area of the cloud will decrease, leading to a relative increase in the IBL pressure and hence allowing the propagation of a D-critical ionisation front.

If the clouds that have been observed are currently underpressured with respect to their IBL then it may be expected that there are (or have been) photoionisation shocks propagating into the cloud. It is therefore likely that any existing star formation in these clouds has been caused via the RDI scenario.

The data that are required on the molecular interior of these clouds, in order to derive the internal pressure, may be derived through molecular line observations. There are a small number of such observations that have previously been published and these, together with the molecular line observations presented in chapter 6, form the basis for our comparison of internal molecular pressures with those determined for IBLs in this work. This subject will be further investigated in Section 6.8.

4.4.1 IBL Pressure

The pressures in the IBL of each cloud for which there was radio data were determined. The pressures were found to be high with a mean of 33.7×10^5 cm^{-3} K (Table 3). These pressures will help to determine the current dynamical state of the clouds. Molecular observations will give the pressures of the neutral molecular material within the clouds. The balance (or lack thereof) will lead to valuable information regarding the possibility of photoionisation induced shocks, which may trigger the formation of protostellar collapse in the case of BRCs.

4.5 Summary

From archival studies of radio, optical and infrared observations, 44 BRCs have been analysed for signs of triggered star formation. 20 cm emission was detected to a level of 3σ ($\sigma \sim 0.45$ mJy beam^{-1}) or greater in 32 of the sample, and using a comparison of various wavelength images, including MSX and DSS, the clouds have been sorted into the four distinct types identified by Thompson et al. (2004b), i.e. Type 1: BRCs, Type 2: broken-rimmed clouds, Type 3: embedded radio sources and Type 4: unassociated radio sources. There are 25 Type 1 sources identified within the sample, and the conditions prevailing within their IBLs have been analysed, including the incident ionising fluxes, electron density and ionised gas pressures. This analysis has almost doubled the number of BRCs that have known IBL conditions.

A comparison of the derived results for SFO 5 with those of Lefloch et al. (1997), reveals a difference in derived IBL pressure of a factor of ∼10, (they derive an external pressure of 300 $\times$ 10^5 cm^{-3} K compared to a pressure derived here of 35.8×10^5 cm^{-3} K). This difference is believed to be due to the differences in observational data, the resolution of observations made of objects at radio wavelengths has been found to significantly affect the measured flux (Urquhart et al, 2005 in press). The observations of Lefloch et al. (1997) were made at 5GHz with a beam of 14″, the NVSS beam size is 45″at 1.4 GHz. The different frequencies and resolutions of these observations mean that significantly different regimes may be being observed. A larger beam size may be expected to dilute flux from concentrated regions, while the different frequency of observations will record different fluxes according to the spectral index of the object.

The large difference between the resolved, and unresolved, observations of the IBL pressure indicate that low resolution radio studies, such as the NVSS, may not accurately describe the detailed pressure balance between the internal molecular pressure of the clouds and the external pressure. The pressures derived from such observations must be treated as global values, and regarded more as a lower limit to the possible pressure acting upon the relevant clouds.

4.6 Conclusions

1. In many cases the predictions of ionising flux from the candidate ionising stars are inconsistent with the observed 20 cm flux. This discrepancy may mean that the assumption that there is negligible absorption is invalid. Other possible causes of this discrepancy include the misclassification of the spectral type of the ionising star, the possible existence of as-yet undiscovered additional OB stars within the region, or an inaccuracy in the distance measurements to the objects.

   It has been noted that flux measurements may be expected to increase with improved resolution, Urquhart et al, (2005 in press) found that flux significantly increased when observations were made of the IBL fluxes associated with southern SFO sources at higher resolution. This may explain the discrepancy between observed and predicted ionising fluxes. Further improved resolution studies are necessary to confirm or contradict this suggestion.

2. The single Type 3 radio source in the survey (SFO 14) has been identified with a known young, embedded cluster containing massive stars (Deharveng et al. 1997). With the 20 cm NVSS data, this has been confirmed as containing early B type stars.

Chapter 5

A SCUBA Survey Of Bright-Rimmed Clouds

5.1 Introduction

In chapter 1 the structure and composition of star-forming regions was discussed, the natal star(s) forming within a molecular cloud are surrounded by a circumstellar disc from which material is accreted onto the still-forming star. Extending beyond this accretion disc, is a protostellar envelope which absorbs and re-emits the radiation emitted from the young star's photosphere. The majority of radiation originating from the star-forming region, visible to the earth-based observer, is emitted in the infrared-submillimetre region of the electromagnetic spectrum. This dust-processed emission is optically thin and serves as a valuable probe of the structure of star-forming regions as this continuum is averaged over a wide range of densities and is relatively unaffected by chemical processes within the cloud compared to molecular line emission.

Dust emission traces the mass distribution of star-forming clouds and may thus be used to find the total mass of a star forming cloud (with a few caveats, the determination of mass relies upon the knowledge of certain values that may not be well defined, e.g. the dust-to-gas ratio of the cloud or, the distance to the cloud from the observer). As the emission is ultimately the result of radiation emitted by the natal star, it is possible to infer information about the type of star embedded within the cloud.

In order to probe the conditions and composition of 45 clouds selected from the SFO catalogue SCUBA was used to obtain submillimetre maps at both 450 μm and 850 μm. These data were used in conjunction with archival IRAS data to define the IR-submillimetre regime of emission arising from the sources. The observational procedure is described in Section 5.2 and the relevant parameters arising from the observations are detailed in Section 5.3. The 2MASS Point Source Catalogue (Cutri et al. 2003) has been used to explore the sample for known IR sources that would associate the clouds with ongoing star formation. The properties of sources found within the optical boundaries of the clouds are presented in Section 5.5

5.2 Observations

Simultaneous 450 and 850 μm images of all 45 targets were obtained using SCUBA (Holland et al. 1999) on the JCMT. SCUBA is described in chapter 2 along with a guide to the processes involved in the data reduction. Jiggle maps were taken over a period ranging from the 2^{nd} November 2001 to the 21^{st} April 2002. In some cases, maps were coadded to improve the signal-to-noise ratio, or to extend the field of view. Observational parameters are summarised in Table 8. The atmospheric opacity was monitored by the Caltech Submillimeter Observatory (CSO) radiometer at 225 GHz, and regular skydips at the azimuth of each observation were performed to estimate the atmospheric zenith optical depth. The two sets of sky observations thus serve as a consistency check and were found to match within reasonable limits.

5.2.1 IRAS HIRES Observations

IRAS HIRES images were obtained from the NASA/IPAC Infrared Science Archive[1]. The fluxes from the IRAS images at 60 μm and 100 μm trace the peak IR/submillimetre emission regions of the dusty objects that have been observed. The default parameters (20 iterations) were used in obtaining the IRAS HIRES images with typical angular resolutions of $90''$x $60''$, and $120''$x $100''$, at 60 μm and 100 μm respectively. The irregular sampling involved in the HIRES processing technique results in variable spatial resolution across any particular image. Absolute calibration uncertainties for IRAS-HIRES derived fluxes are estimated to be 20%, similar to the original IRAS survey, though with generally improved resolution.

IRAS HIRES images are subject to a number of processing artifacts, most notably in this case are the negative 'bowls' which appear around bright sources. When a point source is superposed on a nonzero background, the artifact known as ringing or ripples appears in many image reconstruction algorithms. In Fourier language, the reconstruction process tries to make the image agree with the true scene in the low spatial frequency components (data constraint), without access to the infinitely high spatial frequencies inherent in the point-source scene. The

[1] http://irsa.ipac.caltech.edu

Table 8: Observational parameters for SCUBA jiggle maps.

Date	Source	Integrations[a]	Chop Throw	Representative τ	
				450 μm	850 μm
2^{nd} Nov 2001	SFO 31 & 32	10	120	2.750	0.436
2^{nd} Dec 2001	SFO 23	10	120	2.556	0.288
7^{th} Jan 2002	SFO 11 & 13	10	120	2.493	0.330
10^{th} Jan 2002	SFO 9,10,12,15 & 16	10	120	2.363	0.338
	SFO 14	3	120	2.363	0.338
	SFO 17	5	120	2.363	0.338
11^{th} Jan 2002	SFO 17	5	120	2.170	0.317
	SFO 18	10	120	2.170	0.317
18^{th} Feb 2002	SFO 30	10	180	3.163	0.475
12^{th} Mar 2002	SFO 28 & 29	10	180	2.819	0.379
15^{th} Mar 2002	SFO 24,25,26 & 27	10	180	3.570	0.411
20^{th} Mar 2002	SFO 33	10	180	1.455	0.263
21^{st} Mar 2002	SFO 34	10	180	0.512	0.123
29^{th} Mar 2002	SFO 45	10	180	2.244	0.349
30^{th} Mar 2002	SFO 35 & 36	10	180	1.130	0.256
31^{st} Mar 2002	SFO 37,77,78 & 88	10	180	3.544	0.361
	SFO 87	1	180	3.544	0.361
19^{th} Apr 2002	SFO 4,38,39 & 40	3	180	2.277	0.387
20^{th} Apr 2002	SFO 1,2,3,7,43 & 44	4	180	1.263	0.214
	SFO 41 & 42	3	180	1.263	0.214
	SFO 89	6	180	1.263	0.214
21^{st} Apr 2002	SFO 5 & 6	6	180	2.669	0.394

[a] One SCUBA 'integration' is equivalent to 64 seconds of integration.
The term 'representative' τ means an opacity level measured approximately in the middle of an observing run that was found to be consistent with opacity levels throughout the run.

magnitude of the ringing depends on the strength of the point source, the level of the residual background intensity (after the application of flux bias), and the detector scan pattern. For nonlinear algorithms (such as MCM), the dependence is complicated and difficult to quantify (Cao et al. 1997). This effect occured most obviously at 100 μm. Because of this effect one IRAS-HIRES 100 μm flux had an offset applied (SFO 27 - 9.7 Jy). This offset is approximately %12 of the measured flux and this is not considered to be unreasonable given the expected %20 flux calibaration errors. The offset was applied by biasing the fits image so that the minimum measured flux in the source region was 0 Jy/beam. The integrated flux density was then measured in the normal way. In some cases the negative flux 'bowls' were not distinct enough to measure an offset, although they obviously affected the measured fluxes. For these sources IRAS (60 μm, 100 μm or both) fluxes were dismissed. HIRES 60 μm and 100 μm fluxes used in the determination of the source emission behaviour are presented in Table 9.

Table 9: Fluxes of each source measured in IRAS HIRES images as discussed in the text.

Source	IRAS HIRES Flux(Jy)	
	60 μm	100 μm
SFO 1	94.8	360.0
SFO 2	16.0	—
SFO 5	71.4	—
SFO 7	19.2	—
SFO 9	13.6	48.3
SFO 10	19.4	77.4
SFO 11 SMM1 [a]	17.0	—
SFO 11NE SMM1[a]	10.0	—
SFO 11E SMM1 [a]	20.1	—
SFO 14	382.2	—
SFO 15	9.8	21.6
SFO 27	14.1	78.9
SFO 29	4.8	19.5
SFO 30	706.1	1302.3
SFO 31	29.5	119.7
SFO 32	6.9	22.1
SFO 33	10.2	37.0
SFO 35	6.5	—
SFO 36	16.8	—
SFO 37	29.3	—
SFO 38	72.4	—
SFO 42	7.3	—
SFO 43	75.8	169.2
SFO 44	203.6	—
SFO 87 SMM2	103.0	451.7
SFO 88	161.9	—
SFO 89	129.8	315.4

[a] Taken from Thompson et al. (2004a), — indicates dismissed flux data.

5.3 Results

Multiple measurements were made on blank sky in each image in order to determine the individual r.m.s. (σ) of each observation. 45 submillimetre cores were detected towards 43 BRCS (submillimetre emission was considered a 'detection' if a centrally condensed region exceeded three σ over an area comparable to, or larger than, the beamsize), eight clouds did not yield any detectable cores, SFO 3, SFO 6, SFO 17, SFO 23, SFO 28, SFO 45, SFO 77 and SFO 78.

The detected cores were generally resolved and bright. The properties of these cores are described in the next subsection. Contours of the SCUBA emission are presented, overlaid upon DSS images of each cloud, in Appendix A.

5.3.1 Core Positions, Fluxes And Sizes

The position of each core's peak emission, along with their measured fluxes and effective diameters are given in Table 10. The sources SFO 11, SFO 39 and SFO 87 were found to consist of discrete objects (i.e. separate objects bounded by unbroken contours with peak fluxes greater than 3σ). These separate objects have been designated following the naming convention of Thompson et al. (2004a), i.e. the cloud name from Sugitani & Ogura (1994) followed by a SMM number to indicate submillimetre detections (e.g. SFO 11 SMM1). SMM numbers increase from north to south. There are suggestions that SFO 25 is composed of more than one 'clump' (see chapter 6) and visually, the SCUBA map at 850 μm appears to be separated into two separate regions of emission (Fig. 5.3.1). However, the emission in between the two regions is at a high level ($>13\sigma$) and thus the 'clumps' were not considered sufficiently distinct to determine separate fluxes.

The size of each source was estimated by fitting a Gaussian function to the azimuthally averaged 850 μm flux because of the higher signal-to-noise ratio relative to the 450 μm data. The beam size was taken into account through the assumption of a simple Gaussian source with a Gaussian beam of 14$''$ (Θ^2_{obs}=Θ^2_{beam}+Θ^2_{source}). Distances to the clouds were taken from Sugitani et al. (1991) and Sugitani & Ogura (1994), these allowed a calculation of the physical effective diameter of each core (see Table 10). The core diameters range from 0.02 - 0.29 pc with a mean of 0.11 pc. The size of core may be placed in a context of star formation by considering turbulent motions within molecular clouds. Observed turbulent motions become subsonic on the smallest scales creating smooth, regular structures. The size of the smallest star-forming cores may then be determined by the scale at which turbulence transits from supersonic to subsonic. This is of the order 0.05 - 0.1 pc (Larson 2003) (the resolution of SCUBA is 14$''$, this corresponds to 0.09 pc at the mean distance of the sample, 1.29 kpc). The cores in the sample are evenly distributed in terms of size around this turbulent transitional scale.

5.4 Correlation With Radio Free-Free Emission

In chapter 4 a search of the NVSS archive was described. The archive was used in searching the SFO catalogue for radio detections, 36 clouds from the catalogue are shared between that survey and this, i.e. there are 36 objects for which there is data from the NVSS and at least one SCUBA wavelength. Of these 36 clouds, two were not detected by either survey, six were detected in the SCUBA survey only and two were detected in the NVSS only, leaving 26 clouds that were detected by both the NVSS and the SCUBA survey. The detections (or non-detections) are

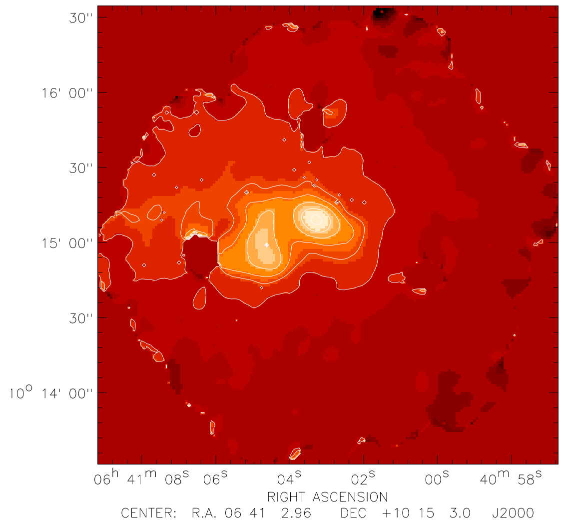

Figure 13: Image of the SCUBA 850 μm emission associated with the cloud SFO 25. Contours start at 3σ and increase in increments of 20% of the peak flux.

summarised in Table 11. This ~80% correlation between the two surveys implies a connection between the free-free emission at the rims of the clouds and the formation of warm dust cores within the clouds themselves.

5.5 Associated Infrared Objects-2MASS Data

The 2MASS catalogue was searched for near-infrared sources within the optical bounds of the clouds surveyed. Detections of young, star-forming objects would indicate the presence of ongoing star-formation within the clouds. The nature of each of these sources may be determined by their $J-H$ and $H-K_s$ colours using the $J-H$ and $H-K_s$ colour diagram method described in Lada & Adams (1992). An example of this type of diagram is shown in Fig. 14, with similar diagrams for the rest of the clouds in the survey presented in Appendix A. The solid lines represent the colours of main sequence and giant stars (Koornneef 1983), while the dotted line shows the colours of Classical T-Tauri Stars (CTTS) (Meyer et al. 1997).

YSOs have an extended circumstellar envelope. The size and mass of this envelope is determined by the amount of available material, the mass of the YSO itself and the age of the object. The circumstellar envelope absorbs and re-emits the light emitted by the star embedded within the cloud, thus leading to the extincted light observed in the infrared regime. This light may be differentiated from older stars that have had their radiation extincted by large amounts of intervening dust through their infrared colours.

As a source is subjected to higher levels of extinction (larger intervening columns of dust) it moves towards the top right corner of the diagram, following the reddening tracks shown by dashed lines in Fig. 14. Thus, sources found to lie to the left of the middle reddening track are likely to be main-sequence or giant stars, while those sources that lie between the middle and rightmost track may be identified as CTTS. Sources to the right of the rightmost track represent Class I protostars hidden by a large, extended dusty envelope.

A large number of CTTS and/or Class I protostars found to be associated with a cloud would show the presence of ongoing early star-formation within the cloud.

The errors in the J, H and K_s band fluxes are such that a clear distinction between the different types of source seen towards each cloud is not possible. Lada & Adams (1992) note that there is an inherent uncertainty in the identification of the individual type of YSO. Although main sequence stars and YSOs occupy different regions of $J - H$ vs. $H - K_s$ colour-colour diagrams species such as weak-line T Tauris, classical T Tauris, class I protostars and Herbig AeBe stars may overlap.

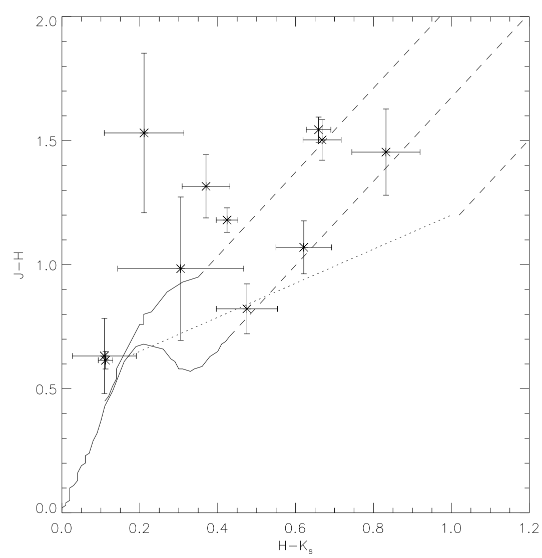

Figure 14: J-H versus H-K_s diagrams of the 2MASS sources associated with the cloud SFO 1. The solid lines represent the unreddened locuses of main sequence and giant stars from Koornneef (1983) The dotted line represents the classical T-Tauri locus of Meyer et al. (1997). Reddening tracks are shown by dashed lines.

The total numbers of candidate protostellar objects for each source are shown in Table 12, of 43 clouds there are 5 which have no associated 2MASS point sources which have colours consistent with protostellar objects, SFO 1, 23, 78, 88 and 89.

The limiting magnitudes of the 2MASS are 15.8 in the J band, 15.1 at the H band frequency and 14.3 in the K_s band. The average K-band extinction of the sample set ranges from 0.3 to 157.8 with a mean of 19.9 (the determination of K-band extinction is discussed in Section 5.7.1), it is clear then that the flux from at least some sources will be attenuated beyond the sensitivity of the 2MASS. The 2MASS point sources that have been identified are likely to be on the side of the cloud facing the observer, where there is less material for their radiation to pass through. The numbers of identified YSOs found then probably do not accurately trace the star formation within the clouds but their presence is a good indicator that star formation is likely. Deeper near-infrared observations are necessary to ascertain the young stellar presence within each cloud.

5.6 Observational Summary

45 targets were observed at 450 and 850 μm using the SCUBA on the JCMT. Observations towards nine of these clouds resulted in non-detections at 850 μm. One BRC was not observed at this wavelength due to corrupted data. 26 BRCs were not detected at 450 μm, though the one non-detection at 850 μm (SFO 34) was detected at this wavelength. The peak and integrated fluxes of each source, along with their physical diameter have been determined.

IRAS fluxes pertinent to the sources have been determined from IRAS HIRES images. In addition, near-infrared sources associated with the SCUBA sources have been identified from the 2MASS and classified using the J-H and H-K_s colour-colour diagram method of Lada & Adams (1992).

5.7 Temperature, Mass And Density

In section 3.3 the process of greybody modelling was described which enables the derivation of some of the important physical properties of the clouds that have been observed.

From the submillimetre continuum maps presented in Appendix A, the derivation of each cloud's temperature, mass and density is possible.

5.7.1 Dust Continuum

A single temperature greybody model was fitted to the Spectral Energy Distribution (SED) of each core using their dust continuum emission observed with SCUBA at 450 and 850 μm (where detected), IRAS HIRES fluxes at 60 and 100 μm where available and fluxes taken from other works revealed through a search of the SIMBAD database of astronomical catalogues[2] (see Table 14 for references). IRAS fluxes at 12 μm and 25 μm were disregarded as it has been found that these fluxes are generally not well fitted by a single temperature greybody (Thompson et al. 2004b). This is likely due to the discrepancy in relative optical depths, the mid-IR emission coming from regions in which the column densities are lower than that dictated by the SED peak and submillimetre emission (Hatchell & van der Tak 2003). This has been suggested as possibly being due to outflow cavities, clumpy distributions and protostellar disks.

IRAS fluxes at 100 μm were found to be generally unreliable due to confusion and negative 'bowling' surrounding the sources. Where possible the 100 μm flux has been included or rescaled by adding the absolute negative flux per beam in the immediate surrounding area to the measured flux. The temperature of the illuminating internal source and global optical depth of each object were determined by a greybody fit of the form:

$$F_\nu = \Omega B_\nu(T_d)(1 - e^{-\tau_\nu}), \tag{85}$$

as described in section 3.3.

The dust temperatures resulting from the greybody analysis, along with core masses and H_2 number densities (derived assuming spherical geometry at the effective core diameter), are presented in Table 13. The dust temperatures and luminosities found from fitting greybody curves to the fluxes found in Table 14 were not found to be overly sensitive to the number of flux measurements. The majority of the sample was analysed using only three or four flux measurements, usually taken from 60 μm and 100 μm IRAS measurements and the 450 μm and 850 μm SCUBA observations. However, a small number of sources had many flux measurements available. For example, SFO 38 had a total of 11 data points used in fitting a greybody curve, fitting a greybody curve to the IRAS and SCUBA data only for SFO 38 had no effect upon the dust temperature value and altered the determined luminosity by less than 1%. Fitting to only the IRAS and SCUBA data has thus been assumed to be reliable in determining the temperatures and luminosities of these sources, at least as far as the whole practice of greybody fitting may be. It should be pointed out that this method appears valid $for\ these\ cases$, no claims are made on the validity of this method in more general scenarios.

Dust temperatures for the sources SFO 25, SFO 39 SMM1 and SFO 39 SMM2 were derived from their observed 850/450 μm flux ratios. The IRAS fluxes associated with these objects were too poor to fit an SED i.e. the fluxes did not appear to lie upon the normal curve of a protostellar SED, in these cases either the simple model we are using to fit these fluxes is inadequate, or the

[2] http://simbad.u-strasbg.fr

IRAS data may be inadequate to determine the flux associated with the protostellar sources.. In the cases of SFO 39 SMM1 and SFO 39 SMM2 were confused between the sources.

Dust temperatures resulting from greybody fitting range from 21 to 33 K with a mean of 26 K. The temperatures determined from the 450/850 flux ratios range from 9 to 76 K; this reflects the greater uncertainty in determinations of temperature made using this method. Flux errors of $\sim$ 20% lead to errors of only 1-2 K in dust temperature as determined by greybody fitting, however when determinations are made using only two points the resultant temperature is only accurate to within a factor of $\sim$ 2. The temperatures determined in this analysis are significantly higher than those reported for starless cores ($\sim$ 10 K), indicating the presence of an internal heating source within the clouds.

Masses for the cores were found by adopting the method of Hildebrand (1983) for an optically thin cloud with a uniform temperature, i.e.

$$M = \frac{d^2 F_\nu C_\nu}{B_\nu(T_d)}. \tag{86}$$

The results are shown in the second and third columns of Table 13. The errors in the mass and density of the cores are generally dominated by temperature effects in the non-linear Planck function in Eq. 16. Typical values of observed 850 μm flux and SED determined dust temperature have errors of $\sim$ 10% and $\pm$ 1-2 K respectively leading to an factor of $\sim \sqrt{2}$ error in mass and density. However, in the case of low signal-to-noise ratios this error may rise to a factor of 10 as in the case of SFO 11E SMM2 (Thompson et al. 2004a).

Table 10: Core positions and fluxes.

Source	α_{2000}	δ_{2000}	Peak Flux(Jy/beam) 450 μm	Peak Flux(Jy/beam) 850 μm	Integrated Flux (Jy) 450 μm	Integrated Flux (Jy) 850 μm
SFO 1	23 59 32.3	+67 24 04	4.1±0.3	0.68±0.07	9.6±0.7	2.08±0.21
SFO 2	00 04 00.4	+68 35 18	3.8±0.3	0.66±0.03	25.1±2.0	5.75±0.26
SFO 3	00 05 22.3	+67 17 34	<2.0	—	[a]	[a]
SFO 4	00 59 01.5	+60 53 30	—	0.20±0.02	[a]	4.49±0.46
SFO 5	02 29 02.3	+61 33 33	<5.5	1.31±0.05	[a]	5.70±0.22
SFO 6	02 34 46.0	+60 47 46	<4.8	<0.73	[a]	[a]
SFO 7	02 34 48.0	+61 46 29	9.8±0.5	1.18±0.07	38.1±1.9	6.42±0.38
SFO 9	02 36 23.2	+61 23 59	<1.4	0.17±0.03	[a]	1.14±0.20
SFO 10	02 48 10.0	+60 25 00	<1.5	0.16±0.02	[a]	0.60±0.08
SFO 11 SMM1 [c]	02 51 33.7	+60 03 54	1.2±0.2	0.23±0.01	8.1±1.4	1.42±0.15
SFO 11 SMM2 [c]	02 51 25.0	+60 03 42	0.7±0.2	0.15±0.01	5.2±0.9	0.53±0.06
SFO 11 SMM3 [c]	02 51 29.6	+60 03 01	0.7±0.2	0.13±0.01	2.5±0.6	0.27±0.05
SFO 11NE SMM1[c]	02 51 53.6	+60 07 00	1.6±0.1	0.34±0.01	4.0±0.5	0.92±0.10
SFO 11NE SMM2[c]	02 51 59.5	+60 06 27	1.0±0.1	0.25±0.01	2.7±0.3	0.54±0.08
SFO 11E SMM1 [c]	02 52 16.8	+60 03 19	5.8±0.3	0.48±0.01	15.5±1.4	1.29±0.10
SFO 11E SMM2 [c]	02 52 15.9	+60 02 29	—	0.21±0.01	3.9±0.7	0.34±0.25
SFO 11E SMM3 [c]	02 52 19.0	+60 02 17	2.7±0.3	0.26±0.01	3.2±0.5	0.40±0.23
SFO 12	02 55 01.6	+60 35 43	<1.8	0.62±0.03	[a]	3.13±0.15
SFO 13	03 00 56.6	+60 40 24	<1.7	0.49±0.04	[a]	7.33±0.60
SFO 14	03 01 31.4	+60 29 20	13.8±1.0	2.38±0.11	42.6±3.1	16.59±0.77
SFO 15	05 23 27.4	+33 11 50	<1.0	0.09±0.02	[a]	0.18±0.04
SFO 16	05 19 48.4	-05 52 04	<1.5	0.65±0.05	[a]	5.68±0.44
SFO 17	05 31 27.8	+12 05 23	<0.4	<0.41	[a]	[a]
SFO 18	05 44 29.7	+09 08 55	1.1±0.1	0.69±0.04	3.5±0.3	7.55±0.44
SFO 23	06 22 58.7	+23 09 59	<2.0	<0.26	[a]	[a]
SFO 24	06 34 53.1	+04 25 31	<13.9	0.72±0.03	[a]	1.12±0.05
SFO 25	06 41 03.3	+10 15 09	44.4±7.3	1.61±0.07	48.4±8.0	13.17±0.57
SFO 26	07 03 45.3	-11 46 31	<1.7	0.18±0.03	[a]	0.80±0.13
SFO 27	07 03 57.5	-11 22 48	<1.8	0.53±0.08	[a]	3.32±0.50
SFO 28	07 04 44.2	-10 21 43	<3.3	<0.74	[a]	[a]
SFO 29	07 04 50.0	-12 09 49	<9.7	0.74±0.17	[a]	1.10±0.25
SFO 30	18 18 46.8	-13 44 28	2.3±0.2	1.61±0.04	8.8±0.8	10.83±0.27
SFO 31	20 50 43.1	+44 21 56	2.4±0.2	0.62±0.13	3.6±0.3	0.41±0.09
SFO 32	21 32 29.1	+57 24 33	<0.7	0.19±0.02	[a]	0.31±0.03
SFO 33	21 33 12.8	+57 30 16	<0.6	0.12±0.03	[a]	0.13±0.03
SFO 34	21 33 32.3	+58 03 31	2.8±0.1	[b]	11.7±0.4	[b]
SFO 35	21 36 01.6	+58 30 57	1.3±0.1	0.18±0.04	6.3±0.5	1.38±0.31
SFO 36	21 36 07.4	+57 26 41	9.4±0.2	1.44±0.06	47.2±1.0	7.12±0.30
SFO 37	21 40 29.0	+56 35 53	11.3±3.2	0.82±0.05	7.2±2.0	1.85±0.11
SFO 38	21 40 41.6	+58 16 14	27.7±0.5	3.90±0.13	133.0±2.4	24.18±0.81
SFO 39 SMM1	21 46 01.3	+57 27 46	4.9±0.5	0.85±0.03	22.3±2.3	4.92±0.17
SFO 39 SMM2	21 46 07.0	+57 26 38	4.6±0.5	0.79±0.03	20.1±2.2	3.63±0.14
SFO 40	21 46 10.9	+57 09 33	<1.0	0.29±0.03	[a]	4.24±0.44
SFO 42	21 46 40.5	+57 12 42	2.7±0.4	0.23±0.04	3.76±0.6	1.32±0.23
SFO 43	22 47 49.3	+58 02 51	3.8±0.3	0.67±0.04	8.5±0.7	3.77±0.23
SFO 44	22 28 51.1	+64 13 42	38.0±0.3	3.48±0.03	94.9±0.7	15.52±0.13
SFO 45	07 18 23.3	-22 06 20	<2.8	<0.51	[a]	[a]
SFO 77	16 19 53.6	-25 33 43	<22.1	<0.39	[a]	[a]
SFO 78	16 20 52.7	-25 08 11	<19.3	<0.34	[a]	[a]
SFO 87 SMM1	18 02 52.7	-24 21 27	<13.9	0.67±0.06	[a]	3.43±0.31
SFO 87 SMM2	18 02 49.6	-24 22 26	<13.9	0.65±0.06	[a]	3.21±0.30
SFO 88	18 04 11.5	-24 06 40	44.1±5.3	0.83±0.03	298.4±35.9	28.12±1.02
SFO 89	18 09 56.6	-24 04 20	3.3±0.3	0.48±0.04	9.0±0.8	6.57±0.41

[a]non-detection.[b]Image corrupted.[c]From (Thompson et al. 2004a).— indicates non-availability of data.
< indicates that the value is a three σ upper limit.

Table 11: Table listing detections/non-detections of sources.

Source	SCUBA 450 μm	SCUBA 850 μm	NVSS 20 cm
SFO 1	$\surd$	$\surd$	$\surd$
SFO 2	$\surd$	$\surd$	$\surd$
SFO 3	$\times$	$\times$	$\times$
SFO 4	$\times$	$\surd$	$\surd$
SFO 5	$\times$	$\surd$	$\surd$
SFO 6	$\times$	$\times$	$\surd$
SFO 7	$\surd$	$\surd$	$\surd$
SFO 8	$\times$	$\times$	$\times$
SFO 9	$\times$	$\surd$	$\times$
SFO 10	$\times$	$\surd$	$\surd$
SFO 11 SMM1	$\surd$	$\surd$	$\surd$
SFO 11 SMM2	$\surd$	$\surd$	$\times$
SFO 11 SMM3	$\surd$	$\surd$	$\times$
SFO 11NE SMM1	$\surd$	$\surd$	$\times$
SFO 11NE SMM2	$\surd$	$\surd$	$\times$
SFO 11E SMM1	$\surd$	$\surd$	$\times$
SFO 11E SMM2	$\surd$	$\surd$	$\times$
SFO 11E SMM3	$\surd$	$\surd$	$\times$
SFO 12	$\times$	$\surd$	$\surd$
SFO 13	$\times$	$\surd$	$\surd$
SFO 14	$\surd$	$\surd$	$\surd$
SFO 15	$\times$	$\surd$	$\surd$
SFO 16	$\times$	$\surd$	$\surd$
SFO 17	$\times$	$\times$	$\surd$
SFO 18	$\surd$	$\surd$	$\surd$
SFO 19	$\times$	$\times$	$\times$
SFO 20	$\times$	$\times$	$\times$
SFO 21	$\times$	$\times$	$\surd$
SFO 22	$\times$	$\times$	$\times$
SFO 23	$\times$	$\times$	$\times$
SFO 24	$\times$	$\surd$	$\times$
SFO 25	$\surd$	$\surd$	$\surd$
SFO 26	$\times$	$\surd$	$\times$
SFO 27	$\times$	$\surd$	$\surd$
SFO 28	$\times$	$\times$	$\surd$
SFO 29	$\times$	$\surd$	$\surd$
SFO 30	$\surd$	$\surd$	$\surd$
SFO 31	$\surd$	$\surd$	$\surd$
SFO 32	$\times$	$\surd$	$\surd$
SFO 33	$\times$	$\surd$	$\times$
SFO 34	$\surd$	$\times$	$\times$
SFO 35	$\surd$	$\surd$	$\surd$
SFO 36	$\surd$	$\surd$	$\surd$
SFO 37	$\surd$	$\surd$	$\surd$
SFO 38	$\surd$	$\surd$	$\surd$
SFO 39 SMM1	$\surd$	$\surd$	$\times$
SFO 39 SMM2	$\surd$	$\surd$	$\times$
SFO 40	$\times$	$\surd$	$\surd$
SFO 41	$\times$	$\times$	$\surd$
SFO 42	$\surd$	$\surd$	$\surd$
SFO 43	$\surd$	$\surd$	$\surd$
SFO 44	$\surd$	$\surd$	$\surd$
SFO 45	$\times$	$\times$	$\times$
SFO 77	$\times$	$\times$	$\times$
SFO 78	$\times$	$\times$	$\times$
SFO 87 SMM1	$\times$	$\surd$	$\times$
SFO 87 SMM2	$\times$	$\surd$	$\times$
SFO 88	$\surd$	$\surd$	$\times$
SFO 89	$\surd$	$\surd$	$\times$

$\surd$ denotes a detection, $\times$ denotes a non-detection

Table 12: Numbers of class I protostellar candidates (YSO) or candidate T-Tauri stars (TTS) identified from the JHK$_s$ diagrams (Appendix A) for all sources

Source	Number of associated YSO	Number of associated CTTS	Source	Number of associated YSO	Number of associated CTTS
1	0	0	28[a]	0	1
2	7	27	29	1	3
3[a]	0	2	30	0	9
4	0	4	31	0	4
5	0	7	32	0	7
6[a]	1	7	33	0	2
7	0	13	34	0	1
9	0	4	35	0	4
10	0	9	36	3	4
11	5	13	37	2	2
12	0	13	38	3	12
13	1	10	39	1	6
14	4	18	40	1	5
15	0	2	42	1	1
16	3	0	43	2	4
17[a]	0	4	44	3	5
18	0	3	45[a]	2	6
23[a]	1	4	77[a]	0	2
24	0	0	78[a]	0	0
25	2	6	87	0	1
26	0	2	88	0	0
27	1	9	89	0	0

[a]Non-detections at SCUBA wavelengths

Table 13: Core properties determined from greybody fits.

Source	T_d (K)	M ($M_\odot$)	$Log_{10}(n)$ cm^{-3}	A_V	A_K
SFO 1	27	4.9	5.6	33.2	3.7
SFO 2	21	19.0	5.9	80.1	9.0
SFO 5	26	69.7	5.9	118.7	13.3
SFO 7	23	93.3	6.0	166.2	18.7
SFO 9	27	13.3	6.5	193.5	21.7
SFO 10	31	5.9	6.8	204.2	22.9
SFO 11 SMM1	23	20.6	4.5	9.7	1.1
SFO 11 SMM2	32	4.9	4.3	4.6	0.5
SFO 11 SMM3	27	3.1	4.1	2.9	0.3
SFO 11NE SMM1	23	13.4	4.5	8.5	1.0
SFO 11NE SMM2	11	26.4	5.3	38.0	4.3
SFO 11E SMM1	23	18.7	4.5	9.5	1.1
SFO 11E SMM2	76	1.1	4.3	2.9	0.3
SFO 11E SMM3	19	7.7	5.3	23.6	2.7
SFO 14	29	175.5	5.9	162.4	18.2
SFO 15	29	6.1	5.2	19.2	2.2
SFO 25	9	164.7	7.3	1404.8	157.8
SFO 27	23	17.7	6.4	170.6	19.2
SFO 29	22	6.2	5.7	42.2	4.7
SFO 30	33	129.9	5.6	93.6	10.5
SFO 31	27	1.3	5.7	23.3	2.6
SFO 32	22	0.8	5.6	16.3	1.8
SFO 33	27	0.2	5.9	19.7	2.2
SFO 35	22	3.3	6.2	70.5	7.9
SFO 36	23	16.1	6.7	253.0	28.4
SFO 37	27	3.3	6.6	135.7	15.2
SFO 38	24	51.5	6.5	281.4	31.6
SFO 39 SMM1	9	56.9	6.9	526.9	59.2
SFO 39 SMM2	10	33.5	7.5	1129.5	126.9
SFO 42	24	2.8	6.6	131.3	14.8
SFO 43	28	66.8	5.3	52.2	5.9
SFO 44	31	34.5	7.0	497.1	55.9
SFO 87 SMM1	29	19.1	6.1	117.6	13.2
SFO 87 SMM2	29	17.9	6.4	165.4	18.6
SFO 88	23	215.3	5.5	91.7	10.3
SFO 89	28	38.4	5.8	87.5	9.8

Table 14: Fluxes used in greybody fits.

Source	F_{60} (Jy)	F_{100} (Jy)	F_{450} (Jy)	F_{850} (Jy)	F_{1200} (Jy)	F_{1250} (Jy)	F_{1300} (Jy)	F_{2000} (Jy)	F_{2700} (Jy)	F_{2730} (Jy)	F_{3100} (Jy)	F_{3260} (Jy)	F_{3410} (Jy)
SFO 1	95	360	9.6	2.1	—	—	—	—	—	—	—	—	—
SFO 2	16	—	25.1	5.7	—	—	—	—	—	—	—	—	—
SFO 5	71	—	—	5.7	—	0.3^a	—	0.1^b	—	—	—	—	—
SFO 7	19	—	38.1	6.4	—	—	—	—	—	—	—	—	—
SFO 9	14	48	—	1.1	—	—	—	—	—	—	—	—	—
SFO 10	19	77	—	0.6	—	—	—	—	—	—	—	—	—
SFO 14	382	—	42.6	16.6	—	—	—	0.3^b	—	—	—	—	—
SFO 15	10	22	—	0.2	—	—	—	—	—	—	—	—	—
SFO 25	—	—	48.4	13.2	—	—	—	—	—	—	—	—	—
SFO 27	14	79	—	3.3	—	—	—	—	—	—	—	—	—
SFO 29	5	20	—	1.1	—	—	—	—	—	—	—	—	—
SFO 30	706	1302	8.8	10.8	—	—	—	—	—	—	—	—	—
SFO 31	30	120	3.6	0.4	—	—	—	—	—	—	—	—	—
SFO 32	7	63	—	0.3	—	—	—	—	—	—	—	—	—
SFO 33	10	37	—	0.1	—	—	—	—	—	—	—	—	—
SFO 35	6	—	6.3	1.4	—	—	—	—	—	—	—	—	—
SFO 36	17	—	47.2	7.1	—	—	—	—	—	—	—	—	—
SFO 37	29	—	7.2	1.8	—	—	—	0.1^b	—	—	—	—	—
SFO 38	72	—	133.0	24.2	0.7^c	—	3.6^d	0.9^b	0.09^e	0.08^f	0.06	0.04^f	0.04^f
SFO 39 SMM1	19	—	20.0	4.9	—	—	—	—	—	—	—	—	—
SFO 39 SMM2	19	33	16.4	3.6	—	—	—	—	—	—	—	—	—
SFO 42	7	—	3.8	1.3	—	—	—	—	—	—	—	—	—
SFO 43	76	169	8.5	3.8	—	—	—	—	—	—	—	—	—
SFO 44	204	—	95.0	15.5	—	—	—	0.4^b	0.07^e	—	—	—	—
SFO 87 SMM1	103	452	—	3.4	—	—	—	—	—	—	—	—	—
SFO 87 SMM2	103	452	—	3.2	—	—	—	—	—	—	—	—	—
SFO 88	162	—	298.4	28	—	—	—	—	—	—	—	—	—
SFO 89	130	315	9.0	6.6	—	—	—	—	—	—	—	—	—

The fluxes used in fitting greybody curves. The subscript denotes the wavelength of the measurement in microns. Additional observational data taken from:[a](Lefloch et al. 1997);[b](Sugitani et al. 2000);[c](Beltrán et al. 2002); [d](Walker et al. 1990);[e](Wilking et al. 1989);[f](Codella et al. 2001)

Visual extinctions toward each core have been derived from their submillimetre fluxes following the method of Thompson et al. (2004a). From Mitchell et al. (2001),

$$F_\nu = \Omega B_\nu(T_d)\kappa_\nu m_H \frac{N_H}{E(B-V)}\frac{1}{R}A_{\mathrm{v}}, \tag{87}$$

where the total opacity of gas and dust is parameterised by κ_ν, functionally equivalent to the reciprocal of the mass conversion factor C_ν, m_H is the molecular mass of interstellar material, $N_H/E(B-V)$ is the conversion factor between column density of hydrogen nuclei and the selective absorption at the relevant wavelength. Following Mitchell et al. (2001) (and references therein) values of $N_H/E(B-V)$ = 5.8 x 10^{21} cm^{-2} mag^{-1} and R = 3.1 have been assumed. The K-band extinction A_K of each source was found by multiplying by the ratio $A_V/A_K = 8.9$ following Rieke & Lebofsky (1985). The derived values of A_V and A_K are listed in Table 13.

5.8 Analysis

5.8.1 Cloud Classification

Sugitani et al. (1991) classified their catalogue as three morphological types based upon the curvature exhibited by the BRC (see Fig. 15). Their classifications are as follows, with rim sizes, length (l) and width (w) defined in Fig. 15: (1) Type A, moderately curved rim with a length to width ratio, l/w, of less than 0.5; (2) Type B, tightly curved rim with l/w greater than 0.5 and; (3) Type C, cometary rim.

These three types closely relate to the development of clouds under the influence of ionising sources. The three general rim types, A, B and C, closely match the Lefloch & Lazareff (1994) RDI model snapshots at 0.036, 0.126 and 0.210 Myr respectively (Fig. 16). This strongly suggests that the variation in the large scale morphology represents the duration of each clouds exposure to ionising radiation, rather than a fundamental difference in structure or composition. This is further supported by the fact that Lefloch & Lazareff (1994) found no significant effects in the morphological evolution of the clouds due to varying initial conditions.

5.8.2 Cloud Morphology

Any morphological evolution of the clouds as suggested by Lefloch & Lazareff (1994) might be expected to be apparent in the observed properties of the BRCs in this survey. Both in general appearance and the properties of the protostellar cores within the clouds. In Table 15 the morphology of the SCUBA emission is commented upon, with reference to the rim type as

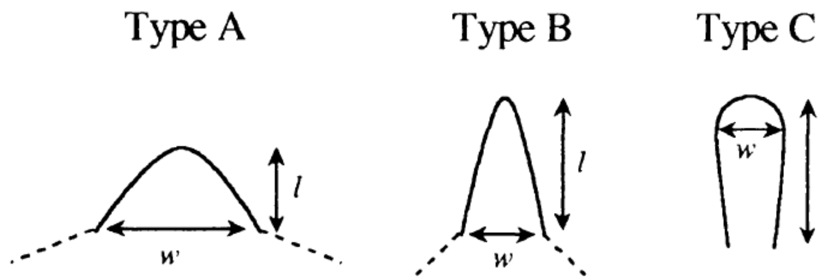

Figure 15: Classification of rim type and definition of rim size from Sugitani et al. (1991).

described by Sugitani et al. (1991), the NVSS radio emission and, where appropriate, the MSX 8.3 μm emission.

The SCUBA images of the cloud sample show submillimetre cores generally set back from the optical bright rim (Appendix A). The submillimetre core positions are generally consistent with the IRAS source positions presented in Sugitani et al. (1991) and Sugitani & Ogura (1994), though some discrepancy may be due to the IRAS tracing the more diffuse dust surrounding the cores. Submillimetre and IRAS positions generally match to within the limits defined by the IRAS beam size ($120'' \times 100''$at 100 μm).

The submillimetre emission from each core is approximately circular at the 50% flux level. Below the 50% flux level the weaker, more diffuse, submillimetre emission from each source generally follows the optical boundaries of the bright rimmed clouds and thus may show a cometary morphology (e.g. SFO 11E and SFO 13, Fig. 17). A general summary of morphology is then: approximately circular contours surrounded by diffuse emission following the optical cloud morphology and often elongated along the direction of the ionising source, exemplified in Fig. 18.

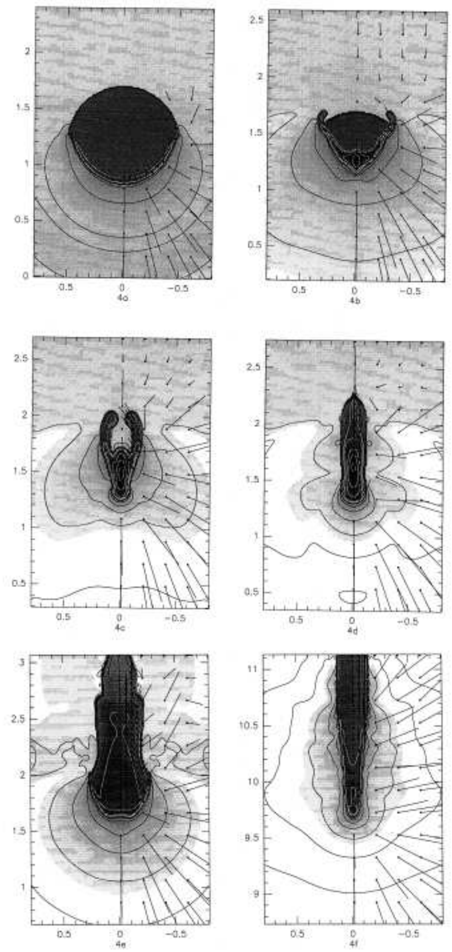

Figure 16: Images of model 2 from Lefloch & Lazareff (1994): Evolution from the early stages of collapse to the maximum compression stage. The ionizing flux shines from the bottom of the page. Snapshots are displayed from left to right and top to bottom: t=0.036 My **a**, 0.126 My **b**, 0.183 My **c**, 0.210 My **d**, Reexpansion stage (t=0.37 My) **e** and cometary phase (t=1.30 My) **f**. Density contours are spaced by $\Delta \log \rho = 0.5$. Coordinates are in pc. Velocities are represented by vectors of length $u\delta t$, with the scaling time δt=0.02 My.

Table 15: Rim type and morphology of SCUBA sources

Source	Rim Type	Comments
SFO 1	B	Core located at head of cloud with diffuse emission extending away from the rim. Radio and MSX emission is coincident with the submillimetre emission.
SFO 2	A	Core set back from rim, diffuse emission between rim and core. Radio emission is concentrated around rim, away from core.
SFO 4	B	Core located at head of cloud with diffuse emission surrounding the core. Radio and MSX emission is coincident with the submillimetre emission.
SFO 5	B	Core located at head of cloud with diffuse emission extending away from the rim. Radio and MSX emission is coincident with the submillimetre emission.
SFO 7	B	Core located at head of cloud with diffuse emission extending away from the rim. Radio and MSX emission is coincident with the submillimetre emission.
SFO 10	A	Core located close to rim, no extended, diffuse emission. Radio and MSX emission is coincident with the submillimetre emission.
SFO 11	A	Core located at head of cloud with diffuse emission extending away from the rim. Radio and MSX emission is coincident with the submillimetre emission.
SFO 11NE	A	Core located at head of cloud with diffuse emission extending away from the rim. Radio and MSX emission is coincident with the submillimetre emission.
SFO 11E	A	Core located at head of cloud with diffuse emission extending away from the rim. Radio and MSX emission is coincident with the submillimetre emission.
SFO 12	B	Core located at head of cloud with diffuse emission extending away from the rim. Radio and MSX emission is coincident with the submillimetre emission.
SFO 13	B	Core located at head of cloud with diffuse emission extending away from the rim. Radio and MSX emission is coincident with the submillimetre emission.
SFO 14	A	Core located at head of cloud with diffuse emission surrounding the core. Radio emission is concentrated around rim, away from core. MSX emission is coincident with the submillimetre emission.
SFO 15	B	Core set back from rim,Radio emission is concentrated around rim, away from core. MSX emission is coincident with the submillimetre emission.
SFO 25	B	Core set back from rim with diffuse emission extending away from the rim. Radio emission is concentrated around rim, away from core. MSX emission is coincident with the submillimetre emission.
SFO 27	A	Core set back from rim. Radio emission is concentrated around rim, away from core. High concentration of MSX emission away from submillimetre core.
SFO 29	A	Core set back from rim.

Table 15: (Cont.)Rim type and morphology of SCUBA sources

Source	Rim Type	Comments
SFO 30	B	Core located at head of cloud with diffuse emission surrounding the core. Radio emission is concentrated around rim, away from core. MSX emission is coincident with the submillimetre emission.
SFO 31	A	Core set back from rim. Radio emission is concentrated around rim, away from core. MSX emission is coincident with the submillimetre emission.
SFO 32	A	Core located at head of cloud. Radio emission is coincident with the submillimetre emission. MSX emission is concentrated away from the submillimetre emission.
SFO 33	A	Core set back from rim.
SFO 35	A	Core located at head of cloud with diffuse emission extending away from the rim. Radio and MSX emission is coincident with the submillimetre emission.
SFO 36	A	Core located at head of cloud with diffuse emission extending away from the rim. Radio emission is coincident with the submillimetre emission.MSX emission is concentrated away from the submillimetre emission.
SFO 37	C	Core located at head of cloud. Radio and MSX emission is coincident with the submillimetre emission.
SFO 38	A	Core set back from head of cloud with diffuse emission extending away from the rim. Radio emission is concentrated around rim and MSX emission is coincident with the submillimetre emission.
SFO 40	A	Core set back from head of cloud with diffuse emission surrounding the core. Radio emission is concentrated around rim, away from core. MSX emission is coincident with the submillimetre emission.
SFO 42	A	Core located at head of cloud with diffuse emission surrounding the core. Radio and MSX emission is coincident with the submillimetre emission.
SFO 43	B	Core located at head of cloud with diffuse emission extending away from the rim. Radio and MSX emission is coincident with the submillimetre emission.
SFO 44	A	Core set back from head of cloud with diffuse emission surrounding the core. Radio emission is coincident with the submillimetre emission.
SFO 87	B	Core set back from head of cloud with diffuse emission surrounding the core.
SFO 88	A	Core at head of cloud with diffuse emission surrounding the core.
SFO 89	A	Core set back from head of cloud with diffuse emission surrounding the core.

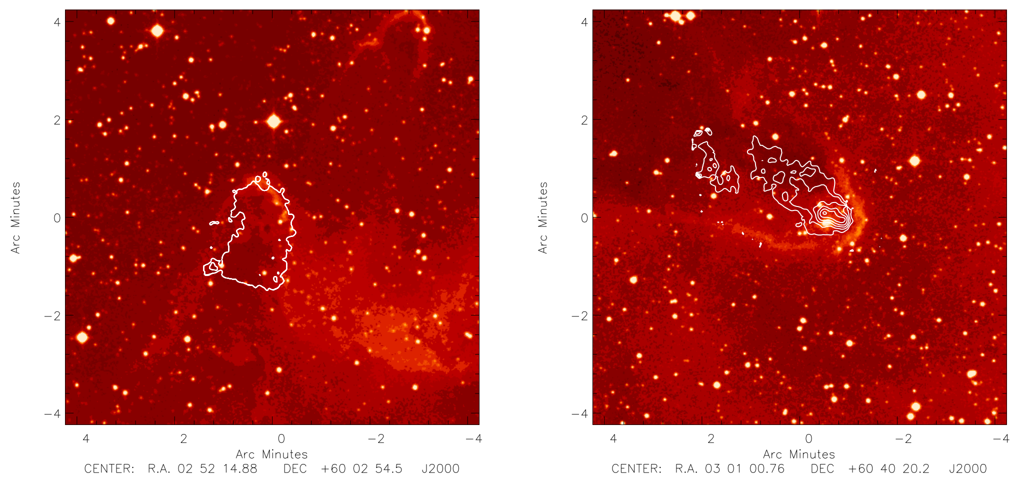

Figure 17: SCUBA contours overlaid on DSS images of SFO 11E (left) and SFO 13 (right). Contours start at 3σ and increase in increments of 20% of the peak flux.

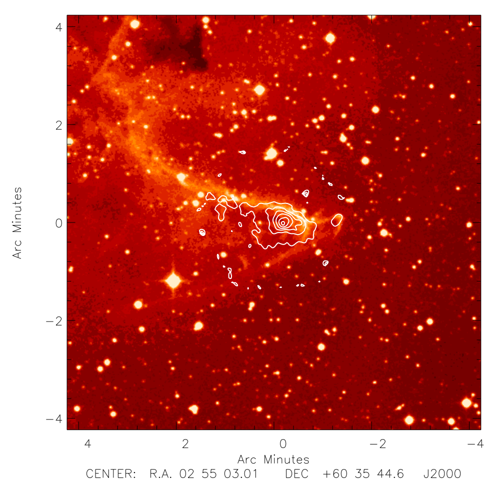

Figure 18: SCUBA contours overlaid on a DSS image of SFO 12. Contours start at 3σ and increase in increments of 20% of the peak flux.

The observed clouds may be separated into groups based upon their morphological features. The following features have been considered, whether the submillimetre cores are near the edge of the cloud or embedded within it, whether the cores are condensed sources or have more diffuse emission associated with them and whether the submillimetre emission is coincident with the radio emission detected by the NVSS. These results are all very subjective and are not based upon quantitative measurements. This analysis represents a 'first look' at the data. The results are summarised in Table 16.

Table 16: SCUBA source morphology summary.

Morphological Feature	Number Of Rim Type 'A'	Number Of Rim Type 'B'	Total Number
Cores near cloud edge.	10	8	18(30)
Cores embedded within cloud.	9	3	12(30)
Diffuse emission.	13	10	23(30)
No diffuse emission.	6	1	7(30)
Correlated radio emission.	9	7	16(25)
Non-correlated radio emission.	6	3	9 (25)

Table 16 shows the proportion of SCUBA sources that fall into the morphological categories described above. The sources are split into those of type 'A' rim morphology and those of type 'B' rim morphology. The totals are shown in the right hand column with the total sample size in brackets, the reason for the slightly smaller sample size when comparing the correlation of radio emission with SCUBA detections is that only 26 of the sample have information at both of these wavelengths (see Table 11) and one of these (SFO 37) is of type 'C' rim morphology which has been discounted due to the lack of statistical significance.

The submillimetre cores embedded within the clouds tend to be located near the rim (as opposed to the centre of the cloud) in a ratio of 3/2. The cores that are placed toward the rim do not show any trend toward either type 'A' or 'B' rim morphology. However, those cores that appear to be more deeply embedded within the clouds tend to be of type 'A' with a 75% majority. Note that care must be taken in this analysis. Projection effects mean that a core close to a bright rim in the presented images might be further away than it appears. 77% of the sample have diffuse emission associated with them. These clouds are not predominately of one rim type, though those that are not associated with diffuse emission are of type 'A' with only one exception.

The number of clouds that have radio emission correlated with the submillimetre cores is high (64%), considering that more radio emission might be expected to arise from the ionisation of the clouds at their bright rims than from the embedded cores. There does not appear to be any trend of rim type for the cores that have radio emission coincident with their submillimetre emission. However, there are twice as many type 'A' rims that have non-correlated radio emission as type 'B'.

5.8.3 Morphological Analysis

The appearance of the SCUBA cores detected in this survey has been considered with respect to the general morphology of the clouds. Clouds defined as being of type 'A' morphology are equally distributed between those with cores near their optically bright rims, and cores embedded further within the cloud. This correlation of cores with the bright rims shows that type 'B' clouds have fewer cores deeply embedded within the clouds, while the number of type 'B' clouds with cores near their bright rims is approximately equal with that of type 'A' clouds. Interpreting the apparent lack of type 'B' clouds with correlated rims/cores in light of the morphological evolution models of Lefloch & Lazareff (1994) leads to the following scenario, cores within the clouds are being gradually exposed through the photoevaporation of the surrounding material. While these clouds evolve from type 'A' to type 'B' the surrounding material is eroded away, leading to the appearance that any embedded cores would be moving toward the rim of the cloud. The predominance of type 'A' morphology in cores that are embedded deep within the clouds is due to the 'youth' of those clouds.

The clouds that are associated with diffuse submillimetre emission are type 'A' by a large factor, not as might be expected in the evolutionary scenario as suggested by Lefloch & Lazareff (1994). The lack of diffuse emission in type 'B' clouds may be interpreted as a lack of warm dust surrounding the protostellar cores, suggesting that the protostellar envelopes from which the natal stars are accreting material, have been depleted. This interpretation would mean that, on average, the clouds without the diffuse emission would be further evolved. The cores in question are all relatively low in mass, suggesting the possibility that star formation in these clouds has halted at this stage due to either a lack of available accretable material or low initial clump mass.

Appendix A contains images of the clouds superimposed with radio contours. There are two distinct situations represented in these images. In some of the sample (e.g. SFO 1, SFO 5 and SFO 12) there is good correlation of the position of peak emission, implying that the radio emission is in fact related to the submillimetre emission. This is suggestive of an already-formed radio source embedded within the dust cloud (e.g. a HII region). The rest of the sample (e.g. SFO 2, SFO 14, SFO 25, SFO 31 and SFO 38) show submillimetre emission separated from the radio emission, which is associated with the bright ionised optical rim of the cloud.

Grouping the cores in the sample according to the classifications of Sugitani et al. (1991) (Table 17) does not show any significant differences in the derived core properties (e.g. mass, density and extinction). This is not what might be expected if the rim types are indeed an evolutionary sequence. One would naively expect to find star formation that is more developed in the clouds that are further evolved. This suggests two possible scenarios.

1. The timescale for the development of rim type is short compared to star formation. Thus, assuming that the stars are formed as a result of the interaction of the ionisation front with the BRC, these stars begin to form quickly as a result of this influence. The clouds then rapidly evolve through the suggested development of rim type.

2. The formation of stars within the BRCs is unrelated to the interaction of the ionisation front with the BRC. In this case the development of stars within the clouds would be

random and unconnected to the shape of the exterior cloud.

Variations in temperature, mass, density, and extinction are close to being within the mean errors. These variations decrease to within mean errors when the less reliable values determined from flux ratios are discounted. The observations consist of only one rim identified as Type C. Thus to infer information about the Type C rims, and thus a comparison of the generic properties of these rims, is unwarranted. SFO 36 was identified by Sugitani et al. (1991) as 'A or C'. Based upon the position and morphology of the submillimetre emission presented in these images the identification of SFO 36 as Type 'A' morphology is evident (see Fig. 19).

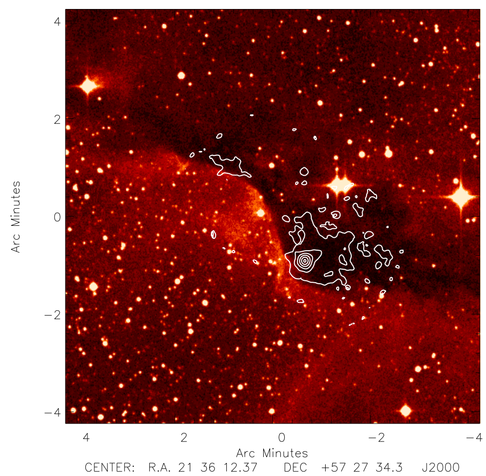

Figure 19: SCUBA contours overlaid on a DSS image of SFO 36. Contours start at 3σ ($\sigma = 0.17$ Jy beam^{-1}) and increase in increments of 20% of the peak flux.

Table 17: Mean core properties grouped as rim type.

Rim Type	T_d (K)	M ($M_\odot$)	Log_{10}(n) cm^{-3}	A_V
A	26(0.8)	32.2(14.3)	5.8(0.2)	114.5(29.0)
B	25(3.7)	46.0(11.4)	5.8(0.2)	246.5(99.1)
C	27(2.0)	3.3(0.4)	6.6(0.1)	135.7(14.9)

5.8.4 Core Internal Sources

Using the Far InfraRed (FIR) and submillimetre fluxes of the sources allows the estimation of the spectral class of any YSO's that may be present in the cloud cores. The luminosities of each source were estimated by integrating under the greybody curve fitted to each cloud's observed fluxes, as presented in Table 13. Distances to each source were taken from Sugitani et al. (1991) and Sugitani & Ogura (1994). The assumption has been made that all of the luminosity arises from a single embedded YSO. The derived properties of the internal sources are presented in Table 18.

Table 18: Core internal source properties determined from greybody fits.

Source	Luminosity ($L_\odot$)	T_{eff} (K)	Spectral Type[a]	Distance To Cloud[b] (kpc)	$L_{submillimetre}/L_{bol}$ (x 10^{-3})
SFO 1	246	14200	B6	0.85	8.3
SFO 2	127	12500	B7	0.85	22.7
SFO 5	1511	18900	B3	1.9	11.9
SFO 7	961	17700	B4	1.9	20.6
SFO 9	179	13400	B6	1.9	9.5
SFO 10	276	14500	B5	1.9	9.6
SFO 14	4528	22100	B1.5	1.9	7.7
SFO 15	269	14400	B6	3.4	5.3
SFO 27	116	12300	B7	1.15	17.3
SFO 29	31	8900	A2	1.15	16.6
SFO 30	7051	24100	B1.5	2.2	3.8
SFO 31	112	12200	B7	1.0	8.7
SFO 32	37	9300	A1	0.75	19.8
SFO 33	20	7800	A6	0.75	8.3
SFO 35	30	8800	A2	0.75	18.8
SFO 36	147	12900	B6	0.75	25.4
SFO 37	70	11000	B8	0.75	9.9
SFO 38	506	16000	B4	0.75	21.5
SFO 42	28	8600	A4	0.75	14.4
SFO 43	1083	18000	B3	0.75	6.3
SFO 44	812	17300	B4	0.75	14.1
SFO 87 SMM1	825	17300	B4	1.38	8.7
SFO 87 SMM2	824	17300	B4	1.38	8.7
SFO 88	3806	21500	B2	1.38	20.0
SFO 89	640	16700	B4	1.38	6.7

[a] Spectral types taken from de Jager & Nieuwenhuijzen (1987)
[b] Distances taken from Sugitani et al. (1991) and Sugitani & Ogura (1994)

While the assumption that all FIR and submillimetre luminosity is due to a single source may be crude, it enables an initial estimate. Wood & Churchwell (1989) showed that, for a realistic mass function, the spectral type of the most massive member in a cluster is only 1.5-2 spectral classes lower than that derived for the single embedded star case. This applies explicitly to high-mass stars, valid in this analysis as the mean effective temperature of internal sources in the sample is 14,700 K, corresponding to a spectral type of B5. The limiting flux sensitivity of the original IRAS survey was $\sim$ 0.5 Jy at 60 μm and $\sim$ 1.5 Jy at 100 μm, which at the distances of the clouds (mean = 1.29 kpc) corresponds to a limiting bolometric luminosity sensitivity of $\sim$ 3 $L_\odot$. These flux density limits may be expected to increase for extended sources, however, none of these sources are expected to be extended on the scale of the IRAS beam. By calculating the maximum luminosity observable given these fluxes the IRAS sensitivity limit has been plotted as a function of distance in Fig. 20. By plotting the luminosities of the SCUBA sample on the same axes it is evident that the IRAS sensitivity limit is not responsible for bias in the sample.

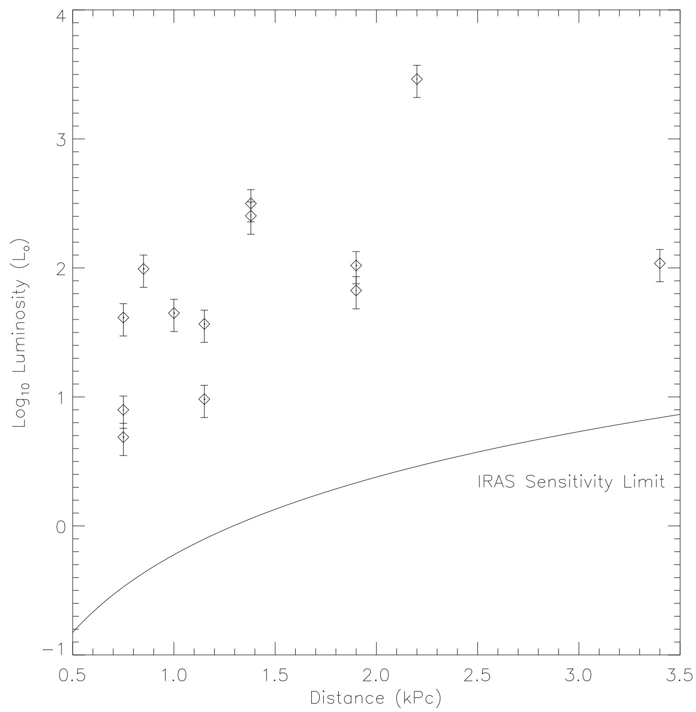

Figure 20: The luminosities of the SCUBA sample plotted as a function of distance (diamonds), the solid line represents the sensitivity limit of the IRAS. All luminosities (including the IRAS sensitivity limit) are measured over the range 60 μm - 100 μm.

5.8.5 Classification of the Internal Sources

Andre et al. (1993) defined Class 0 protostars as those obeying the approximate relationship $L_{submillimetre}/L_{bol} \gtrsim 5 \times 10^{-3}$. The clouds that have been modelled using the greybody analysis described in Section 3.3 all obey this relationship within the errors (see Table 18). The definition of $L_{submillimetre}$ as the luminosity radiated longward of 350 μm has been adopted here.
The dust temperatures that have been found for the cores in the sample presented here are higher than that normally found for starless cores ($T_D \sim 10$ K (Evans 1999)), suggesting that there is an internal heating mechanism acting within the cores. This, together with evidence of outflow activity in a significant proportion of the sample (see chapter 6), strongly supports the presence of star forming activity within the sample.

The bolometric luminosities derived for the clouds in this survey range from 20 $L_\odot$, typical of class 0 and class I protostellar objects (Andre et al. 1993; Chandler & Richer 2000), to 7051 $L_\odot$, more indicative of massive star formation (Mueller et al. 2002). The mean luminosity found for the sample is 969 $L_\odot$. This suggests that the sample consists largely of intermediate - high-mass star forming regions, or that the cores may be forming multiple stars. Although this trend may be due to selection effects, or instrumentational sensitivity limits, it has been shown in Section 5.8.6 that the mass spectrum of the sample indicates that intermediate-high mass star-formation, or the formation of clusters, is dominant in BRCs.

5.8.6 The Mass Function Of The SFO Catalogue

The Initial Mass Function (IMF) is a key diagnostic in distinguishing between various regimes of star formation processes, defining an IMF in a particular region and reproducing that IMF is a much sought-after goal in modern star formation that is still highly contentious. Paraphrasing Kroupa et al. (1990) it is a subject, like the stars themselves, that has produced more heat than light. Comparing masses and luminosities to generally observed functions is a useful, if inconclusive, tool. The mass function that is commonly used for comparison is that defined by Salpeter (1955), who defined a function describing main sequence stars as:

$$\frac{dN(M)}{dM} \propto M^{-2.35} \tag{88}$$

i.e. the number of stars observed with masses in the interval, M to M+dM, is proportional to the mass to the power of -2.35. This relation has been refined in different circumstances in an attempt to describe stars that are observed to have number functions differing from that presented in Salpeter (1955). For example, Kroupa et al. (1990) defines a mass function that takes the form of a Gaussian in $\log_{10}$ for mass for stellar masses less than 0.35 $M_\odot$, and is invariable for masses greater than 0.35 $M_\odot$ in an attempt to better understand the star formation rates of stars at the low-mass end of the spectrum. Blitz (1993) found an observed mass spectrum for 'clumps' within Giant Molecular Clouds (GMC) that obeyed

$$\frac{dN(M)}{dM} \propto M^{-1.54} \tag{89}$$

The masses that have been found from Eq. 16 for the detected cores in this survey are presented in Table 13. The corresponding mass spectrum arising from this sample is presented in Figure 21. The Salpeter and Blitz slopes are also presented for comparison.

As can be seen, the mass spectrum is very flat at masses below ∼5 $M_\odot$, then falls away with a slightly greater rate than that described by Blitz. The reason for the flatness of the spectrum at masses below ∼5 $M_\odot$ is that this is approaching the sensitivity limit of the SCUBA observations. The masses presented here are derived from SCUBA 850 μm fluxes. A typical

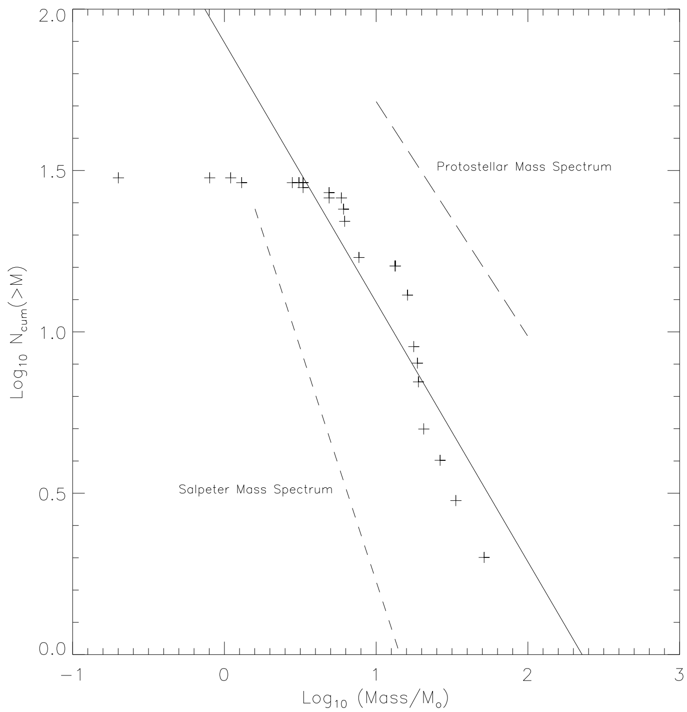

Figure 21: The mass spectrum of the sources detected by SCUBA in this survey. The long-dash line represents the giant molecular cloud clump mass function taken from Blitz (1993) and the short-dash line represents the well-known Salpeter slope (Salpeter 1955). The solid line represents a best fit to the data from the presented sample.

r.m.s. from the 850 μm SCUBA maps is $\sim$0.275 Jy, using other mean values in equation 86 (mean T=26K, mean d=1.29 kPc) along with a three-σ flux detection limit yields a minimum observable mass of 4.7 $M_{\odot}$. This closely matches the 'knee' of the observed mass spectrum. For this reason the sample is suspected to be incomplete at low masses and the slope of the mass spectrum has been calculated accordingly. The Blitz line is proportional to $M^{-0.7}$ in a cumulative mass function, the bestfit represented by a solid line here is proportional to $M^{-0.8\pm0.4}$ (*cf* the Salpeter slope, which is proportional to $M^{-1.5}$ when plotted cumulatively). The usefulness of a comparison with the spectrum presented by Blitz is questionable as his spectrum is based upon observations of GMC 'clumps' which are not necessarily star-forming and, furthermore, may not even be gravitationally bound. The usefulness of a comparison with the Salpeter slope may also be dubious as the Salpeter slope describes stars upon the main sequence, whereas this sample is comprised of YSO's which fundamentally different astronomical objects. However, an important question is addressed by a comparison of the SCUBA data with the Salpeter slope. As mentioned in Section 5.8.4, the sensitivity of IRAS limits the sample to sources above $\sim$ 3 $L_{\odot}$ at a mean distance of 1.29 kpc. However, by plotting the luminosity/distance relationship of these sources (Fig. 20) it can be seen that the sample lies well above this sensitivity limit, and that the slope of the spectrum is in fact significantly shallower than that of the Salpeter function. This strongly suggests that, although the sample may be biased towards high mass/luminosity sources, the preponderance of these sources is due to a real trend, and that BRCs do have a tendency to produce stars which are higher in luminosity than stars formed in isolation. This may mean that, rather than higher mass stars being formed within BRCs, BRCs are more efficiently producing *clusters* of stars.

This hypothesis is upheld by comparison with data taken from Mitchell et al. (2001), in which 850 μm SCUBA maps are presented of 67 discrete continuum sources in the Orion B molecular cloud, some of which are shown to be star-forming. Mitchell et al. (2001) define a mass for each 'clump' through assuming a dust temperature, T_d, via:

$$M_{clump} = 1.50 \times S_{850}[exp\left(\frac{17K}{T_d}\right) - 1] \times \left(\frac{\kappa_{850}}{0.01\ cm^2\ g^{-1}}\right)^{-1} M_{\odot} \tag{90}$$

where S_{850} is the 850 μm flux enclosed within the clump boundary measured in Janskys and κ_{850} is the mass absorption coefficient at 850 μm, functionally equivalent to the reciprocal of the mass conversion factor C_ν (see Section 3.3). Mitchell et al. (2001) use fluxes for each clump taken from a $21''$ aperture and assumes a value for κ_{850} of 0.01 cm g^{-1} to find masses for a small sample of the clumps in their survey. In order to find masses for the complete sample of their observations a dust temperature of 20 K has been assumed, as the 850 μm fluxes within a $21''$ aperture are not available, and to maintain consistency with the method presented here, the total integrated flux has been used along with a different value of κ_{850}=0.02 cm^2g^{-1}. The masses found here agree well with those presented for the smaller sample within Mitchell et al. (2001).

Plotting the mass spectrum of the clumps observed within Mitchell et al. (2001) is probably a better comparison to the BRCs that have been observed here than the Salpeter function, or the Blitz observed clump mass spectrum. As well as the protostellar clumps being similar objects to this sample, the important difference being the illumination of the clouds by nearby massive stars, the methods used to derive their masses are identical, whereas the Salpeter and Blitz spectra are based upon various observations and assumptions. It should be noted that Orion B is a single distance sample, while this sample represents BRCs at a range of distances which may not be well known. This could possibly introduce errors into the sample. It should be noted that the survey of Mitchell et al. (2001) is more sensitive to lower mass stars. Their flux detection limit is very similar to that found here ($\sigma \sim 0.083$ Jy) but, due to the proximity of their sample in comparison to this (0.45 kpc vs. an average of 1.29 kpc) they were able to detect smaller core masses ($\sim 1\ M_\odot$ vs.$\sim 5\ M_\odot$). This is the reason for the lower level of the 'knee' in their observations where the mass spectrum begins to tail off. As with our own mass spectrum the lower masses have not been used in a best-fit slope to the mass spectrum in order to reduce the effects that an incomplete sample may have on the determination.

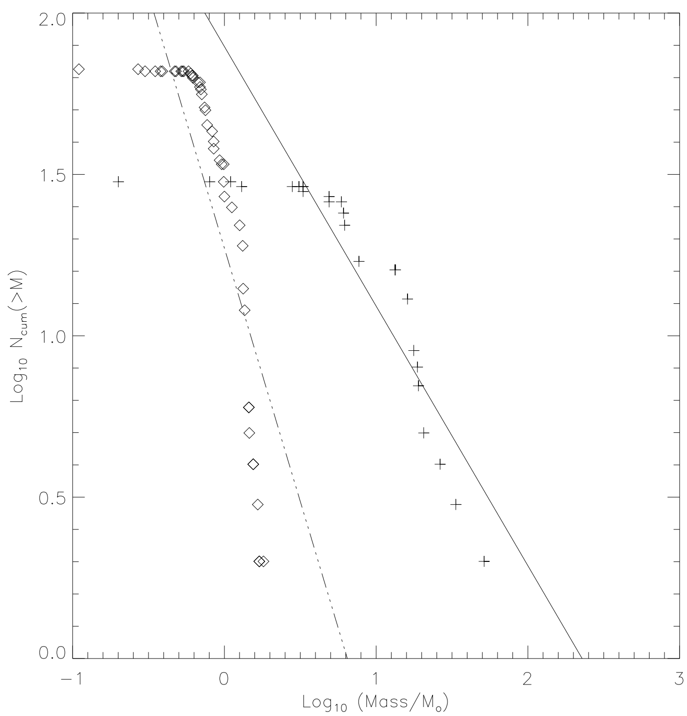

Figure 22: The mass spectrum of the sources detected by SCUBA in this survey and in the survey of Mitchell et al. (2001). The solid line is a best fit to our data above the mean sensitivity limit, the dash-dot line is a best fit to the data of Mitchell et al. (2001).

The mass spectrum taken from data presented in Mitchell et al. (2001) (Fig. 22) again supports the conclusion that BRCs preferentially form higher mass stars, or clusters, than star-forming clouds in regions less affected by external radiation. The slope of the mass spectrum taken from the SFO catalogue is significantly shallower than that taken from the Mitchell et al. (2001) survey, showing a rate of high mass star-formation that considerably exceeds that found in the Orion B molecular cloud. To further investigate this trend, more statistics are necessary, both in the numbers of protostellar cores found in BRCs and the masses of protostellar cores taken from other 850 μm studies. In order for a proper comparison to be made between samples more flux data is necessary, allowing the dust temperature to be more accurately determined for the sample of Mitchell et al. (2001).

5.9 Has The Star Formation In The Sample Been Induced?

The BRCs in the sample have been subjected to the ionisation of an illuminating source for varying durations. The clouds have also been associated with YSO and CTTS candidates. By correlating this time period with the ages of the detected YSO and CTTS it is possible to determine the likelihood that the observed star formation may have been triggered. The initial expansion of the HII region is rapid up to the radius of the Strömgren sphere, ranging from 0.01 to 4 pc dependant upon the spectral type of the ionising star. Following this rapid expansion the ionisation front moves outward much more slowly, at approximately the sound speed of the ionised gas, $\sim$ 11.4 km s^{-1}.

Source	Cloud Radius (pc)	Projected Distance between Bright Rim and Ionising Star(pc)	Ionisation Front Expansion Period(Myr)	Cloud Shock Crossing Time(Myr)	Total Time (Myr)
1	0.15	3.8	0.3	0.3	0.6
2	0.23	17.7	1.5	0.4	2.0
5	0.35	14.9	1.3	0.7	2.0
7	0.8325	13.4	1.1	1.6	2.8
9	0.105	14.7	1.3	0.2	1.5
10	0.23	12.1	1.0	0.4	1.5
14	0.49	9.1	0.8	1.0	1.7
15	0.36	22.3	1.9	0.7	2.6
27	0.19	4.4	0.4	0.4	0.8
29	0.19	9.8	0.8	0.4	1.2
30	0.66	1.2	0.1	1.3	1.4
31	0.23	20.6	1.8	0.4	2.2
32	0.085	11.4	1.0	0.2	1.2
33	0.07	10.1	0.9	0.1	1.0
35	0.175	14.4	1.2	0.4	1.6
36	0.485	5.0	0.4	1.0	1.4
37	0.095	12.0	1.0	0.2	1.2
38	0.2775	10.7	0.9	0.5	1.5
42	0.125	14.1	1.2	0.3	1.5
43	0.3875	1.7	0.1	0.8	0.9
44	0.18	7.3	0.6	0.4	1.0
87	0.4275	5.5	0.5	0.8	1.3
88	0.405	6.3	0.5	0.8	1.3
89	0.095	4.1	0.4	0.2	0.5

Table 19: Cloud radii, distances to ionising stars and the time required for the interaction of ionising radiation.

The sound speed in the neutral molecular material contained within the cometary globule itself is ~1 km s^{-1} (Thompson et al. 2004a; White et al. 1999). The large variation in cloud radius leads to a large range of shock crossing times for the clouds in the sample of 0.1 - 1.6 Myr. This range is very large, though the sample is biased toward low crossing times, the mean being 0.6. The total time required for the ionisation front to reach the position observed now, as well as the crossing time necessary for the photoionisation induced shock to disrupt the cloud, in addition to the ages of the protostars that are currently observed ($\sim10^5$yr for Class I YSOs and between $\sim10^5$yr and 10^6yr for CTTS) gives an approximate timescale necessary for RDI to have been the cause of star formation within the clouds. This reveals a set of ages that is consistent with the main sequence lifetimes of the stars identified as being the ionising stars of each BRC in Morgan et al. (2004) and Yamaguchi et al. (1999). This does not, in itself, provide conclusive evidence that the formation of protostars within the clouds is caused by the photoionisation of the clouds. The calculations of the time taken for the ionisation front to reach the bright rims, as well as the calculation of shock crossing times for the clouds themselves are based upon a number of assumptions. These assumptions include the density of the intercloud material (taken to be 10^2 cm^{-3}) as well as a negligible time for the HII region to expand to the Strömgren radius. It has also been assumed that the distance between the ionising star and the bright rim seen in projection against the sky is the actual distance between the two objects, this may not be true, as the ionising star may be in the foreground (or background) relative to the cometary globule. Any possible extinction of the ionising radiation from the star between it and the rim has also been neglected.

The timescales found for the duration of the ionisation occuring at the bright rims are consistent with the ages of the stars forming at the core of the BRCs, though a lot of assumptions have been made in determining the timescale of the ionisation and the comparison is, as yet, inconclusive.

5.10 Discussion

In this section the findings of this chapter will be discussed and summarised in terms of the original objectives of the thesis and the wider context of the subject.

The main purpose of the work in this chapter was to identify areas of the BRCs in the sample that had coalesced into clumps of dust and gas. Any such areas might then be analysed for indicators of star formation.

5.10.1 Cloud Morphology And Physical Properties

A sample of SCUBA sources within BRCs was taken from the observations presented in section 5.2. This sample was compared to emission in the optical, infrared and radio regimes. The morphology of the clouds is, in general, supportive of the scenario proposed by RDI models. That is, a dense core at the head of an elongated column. There was found to be variation in the extent of the column as well as the curvature of the rim itself, though the direction of the elongation of the column was invariably consistent with the direction of the suspected ionising source(s) identified in chapter 4. The SCUBA emission was found to trace cores within the clouds at various distances from the bright rim, consistent with the original IRAS source positions. The submillimetre emission is generally diffuse, tracing the optical boundaries of the cloud but focused upon a central circular region. The distance of the SCUBA cores from the bright optical rim is generally small in terms of the radius of curvature of the cloud, this distance being statistically smaller for clouds with Type 'B' rims. This fact is supportive of the hypothetical evolutionary sequence of the clouds. Firstly, for cores that are near the ionisation front, the corresponding shock crossing time (which needs to be considered when determining the effect of the front upon star formation) is less. In other words, the timescale required for *triggered* star formation becomes shorter and it becomes more likely that the observed cores in the sample were triggered to collapse. Secondly, the clouds that are further along their hypothetical evolutionary sequence are those that have cores nearer to their rims, or, alternatively, may have had the material between them and the ionisation front eroded for a longer period.

There is a distinct lack of examples of Type 'C' rims within the observed sample. This is not predicted through the models of Lefloch & Lazareff (1994) in which Type 'C' rims represent the longest lived stage of development and thus would be expected to be the most predominant in observations. The models neglect to include the heating and ionising effect of any star forming within the cloud. Thus the lack of observations of this morphology may be due to the effects of the newborn star dispersing the material around itself as it emerges from the natal cloud.

Some of the clouds consist of more than one SCUBA core. At the $14''$ resolution of the SCUBA observations, five of the clouds are separable into distinct sources. The properties of these sources are similar, suggesting that more than one star-forming region may be able to coalesce from a single cloud.

Many of the clouds (64%) show correlation between their radio emission and the location of the submillimetre core, indicating that stars embedded in the clouds may already be ionising the molecular material from within. No trend is seen when correlating this coincidence of emission with rim type. A correlation might be expected as radio emission is more likely from the more evolved sources which would then be expected to be found in the later rim type.

The physical properties of the clouds were determined using greybody analyses. The dust temperatures found for the sources are high compared to starless cores (average $T_d = 25$ K), indicating the presence of internal stellar sources in these clouds. This is consistent with the identification of the sources as Class 0 protostars from their $L_{submillimetre}/L_{bol}$ ratio.

As expected in a centrally condensed molecular cloud, the average density of the cores is high, the minimum density found being 1.3×10^4 n(H_2) cm^{-3} for the source SFO 11SMM3. Prestellar cores generally having a density of $\sim 10^5$ n(H_2) cm^{-3}. The mean density of this sample is 6.8 $\times 10^5$ n(H_2) cm^{-3}. This further supports the identification of the sample as Class 0 protostars. The mean luminosity of the sample was 970 $L_\odot$, indicating that the sample is dominated by massive, high-luminosity stars.

5.10.2 The Mass Function Of The Sample

By plotting the mass function of the SCUBA core sample, small deviations from both the Salpeter slope and the Blitz 'clump' function are evident. More striking is the comparison of the cumulative mass function of the sources to that of Mitchell et al. (2001). The sources presented here are distinctively more massive and luminous than the high mass clumps identified by Mitchell et al. (2001). There are some low mass cores that have been detected in this survey, however, the majority of the sample is massive, with a mean mass of 38 $M_\odot$. The selection of the sources within our sample must be considered, and examined, for biasing effects. The sources were originally selected from the Sharpless catalogue of HII regions. Those regions that were found to be associated with IRAS point sources were selected. Bias due to the sensitivity of the IRAS receivers has been ruled out here. The lowest luminosity that IRAS was able to detect is far below the luminosities of the presented sources, confirming that the high mass and luminosities observed are a true trend and not due to instrumental or selection effects. Though the original survey is unbiased toward high-mass sources, the sensitivity of our SCUBA observations means that there is a lower detectability limit of 5 $M_\odot$ at the mean distance of 1.29 kpc. This may lead to a bias on our detections, although this is not expected to unduly affect our observations as, of the 45 sources observed, only eight were not detected at any SCUBA wavelength.

5.10.3 Infrared Sources

Observations of near-infrared sources taken from the 2MASS show the presence of young stars in the vicinity of the majority (89%) of our sample. The BRCs that have been observed are generally associated with young stars and have star forming submillimeter characteristics. The spectral type of the associated sources is not determinable from the current data, however the observed stars are known to be in the relatively early stages of their formation. This association of IR sources with the clouds in our sample bolsters the conclusion that the clouds are star-forming themselves, star formation generally occuring in clusters and associations.

5.10.4 Internal Sources

The internal heating sources of the clouds have been specified by a spectral type, making the assumption that all of the luminosity arising from the cloud is due to the internal heating source.

The tables of Panagia (1973) were used to determine the spectral type of the embedded star. The embedded stars are all massive, with five of the sources falling into the Type A bracket, the remaining 20 all being of Type B or greater. Naturally, this number does not represent our entire sample, but only those for which a determination of luminosity was possible.

5.10.5 Aging The Star Formation

Using the sum of the time periods required for the ionisation front to reach the regions of the bright optical rims, and the shock crossing times of the clouds, it has been found that the age of the observed sources is consistent with that of the duration of ionisation, supporting the RDI scenario. However, although CTTS and YSOs have been observed toward the clouds it is unclear whether or not they might have been formed through RDI. This is explored further in the summary chapter after the pressure balance between the external IBL and molecular material has been determined. This allows a determination of the likelihood of shocks propagating into the clouds. If the clouds are still in a 'pre-shocked' state then it is unlikely that any protostars further along the evolutionary track than the very earliest stages could not have been formed by the interaction of the ionisation front. This does not rule out the possibility of pre-existing star formation within the clouds.

5.11 Conclusions

The sample of detected SCUBA sources has been shown to be consistent with observations of high-mass protostars, the submillimetre luminosity ratio was generally found to match that of Class 0 protostellar objects as described by Andre et al. (1993). The morphology of the cores is consistent with that of the observed optical emission. Radio emission from the sources is usually coincident with the bright optical rim. However, some sources show SCUBA cores that appear to be coincident with the radio emission (all regions of high SCUBA emission are coincident with the original IRAS sources). This suggests the possibility of UCHII regions within the clouds. Although the clouds were examined for possible UCHII regions in chapter 4 and only one was found it may be possible that others exist. UCHII regions are identified through their IRAS colours, the resolution of IRAS is very poor and may well be unable to identify all UCHII regions. The resolution of the NVSS is also much greater than the characteristic size of UCHII regions ($\sim$ 0.1 pc), thus a higher resolution radio study may find traces of the ionisation of the embedded star. In addition, a search of the clouds for seven millimetre emission may reveal Hyper-Compact HII regions (HCHII), the precursors to UCHII regions. These will be described in more detail in chapter 7.

Masses found from the submillimetre observations are high, more so than predicted by the

Salpeter IMF. When compared to other high mass star forming regions the clouds in this study are considerably more massive and have a shallower mass function, suggesting that the clouds presented here are systematically higher in mass than other massive star forming regions. This cannot be definitely ascertained without tighter constraints upon the mass of the clouds. In addition, the comparison of the clouds in this study, which are at varying distances, not all of which are particularly well known, to a single sample is not adequate for a comparison to massive star formation as a whole. Further observations and samples must be obtained in order to rule out the possibility that it is the sample of Mitchell et al. (2001) that is the unusual one. Infrared sources have been found for most of the sample which are positionally coincident with the clouds and there are sources which are candidate CTTS/YSO. The association of these sources with the clouds means that the clouds may generally be associated with star formation. The spectral types of the internal sources in the clouds have been determined. They are consistently massive and luminous though it has not been possible to determine the stellar type of the associated IR sources. The timescale of the star formation within the clouds identified by SCUBA is reasonable, given the amount of time necessary for the ionising star to ionise its surrounding material and then for shocks to propagate into the cloud. However, the age of the IR sources makes them unlikely candidates for triggered star formation. A survey of these objects to determine their true association with the clouds is necessary. Also, the actual development of the shocks within the clouds must be known to determine the likelihood that they may have influenced the star formation efficiency within the clouds.

Chapter 6

Outflow And Infall

6.1 Introduction

Infall and outflow are both indicators of ongoing star formation. The line profiles of optically thick and thin transitions in the molecular gas associated with star forming regions can describe the processes occuring within. The process of infall has, in recent years, been quantified in terms of the line asymmetry found in an optically thick line (Mardones et al. 1997). This asymmetry has been sought for in the northern SFO catalogue using the optically thick HCO^{+} and the optically thin $H^{13}CO^{+}$ lines. The asymmetry has been quantified for the sample and excesses of blue emission, indicating infall, have been examined. Coeval with infall in the starforming process is the process of outflow. Although the exact process(es) driving outflow are not, as yet, fully determined or agreed upon, the presence of molecular flow from a molecular cloud is generally accepted as an indicator of star formation. The line profiles of ^{12}CO line emission have here been observed and examined for evidence of the high velocity dispersions and non-Gaussian line wings associated with molecular flow.

Further observations of carbon containing molecules in the form of ^{13}CO and $C^{18}O$, along with the observations of ^{12}CO allow the determination of the excitation temperatures within the sample as well as column densities. These data allow a derivation of the masses and densities of the clouds which may then be compared to the masses and densities found from submillimetre observations in the previous chapter.

6.2 Observations

The CO and HCO^{+} observations presented in this chapter were made using the A3 receiver in tandem with the DAS backend on the JCMT. The observations were made between the 9th of

February and the 4th of July 2004. The data were reduced using the Starlink software package SPECX. The instrumentation and data reduction are described in chapter 2. The data were taken in flexibly scheduled mode, thus some of the data coverage is incomplete.

6.3 Results

A total of 34 sources were observed (including the distinct clumps within the objects SFO 25, SFO 39 and SFO 87 as separate sources) in at least one of the transitions of ^{12}CO($J = 1 \rightarrow 0$), ^{13}CO($J = 1 \rightarrow 0$), C^{18}O($J = 1 \rightarrow 0$), HCO^{+}($J = 3 \rightarrow 2$) and H^{13}CO($J = 3 \rightarrow 2$). Of these 34 sources only one (SFO 3) was not detected in any of the lines, the detected lines were generally strong (>10 σ). Details of the sources detected in each line are presented in Table 20.

6.4 Individual Sources

A brief synopsis of the ^{12}CO emission associated with the sources detected in this survey is presented here. The profiles of each object's line emission are presented in Appendix A.

6.4.1 Notes On Individual Sources

SFO 7

The line profile of the ^{12}CO emission from SFO 7 is skewed asymmetrically toward the red end of the spectrum with a non-Guassian line wing evident on the blue side. SFO 7 is associated with a high-velocity CO wing (Sugitani et al. 1991).

SFO 14

No CO data were taken for this cloud and only HCO^{+} and H^{13}CO^{+} line profiles are available for analysis here. The HCO^{+} line does show excess wing emission in both the red and blue wings. This cloud is a well studied region within the W3/W4/W5 molecular cloud complex (see chapter 4 and is associated with the infrared stellar cluster AFGL 4029 (Deharveng et al. 1997). Snell et al. (1988) report the presence of a strong molecular outflow.

Table 20: Molecular line survey results

Source	^{12}CO	^{13}CO	C^{18}O	HCO$^+$	H^{13}CO	Comments
SFO 1	^{a}	^{a}	^{a}	$\surd$	$\times$	Inconclusive(1).
SFO 2	^{a}	^{a}	^{a}	$\surd$	$\times$	Inconclusive(1).
SFO 3	$\times$	$\times$	$\times$	$\times$	—	No detection.
SFO 5	$\surd$	$\surd$	$\surd$	$\surd$	$\surd$	Outflow detected(1,2).
SFO 7	$\surd$	$\surd$	$\surd$	$\surd$	$\surd$	See further notes.
SFO 9	$\surd$	$\surd$	$\surd$	$\times$	$\times$	Inconclusive(1).
SFO 10	$\surd$	$\surd$	$\times$	$\times$	$\times$	No outflow detection(1).
SFO 12	^{a}	^{a}	^{a}	$\surd$	—	Inconclusive(1).
						High-velocity CO wing(3).
SFO 13	^{a}	^{a}	^{a}	$\surd$	$\surd$	Inconclusive(1).
						High-velocity CO wing(3).
SFO 14	^{a}	^{a}	^{a}	$\surd$	$\surd$	See further notes.
SFO 15	$\surd$	$\surd$	$\times$	$\times$	$\times$	Outflow detected(1).
SFO 16	$\surd$	$\surd$	$\surd$	$\surd$	$\surd$	Outflow detected(3).
SFO 18	$\surd$	$\surd$	$\surd$	$\surd$	$\surd$	See further notes.
SFO 23	$\surd$	$\surd$	$\surd$	$\surd$	$\times$	Outflow detected(1).
SFO 24	$\surd$	$\surd$	$\surd$	$\surd$	$\times$	See further notes.
SFO 25 SMM1	$\surd$	$\surd$	$\surd$	$\surd$	$\surd$	See further notes.
SFO 25 SMM2	$\surd$	$\surd$	$\surd$	$\surd$	—	See further notes.
SFO 27	$\surd$	$\surd$	$\surd$	$\surd$	$\times$	See further notes.
SFO 30	$\surd$	$\surd$	$\surd$	$\surd$	$\surd$	Outflow detected(1).
SFO 31	$\surd$	$\surd$	$\surd$	$\surd$	$\surd$	Outflow detected(1).
SFO 33	$\surd$	$\surd$	$\surd$	$\surd$	—	No outflow detection(1).
SFO 34	$\surd$	$\surd$	$\surd$	$\surd$	$\surd$	Outflow detected(1).
SFO 36	$\surd$	$\surd$	—	$\surd$	$\surd$	Outflow detected(1).
SFO 37	^{a}	^{a}	^{a}	$\surd$	$\surd$	Known bipolar outflow(4).
SFO 38	^{a}	^{a}	^{a}	$\surd$	$\surd$	Known bipolar outflow(5).
SFO 39	^{a}	^{a}	^{a}	$\surd$	$\surd$	Known bipolar outflow(6).
SFO 43	^{a}	^{a}	^{a}	$\surd$	$\times$	Inconclusive(1).
SFO 44	^{a}	^{a}	^{a}	$\surd$	$\surd$	Known bipolar outflow(5).
SFO 87	$\surd$	$\surd$	$\surd$	^{a}	^{a}	See further notes.
SFO 88	$\surd$	$\surd$	$\surd$	^{a}	^{a}	See further notes.
SFO 89	$\surd$	$\surd$	$\surd$	^{a}	^{a}	No outflow detection(1).

— denotes corrupted or incomplete data, $\surd$ - Source detected in this transition, $\times$ Source not detected in this transition.
^{a} - Source was not observed in this transition.
1-Determination from presented data. 2-Lefloch et al. (1997). 3-Sugitani et al. (1991). 4-Duvert et al. (1990). 5-Sugitani et al. (1989). 6-Fukui et al. (1989).

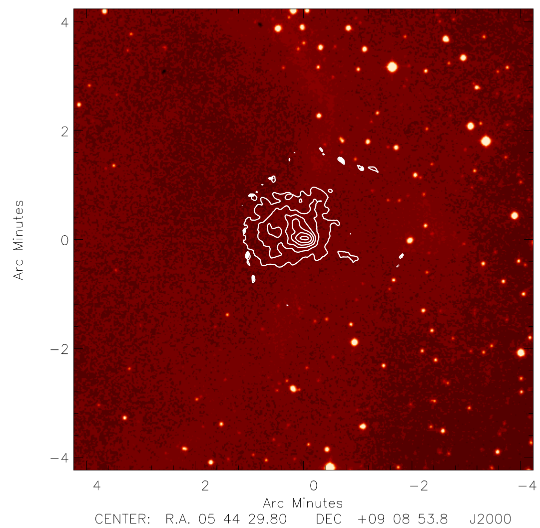

Figure 23: Contours of the SCUBA 850 μm emission associated with the cloud SFO 18 overlaid on a DSS image. The arrow indicates the direction of the suspected ionising star(s). Contours start at 3σ (σ = 0.04 Jy beam^{-1}) and increase in increments of 20% of the peak flux (0.69 Jy beam^{-1}) .

SFO 18

The ^{12}CO emission profile is not smooth and the line is not sufficiently smooth to make assumptions about the presence or otherwise of line wings or asymmetry, however, the ^{13}CO emission has less evident disruption of the line and exhibits some degree of 'skewedness' towards the blue end of the spectrum with a red wing in evidence. This object is the source of a well-known CO ridge and outflow (De Vries et al. 2002; Myers et al. 1988; Lada et al. 1981; Lada & Black 1976). The source was detected with SCUBA and the resulting 850 μm data is shown as contours over a red DSS image in Fig. 6.4.1. Although the ^{12}CO data presented here does not contain any information on the morphology of the CO emission from the cloud, the observations of De Vries et al. (2002) show that the CO emission follows the optical rim and peaks at approximately the same coordinates as the SCUBA emission that was detected in chapter 5.

SFO 24

The ^{12}CO emission in this case has been fitted with a combination of two Gaussians. This double peaked velocity structure is not visible in the optically thin lines of C^{18}O and HCO^{+}. The bluer of these peaks is the more intense with the dip between them skewed toward the positive velocities covered by the line, classically indicative of infall in optically thick CO lines (Leung & Brown 1977 and references therein). The peak of the C^{18}O emission falls between the two peaks of the ^{12}CO emission, supporting a conclusion of infall in this object. Broad wings seen in the ^{12}CO profile are indicative of outflow associated with the region as a whole.

SFO 25

This source is suspected to consist of at least two separate cores, designated as SFO 25 SMM1 and SFO 25 SMM2. These two cores are not readily divisible in the 850 μm SCUBA image of the region (see Fig 5.3.1) but are distinct enough that they were used as two separate sources in the molecular line survey. The fact that the clumps are so close together is the probable cause behind the apparent double-peaked structure visible in the ^{12}CO line emission profile, the velocity components associated with each clump combining along the line of sight. Despite the apparent double peaked structure of the lines associated with SFO 25 SMM1 and SFO 25 SMM2 the lines are fitted better by a single Gaussian and thus this method has been adopted. There is a third 'bump' present in both of the spectra, the structure of this cloud core is obviously complicated and inferences of outflow signatures cannot be supported.

SFO 27

This source has extended ^{12}CO line emission reminiscent of the double-peaked structure seen in the clouds SFO 25 SMM1 and SFO 25 SMM2. This is not evident in the other lines but it is likely that this is the result of fragmented structure within the cloud.

SFO 87

This SFO object is known to consist of at least three separate 'clumps'. Numbered one to three from north to south, the spectra of all three clumps show a double-peaked structure in the optically thick and moderate lines, however, this structure is only seen in the optically thin C^{18}O line for one of the clumps, SFO 87SMM2. The large difference in velocity between the two peaks suggests that possibly an unassociated object is being viewed along the line of sight to the target of interest, in the case of the optically thick ^{12}CO and moderately optically thick ^{13}CO line emission then this is a likely scenario. However, the C^{18}O gas is optically thin and thus is a tracer of high density, the likelihood of there being two critically dense, unrelated collections of CO along the line of sight within the beam of the JCMT is low. It is likely therefore that these peaks represent variations in the kinematical structure of SFO 87 as a whole.

There are some, slight and inconclusive, suggestions of outflow activity in these line profiles (most notably in the ^{12}CO and ^{13}CO profiles of the cloud SFO 87 SMM3).

SFO 88

The emission from this cloud appears very similar to the profiles seen for SFO 87, there are clear, widely spaced ($\sim$2 km s^{-1}) peaks present in all three CO species, suggestive of the presence of multiple cloud clumps. There is better evidence here for the presence of an outflow in the red region of the ^{12}CO spectrum. This 'bump' is repeated at a lesser degree in the ^{13}CO and C^{18}O spectra.

6.5 Outflow Summary

There is clear outflow activity in a large percentage of the clouds observed, there are 17 clouds in this survey in which outflow activity is positively indicated or previously known (SFO 5, 7, 12, 13, 14, 15, 16, 18, 30, 31, 34, 36, 37, 38, 39, 44 and 88). In addition to this there are six clouds in which there is possible outflow activity visible but which the data are not able to definitively support (SFO 1, 2, 23, 24, 43 and 87). Of the 29 clouds observed in at least one of the 5 emission lines used in the survey there are only five (SFO 10, 25, 27, 33 and 89) which show no evidence whatsoever of molecular outflow, indeed, only three of these truly show no indication of outflow (SFO 10, 33 and 89) as both SFO 25 and 27 show complicated, double-peaked structure.

There is an overwhelming abundance of outflow activity in this sample. Even given the possibility that the objects of the SFO catalogue that were not observed in this survey might yield no signs of outflow, this sample is sufficiently large to assure the reader that outflow is a common occurence within BRCs and that these are generally sites of active star formation.

6.6 Infall

The infall signatures of the clouds from the sample are analysed here, using the high density tracers of HCO$^+$ and H^{13}CO$^+$.

Infall evidence is provided by HCO$^+$ and H^{13}CO$^+$ line velocities of each cloud. HCO$^+$ is expected to be optically thick in this regime and H^{13}CO$^+$ is expected to be optically thin.

The method of defining infall through a normalised velocity difference has been used as defined by Mardones et al. (1997). In order to quantify the asymmetries of the observed lines the non-dimensional parameter δV is employed, where

$$\delta V = \frac{V_{HCO^+} - V_{H^{13}CO^+}}{\Delta V_{H^{13}CO^+}} \tag{91}$$

in which the difference between the peak velocity of each line is normalised through the FWHM of the optically thin H^{13}CO$^+$ line emission, this normalisation removes the dependance of the measured line asymmetry on the velocity dispersion within each cloud and allows for a more accurate comparison within the sample. The velocities measured are those of the *peakintensity* in the spectra, thus in a double peaked profile, the velocity is taken from the more intense peak.

The velocity of each line's peak emission is presented in Table 21 along with the FWHM of the $H^{13}CO^{+}$ line and the resulting δV. A histogram of these data is presented in Fig.6.6, a clear tendency toward negative velocities is apparent. The mean δV of the distribution is -0.11 $\pm$ 0.05, quantifying the asymmetries in the sample is most simply achieved through counting the excess number of sources with significant ($|\delta V| > 0.15$) blue velocities over the sources with red velocities. Again, following Mardones et al. (1997) the 'blue excess' is defined as

$$E = \frac{N_{blue} - N_{red}}{N} \tag{92}$$

where N_{blue} and N_{red} are the number of sources with significant blue and red velocities, respectively and N is the total number of sources (including those with no significant velocities). A 'significant' velocity is defined here as being above 3 times the mean statistical uncertainty in the measurement of δV, 0.05. This is contrast with Mardones et al. (1997) who use a factor of 5 times the mean statistical uncertainty in their sample to define infall. This level of probability was felt to be unwarranted. The blue excess present in the sample is therefore 25%.

Table 21: Line Data.

Source	HCO^{+} Peak Position km s^{-1}	$H^{13}CO^{+}$ Peak Position km s^{-1}	$H^{13}CO^{+}$ Line Width km s^{-1}	δV
SFO 5	-51.46 $\pm$ 1.23	-51.04 $\pm$ 0.82	1.94	-0.22 $\pm$ 0.08
SFO 7	-40.30 $\pm$ 1.61	-40.15 $\pm$ 0.75	1.76	-0.09 $\pm$ 0.03
SFO 13	8.15 $\pm$ 1.30	7.64 $\pm$ 1.15	2.71	0.19 $\pm$ 0.06
SFO 14	-37.93 $\pm$ 1.28	-37.94 $\pm$ 0.75	1.77	0.01 $\pm$ 0.00
SFO 16	8.12 $\pm$ 0.59	8.12 $\pm$ 0.39	0.91	0.00 $\pm$ 0.00
SFO 18	10.81 $\pm$ 1.30	11.31 $\pm$ 0.84	1.97	-0.25 $\pm$ 0.09
SFO 25SMM1	7.37 $\pm$ 1.27	7.53 $\pm$ 0.87	2.05	-0.08 $\pm$ 0.03
SFO 30	19.84 $\pm$ 1.39	20.22 $\pm$ 0.72	1.69	-0.22 $\pm$ 0.08
SFO 31	-2.08 $\pm$ 1.05	-2.16 $\pm$ 0.80	1.89	0.04 $\pm$ 0.01
SFO 34	-4.85 $\pm$ 0.85	-4.67 $\pm$ 0.51	1.21	-0.15 $\pm$ 0.05
SFO 36	-7.69 $\pm$ 0.93	-7.55 $\pm$ 0.65	1.54	-0.09 $\pm$ 0.03
SFO 37	1.03 $\pm$ 0.68	1.20 $\pm$ 0.60	1.41	-0.12 $\pm$ 0.04
SFO 38	-0.12 $\pm$ 2.07	0.55 $\pm$ 0.79	1.86	-0.36 $\pm$ 0.13
SFO 39SMM1	-2.15 $\pm$ 0.75	-2.10 $\pm$ 0.58	1.37	-0.04 $\pm$ 0.01
SFO 39SMM2	-1.57 $\pm$ 0.53	-1.44 $\pm$ 0.42	0.98	-0.13 $\pm$ 0.04
SFO 44	-10.89 $\pm$ 1.07	-10.35 $\pm$ 0.81	1.90	-0.28 $\pm$ 0.10

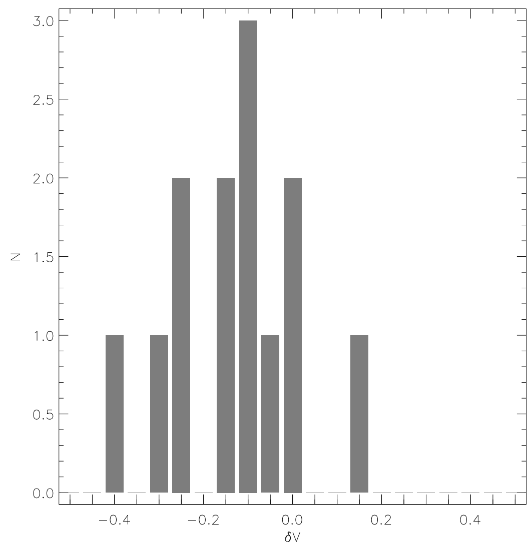

Figure 24: The distribution of the sources detected in both HCO^+ and $H^{13}CO^+$ as a function of the dimensionless parameter δV, a measure of the difference in velocity between the two lines.

6.7 CO Observational Analysis

The optical depth of ^{12}CO, ^{13}CO and $C^{18}O$ within the clouds observed in the (J=3-2) transition may be determined through the relation

$$\frac{T_x}{T_y} = \frac{1 - e^{-\tau_x}}{1 - e^{-\tau_y}} \tag{93}$$

where T and τ represent the brightness temperature and the optical depth of the line in question, the species denoted by the subscript x or y where x and y is 12, 13 or 18. The optical depth of each species is related to each other by the relation $\tau_x = \chi\tau_y$ where, again, x and y can be 12, 13 or 18 and χ is the fractional abundance of species x to species y. The fractional abundance of ^{12}C to ^{13}C is not a fixed standard, a noticeable gradient in the $^{12}C/^{13}C$ ratio with Galactocentric distance has been reported (Savage et al. 2002; Langer & Penzias 1990) with the maximum values of the $^{12}C/^{13}C$ ratio ($\sim$70) reported by Savage et al. (2002) being observed toward photon-dominated regions, similar to the expected environments of the majority of the sample presented here. Recent solid state observations have determined the local ISM $^{12}C/^{13}C$ ratio to have a value of 69 $\pm$ 15, while gas phase studies have yielded values ranging from 40 (Hawkins & Jura 1987) to 150 (Sheffer et al. 1992), a value of $^{12}C/^{13}C = 60$ has been assumed here. In order to determine the ratio of ^{12}CO or ^{13}CO to $C^{18}O$ it is necessary to estimate the ratio of ^{16}O to ^{18}O, this again is a poorly known quantity. However, as some estimate must be made, a value of 500 has been used here in agreement with the value found in presolar meteorite grains in Zinner (1996). A value in approximate agreement with the measurements made from the data collected by Voyager 1 and Voyager 2 ($^{16}O/^{18}O \sim 416$) (Webber et al. 1996). The determinations of the optical depth of $C^{18}O$ in the sources presented here are based upon the ratio of ^{12}CO to $C^{18}O$ as this ratio involves fewer assumptions than the ratio of ^{13}CO to $C^{18}O$. However, a determination of the optical depth of $C^{18}O$ was performed using the ratio of ^{13}CO to $C^{18}O$ to check for consistency and results were in agreement within the errors.

Table 22: CO Temperature Data.

Source	$T_{^{12}CO}$	$\tau_{^{12}CO}$	$T_{^{13}CO}$	$\tau_{^{13}CO}$	$T_{C^{18}O}$	$\tau_{C^{18}O}$
05	22.8 ± 0.14	1.21 ± 0.108	13.1 ± 0.09	0.85 ± 0.154	4.1 ± 0.06	0.20 ± 0.006
07	22.9 ± 0.19	1.05 ± 0.059	10.6 ± 0.05	0.62 ± 0.090	5.5 ± 0.07	0.27 ± 0.016
09	18.5 ± 0.14	0.91 ± 0.016	5.9 ± 0.10	0.38 ± 0.027	0.4 ± 0.10	0.02 ± 0.000
10	9.6 ± 0.15	0.74 ± 0.002	1.2 ± 0.07	0.13 ± 0.003	^{a}	^{a}
15	8.9 ± 0.16	0.77 ± 0.001	0.8 ± 0.19	0.09 ± 0.002	^{a}	^{a}
16	14.1 ± 0.14	1.33 ± 0.173	9.0 ± 0.09	1.02 ± 0.235	5.1 ± 0.05	0.45 ± 0.033
18	7.1 ± 0.07	0.87 ± 0.274	9.1 ± 0.09	^{a}	4.0 ± 0.05	0.45 ± 0.033
23	14.2 ± 0.12	1.16 ± 0.080	7.7 ± 0.10	0.78 ± 0.116	2.2 ± 0.11	0.17 ± 0.005
24	13.8 ± 0.12	1.43 ± 0.237	9.5 ± 0.10	1.17 ± 0.310	3.1 ± 0.09	0.25 ± 0.010
25SMM1	24.2 ± 0.11	1.16 ± 0.071	13.1 ± 0.09	0.78 ± 0.104	3.4 ± 0.05	0.15 ± 0.003
25SMM2	21.6 ± 0.10	1.21 ± 0.075	12.4 ± 0.07	0.85 ± 0.107	3.0 ± 0.09	0.15 ± 0.003
27	19.6 ± 0.19	1.28 ± 0.191	12.0 ± 0.09	0.95 ± 0.266	5.2 ± 0.15	0.31 ± 0.025
30	26.6 ± 0.12	1.18 ± 0.077	14.8 ± 0.07	0.81 ± 0.111	6.9 ± 0.06	0.30 ± 0.013
31	21.5 ± 0.09	0.91 ± 0.010	6.9 ± 0.05	0.39 ± 0.016	1.8 ± 0.05	0.09 ± 0.001
33	19.8 ± 0.09	0.99 ± 0.021	8.1 ± 0.06	0.53 ± 0.033	1.5 ± 0.05	0.08 ± 0.001
34	14.6 ± 0.12	1.13 ± 0.058	7.6 ± 0.06	0.74 ± 0.085	3.6 ± 0.05	0.28 ± 0.011
36	19.0 ± 0.16	1.27 ± 0.149	11.6 ± 0.07	0.94 ± 0.207	^{a}	^{a}
87SMM1	35.9 ± 0.09	0.99 ± 0.019	14.6 ± 0.05	0.52 ± 0.030	5.4 ± 0.05	0.16 ± 0.003
87SMM2	34.4 ± 0.11	0.89 ± 0.010	10.5 ± 0.05	0.36 ± 0.017	2.8 ± 0.05	0.08 ± 0.001
87SMM3	28.0 ± 0.06	1.01 ± 0.017	12.0 ± 0.05	0.56 ± 0.026	4.5 ± 0.06	0.18 ± 0.003
88	35.0 ± 0.15	1.08 ± 0.061	17.0 ± 0.09	0.67 ± 0.092	6.1 ± 0.08	0.19 ± 0.007
89	32.1 ± 0.16	1.09 ± 0.069	15.9 ± 0.09	0.68 ± 0.103	6.5 ± 0.06	0.23 ± 0.009

^{a} - non-detection/τ determination not possible

The corrected receiver temperatures of each of the three CO species observed are presented in Table 22 along with the optical depths derived as described earlier (Section 3.5). Determinations of the optical depth of $C^{18}O$ were not possible for the sources SFO 10, SFO 15 and SFO 36 due to the fact that they were not detected in the $C^{18}O$ transition. The mean optical depth of $C^{18}O$ in this study is noticeably higher than that measured for six clouds from the southern Sugitani catalogue by Urquhart et al (2005, in press), with the measurements presented here averaging $\tau_{C^{18}O} = 0.20$ compared to their $\tau_{C^{18}O} = 0.06$, these values are consistent within the standard deviations of the samples (0.11 and 0.04 respectively) but this discrepancy should be noted.

The excitation temperature of each CO species may be determined from the equation of radiative transfer taken from Myers et al. (1983),

$$T_{ex}^{x} = T_o \left\{ ln\left(1 + \frac{T_o}{J(T_b) + (T_A^*)_x/\eta_b \Phi(1 - e^{-\tau_x})}\right)\right\}^{-1} \tag{94}$$

where T_{ex}^{x} is the excitation temperature of species x, denoted by 12, 13 or 18, $T_o = \frac{h\nu}{k_B}$, $J(T_b) = T_o\left[e^{\frac{T_o}{T_b}} - 1\right]^{-1}$, T_b is the temperature of the ambient background, taken as 2.7 K. T_{Ax}^{*} is the corrected antenna temperature of species x, η_b is the beam efficiency of the telescope (0.57 for the JCMT at 230 GHz), Φ is the beam filling factor (taken as 1 considering that the sources are all extended in comparison to the JCMT beam of 19.7″) and τ_x is the optical depth of the species x. Values for the excitation temperatures derived from observations of each species are presented in Table.23, as expected, it can be seen that the temperatures derived from each species agree with one another to a high degree.

Given the excitation temperature of a species one may determine the column density of that species through Equation 61,

$$N_{Tot} = \frac{3\epsilon_0 k_B^3}{2B}\Big(\frac{T_{ex}}{h\pi\nu\mu}\Big)^2 \frac{(2J+3)}{(J+1)} \frac{e^{hBJ(J+1)/k_B T}}{(2J+1)} \Big(\frac{1}{e^{h\nu/k_B T_{ex}} - 1} - \frac{1}{e^{h\nu/k_B T_{bg}} - 1}\Big)^{-1} \int T_B \mathrm{d}v \tag{95}$$

For $C^{18}O$ observed in the $J = 2 - 1$ transition: $\nu = 219.560353$ GHz, $\mu = 0.11049$ Debyes (Goorvitch 1994) and $B = 54.891421$ GHz. The value of the fraction of $C^{18}O$ compared to H_2 is taken as 1.7×10^{-7} (Goldsmith et al. 1996) and the subsequent values of H_2 column density that have been calculated are presented in Table.23.

The mass of each cloud may be calculated from the beam-averaged column density presented in Table 23 assuming the cloud radii presented in Sugitani et al. (1991) and a percentage by mass of H_2 of 75 %. This analysis also assumes that the clouds are spherically distributed with a uniform density. Masses are presented in Table 23, it can be seen that the variation in cloud mass is very large, ranging from 1.7 to 2236.6 $M_\odot$ with a mean of 416.0 $M_\odot$. Despite this large range in mass the spread in the molecular hydrogen density is small, ranging from 4.0 $\times 10^3$ to 1.0 $\times 10^5$ (mean = 25.8 $\times 10^3$ $\sigma = 21.3 \times 10^3$). A comparison was made of the masses derived here with those derived by De Vries et al. (2002) from HCO^+ observations for the clouds SFO 16, 18 and 25. The masses found by De Vries et al. (2002) are consistently lower than those derived here, with ratios of $M_{C^{18}O}/M_{H^{13}CO} = 3.2$, 1.3 and 3.2 for SFO 16, 18 and 25 respectively. This apparent discrepancy is explained by the fact that HCO^+ is at least moderately thick in these clouds and, as such, does not sample the entire mass of each cloud.

It was not possible to derive masses for the clouds SFO 10, SFO 15 and SFO 36 from the $C^{18}O$ data as they were not detected in this line. Therefore, ^{13}CO linewidths and temperatures

Table 23: CO T_{ex} and N_{col} Data.

Source	T_{ex} (^{12}CO) (K)	T_{ex} (^{13}CO) (K)	T_{ex} ($C^{18}O$) (K)	T_{ex} (ave) (K)	$log_{10}(N(H_2))$ (cm^{-2})	$log_{10}(n(H_2))$ (cm^{-3})	Mass (M$_\odot$)
05	45.49	45.44	44.96	45.30	22.73	4.4	293.06
07	45.67	45.55	46.06	45.76	22.86	4.2	2236.58
09	37.91	38.00	40.70	38.87	21.55	3.7	1.74
10	22.11	22.36	-	22.24	22.16	4.0	34.06^a
15	20.92	21.38	-	21.15	21.90	3.6	45.86^a
16	30.12	29.89	29.87	29.96	22.49	4.2	119.80
18	-	-	24.47	24.47	22.48	4.4	46.04
23	30.30	30.14	29.86	30.10	22.20	3.8	96.65
24	29.59	29.35	29.76	29.57	22.33	4.4	20.02
25SMM1	47.96	47.74	48.12	47.94	22.79	4.5	233.03
25SMM2	43.38	43.28	43.06	43.24	22.71	-	-
27	39.85	39.60	39.48	39.64	22.72	4.7	84.40
30	52.19	52.10	52.01	52.10	23.05	4.4	2177.22
31	43.20	42.77	41.96	42.64	22.50	4.4	74.52
33	40.20	39.81	39.48	39.83	21.93	4.3	1.86
34	31.00	30.70	31.05	30.92	22.35	4.2	43.98
36	38.79	38.66	-	38.72	23.11	4.6	1349.89^a
87SMM1	68.55	68.54	69.43	68.84	22.84	4.4	550.41
87SMM2	65.92	66.29	69.24	67.15	23.01	-	-
87SMM3	54.66	54.43	53.24	54.11	22.63	-	-
88	66.97	66.44	67.19	66.87	22.81	4.4	471.76
89	61.87	61.89	60.83	61.53	22.76	5.0	23.13

- quantity determination not possible ^{a} Density and mass determined through ^{13}CO observations.

were used in these cases. As mentioned previously the clouds SFO 25 and SFO 87 consist of multiple cores, however, here the larger structure has been treated as, at this point, it is the region encapsulated by the optically bright rim that is of interest. Therefore, the column density from each core has been averaged to give density and mass for the cloud as a whole assuming a cloud radius as given by Sugitani et al. (1991).

6.8 Pressure Balances

The pressure of the molecular gas within the clouds in the sample is a result both of turbulent velocities within the cloud interiors, and the thermal pressure. In the case of the clouds being composed mostly of cold (~10K) gas there is a negligible thermal contribution to the internal pressure. From molecular line observations the internal molecular pressures of the cloud sample may be derived using the relation between molecular pressure P$_m$, the square of the turbulent velocity dispersion, σ^2, and the density of the molecular gas, ρ_m; i.e.

$$P_m \simeq \sigma^2 \rho_m \tag{96}$$

The turbulent velocity dispersion may be written in terms of the observed linewidth $\Delta\nu$ as $\sigma^2 = <\Delta\nu>^2/(8\ln 2)$.

The data presented here show that the clouds have global temperatures significantly higher than 10 K. Thermal pressure, whilst still not the dominant factor in the clouds' internal pressure, may not be neglected in this analysis. Therefore, the total internal pressure of each cloud has been calculated via the equation

$$P_m = \sigma^2 \rho_m + \frac{3}{2} N k_B T \tag{97}$$

where N is the number density of particles in the cloud. The pressures of each cloud have been determined using the low column density tracer $C^{18}O$ or, in the cases of SFO 10, SFO 15 and SFO 36, the moderate density tracer ^{13}CO. Again, to analyse the properties of the larger regions encapsulating the cores SFO 25 SMM1, SMM2, SFO87 SMM1, SMM2 and SMM3 the averaged velocity dispersion has been used.
The temperature used to determine the thermal pressure was the mean excitation temperature of all three observed CO lines.

Previous observations of line emission from the northern SFO objects were collected via a SIMBAD search specific to the SFO catalogue. Linewidths taken from the $C^{18}O(J = 1 \rightarrow 0)$ observations of Jansen et al. (1994), and their value for H_2 density have been used to determine an internal molecular pressure for SFO 4. Values for the internal pressure and density of SFO 11 have been taken from Thompson et al. (2004a).

De Vries et al. (2002) conducted a millimetre and submillimetre molecular line survey of BRCs selected from the SFO catalogue. In their survey they observed $C^{18}O$, HCO^+ and N_2H^+ (in addition to other species) emission from the clouds. SFO 13 was not detected in N_2H^+ by De Vries et al. (2002) and its density was thus determined from their HCO^+ observations. Internal molecular pressures for these three clouds were then determined from the linewidths of the $C^{18}O(J = 1 \rightarrow 0)$ observations presented in the same work. $C^{18}O(J = 1 \rightarrow 0)$ linewidths and core densities from Cernicharo et al. (1992) and Duvert et al. (1990) were used to calculate internal pressures for SFO 20 and 37 respectively in preference to the observations of De Vries et al. (2002) due to their superior angular resolution. The pressures used for SFO 4, 11, 11NE, 11E, 13, 20 and 37 are not inclusive of the thermal pressure and so may be assumed to be a lower limit.

The IBL pressures calculated from the NVSS data (for all clouds) range from 16.2 to 85.8 $\times$ 10^5 cm^{-3} K with a mean of 33.7 $\pm$ 8.4 $\times$ 10^5 cm^{-3} K, while the molecular line data that has been collected show a range of internal molecular pressures of 1.5 to 147.0 $\times$ 10^5 cm^{-3} K, with a mean of 49.7 $\times$ 10^5 cm^{-3} K (Table 24).

Table 24: Ionised boundary layer pressures and internal pressures of clouds observed in molecular line wavelengths.

SFO Object	IBL pressure (10^5 cm^{-3} K)	Internal Pressure (10^5 cm^{-3} K)
4[a]	61.8	8.2
5	35.8	67.6
7	16.2	38.3
9	-	9.1
10	50.8	45.8
11[b]	82.0	25.0
11NE[b]	110.0	57.0
11E[b]	150.0	51.0
13[c]	20.0	16.3
15	22.4	11.8
16	-	20.2
18	-	48.6
20[d]	-	6.9
23	-	10.2
24	-	35.0
25	20.8	130.5
27	42.1	94.7
30	44.7	86.9
31	47.5	104.2
33	-	20.8
34	-	20.9
36	17.2	102.3
37[e]	35.1	1.5
87	-	88.3
88	11.3	43.4
89	76.5	147.0

[a]Jansen et al. (1994);[b]Thompson et al. (2004a); [c]De Vries et al. (2002); [d]Cernicharo et al. (1992); [e]Duvert et al. (1990)

Factors contributing to the uncertainties in the values for internal molecular pressure include the accuracy involved in measuring linewidths and the uncertainty in the radii for these clouds taken from Sugitani et al. (1991) (including the assumption of spherical symmetry made in determining volume densities from column densities). It is estimated that uncertainties in the internal molecular pressures presented total no more than a factor of 5.

The clouds SFO 5 has previously been observed by Lefloch et al. (1997), the pressure found using their observations is consistent with that found here (32.3/67.6) given this large uncertainty.

Of the 17 clouds for which the pressure balance has been analysed, two of them (SFO 4 and SFO 37) fall below the line delineating pressure balance (including the range of error, see Fig. 25), indicating that these are underpressured with respect to the relevant IBL. The internal pressures within these two clouds have been determined from observations found in the literature and not from the observations here. Thus, subtle differences may be expected, not least of which the inclusion of thermal pressure. Two clouds, (SFO 25 and SFO 36) lie above the pressure balance line (including the range of error), indicating that their respective IBLs are unlikely to affect their development.

In addition to the clouds that have been identified here as being in pressure balance with their IBL's, Cernicharo et al. (1992) present observational evidence that SFO 20 (ORI-I-2) is undergoing RDI. They find a bipolar outflow emanating from the source, and while their evidence is not definitive, they conclude that the UV field present due to the illuminating star, σ-Ori, has strongly modified the evolution of the primitive globule and strongly increased its star formation potential.

The mean internal pressure of the clouds for which there are molecular line data is 49.7×10^5 cm^{-3} K (consistent with the results of Thompson et al. (2004b) who find an internal molecular pressure of 15×10^5 cm^{-3} K). The remainder of our clouds for which there are 20 cm data but no molecular data, have been found to have ionised gas pressures generally higher than this with a mean of 33.7 ± 8.4. Most of the clouds within the sample are therefore candidates for the possible propagation of photoionisation induced shocks into their interiors, although as this determination is based upon a global mean of internal pressure no definitive statements can be made. SFO 25 and SFO 36 show internal pressures that place them above the pressure balance threshold so at least some of the sample is unlikely to be affected by the interaction of the IBL.

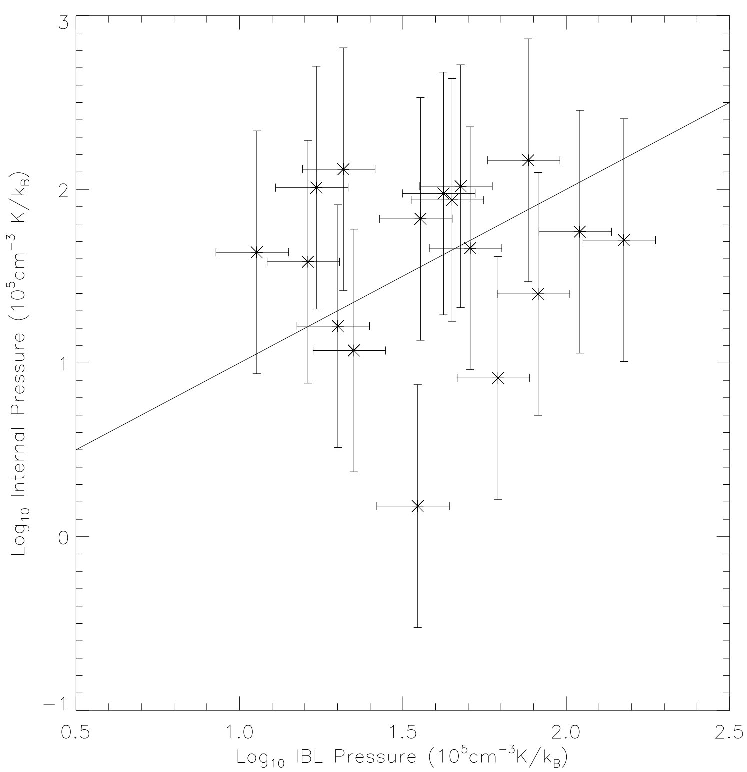

Figure 25: Graph of internal molecular pressure versus IBL pressure. Error bars in IBL pressure represent an approximate 75% uncertainty in the assumption that $T_e = 10^4$. The solid line indicates pressure balance between the internal and external pressures.

6.9 Mass Analysis

Table 25 compares the CO derived masses for the clouds in the sample with those derived from SCUBA continuum observations in chapter 5. It can be seen that there is generally more mass visible in CO line emission than in the IR/submillimetre continuum. There are two values of $\mathrm{Mass}_{850}/\mathrm{Mass}_{CO}$ that show an excess of mass at 850 μm here (SFO 9, and SFO 89). Depletion of CO here is probably not a good explanation for these values of $\mathrm{Mass}_{850}/\mathrm{Mass}_{CO}$ as the dust temperature recorded for these clouds (chapter 5) is generally higher than the ~10 K that is required for depletion. The abundance of CO mass over the mass derived from the 850 μm flux is in contrast to Mitchell et al. (2001) who find the opposite abundance without exception in their sample of submillimetre cores in the Orion B molecular cloud. The observations of Mitchell et al. (2001) were made in a mapping mode, though the observations did have the same resolution as those presented here (having used the same receiver) and the source size they used in determining the masses they derive was this beam size. Thus a comparison here of $\mathrm{Mass}_{850}/\mathrm{Mass}_{CO}$ ratios is valid.

6.10 Temperature Ratios

Plotting the ratio of the dust temperature of each source as determined through SED fitting (see chapter 5) against the average excitation temperature of the three CO species (see Table 22) shows the relationship between these two quantities. Fig. 6.10 shows $\mathrm{T}_{dust}/\mathrm{T}_{CO_{ex}}$ against $\mathrm{T}_{CO_{ex}}$ on a log-log scale. There is clear clustering of the data points, to which a line of best fit has been determined, shown on the diagram. The best fit line shows a relationship of log $(\mathrm{T}_{dust}/\mathrm{T}_{CO_{ex}}) \propto$ log $(\mathrm{T}_{CO_{ex}})^P$, where the P exponent is measured as -1.12 for the displayed temperatures. This exponent shows that the dust temperature of the clouds as a whole is approximately constant across a wide range of CO temperatures. There is an outlier in each plot, seen in Fig. 6.10 as the crossed square at approximately Log T_{CO} = 1.65, Log $\mathrm{T}_{dust}/\mathrm{T}_{CO}$ = -0.7. This point represents SFO 25, a complex source composed of more than one protostellar core. SFO 25 is the only source in the sample with dust temperatures low enough for depletion to occur. This source should be treated with caution, the excitation temperature measured for this source is $\sim$ 50K, while the SCUBA measured dust temperature indicates a dust temperature of only 9K, supporting the conclusion that this source, if not all of the sources are not thermalised. However, the SCUBA measured dust temperature was determined using only two flux measurements, leading to a much higher uncertainty in this dust temperature than most of the other sources (See Section 5.7.1). The independance of dust temperature with respect to CO temperature indicates that these sources are not thermalised, i.e. the materials are not mixed and are not expected to be in equilibrium. This is what might be expected in a young protostar beginning the collapse phase of its evolution.

Table 25: Comparison of SED derived masses with CO derived masses.

Source	$Mass_{850}$ ($M_\odot$)	$Mass_{CO}$ ($M_\odot$)	$Mass_{850}/Mass_{CO}$
05	69.7	293.06	0.28
07	93.3	2236.58	0.04
09	13.3	1.74	7.64
10	5.9	34.06[a]	0.17
15	6.1	45.86[a]	0.13
25	164.7	233.03	0.71
27	17.7	84.40	0.21
30	129.9	2177.22	0.06
31	1.3	74.52	0.02
33	0.2	1.86	0.11
36	16.1	1349.89[a]	0.01
87	18.5	550.41	0.03
88	215.3	471.76	0.46
89	38.4	23.13	1.66

[a] Density and mass determined through ^{13}CO observations.

6.11 Virial Mass

In order to determine the extent of the influence of the external pressure exerted on the observed clouds by the IBL the virial mass of each cloud has been calculated. This is the mass above which the cloud is unstable to collapse. The virial mass is independent of external pressure and thus may help to determine the likelihood that the observed clouds would have collapsed regardless of the external ionisation. The virial mass is determined from the equation (Evans 1999)

$$M_V = 210 M_\odot R(pc)[\Delta v(kms^{-1})]^2 \tag{98}$$

where R is the radius of the region and Δv is the FWHM line width of the cloud. Note that R here will be taken as the core radius as measured from our SCUBA observations, as this is the region that may be expected to collapse, not the cloud as a whole. The line used to determine Δv is the $C^{18}O$ line as this is the most optically thin line, thus tracing a higher proportion of the material.

The cloud sample is split approximately half and half between those clouds that are stable against collapse (ten of the sample), ignoring the external pressure of the IBL and those whose mass suggests that collapse would occur in any case. This calculation of the virial mass neglects any pressure resulting from magnetic fields that would act to support the clouds against collapse.

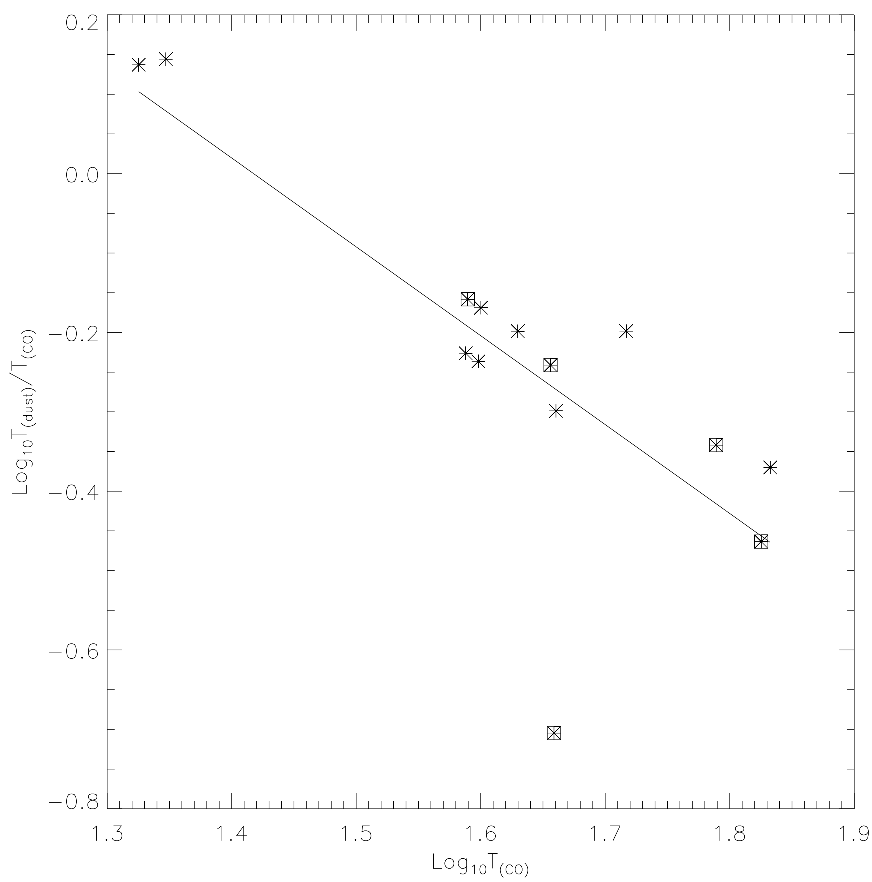

Figure 26: Ratio of the SED derived dust temperature to the CO excitation temperature as a function of CO excitation temperature on a log-log scale. Asterix represent those sources with a higher mass found in the CO line emission than in the Continuum, while squares represent those with a higher continuum mass. The straight line shows a linear best fit.

Table 26: Virial Mass Parameters

Source	R (pc)	Line Width (km s^{-1})	M$_V$ (M$_\odot$)	M$_{PV}$ (M$_\odot$)	M$_{850}$ (M$_\odot$)	M$_{850}$/M$_{PV}$
SFO 5	0.08	1.87	58.75	93.02	69.7	0.75
SFO 7	0.07	1.83	49.23	126.82	93.3	0.74
SFO 9	0.03	1.40	12.35	-	13.3	-
SFO 10	0.01	2.68[a]	15.08	329.43	5.9	0.02
SFO 11 SMM1[b]	0.14	1.2	42.34	10.4	20.6	1.98
SFO 11NE SMM1[b]	0.12	1.8	81.65	45.4	13.4	0.30
SFO 11E SMM1[b]	0.14	1.7	84.97	31.2	18.7	0.60
SFO 13	0.12	4.0[c]	403.20	2605.43	54.0[c]	0.02
SFO 15	0.05	2.25[a]	53.16	246.47	6.1	0.02
SFO 16	0.01	1.15	2.78	-	-	-
SFO 18	0.03	1.60	16.13	-	-	-
SFO 24	0.01	1.31	3.60	-	-	-
SFO 25	0.04	2.51	52.92	396.11	164.7	0.42
SFO 27	0.03	1.58	15.73	43.72	17.7	0.40
SFO 30	0.12	2.05	105.90	120.23	129.9	1.08
SFO 31	0.03	2.61	42.92	306.46	1.3	0.004
SFO 33	0.01	0.88	1.63	-	0.2	-
SFO 34	0.03	1.16	8.48	-	-	-
SFO 36	0.03	1.78[a]	19.96	110.17	16.1	0.15
SFO 87 SMM1	0.04	1.29	13.98	-	19.1	-
SFO 87 SMM2	0.03	3.80	90.97	-	17.9	-
SFO 88	0.14	1.10	35.57	19.82	215.3	10.86
SFO 89	0.06	0.98	12.10	4.80	38.4	8.00

a - ^{13}CO linewidth used due to lack of C^{18}O data.
b - Data taken from Thompson et al. (2004b)
c - Data taken from De Vries et al. (2002)

6.11.1 Pressurised Virial Mass

The effect of the IBL upon the stability of the cores in the sample may be estimated using a modified equation for the virial mass of each cloud. Accounting for an external pressure upon the clouds (though still ignoring possible magnetic support) gives the critical mass for collapse, M_{PV}, as, (Thompson et al. 2004b)

$$M_{PV}(kg) = 5.8 \times 10^{-2} \frac{\langle \Delta v \rangle^4}{G^{3/2} P_{ext}^{1/2}} \tag{99}$$

where, G is the gravitational constant.

A perhaps surprising result here is that most of the sample have pressurised virial masses which are *larger* than the virial mass calculated in the usual way, neglecting external pressure. No trend has been noted in these clouds with respect to line width and external pressure, the clouds lie at seemingly random points in the range of both of those parameters. It should be noted that the pressurised virial mass is only accurate to approximately a factor of 2, predominately due to the uncertainty in line width as this factor is to the fourth power.

Of the eight clouds for which $M_{PV} > M_V$, only one (SFO 7) has a mass greater than its pressurised virial mass. Thus, the majority of the clouds for which $M_{PV} > M_V$ may be expected to be stable against collapse, or indeed, to be in the process of being dissipated and dispersed by the ionisation front. This must be investigated further as the errors inherent in this analysis do not allow a definitive conclusion to be made.

6.12 Discussion

Molecular line observations were performed in order to look for signatures of star formation in the sources from the northern SFO catalogue. In addition, the analysis of the line emission enables the verification of the physical properties of the clouds determined from submillimetre continuum observations presented in chapter 5.

6.12.1 Outflow

Many of the observed clouds show outflow activity, the clear detections of outflow (including those clouds which have been previously identified as having outflow activity present) number 17 in a sample of 30. It is not evident, without mapping the CO emission associated with the clouds, what the cause of the outflow is in any particular cloud. It is possible that the flow detected is due to photoevaporative flow from the surface of the clouds. Higher resolution studies and mapping are necessary to definitively associate the broad wings generally found in the spectra of the clouds with star-forming activity. The emission detected is not likely to be due to photoevaporative outflow as line wings are generally present in both the red and blue wings of the line profile. Because of their nature, the BRCs are only normally seen in profile. Because ^{12}CO is optically thick we might then expect to only observe a photoevaporative flow from the side of the cloud facing us. It is also unclear whether the amounts of ^{12}CO in the observed J=2-1 transition in a photoevaporative flow are significant.

6.12.2 Infall

Infall in the sample of clouds was not found in as many cases as expected given the number of outflow detections. While the majority of the clouds do show negative velocity excesses, indicating infall, the magnitude of the relevant velocities is rather low. Only 25% of the clouds have significant negative velocity excesses (despite adopting a rather less rigorous selection criteria than Mardones et al. (1997), who used a 5σ lower limit in comparison to the 3σ used here).

The number of clouds lacking significant infall signatures may be a result of poor velocity resolution, rather than a true representation of the situation occurring in BRCs. There is a very definite trend in these sources toward a negative velocity excess, however, higher velocity resolution observations are necessary in order to determine the full significance of this trend. Mardones et al. (1997) found that, for their sample of protostars (which was not restricted by mass or luminosity) they found a 47% negative velocity excess from the protostars in their sample defined as Class 0 type. Note that they used a far more rigorous selection criterion in their method, using a value of $\delta V = 0.25$ in comparison to the $\delta V = 0.15$ used here. This suggests that infall is not predominant, or may even be inhibited, in our sample as compared to other Class 0 protostellar sources.

6.12.3 Pressure Balance

The pressures of the IBL of the clouds for which there were radio data were determined in chapter 4. In this chapter the internal molecular pressure of the clouds has been determined where possible. This (along with data from the literature) has led to a total of 17 clouds for which these pressures may be directly compared. The majority of the clouds for which an analysis is possible show an approximate equilibrium between the external pressure of the IBL and the internal molecular pressure.

Whilst there are large errors inherent in the analysis, the majority, if not all, of this sample of clouds are all expected to be in approximate pressure balance with their respective IBLs. The clouds have therefore undergone, or are in the latter stages of undergoing the propagation of shocks into their interiors. Therefore, the observed star formation which is occuring in the clouds may well have been triggered by these shocks.

The shock crossing times for the observed BRCs is of order 1 Myr, which is the length of time that might reasonably be expected for a cloud to reach an equilibrium between its external and internal pressures. The observed star formation is unlikely to be older than $\sim 10^5$ yr, thus, the observed star formation is consistent with the timescale of ionisation. A weighted average of the pressures found for each cloud (weighting via the error in the measurements) reveals a slightly greater disparity between the internal and external pressures. The mean average of the internal pressures of the clouds is 21.0×10^5 cm^{-3} K while the mean average of the external pressures is 33.7×10^5 cm^{-3} K. The weighted averages of these two quantities are 14.7 and 30.8×10^5 cm^{-3} K respectively. This may indicate that the clouds are not in fact in pressure equilibrium and that they may still be undergoing the propagation of shocks into their interiors. This, however, does not rule out the possibility that the observed star formation has been triggered. As these clouds are close to pressure equilibrium, if not actually equalised, then this may indicate that the shocks have had sufficient effect upon the clouds to have dynamically altered the clouds evolution.

6.12.4 CO Masses And Temperatures

Masses were derived from the $C^{18}O$ observations presented in this chapter, it is expected that $C^{18}O$ is not depleted in these clouds as the mean dust temperature in these clouds (25 K) is significantly higher than that required for depletion ($\sim$ 10 K). The results are not generally consistent with the masses found from submillimetre observations presented in chapter 5. The masses derived from the $C^{18}O$ data are systematically larger than those derived from submillimetre flux. Class 0 protostars are expected to have a large amount of mass in their surrounding envelopes. Submillimetre observations of cores in the Orion molecular cloud (Mitchell et al. 2001) show an abundance of dust mass over CO mass without exception throughout a large sample, suggesting that some effect is occuring in BRCs that alters this behaviour. Of course it may be that the Orion molecular cloud is strange in itself and that this sample is the ordinary one, more submillimetre observations of high-mass star-forming regions need to be analysed in order to determine the cause behind this discrepancy. It is possible that the CO observations are tracing more extended material surrounding the submillimetre cores and that there is a higher proportion of gas surrounding these cores than that found in the region surrounding the cores of the Orion molecular cloud.

The excitation temperatures of CO in the cloud sample show no correlation with the derived dust temperature. The temperatures derived in chapter 5 are remarkably consistent across a wide range of CO temperatures, suggesting that chemistry in the extended, dusty, envelope is independent of the gas-phase chemistry.

6.12.5 Virial Masses

From the linewidths of $C^{18}O$ and the radii taken from the SCUBA core observations in the submillimetre regime, the virial mass of these clouds may be determined. Here the likelihood of collapse in these clouds can be directly measured. The clouds that have the required data for the calculation to be made are split between those that are stable against collapse and those that are not. The mass used for comparison being the mass determined from the 850 μm flux measurement. Some of the clouds are stable against collapse in this analysis (SFO 10, 11 SMM1, 11E SMM1, 11NE SMM1, 13, 15, 31, 33, 36 and 87SMM2). Nevertheless most of these clouds do show some evidence of star formation. This suggests that other processes may be influencing the development of these clouds, in order to investigate this the *pressurised* virial mass was calculated. This accounts for the influence of the external ionisation front upon the clouds and includes the effects of the increased pressure.

A surprising result of the pressurised virial mass analysis is that the majority of the clouds for which the analysis was possible (ten out of fifteen) have pressurised virial masses that are larger than the virial mass calculated in the normal way. Thus, the effect of the ionising radiation has been to *inhibit* the collapse of condensations within the cloud. This is generally not expected to occur in triggered star formation regions, though it has been suggested that this might be the effect, at least in low mass star-forming regions (Whitworth, *priv. comm.*).

6.13 Summary And Conclusions

The temperatures, masses and densities of a large proportion of the northern SFO catalogue have been determined, showing values consistent with star-forming regions, and supporting the observations presented in chapter 5.

Evidence of outflow has been observed in the majority of the sample, along with a negative velocity excess, suggesting infall in a significant proportion of the sample. These sources have thus been shown to be active sites of star formation.

The temperatures of our sources, as measured from SED fitting also presented in chapter 5, have been shown to be approximately constant over a range of CO temperatures. Suggesting an independence of thermal interaction between the extended protostellar envelope and the internal star-forming regions.

In comparing the ratio of cloud dust mass to the mass determined through CO column density ($\mathrm{Mass}_{850}/\mathrm{Mass}_{CO}$) a trend was found for there to be an excess of Mass_{CO}. This is in direct contrast to the observations of submillimetre cores in the Orion molecular cloud made by Mitchell et al. (2001).

All of the clouds in the sample have been shown to have undergone, or be undergoing, photoionisation induced shocks which are propagating into their interiors, with all but four of the sample likely to be in pressure equilibrium. A state of equilibrium suggests that two of the clouds are in, or approaching, a post-shocked state, having been subjected to shocks that have now had most of their energy dissipated, leaving a D-type ionisation front at the surface of the cloud. This ionisation front will continue to propagate into the cloud until either the source of the ionisation is exhausted or the cloud is completely dispersed. Any star formation detected within clouds that have reached this equilibrium state is conceivably due to the triggering of collapse via the shock wave mechanism.

Clouds that are currently undergoing the propagation of shocks into their interior are unlikely to contain star-formation that is due to the triggering of collapse. Four of the clouds that have been identified as being in a state of pressure imbalance (SFO 4, SFO 25, SFO 36 and SFO 37) may be split into two subdivisions. SFO 4 and SFO 37 appear to be underpressured (high relative IBL pressure) and are small (0.03 pc) and low in mass (0.09[1] and 3.3 $M_\odot$ respectively).

[1]determined from the density stated by Jansen et al. (1994) and the radius of Sugitani et al. (1991)

The rim types as discussed in chapter 5 are 'b' and 'c' respectively. Considering the evolutionary rim type scenario of Lefloch & Lazareff (1994) along with the categorisation of clouds as defined by Bertoldi (1989) how are the morphologies of SFO 4 and SFO 37 to be interpreted? If the column densities of the two clouds are sufficient then it may be expected that the ionisation-induced shocks currently propagating into them will cause the internal molecular pressure to equalise with that of the IBL, if this is the case then the clouds may be expected to follow the same evolutionary track as the other clouds in our sample.

The other two clouds that appear to be in a state of pressure imbalance are apparently overpressured (high relative internal pressure). SFO 25 and SFO 36 are also relatively small with effective diameters of 0.07 and 0.05 pc respectively but they are among the more massive of the cores at 164.7 and 16.1 $M_{\odot}$ respectively. The internal pressure of these clouds means that any star formation found within in them is unlikely to have been triggered by external effects. A determination of the virial masses of each cloud (for which there is data) shows that, for the majority of the sample (ten of fifteen), the external pressure of the IBL appears to be having a dissipative effect upon the clouds. This does not necessarily preclude the possibility of star formation within the clouds, but does suggest that, in general, the effect of ionisation of BRCs may be a hindrance rather than an aid to star formation. The conclusion is that while triggered star formation through RDI is still a plausible scenario, the exact contribution of ionisation toward star formation efficiency is, as yet, undetermined.

Chapter 7

Summary And Conclusions

The work presented in this thesis consists of a large body of observational data, taken towards a number of molecular clouds in ionised surroundings. The observations contain a great deal of information about the clouds, from quantifying the environment of the molecular clouds, to separating the clouds into submillimetre cores and identifying their structure.

7.1 Observational Summary

Data archives were searched for the regions covered in the entire northern SFO catalogue. Archives of radio, optical and infrared data all yielded detections and the subsequent data were analysed. Radio wave 20 cm emission was detected to a level of 3σ, or greater, in 32 of the sample, with correlating infrared data for all but two of the northern SFO catalogue.

Original observations were performed of 45 BRCs at 450 and 850 μm using the SCUBA on the JCMT. Eight of these clouds did not yield detections, though a total of 45 submillimetre cores were detected in the remaining 37 clouds. By defining an SED of the observed sources using these observations, archival data and data published in the literature, the dust temperatures and luminosities of the sources have been determined. This has allowed a definition of the stellar type of the embedded source(s). From the submillimetre flux the masses of the clouds has been ascertained. The observed submillimeter luminosity showed that all of the sources were consistent with being Class 0 protostars.

Observations were performed to measure the emission from molecular level transitions in ^{12}CO, ^{13}CO, $C^{18}O$, HCO^+ and $H^{13}CO^+$ with detections in 20, 20, 17, 24 and 15 of the sample respectively. The observations led to determinations of the temperatures, masses and densities of the clouds, as well as indicating signs of infall and outflow in a significant proportion of the sample. All of these measurements support the identification of these regions as being star-forming. The linewidths of $C^{18}O$ allowed a determination of the internal molecular pressures of the clouds.

7.2 Discussion

A survey of the northern catalogue of BRCs has been presented, a picture has been formed of high-mass, high-luminosity stars, deeply embedded within their natal molecular clouds. These clouds are being heated by internal sources and are regions of noticeable, star-forming activity, including molecular outflow and infall (albeit at a slower rate than might be expected in a Class 0 protostar). The clouds have been well described in terms of their physical properties; temperatures, masses, densities and pressures are all known for a significant number of the sample. These properties again all support the identification of these regions as high-mass star-forming regions. Through radio observations the exterior pressure acting upon the molecular clouds has been determined. The clouds are generally confined by an IBL in approximate pressure equilibrium. The pressure gradient that is presumed to have existed in the past is thought to have acted upon the clouds so as to send shocks into the interior, the diagnostics of the pressure gradient for the 17 clouds for which there are the relevant data show that, within reasonable errors, all of the clouds bar two have been shocked by the influence of a photoionisation front produced by a nearby massive star. The ionising star in question is not always consistent with the level of ionising radiation measured at the head of the cloud. No consistent trend has been found to explain this discrepancy, further studies into the exact dynamical effect of massive ionising stars upon molecular clouds are necessary.

The stability of the cores found in the clouds is unexpected. Warm submillimetre cores (and thus, presumably, protostars) seem to be extremely prevalant amongst BRCs, at least those emitting radiation in the IR regime. However, an analysis of the virial masses of these clouds in comparison to the masses measured from the submillimetre flux show that the ionising radiation is apparently having a dispersive effect upon the clouds.

7.2.1 Triggered Or Inhibited Star Formation?

High mass star-forming regions have been discovered in many of the northern SFO catalogue of BRCs. Preliminary radio observations of the clouds, combined with molecular line transition observations show that the clouds are in an approximate pressure balance, with the pressure caused through the effects of the IBL on the clouds' exterior balanced by that of the internal molecular material. This evidence is highly suggestive of the RDI scenario, in which the clouds are triggered to collapse through shocks driven into their interior. The clouds are generally expected to reach equilibrium with the exterior pressure within a shock crossing time, i.e. the time in which it takes the the shock to traverse the whole cloud. This crossing time is the amount of time generally accepted to be the time required for an exterior influence to affect a cloud, thus, the clouds in which we find star formation are those that we expect to find equilibrium between the exterior IBL pressure and the internal molecular pressure, this appears to be the case.

There are other factors which seem to contradict the conclusions of star formation in these clouds. Firstly, although infall does seem to be prevalent in these clouds, it can only be confirmed with any certainty for a very few of the clouds. If these clouds are truly star-forming, then infall should be found for a large majority of these clouds. In addition to this, the infall that has been found is of a small magnitude. Even the largest velocity excesses found in our sample are small compared to those found in normal Class 0 protostars (Mardones et al. 1997).

As well as this low infall rate, it has been found that the effect of the exterior IBL influence is, in fact, dissipative rather than acting to condense the discovered cores. The exterior pressure has the effect of increasing the virial mass of the cloud, thus making the cloud more stable against collapse, rather than causing it collapse as predicted in the RDI scenario. It should be noted that the pressurised virial mass has been calculated as if the external bounds the cloud uniformly, whereas any pressure that the IBL may exert upon a BRC is likely to be concentrated along a single axis. This situation may be analysed using dynamical modelling but is beyond the scope of this thesis.

The interpretation of the pressurised virial mass analysis must be approached with care, due to the large errors. However one interpretation of the (assumed real) large pressurised virial mass is that the clouds might be in their 'rebound' phase. The models of Lefloch & Lazareff (1994) show that the compression of the cloud through an exterior influence may in fact 'overshoot' and the cores may re-expand for a short time before collapsing again. If the clouds that we have observed are in fact at this point in their evolution then this would explain the slow infall rates and high pressurised virial masses. This re-expansion phase is expected to be of the same order as that of star formation itself, it is also expected to be oscillatory. Thus, the low infall rates and high pressurised virial masses are not necessarily contradictory to the triggered star formation scenario. However, if this oscillation is the cause then it is perhaps surprising that these factors are found in the vast majority of the clouds, rather than the sample being divided between those in a compression phase and those in a re-expansion phase.

The interpretation that the clouds are in a re-expansion phase may be supported by the low infall magnitudes that are seen. However, another scenario is possible. The infall rate is known to drop as stars progress from Class 0 to Class I protostars (Mardones et al. 1997). The ages of the sources in question must be determined accurately, to see if the lack of observed infall may be due to the sources being older than supposed.

7.2.2 Star Formation Time Scales

Once a cloud has reached equilbrium then it might be expected to have a reasonably long life time, despite being ionised and dispersed both from without and within. Of the 17 clouds which have enough available data for us to determine their pressure balance, 15 of them seem to be in pressure equilibrium with respect to their IBLs. Four clouds were found that seem unlikely to be in pressure equilibrium, SFO 4, SFO 25, SFO 36 and SFO 37. These clouds contain (possibly) protostellar cores, though unfortunately data is not sufficient to determine the presence, or otherwise, of an internal heating source in these clouds. SFO 4 is fairly dense ($\sim 5\times10^4$cm^{-3} (Jansen et al. 1994)) and the lack of observed star formation may be interpreted as supporting evidence of the RDI scenario. In this case, triggered star formation may not be expected to occur until the cloud has reached pressure equilibrium with its external IBL. The cloud is interpreted as still undergoing the propagation of photoionisation induced shocks into its interior. SFO 37 is expected to contain an embedded YSO (De Vries et al. 2002) and has previously been reported to contain an outflow (Duvert et al. 1990). Any present star formation is likely to have existed prior to the development of the cloud's IBL, though better quality observations are necessary in order to determine a better analysis of the pressure balance occuring in both this cloud and SFO 4.

SFO 25 and SFO 36 are found to have internal pressures greater than that of the IBLs impinging upon them, these clouds are therefore unlikely to have been affected by any interaction with the IBL. Any star formation that may be found within these clouds is therefore unlikely to be triggered by the propagation of photoionisation induced shocks. A notable aspect in our survey is the lack of type 'C' rims as defined by Sugitani et al. (1991). From the evolutionary model of triggered star formation that has been the most likely scenario put forward by this thesis, this phase should be the longest lived, however, only two examples exist in the entire northern SFO catalogue of 44 objects. This suggests a short lifetime for BRCs. The clouds appear to interact with the impinging ionisation front, rapidly form stars within them which, along with the continuing exterior ionisation, ionise and disperse the natal cloud on short timescales. Of course, this cannot be verified without a determined observational effort to identify more BRCs in the process of star formation.

The small infall velocities seen in the clouds have been suggested as being due to the sources approaching the Class I protostellar phase. This matter cannot be addressed without further observations in order to determine the exact stage of star formation within the cloud and the dynamical timescale of the ionisation front's effect.

7.3 Conclusions

Radio, optical and infrared observations of 44 BRCs have identified 25 molecular clouds from the northern SFO catalogue which have free-free emission emanating from their optically bright rims. The physical properties of the IBLs associated with this free-free emission have been determined, including the incident ionising fluxes, electron density and ionised gas pressures. Few BRCS have been studied in such detail previously and the analysis presented here has significantly increased the number of BRCs with known IBL conditions. The analysis presented in this thesis has been found to be consistent with previous observations.

The illuminating sources of the clouds in the northern hemisphere have been identified and the predicted fluxes of these stars falling upon the bright rims have been calculated. In a large number of cases these predicted fluxes are inconsistent with the radio emission measured at the rim. Negligible absorption between the star and rim has been assumed and this may be the cause of the inconsistency, though higher resolution studies are necessary to confirm the properties of the emission. Star-rim distances are not well known and these, along with illuminating stars' stellar type must be further explored as a source of error. In addition the contribution of, as yet unidentified, stars to the ionisation of the rims must be determined, if only to rule out this possibility.

A sample of SCUBA sources within BRCs has been observed, this survey found SCUBA cores in a large number of the sample that were generally consistent with the positions of the IRAS sources identified in the original survey of Sugitani et al. (1991). The high resolution of the SCUBA observations in comparison to the original IRAS survey has revealed the presence of multiple cores in some cases. Five of the clouds show the presence of more than one submillimetre core, though higher resolution studies are needed to separate the flux from the different sources and identify the multiplicity of cores in other clouds that may have been unresolvable.

The submillimetre emission has been compared to emission in the optical, infrared and radio regimes in order to determine the morphology and possible nature of the emission. The morphology of the clouds is, in general, supportive of the scenario proposed by RDI models; a dense core at the head of an elongated column. There was found to be variation in the extent of the column as well as the curvature of the rim itself, though the direction of the elongation of the column was invariably consistent with the direction of the suspected ionising source(s).

Star formation within the clouds is indicated by the physical properties of the clouds as determined from the SCUBA observations. The dust temperatures found within the clouds are high compared to starless cores, indicating the presence of an internal heating source. We have found high masses and densities within the clouds. These masses have been found to exceed that of other known submillimetre sources and at a higher rate than that predicted by the Salpeter slope.

The association of mid-infrared sources within the cloud sample is suggestive that the clouds are themselves star-forming, examination of the sources in the surrounding area are necessary to estimate the likelihood that the infrared sources are truly associated with the clouds and not a chance superposition. The internal heating sources of the clouds have been specified with a spectral type, making the assumption that all of the luminosity arising from the cloud is due to the internal heating source. These internal sources were high in mass and luminosity with the majority of the sources being Type O or B stars. The timescale for OB stars to form is relatively short, they quickly ionise their local surroundings and emerge from their natal cloud. The ages of the stars associated with the cloud, do not contradict the possibility that these stars have previously been formed as a result of the ionisation of the cloud when compared to the timescale required for the ionisation front to reach the regions of the bright optical rims and the shock crossing times of the clouds. Small pressure gradients were found through analysing the free-free emission from the bright rims and comparing it to the internal molecular pressures of the clouds as found through CO observations. These small pressure gradients indicate that the clouds have undergone the process of being shocked and thus the ionisation front has been present for a significant period. Thus any existing stars in the region are likely to have been caused by the propagation of photoionisation induced shocks.

The observations of molecular lines in the clouds have supported the presence of star-forming regions. The physical properties that have been derived from the observations are consistent with those found from the submillimetre observations presented in chapter 5 which again, show high mass regions which are expected to be forming high mass stars. Molecular outflow was detected (or previously known) in a large proportion of the sample, which indicates the early stages of star formation and is consistent with the classification of these sources as Class 0 protostars. Infall was detected in 25% of the sources, though this is of a small magnitude in comparison to other protostellar sources, e.g. those of Mardones et al. (1997). The small magnitude of the infall may be due to a number of reasons, primarily, it is possible that the cloud is in a 're-expansion' phase as suggested by the models of Lefloch & Lazareff (1994), this is supported by the low pressurised virial masses of the clouds. On the other hand, the cores that are thought to be star-forming Class 0 objects may in fact be even older and may be at the end of their infall stage. This is an unlikely scenario, although it cannot be ruled out.

7.4 Further Work

Higher resolution studies of these clouds are necessary at a multitude of wavelengths for many reasons. The radio continuum observations presented here have led to some interesting results for the IBLs of BRCs, however, they have suggested many more questions. The inconsistency of the predicted fluxes from the identified stars with that measured in the NVSS snapshots is presently unexplained. Higher resolution studies may improve the accuracy of this emission calculation, especially if some of the emission is, in fact, associated with an embedded star within the cloud. At higher resolution the morphology of the cloud in terms of its radio emission, especially when compared to submillimetre emission, should show the interaction between the ionisation front at the rim of the cloud in far greater detail than is presently possible using the NVSS. Higher resolution studies of these clouds may reveal the presence of UCHII regions which are definite indicators of star formation. If the clouds are at the very earliest stages of star formation, as suspected, then a 7 millimetre study at high resolution may reveal the presence of Hyper-Compact HII (HCHII) regions which are of order 0.01 pc in size with electron densities $\sim 10^5$ cm^{-3}, ten times smaller and a hundred times denser than UCHII regions. HCHII regions are thought to trace the very first stages of a young star beginning to ionise its surroundings.

Higher resolution studies of the clouds in the submillimetre regime would help to separate multiple cores within the clouds and determine the probability that *clusters* are being formed within these clouds. Also, the properties of the dust emission and delineating the emission from separate regions of dust and gas, may be achieved in this way. $\sim$ arcsecond resolution is possible at millimetre wavelengths using the IRAM Plateau De Bure interferometer. Similar resolution is also achievable at below millimetre wavelengths using the Submillimetre Array in Hawaii. These instruments indicate the move toward interferometry that is necessary for detailed study of these regions. The introduction of the ALMA array in Chile in around 2010 will revolutionise the possibilities of submillimetre astronomy.

Molecular line transitions can tell us much about these clouds. The observations presented here are single pointing, intermediate resolution studies. Mapping of our sources at high resolution using various molecular species will reveal the answers to many questions about these clouds. Ammonia has already been observed in the northern clouds of this survey (Morgan 2005, in prep.) using similar resolution, single pointing spectra. The results support the presence of dense star-forming regions and, at the present stage, seem to support the observations presented here. Ammonia traces old, dense regions of molecular clouds, while CCS is a tracer of chemical youth in star forming clouds, and by mapping the two species at high resolution towards the clouds we should be able to determine any gradient of evolution as might be expected in the RDI scenario.

Shock tracers within the clouds, studied at high resolution, may allow a determination of the timescale over which the clouds have been being ionised. The location and intensities of these shock tracers, when mapped, will inform upon the exact effect of the ionisation front. A search for masers associated with the clouds in our survey would allow us to both definitively associate the clouds with star formation as well as age them. Different types of maser are associated with different ages of star formation (though there is no hard definition of which regions may be associated with which type of maser). Generally speaking methanol masers trace the earliest stages of star formation (e.g. Mcdonald & Alvey (2002); Pestalozzi et al. (2003); Pestalozzi (2004); Minier et al. (2005)). SiO and H_2O masers are associated with outflows and accretion (e.g. Patel et al. (2001); Seth et al. (2002); Gallimore et al. (2003); Imai et al. (2004)), the intermediary stages of star formation, while OH masers are found at the edges of UCHII regions, once stars have ignited and are actually starting to ionised their surroundings (e.g. Baudry & Diamond (1991); Rovenskaya (1994); Wyrowski et al. (1997); Desmurs & Baudry (1998)).

Large scale surveys are underway to fully explore the role of massive star formation in the Galaxy. The Reddened MSX Survey (RMS) currently underway at Leeds University is examining over 2000 sites of Galactic star formation. The RMS will cover every known Galactic high-mass star formation region using radio and infrared emission. The survey will include CO spectra and maser searches for every object. The properties of BRCs can no longer be defined through studies of single objects. Even as a collection of objects the SFO catalogue does not treat the role of a massive star upon its surroundings in terms of the region in which it is set. Whole complexes of molecular gas must be studied in order to determine the effects of triggered star formation at all scales. A project is underway by the author to fully analyse specific HII regions for signs of triggered star formation in these regions as a whole.

7.4.1 Modelling

The models of triggered star formation regions that have been used as a template for the scenario investigated in this thesis need to be updated. Any modelling of star formation is usually widely contested, the sheer range of physical parameters is so large that it is often felt no model can accurately incorporate all of the processes involved. It is evident here that the inclusion of heating by internal sources is necessary for the accurate modelling of these clouds. The issue of turbulence is currently the focus of many models and hopefully the successful outcome will be a fully descriptive analytical model of the process of star formation. However, at present, important factors such as the influence of the new star upon its surroundings and magnetic fields are not included in most models. Until all processes are adequately accounted for then many questions will remain in star formation, which the observational data currently available are simply unable to answer.

Appendix A

Images

A.1 Description Of Plots And Images

Data for all of the SFO clouds are presented in the following pages, spectral lines are presented with corrected antenna temperature, T_A^*, plotted against doppler shifted velocity, V_{LSR}. Where more than one line has been observed these lines are plotted on the same axes with zero temperature baselines drawn. The species are labelled along with any factor that it may have been necessary to multiply the line by for clarity.

NVSS 20 cm contours are overlaid upon DSS images with arrows pointing in the direction of ionising source(s), the arrows are based at the coordinates of the IRAS source catalogued in Sugitani et al. (1991). NVSS contours start at 3σ and increase in increments of 20% of the peak flux value. The NVSS beam size is $45''$at FWHM.

MSX 8.3 μm contours are also overlaid on DSS images. The MSX images were smoothed to the same resolution as the NVSS images ($45''$). MSX contours start at 3σ and increase in increments of 20% of the peak flux value, unless otherwise stated.

SCUBA 850 μm contours are overlaid on DSS images. Contours start at 3σ and increase in increments of 20% of the peak flux value unless otherwise stated. Infrared sources from the 2MASS Point Source Catalogue (Cutri et al. 2003) are shown as triangles.

J-H versus H-K_s colours of the 2MASS sources associated with each cloud are plotted along with a figure of the SED plot of the object composed from a best fit to various observed fluxes where possible. J-H versus H-K_s colour diagrams have solid lines representing the unreddened loci of main sequence and giant stars from Koornneef (1983). Dotted lines represent the classical T-Tauri locus of Meyer et al. (1997). Reddening tracks are shown by dashed lines.

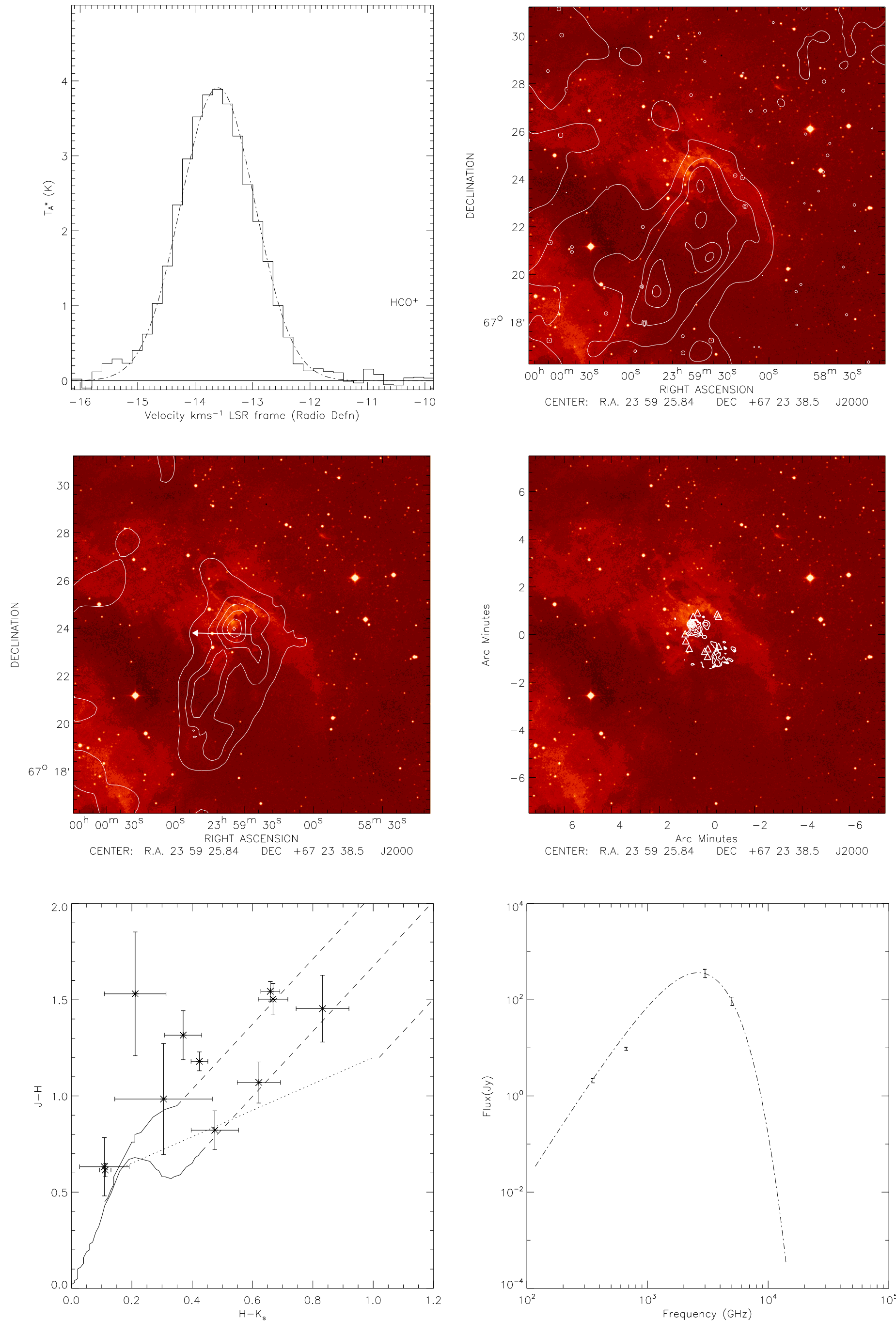

Figure 27: Plots and images associated with the object SFO 1. In the top left is a representation of all spectra observed for this object. The top right image shows MSX 8.3 μm emission contours overlaid on a DSS image. The centre left image is of NVSS 20 cm emission contours overlaid on a DSS image. Arrows show the direction of the ionising source(s). The centre right image shows SCUBA 850 μm contours overlaid on a DSS image, infrared sources from the 2MASS Point Source Catalogue (Cutri et al. 2003) are shown as triangles. The bottom left plot shows the J-H versus H-K$_s$ colours of the 2MASS sources associated with the cloud while the bottom right image shows the SED plot of the object composed from a best fit to various observed fluxes. Peak and r.m.s. flux levels are as follows, MSX peak = 67.1 10^5 W m^{-2} sr^{-1}, MSX 3σ = 2.12 10^5 W m^{-2} sr^{-1}. NVSS peak = 69.2 mJy beam^{-1}, NVSS 3σ = 2.78 mJy beam^{-1}. SCUBA peak = 0.68 Jy beam^{-1}, SCUBA 3σ = 0.21 Jy beam^{-1}.

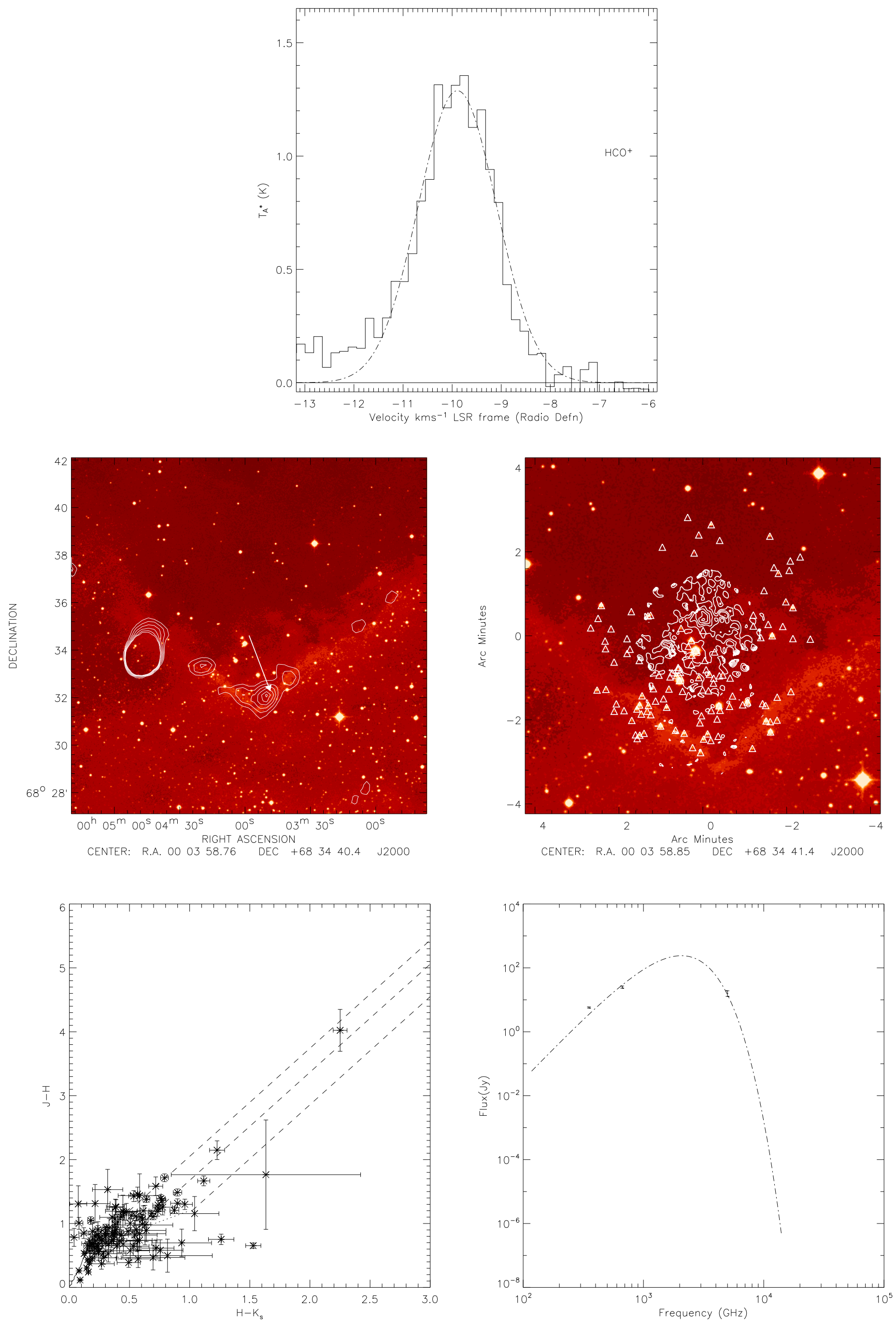

Figure 27: Plots and images associated with the object SFO 2. At the top is a representation of all spectra observed for this object. The centre left image is of NVSS 20 cm emission contours overlaid on a DSS image. Arrows show the direction of the ionising source(s). The centre right image shows SCUBA 850 μm contours overlaid on a DSS image, infrared sources from the 2MASS Point Source Catalogue (Cutri et al. 2003) are shown as triangles. The bottom left plot shows the J-H versus H-K$_s$ colours of the 2MASS sources associated with the cloud while the bottom right image shows the SED plot of the object composed from a best fit to various observed fluxes. Peak and r.m.s. flux levels are as follows, NVSS peak = 4.40 mJy beam^{-1}, NVSS 3σ = 1.81 mJy beam^{-1}. SCUBA peak = 0.66 Jy beam^{-1}, SCUBA 3σ = 0.08 Jy beam^{-1}.

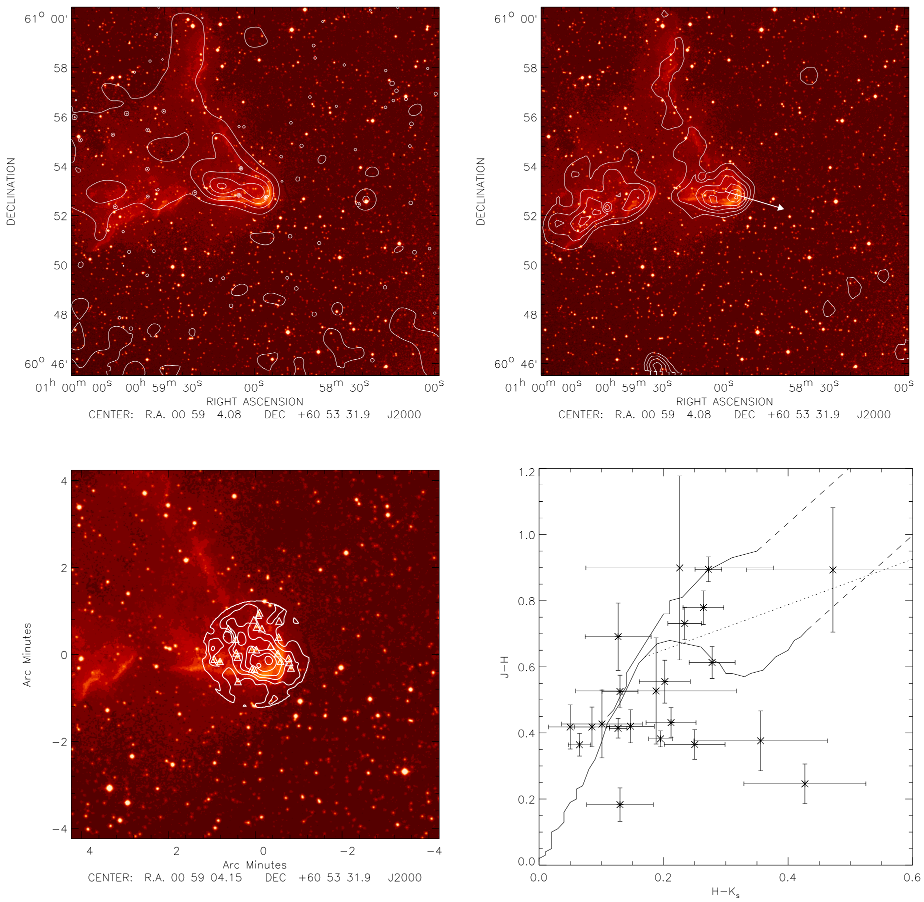

Figure 27: Plots and images associated with the object SFO 4. The top left image shows MSX 8.3 μm emission contours overlaid on a DSS image. The top right image is of NVSS 20 cm emission contours overlaid on a DSS image. Arrows show the direction of the ionising source(s). The bottom left image shows SCUBA 850 μm contours overlaid on a DSS image, infrared sources from the 2MASS Point Source Catalogue (Cutri et al. 2003) are shown as triangles. The bottom right plot shows the J-H versus H-K$_s$ colours of the 2MASS sources associated with the cloud. Peak and r.m.s. flux levels are as follows, MSX peak = 16.3 10^5 W m^{-2} sr^{-1}, MSX 3σ = 1.43 10^5 W m^{-2} sr^{-1}. NVSS peak = 5.35 mJy beam^{-1}, NVSS 3σ = 1.24 mJy beam^{-1}. SCUBA peak = 0.20 Jy beam^{-1}, SCUBA 3σ = 0.06 Jy beam^{-1}.

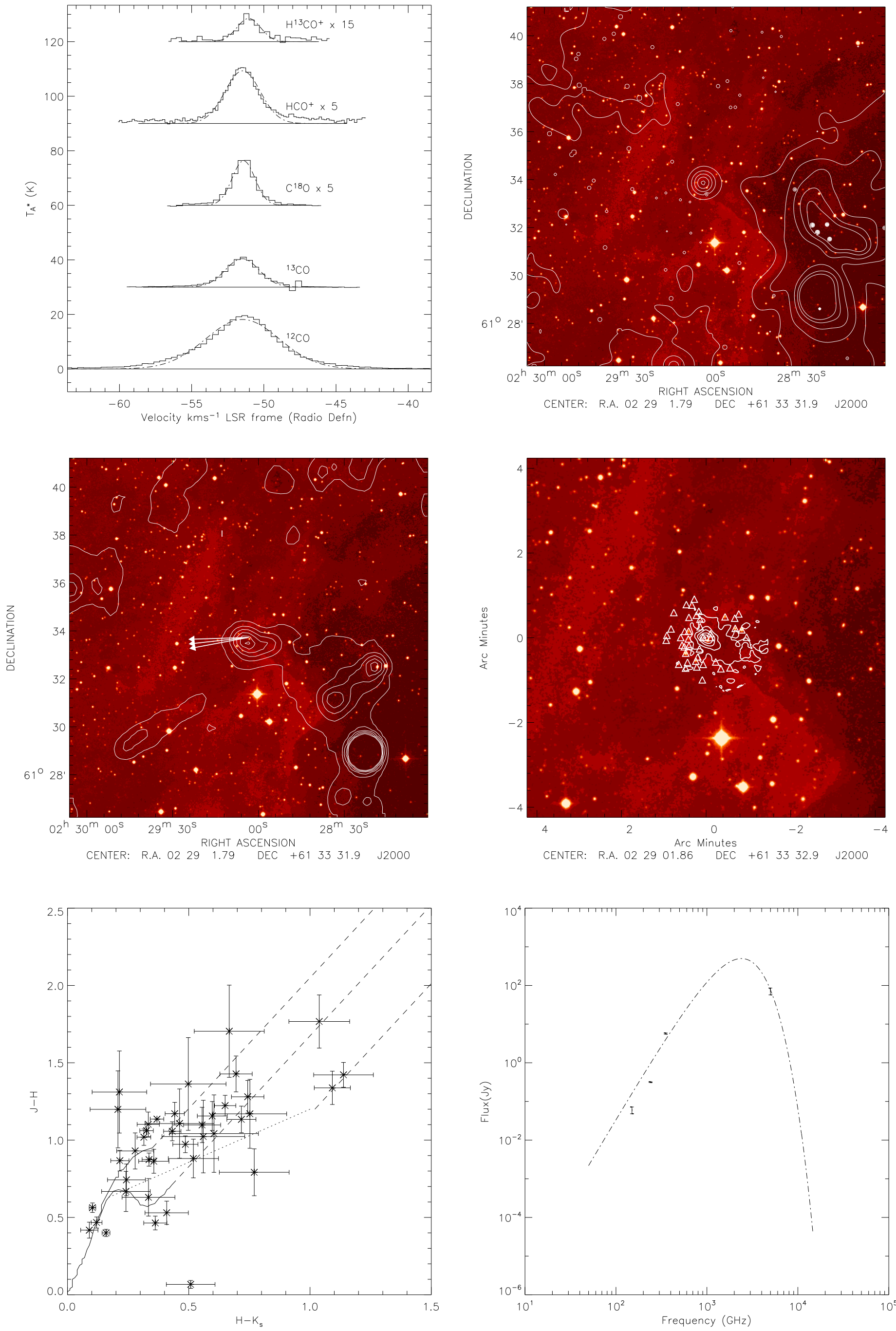

Figure 27: Plots and images associated with the object SFO 5. In the top left is a representation of all spectra observed for this object. The top right image shows MSX 8.3 μm emission contours overlaid on a DSS image. The centre left image is of NVSS 20 cm emission contours overlaid on a DSS image. Arrows show the direction of the ionising source(s). The centre right image shows SCUBA 850 μm contours overlaid on a DSS image, infrared sources from the 2MASS Point Source Catalogue (Cutri et al. 2003) are shown as triangles. The bottom left plot shows the J-H versus H-K$_s$ colours of the 2MASS sources associated with the cloud while the bottom right image shows the SED plot of the object composed from a best fit to various observed fluxes. Peak and r.m.s. flux levels are as follows, MSX peak = 54.8 10^5 W m^{-2} sr^{-1}, MSX 3σ = 3.32 10^5 W m^{-2} sr^{-1}. NVSS peak = 11.50 mJy beam^{-1}, NVSS 3σ = 1.11 mJy beam^{-1}. SCUBA peak = 1.31 Jy beam^{-1}, SCUBA 3σ = 0.15 Jy beam^{-1}.

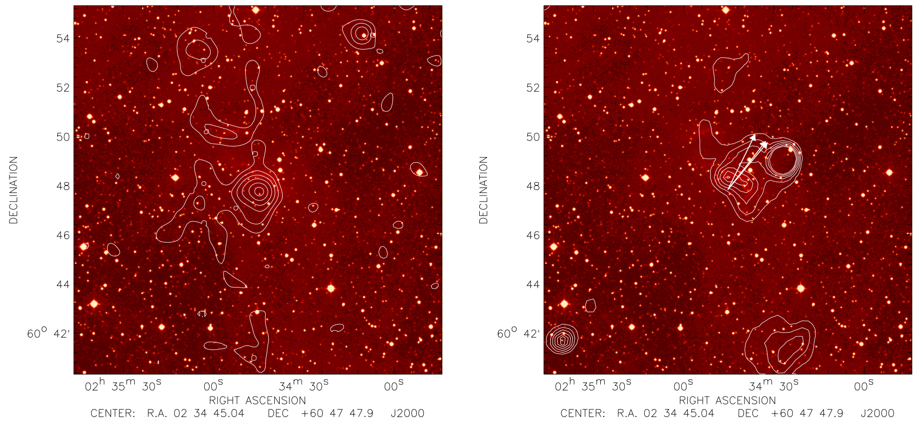

Figure 27: Plots and images associated with the object SFO 6. The left image shows MSX 8.3 μm emission contours overlaid on a DSS image and the right image is of NVSS 20 cm emission contours overlaid on a DSS image. Arrows show the direction of the ionising source(s). MSX contours start at 6σ for clarity. Peak and r.m.s. flux levels are as follows, MSX peak = 6.9 10^5 W m^{-2} sr^{-1}, MSX 3σ = 2.91 10^5 W m^{-2} sr^{-1}. NVSS peak = 4.59 mJy beam^{-1}, NVSS 3σ = 1.22 mJy beam^{-1}.

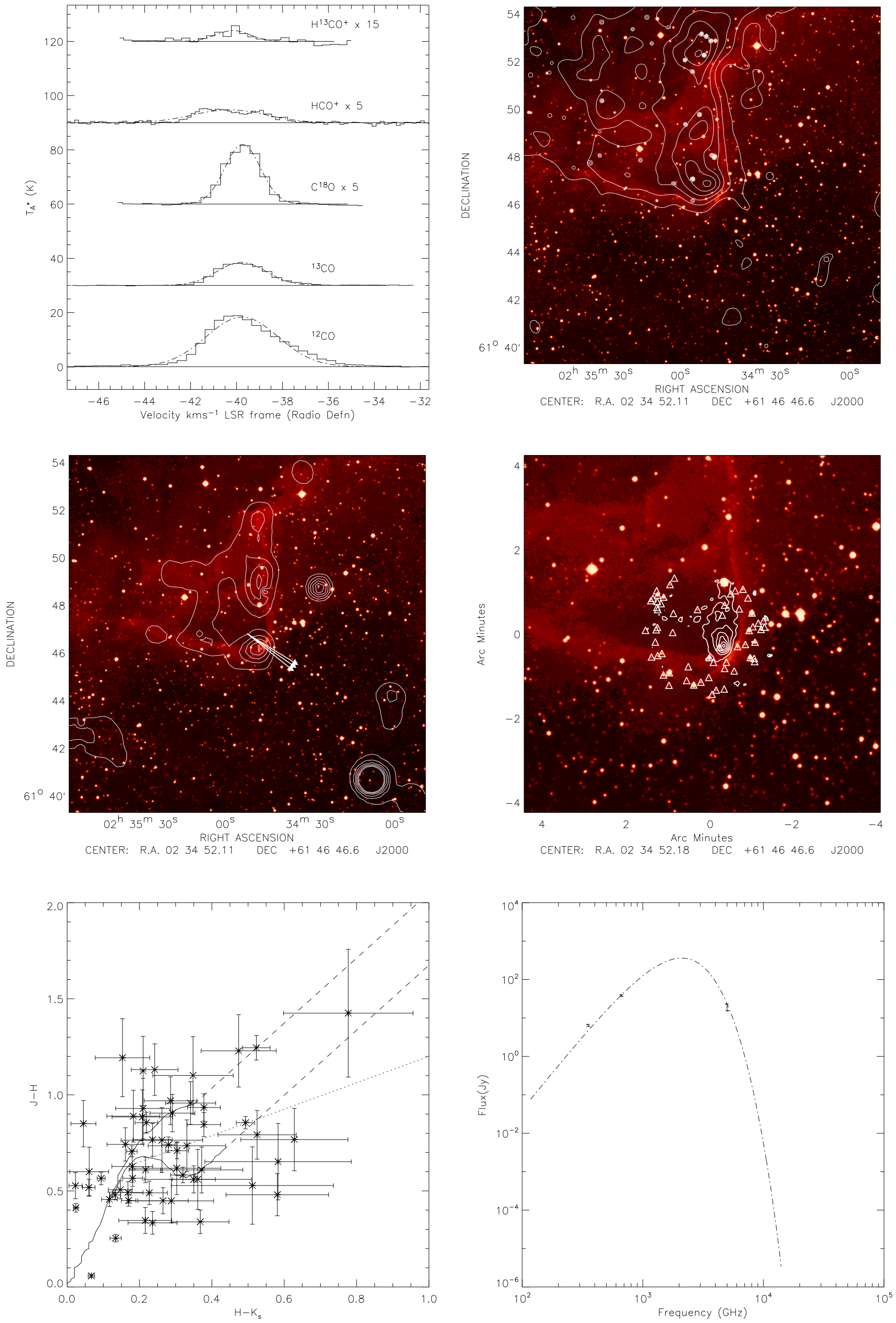

Figure 27: Plots and images associated with the object SFO 7. In the top left is a representation of all spectra observed for this object. The top right image shows MSX 8.3 μm emission contours overlaid on a DSS image. The centre left image is of NVSS 20 cm emission contours overlaid on a DSS image. Arrows show the direction of the ionising source(s). The centre right image shows SCUBA 850 μm contours overlaid on a DSS image, infrared sources from the 2MASS Point Source Catalogue (Cutri et al. 2003) are shown as triangles. The bottom left plot shows the J-H versus H-K$_s$ colours of the 2MASS sources associated with the cloud while the bottom right image shows the SED plot of the object composed from a best fit to various observed fluxes. MSX contours start at 6σ for clarity. Peak and r.m.s. flux levels are as follows, MSX peak = 13.3 10^5 W m^{-2} sr^{-1}, MSX 3σ = 2.96 10^5 W m^{-2} sr^{-1}. NVSS peak = 11.68 mJy beam^{-1}, NVSS 3σ = 1.86 mJy beam^{-1}. SCUBA peak = 1.18 Jy beam^{-1}, SCUBA 3σ = 0.22 Jy beam^{-1}.

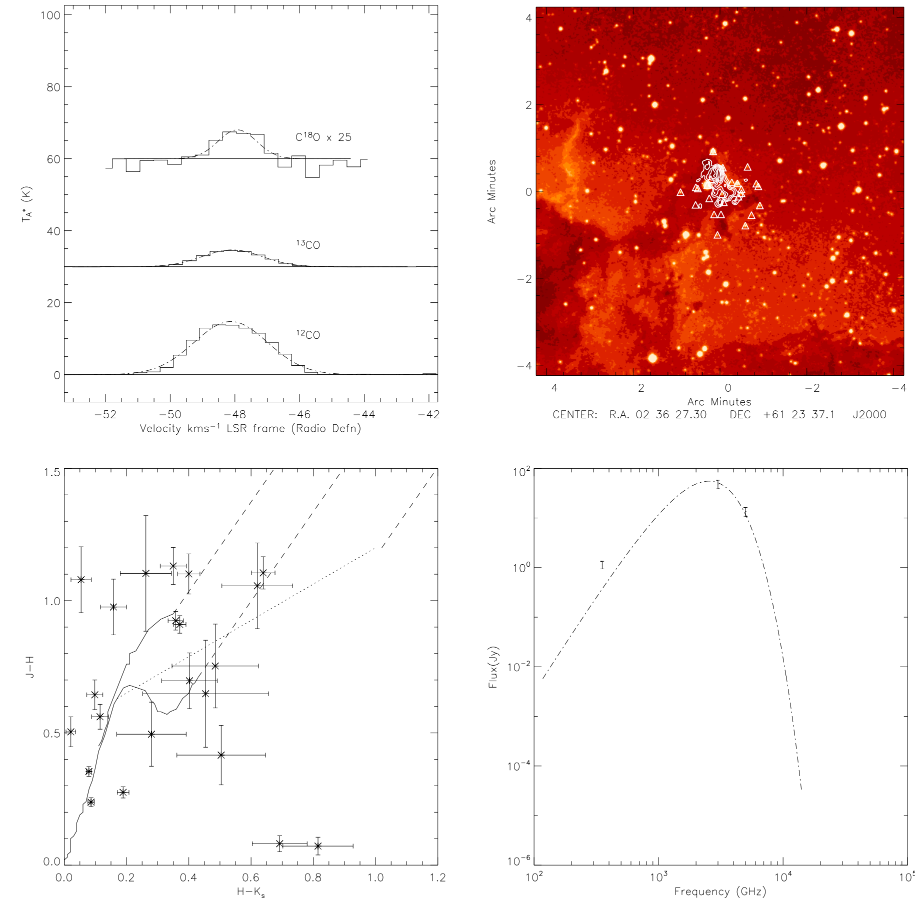

Figure 27: Plots and images associated with the object SFO 9. In the top left is a representation of all spectra observed for this object. The top right image shows SCUBA 850 μm contours overlaid on a DSS image, infrared sources from the 2MASS Point Source Catalogue (Cutri et al. 2003) are shown as triangles. The bottom left plot shows the J-H versus H-K$_s$ colours of the 2MASS sources associated with the cloud while the bottom right image shows the SED plot of the object composed from a best fit to various observed fluxes. Peak and r.m.s. flux levels are as follows, SCUBA peak = 0.17 Jy beam^{-1}, SCUBA 3σ = 0.08 Jy beam^{-1}.

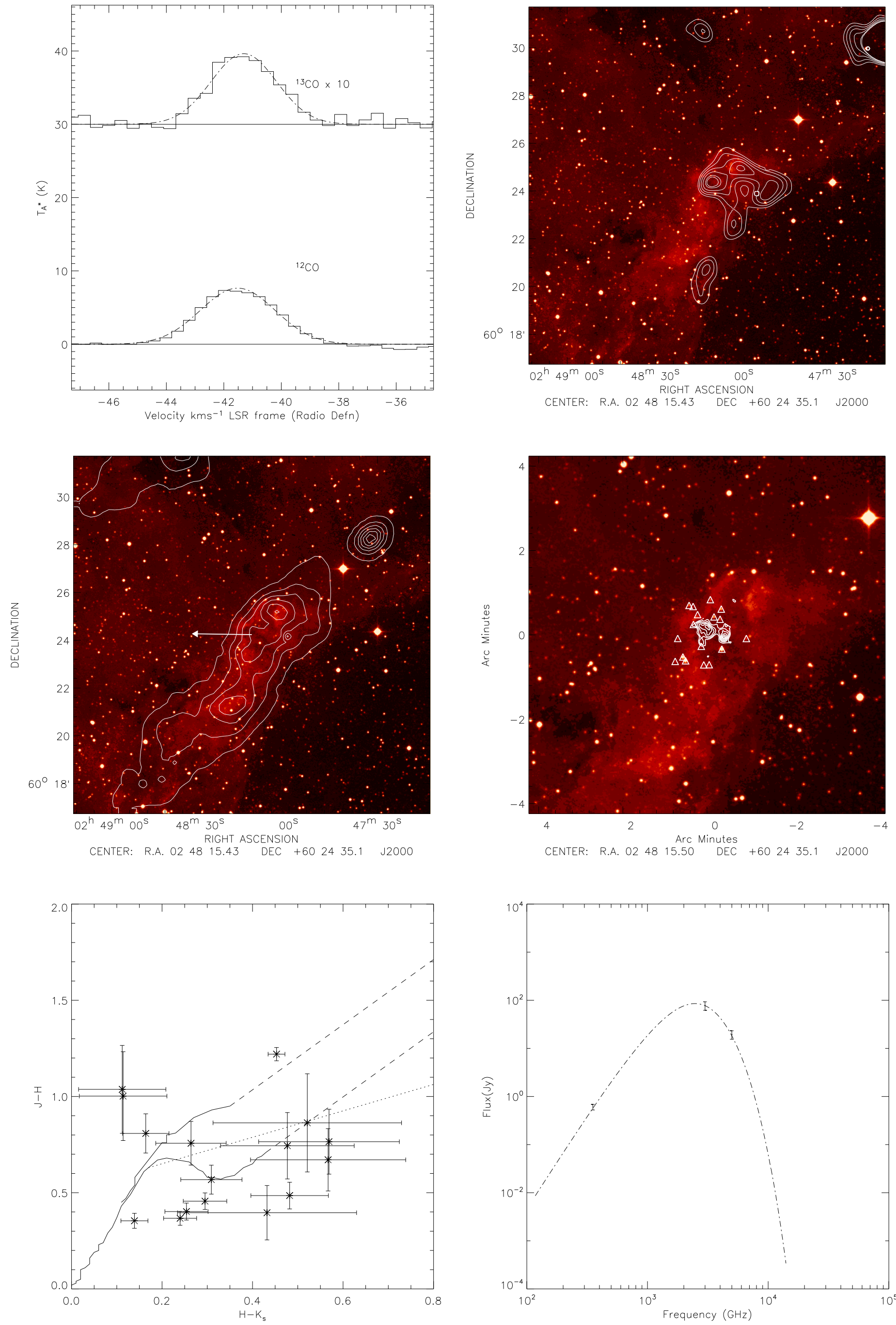

Figure 27: Plots and images associated with the object SFO 10. In the top left is a representation of all spectra observed for this object. The top right image shows MSX 8.3 μm emission contours overlaid on a DSS image. The centre left image is of NVSS 20 cm emission contours overlaid on a DSS image. Arrows show the direction of the ionising source(s). The centre right image shows SCUBA 850 μm contours overlaid on a DSS image, infrared sources from the 2MASS Point Source Catalogue (Cutri et al. 2003) are shown as triangles. The bottom left plot shows the J-H versus H-K$_s$ colours of the 2MASS sources associated with the cloud while the bottom right image shows the SED plot of the object composed from a best fit to various observed fluxes. MSX contours start at 9σ for clarity. Peak and r.m.s. flux levels are as follows, MSX peak = 12.3 10^5 W m^{-2} sr^{-1}, MSX 3σ = 9.25 10^5 W m^{-2} sr^{-1}. NVSS peak = 30.73 mJy beam^{-1}, NVSS 3σ = 2.12 mJy beam^{-1}. SCUBA peak = 0.16 Jy beam^{-1}, SCUBA 3σ = 0.07 Jy beam^{-1}.

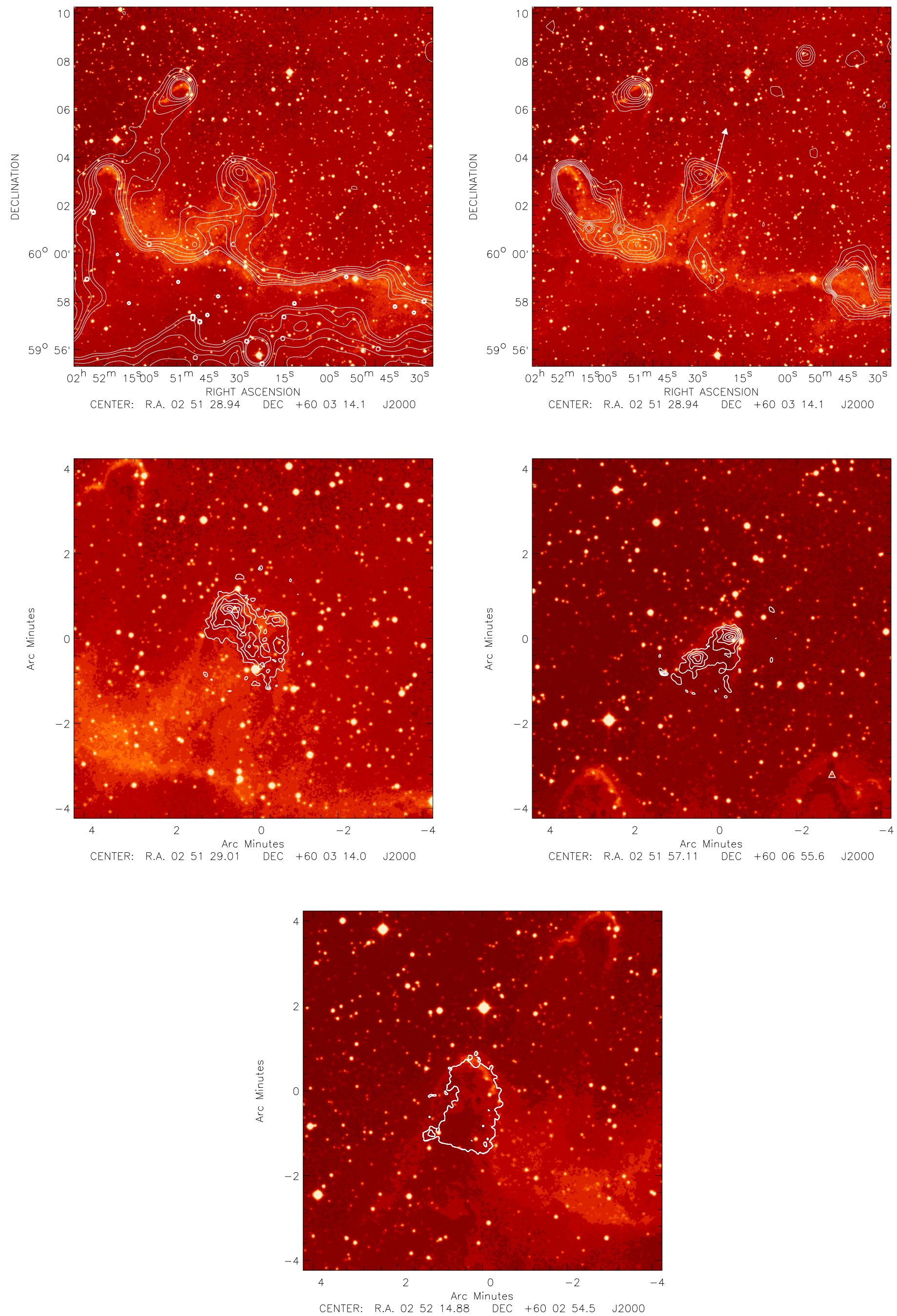

Figure 27: Plots and images associated with the object SFO 11. The top left image shows MSX 8.3 μm emission contours overlaid on a DSS image. The top right image is of NVSS 20 cm emission contours overlaid on a DSS image. Arrows show the direction of the ionising source(s). The centre left, centre right, and bottom images show SCUBA 850 μm contours overlaid on DSS images of the three separate clumps associated with SFO 11, 11, 11NE and 11E respectively. Infrared sources from the 2MASS Point Source Catalogue (Cutri et al. 2003) are shown as triangles. MSX contours start at 9σ for clarity. Peak and r.m.s. flux levels are as follows, MSX peak = 5.8 10^5 W m^{-2} sr^{-1}, MSX 3σ = 2.93 10^5 W m^{-2} sr^{-1}. NVSS peak = 4.01 mJy beam^{-1}, NVSS 3σ = 1.29 mJy beam^{-1}. SCUBA peak (11) = 0.23 Jy beam^{-1}, SCUBA 3σ (11) = 0.04 Jy beam^{-1}, SCUBA peak (11NE) = 0.34 Jy beam^{-1}, SCUBA 3σ (11NE) = 0.06 Jy beam^{-1}, SCUBA peak (11E) = 0.48 Jy beam^{-1}, SCUBA 3σ (11E) = 0.05 Jy beam^{-1}.

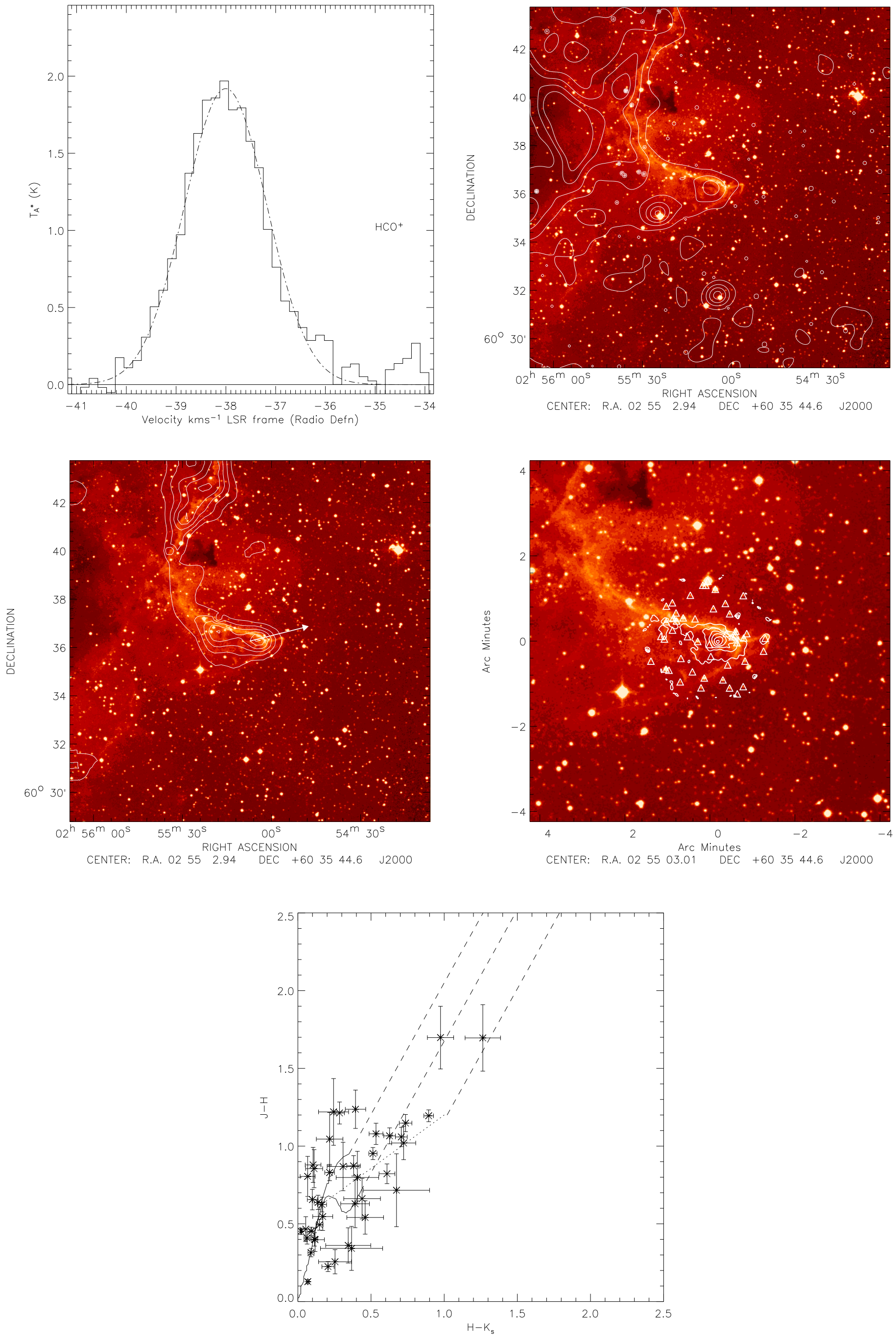

Figure 27: Plots and images associated with the object SFO 12. In the top left is a representation of all spectra observed for this object. The top right image shows MSX 8.3 μm emission contours overlaid on a DSS image. The centre left image is of NVSS 20 cm emission contours overlaid on a DSS image. Arrows show the direction of the ionising source(s). The centre right image shows SCUBA 850 μm contours overlaid on a DSS image, infrared sources from the 2MASS Point Source Catalogue (Cutri et al. 2003) are shown as triangles. The bottom plot shows the J-H versus H-K$_s$ colours of the 2MASS sources associated with the cloud. Peak and r.m.s. flux levels are as follows, MSX peak = 14.1 10^5 W m^{-2} sr^{-1}, MSX 3σ = 1.71 10^5 W m^{-2} sr^{-1}. NVSS peak = 12.01 mJy beam^{-1}, NVSS 3σ = 1.79 mJy beam^{-1}. SCUBA peak = 0.62 Jy beam^{-1}, SCUBA 3σ = 0.08 Jy beam^{-1}.

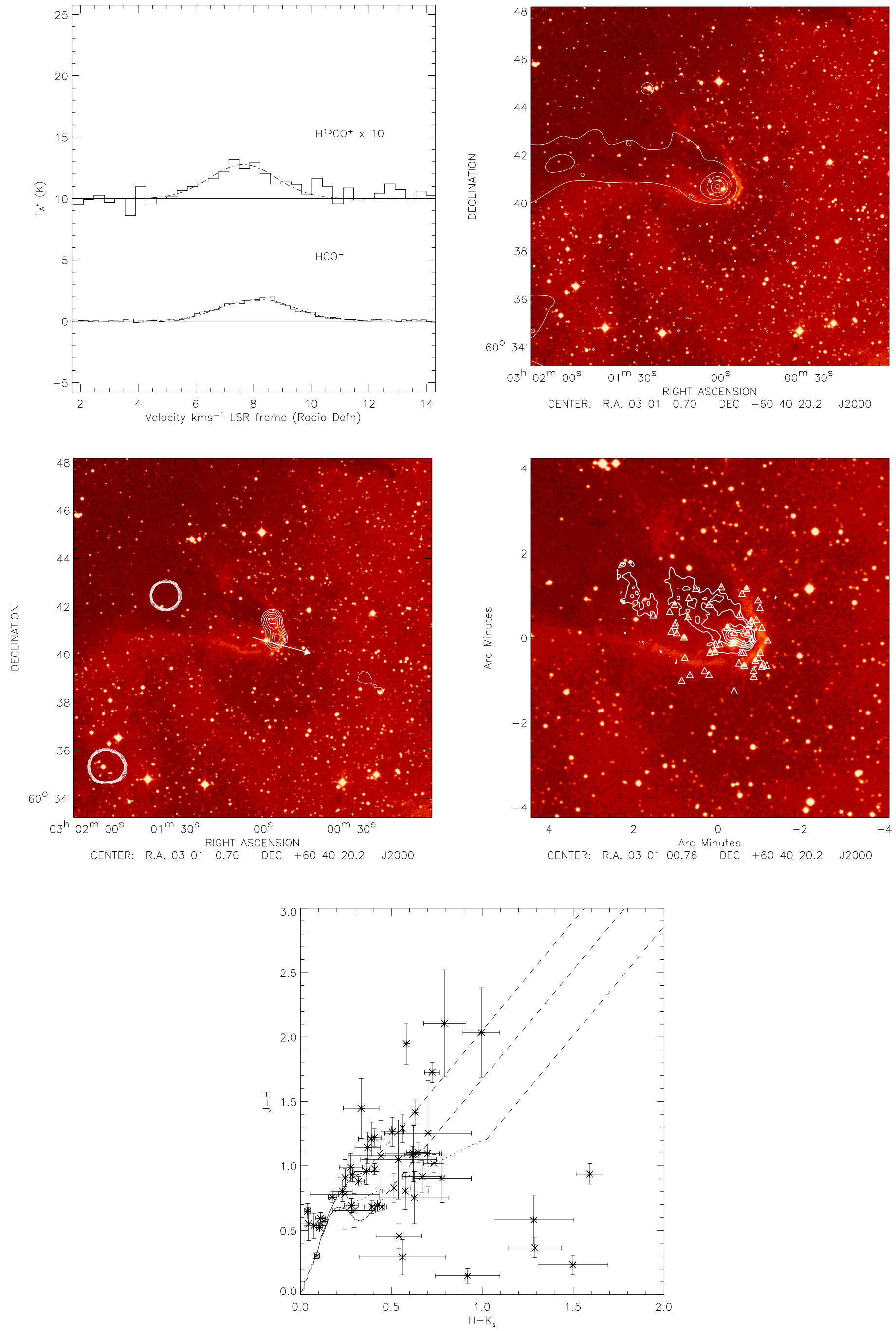

Figure 27: Plots and images associated with the object SFO 13. In the top left is a representation of all spectra observed for this object. The top right image shows MSX 8.3 μm emission contours overlaid on a DSS image. The centre left image is of NVSS 20 cm emission contours overlaid on a DSS image. Arrows show the direction of the ionising source(s). The centre right image shows SCUBA 850 μm contours overlaid on a DSS image, infrared sources from the 2MASS Point Source Catalogue (Cutri et al. 2003) are shown as triangles. The bottom plot shows the J-H versus H-K$_s$ colours of the 2MASS sources associated with the cloud. Peak and r.m.s. flux levels are as follows, MSX peak = 37.8 10^5 W m^{-2} sr^{-1}, MSX 3σ = 1.17 10^5 W m^{-2} sr^{-1}. NVSS peak = 3.75 mJy beam^{-1}, NVSS 3σ = 2.16 mJy beam^{-1}. SCUBA peak = 0.49 Jy beam^{-1}, SCUBA 3σ = 0.12 Jy beam^{-1}.

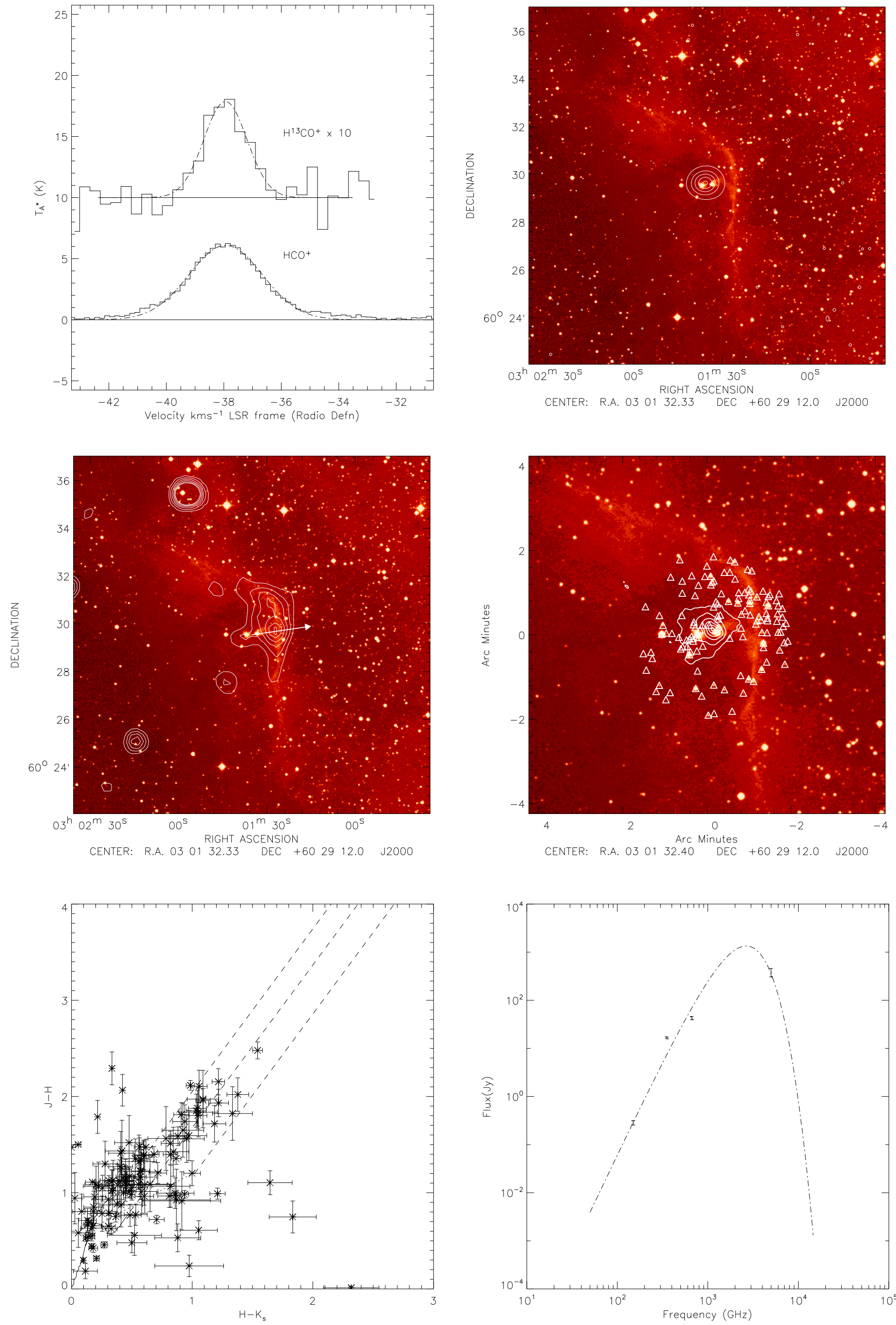

Figure 27: Plots and images associated with the object SFO 14. In the top left is a representation of all spectra observed for this object. The top right image shows MSX 8.3 μm emission contours overlaid on a DSS image. The centre left image is of NVSS 20 cm emission contours overlaid on a DSS image. Arrows show the direction of the ionising source(s). The centre right image shows SCUBA 850 μm contours overlaid on a DSS image, infrared sources from the 2MASS Point Source Catalogue (Cutri et al. 2003) are shown as triangles. The bottom left plot shows the J-H versus H-K$_s$ colours of the 2MASS sources associated with the cloud while the bottom right image shows the SED plot of the object composed from a best fit to various observed fluxes. Peak and r.m.s. flux levels are as follows, MSX peak = 155.3 10^5 W m^{-2} sr^{-1}, MSX 3σ = 1.45 10^5 W m^{-2} sr^{-1}. NVSS peak = 8.13 mJy beam^{-1}, NVSS 3σ = 2.02 mJy beam^{-1}. SCUBA peak = 2.38 Jy beam^{-1}, SCUBA 3σ = 0.34 Jy beam^{-1}.

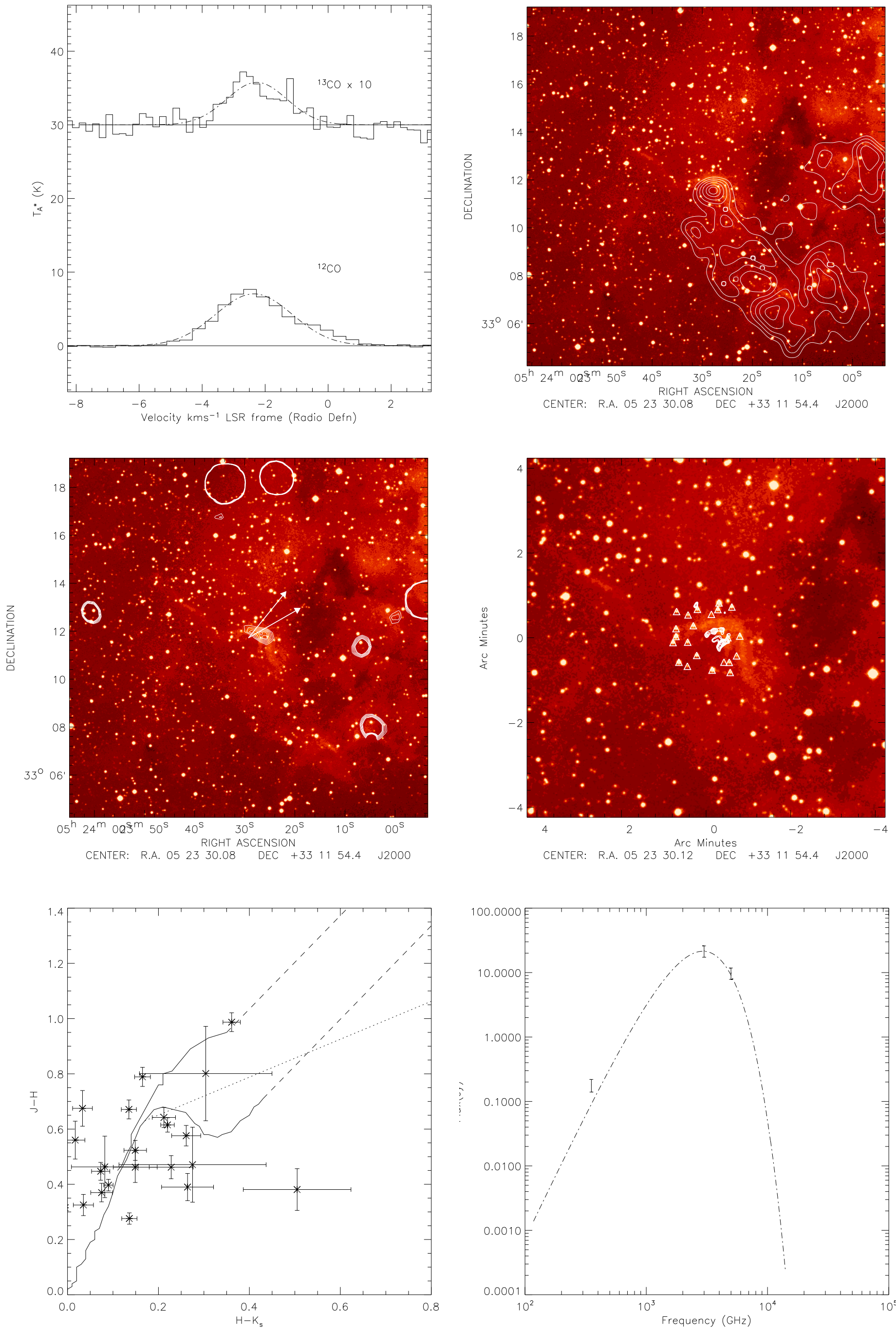

Figure 27: Plots and images associated with the object SFO 15. In the top left is a representation of all spectra observed for this object. The top right image shows MSX 8.3 μm emission contours overlaid on a DSS image. The centre left image is of NVSS 20 cm emission contours overlaid on a DSS image. Arrows show the direction of the ionising source(s). The centre right image shows SCUBA 850 μm contours overlaid on a DSS image, infrared sources from the 2MASS Point Source Catalogue (Cutri et al. 2003) are shown as triangles. The bottom left plot shows the J-H versus H-K$_s$ colours of the 2MASS sources associated with the cloud while the bottom right image shows the SED plot of the object composed from a best fit to various observed fluxes. MSX contours start at 12σ for clarity. Peak and r.m.s. flux levels are as follows, MSX peak = 6.7 10^5 W m^{-2} sr^{-1}, MSX 3σ = 4.12 10^5 W m^{-2} sr^{-1}. NVSS peak = 3.30 mJy beam^{-1}, NVSS 3σ = 2.34 mJy beam^{-1}. SCUBA peak = 0.09 Jy beam^{-1}, SCUBA 3σ = 0.05 Jy beam^{-1}.

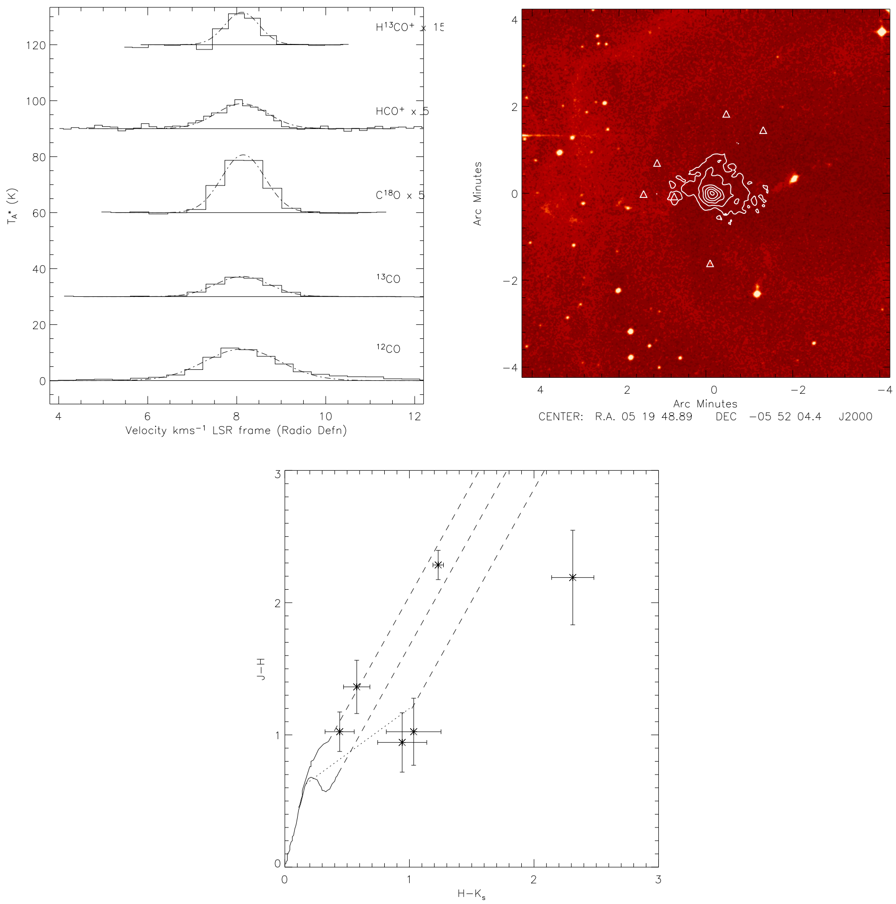

Figure 27: Plots and images associated with the object SFO 16. On the top left is a representation of all spectra observed for this object. The top right image shows SCUBA 850 μm contours overlaid on a DSS image, infrared sources from the 2MASS Point Source Catalogue (Cutri et al. 2003) are shown as triangles. The plot on the bottom shows the J-H versus H-K$_s$ colours of the 2MASS sources associated with the cloud. Peak and r.m.s. flux levels are as follows, SCUBA peak = 0.65 Jy beam^{-1}, SCUBA 3σ = 0.15 Jy beam^{-1}.

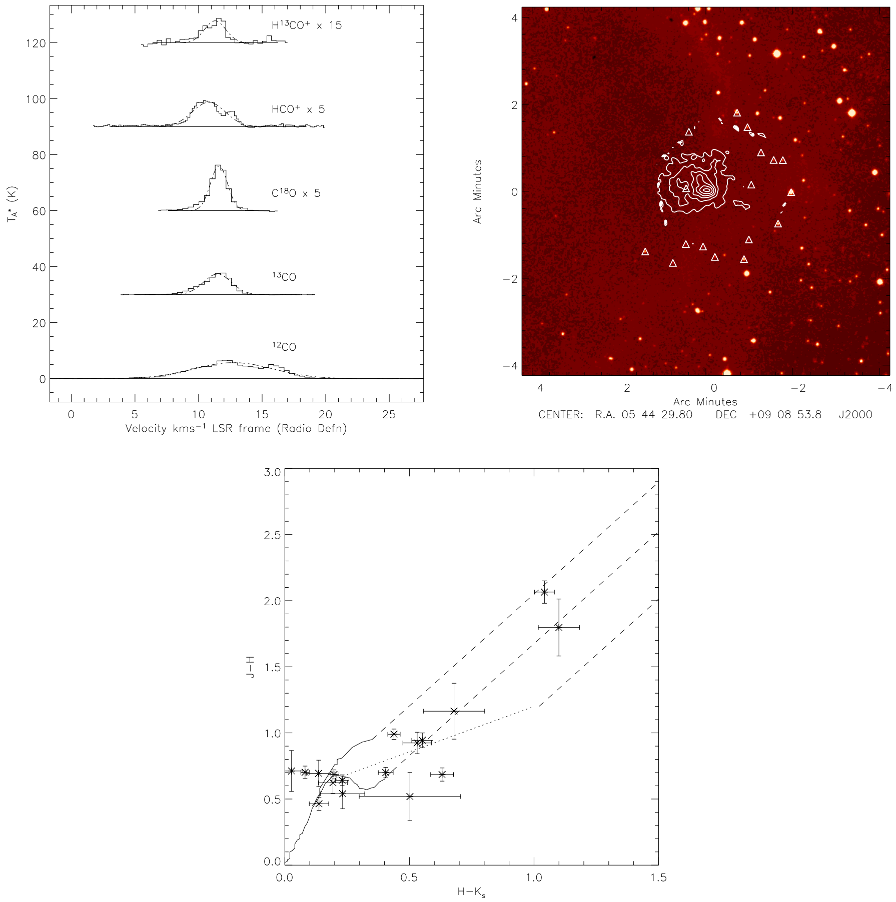

Figure 27: Plots and images associated with the object SFO 18. On the top left is a representation of all spectra observed for this object. The top right image shows SCUBA 850 μm contours overlaid on a DSS image, infrared sources from the 2MASS Point Source Catalogue (Cutri et al. 2003) are shown as triangles. The plot on the bottom shows the J-H versus H-K$_s$ colours of the 2MASS sources associated with the cloud. Peak and r.m.s. flux levels are as follows, SCUBA peak = 0.69 Jy beam^{-1}, SCUBA 3σ = 0.12 Jy beam^{-1}.

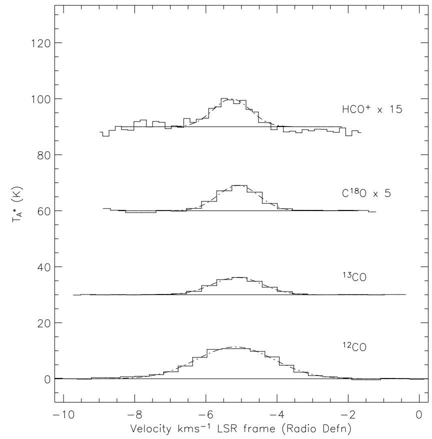

Figure 27: The spectra associated with the object SFO 23.

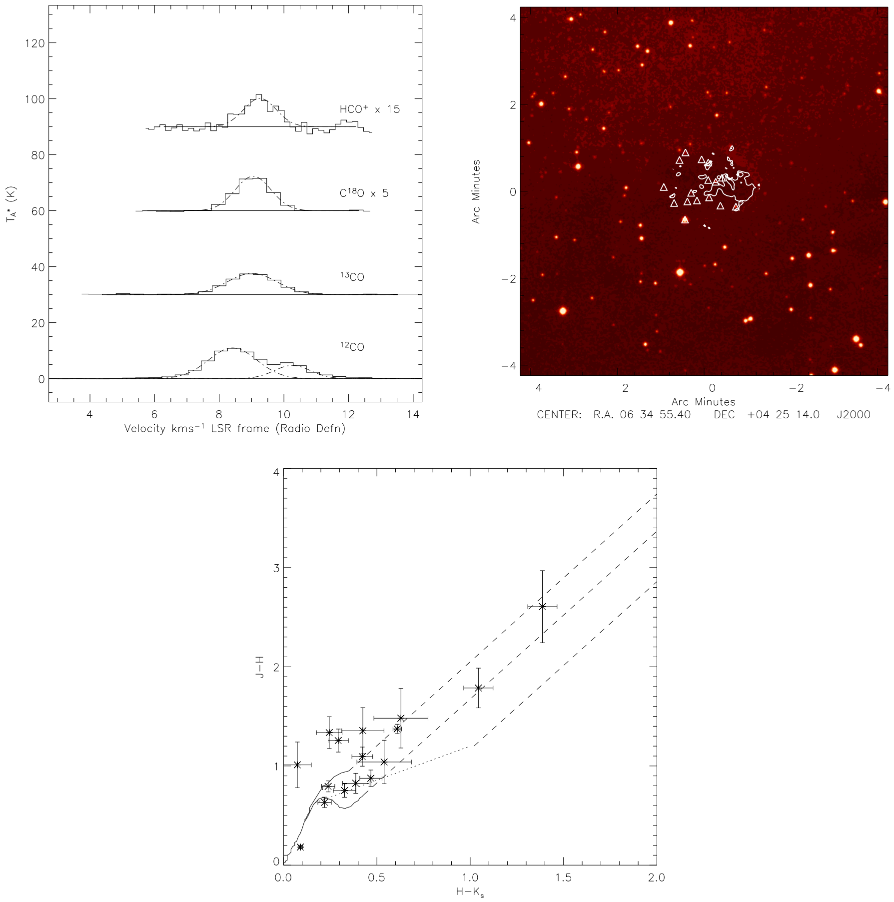

Figure 27: Plots and images associated with the object SFO 24. On the top left is a representation of all spectra observed for this object. The top right image shows SCUBA 850 μm contours overlaid on a DSS image, infrared sources from the 2MASS Point Source Catalogue (Cutri et al. 2003) are shown as triangles. The plot on the bottom shows the J-H versus H-K_s colours of the 2MASS sources associated with the cloud. Peak and r.m.s. flux levels are as follows, SCUBA peak = 0.72 Jy beam^{-1}, SCUBA 3σ = 0.09 Jy beam^{-1}.

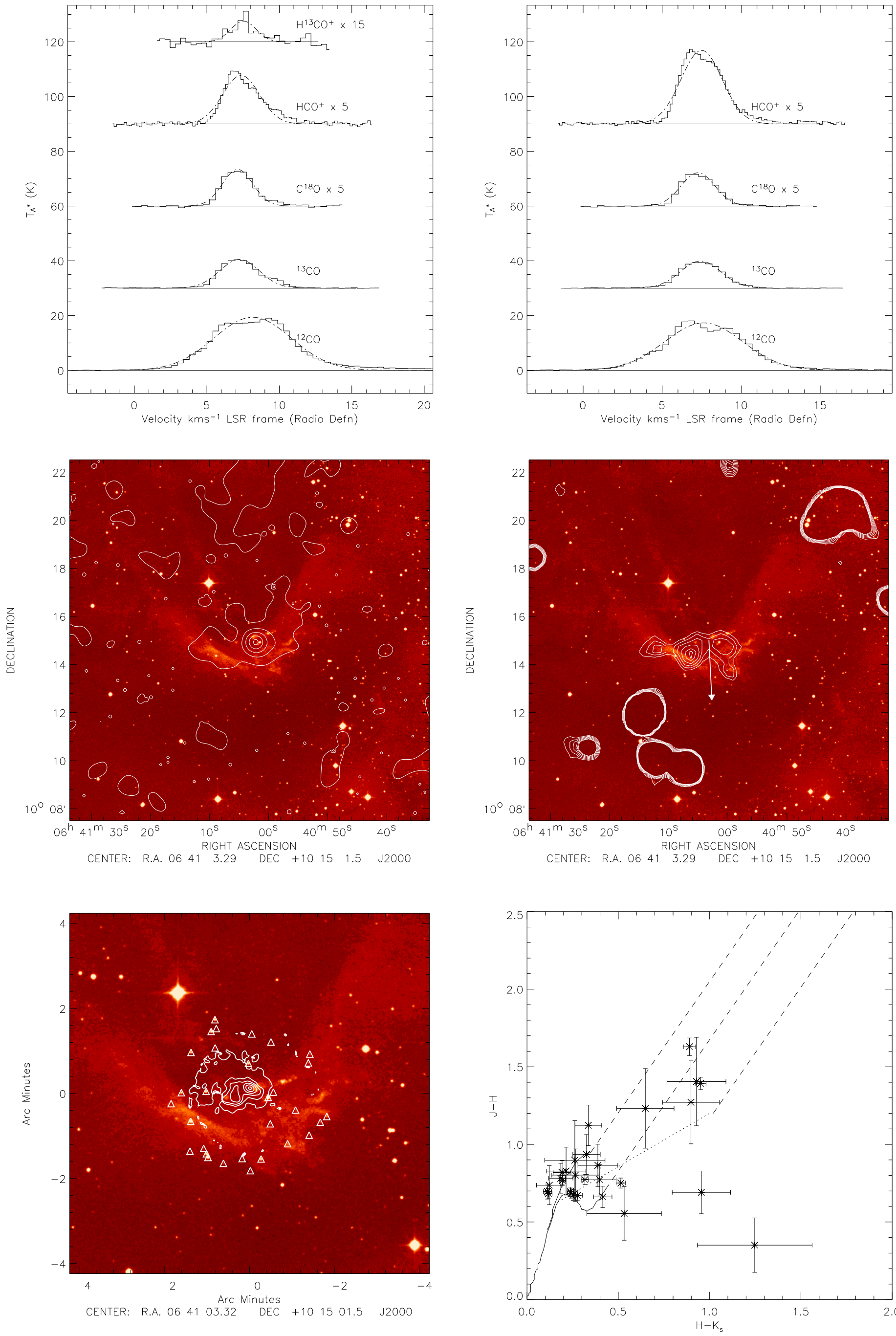

Figure 27: Plots and images associated with the object SFO 25. In the top two panels are representations of all spectra observed for the objects SFO 25 SMM1 and SMM2 on the left and right respectively. The centre left image shows MSX 8.3 μm emission contours overlaid on a DSS image. The centre right image is of NVSS 20 cm emission contours overlaid on a DSS image. Arrows show the direction of the ionising source(s). The bottom left image shows SCUBA 850 μm contours overlaid on a DSS image, infrared sources from the 2MASS Point Source Catalogue (Cutri et al. 2003) are shown as triangles. The bottom right plot shows the J-H versus H-K$_s$ colours of the 2MASS sources associated with the cloud. Peak and r.m.s. flux levels are as follows, MSX peak = 10.2 10^5 W m^{-2} sr^{-1}, MSX 3σ = 1.34 10^5 W m^{-2} sr^{-1}. NVSS peak = 2.98 mJy beam^{-1}, NVSS 3σ = 1.59 mJy beam^{-1}. SCUBA peak = 1.61 Jy beam^{-1}, SCUBA 3σ = 0.20 Jy beam^{-1}.

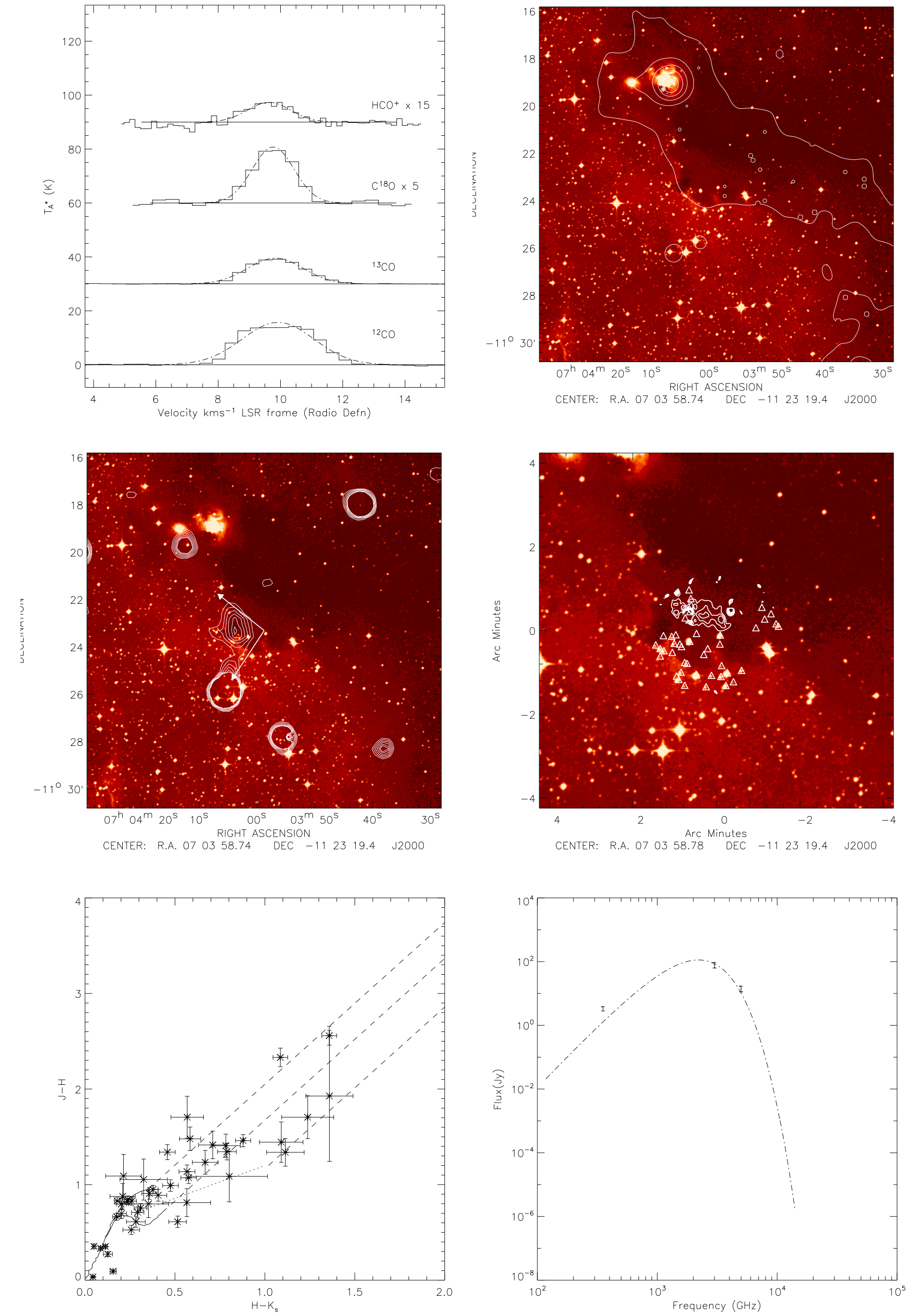

Figure 27: Plots and images associated with the object SFO 27. In the top left is a representation of all spectra observed for this object. The top right image shows MSX 8.3 μm emission contours overlaid on a DSS image. The centre left image is of NVSS 20 cm emission contours overlaid on a DSS image. Arrows show the direction of the ionising source(s). The centre right image shows SCUBA 850 μm contours overlaid on a DSS image, infrared sources from the 2MASS Point Source Catalogue (Cutri et al. 2003) are shown as triangles. The bottom left plot shows the J-H versus H-K$_s$ colours of the 2MASS sources associated with the cloud while the bottom right image shows the SED plot of the object composed from a best fit to various observed fluxes. MSX contours start at 18σ for clarity. Peak and r.m.s. flux levels are as follows, MSX peak = 113.4 10^5 W m^{-2} sr^{-1}, MSX 3σ = 8.40 10^5 W m^{-2} sr^{-1}. NVSS peak = 3.56 mJy beam^{-1}, NVSS 3σ = 1.53 mJy beam^{-1}. SCUBA peak = 0.53 Jy beam^{-1}, SCUBA 3σ = 0.25 Jy beam^{-1}.

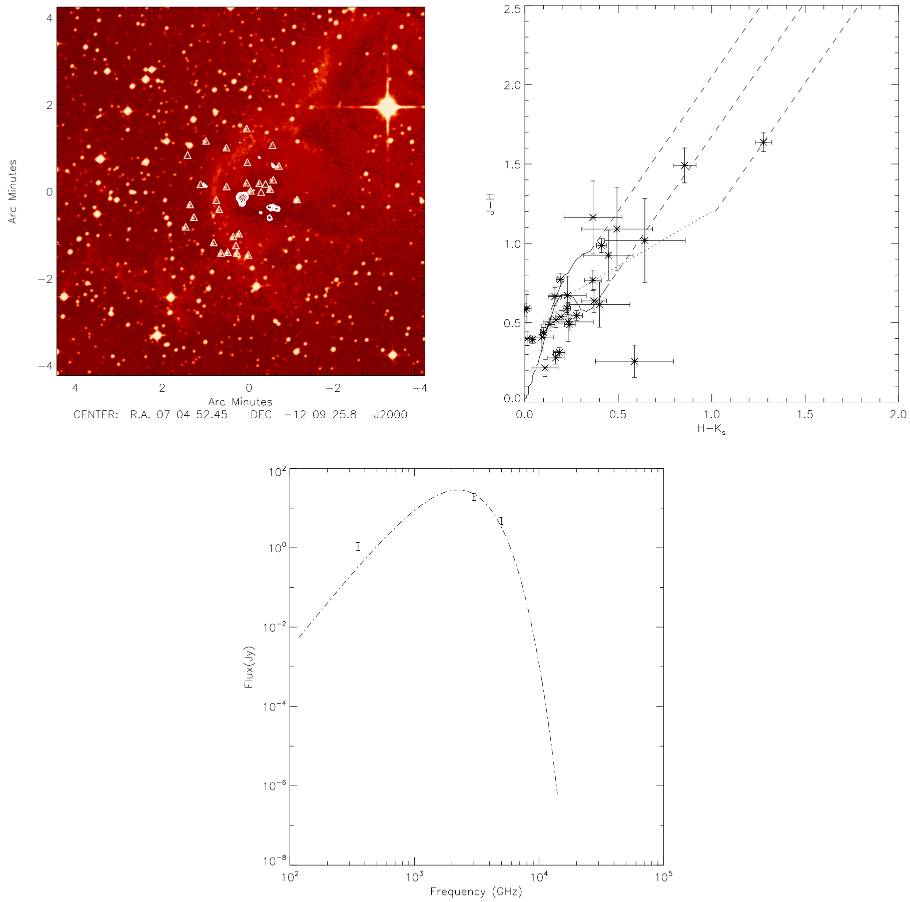

Figure 27: Plots and images associated with the object SFO 29. The top left image shows SCUBA 850 μm contours overlaid on a DSS image, infrared sources from the 2MASS Point Source Catalogue (Cutri et al. 2003) are shown as triangles. The top right plot shows the J-H versus H-K$_s$ colours of the 2MASS sources associated with the cloud while the bottom image shows the SED plot of the object composed from a best fit to various observed fluxes. Peak and r.m.s. flux levels are as follows, SCUBA peak = 0.74 Jy beam^{-1}, SCUBA 3σ = 0.51 Jy beam^{-1}.

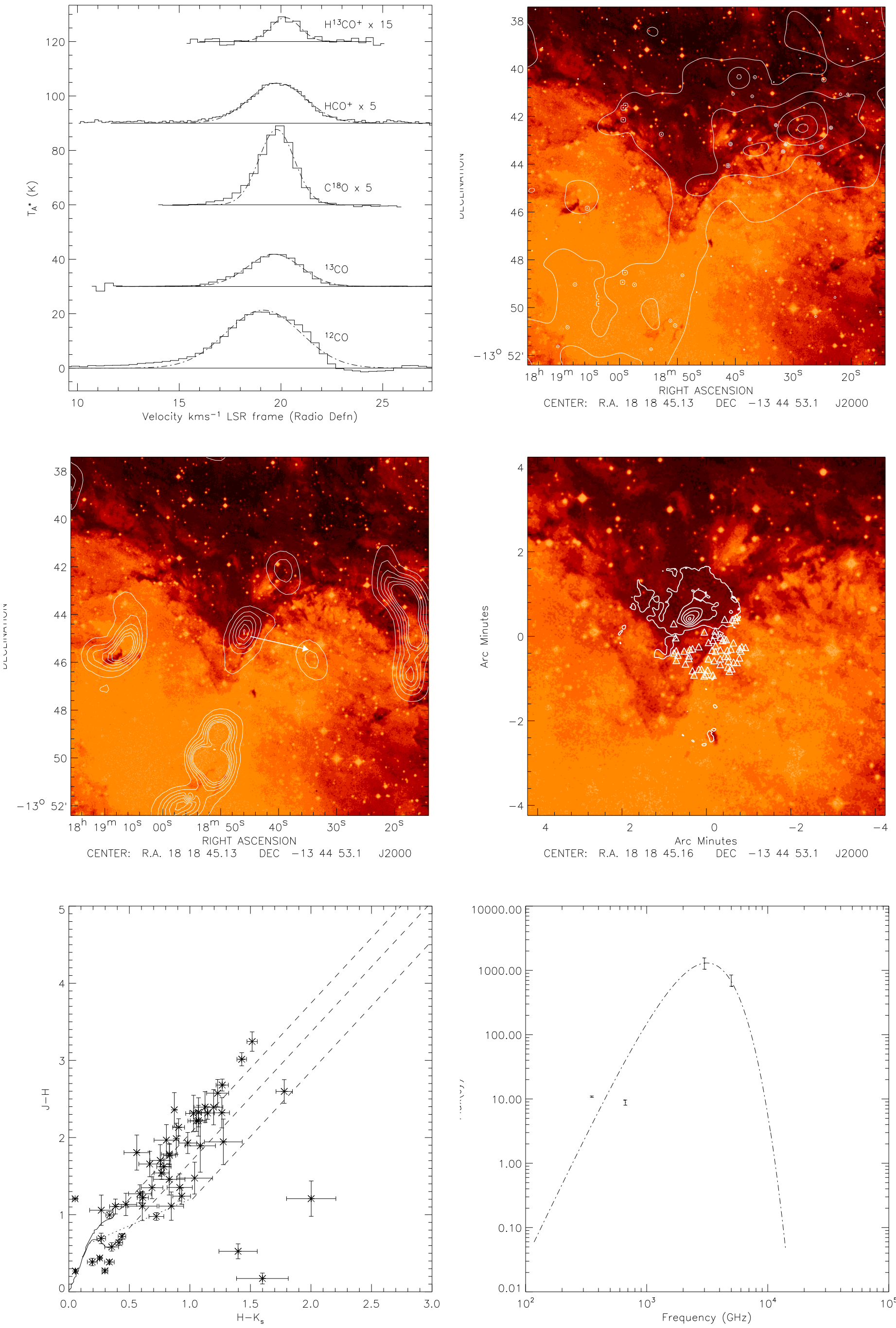

Figure 27: Plots and images associated with the object SFO 30. In the top left is a representation of all spectra observed for this object. The top right image shows MSX 8.3 μm emission contours overlaid on a DSS image. The centre left image is of NVSS 20 cm emission contours overlaid on a DSS image. Arrows show the direction of the ionising source(s). The centre right image shows SCUBA 850 μm contours overlaid on a DSS image, infrared sources from the 2MASS Point Source Catalogue (Cutri et al. 2003) are shown as triangles. The bottom left plot shows the J-H versus H-K$_s$ colours of the 2MASS sources associated with the cloud while the bottom right image shows the SED plot of the object composed from a best fit to various observed fluxes. Peak and r.m.s. flux levels are as follows, MSX peak = 226.6 10^5 W m^{-2} sr^{-1}, MSX 3σ = 11.75 10^5 W m^{-2} sr^{-1}. NVSS peak = 57.15 mJy beam^{-1}, NVSS 3σ = 7.29 mJy beam^{-1}. SCUBA peak = 1.61 Jy beam^{-1}, SCUBA 3σ = 0.11 Jy beam^{-1}.

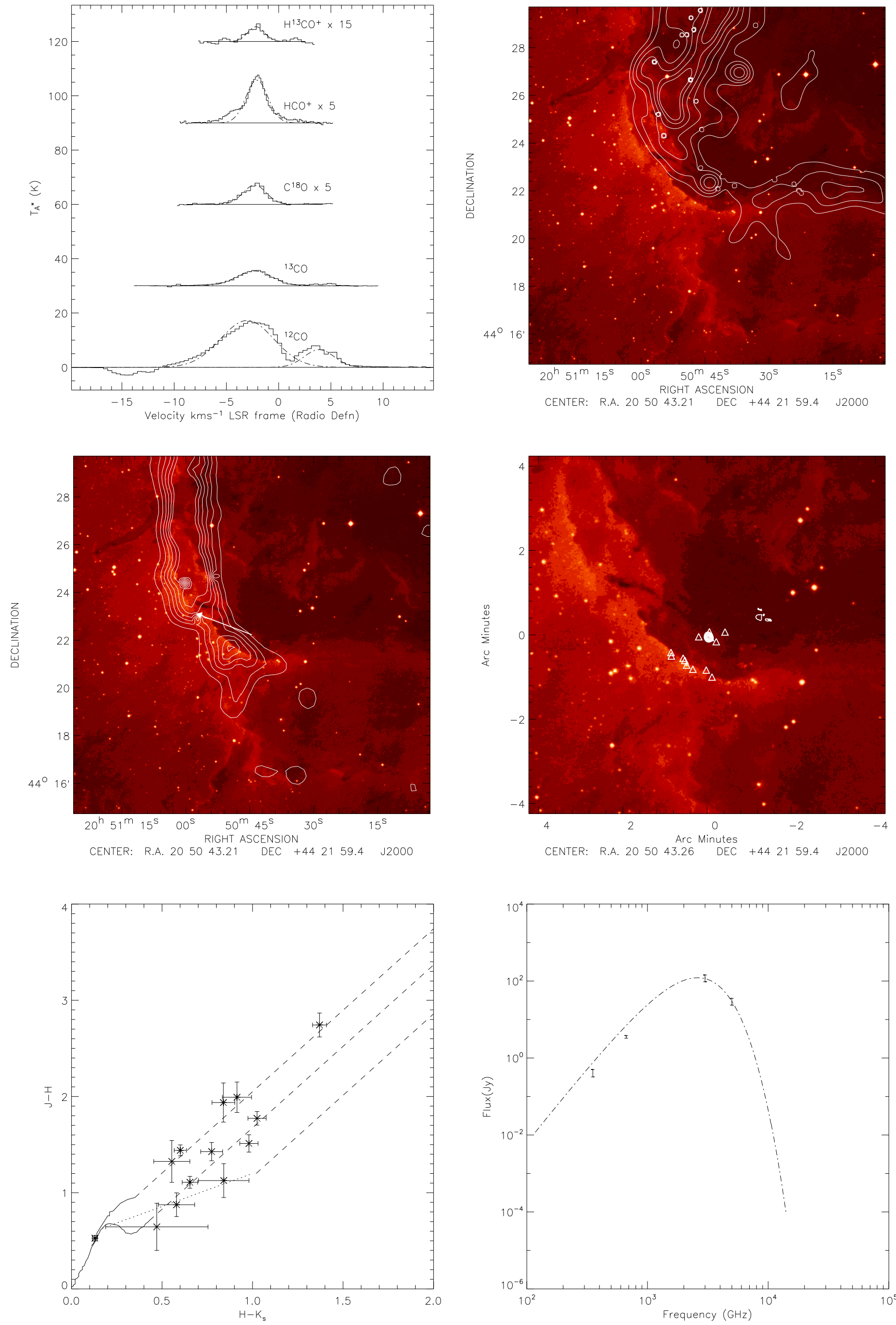

Figure 27: Plots and images associated with the object SFO 31. In the top left is a representation of all spectra observed for this object. The top right image shows MSX 8.3 μm emission contours overlaid on a DSS image. The centre left image is of NVSS 20 cm emission contours overlaid on a DSS image. Arrows show the direction of the ionising source(s). The centre right image shows SCUBA 850 μm contours overlaid on a DSS image, infrared sources from the 2MASS Point Source Catalogue (Cutri et al. 2003) are shown as triangles. The bottom left plot shows the J-H versus H-K$_s$ colours of the 2MASS sources associated with the cloud while the bottom right image shows the SED plot of the object composed from a best fit to various observed fluxes. MSX contours start at 21σ for clarity. Peak and r.m.s. flux levels are as follows, MSX peak = 26.4 10^5 W m^{-2} sr^{-1}, MSX 3σ = 14.80 10^5 W m^{-2} sr^{-1}. NVSS peak = 12.84 mJy beam^{-1}, NVSS 3σ = 1.87 mJy beam^{-1}. SCUBA peak = 0.62 Jy beam^{-1}, SCUBA 3σ = 0.40 Jy beam^{-1}.

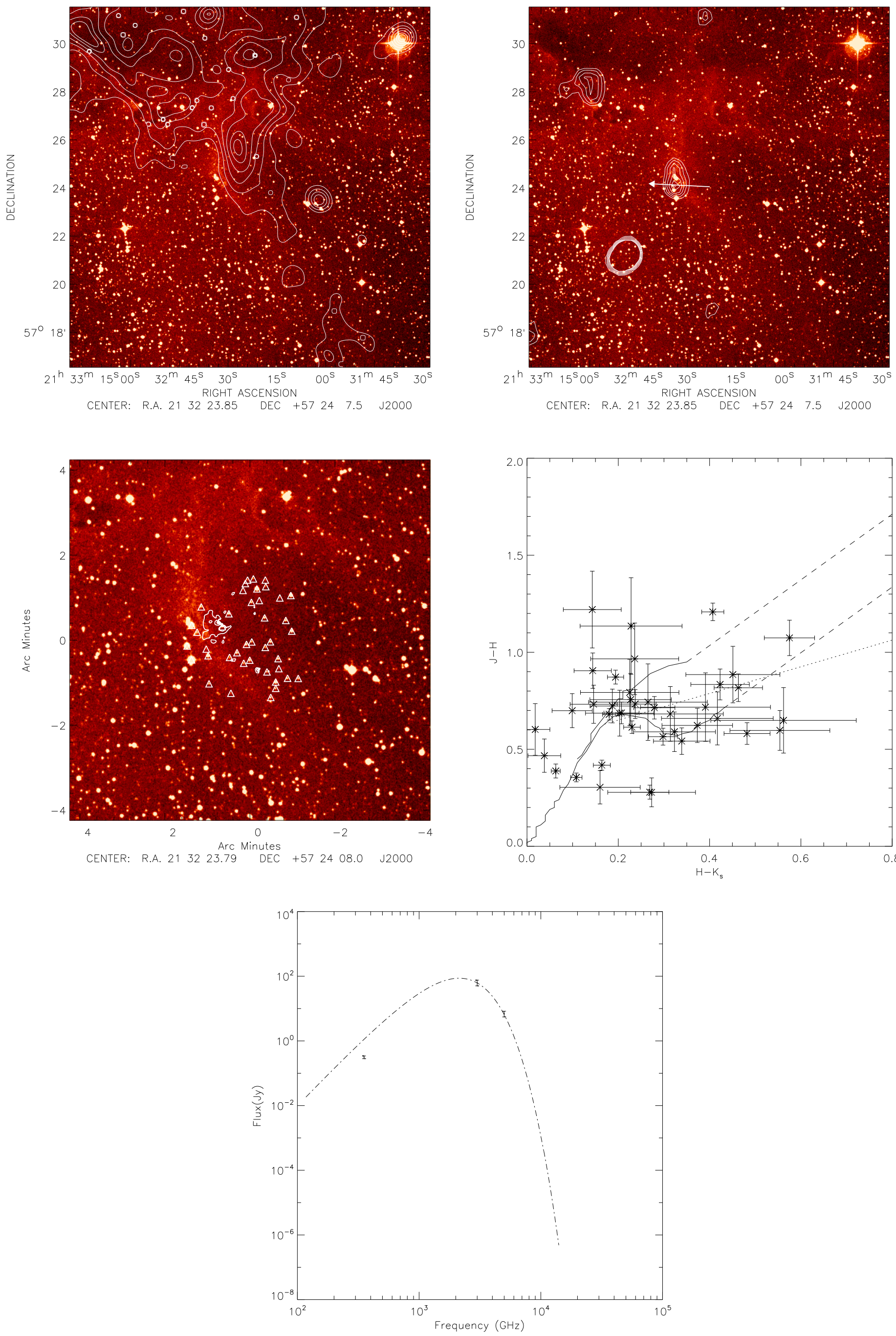

Figure 27: Plots and images associated with the object SFO 32. The top left image shows MSX 8.3 μm emission contours overlaid on a DSS image. The top right image is of NVSS 20 cm emission contours overlaid on a DSS image. Arrows show the direction of the ionising source(s). The centre left image shows SCUBA 850 μm contours overlaid on a DSS image, infrared sources from the 2MASS Point Source Catalogue (Cutri et al. 2003) are shown as triangles. The centre right plot shows the J-H versus H-K$_s$ colours of the 2MASS sources associated with the cloud while the bottom image shows the SED plot of the object composed from a best fit to various observed fluxes. MSX contours start at 9σ for clarity. Peak and r.m.s. flux levels are as follows, MSX peak = 8.2 10^5 W m^{-2} sr^{-1}, MSX 3σ = 4.35 10^5 W m^{-2} sr^{-1}. NVSS peak = 2.95 mJy beam^{-1}, NVSS 3σ = 1.42 mJy beam^{-1}. SCUBA peak = 0.19 Jy beam^{-1}, SCUBA 3σ = 0.05 Jy beam^{-1}.

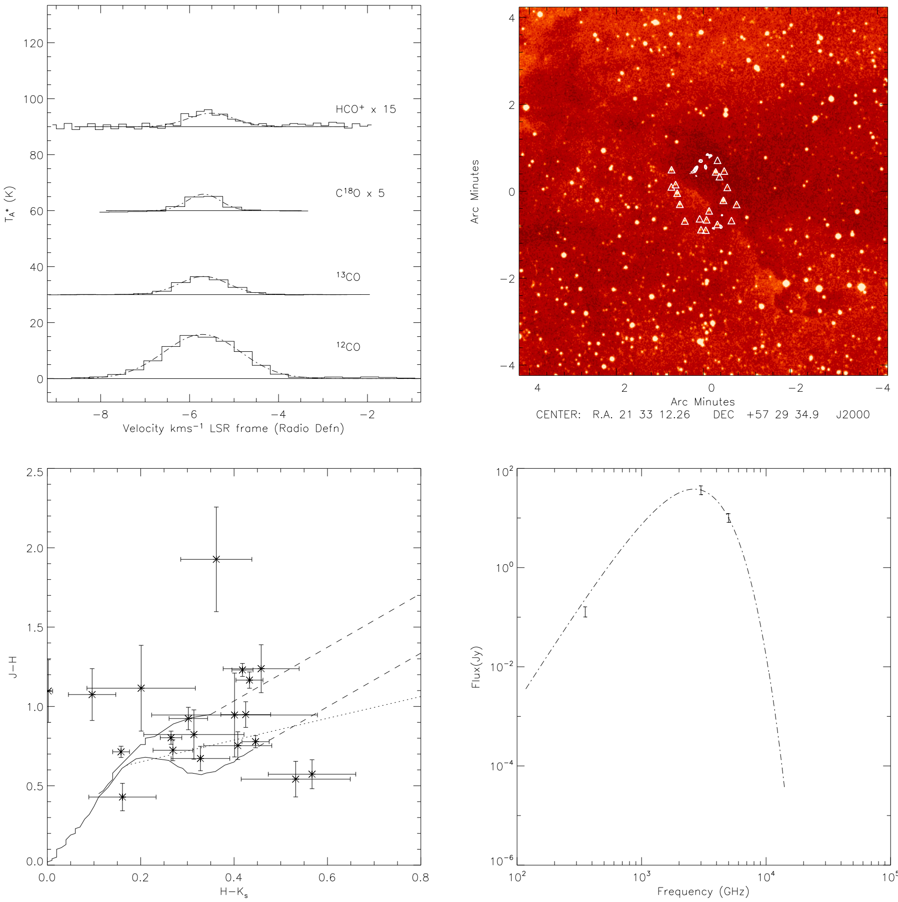

Figure 27: Plots and images associated with the object SFO 33. In the top left is a representation of all spectra observed for this object. The top right image shows SCUBA 850 μm contours overlaid on a DSS image, infrared sources from the 2MASS Point Source Catalogue (Cutri et al. 2003) are shown as triangles. The bottom left plot shows the J-H versus H-K$_s$ colours of the 2MASS sources associated with the cloud while the bottom right image shows the SED plot of the object composed from a best fit to various observed fluxes. Peak and r.m.s. flux levels are as follows, SCUBA peak = 0.12 Jy beam^{-1}, SCUBA 3σ = 0.10 Jy beam^{-1}.

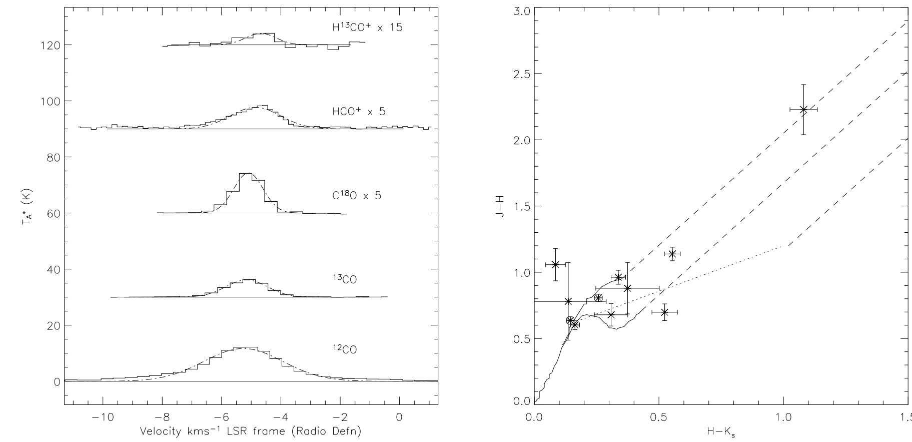

Figure 27: Plots and images associated with the object SFO 34. On the left is a representation of all spectra observed for this object. The plot on the right shows the J-H versus H-K$_s$ colours of the 2MASS sources associated with the cloud.

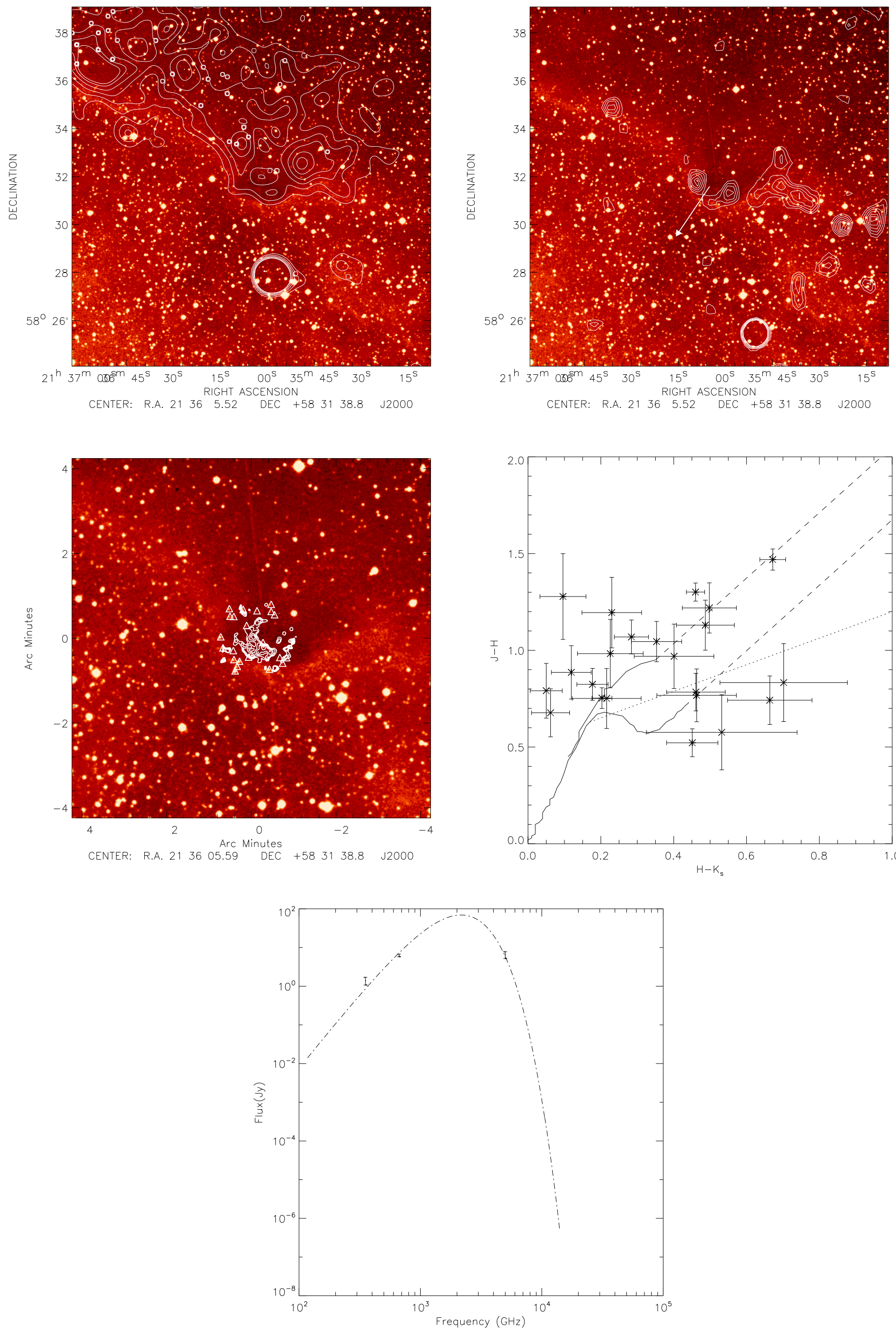

Figure 27: Plots and images associated with the object SFO 35. The top left image shows MSX 8.3 μm emission contours overlaid on a DSS image. The top right image is of NVSS 20 cm emission contours overlaid on a DSS image. Arrows show the direction of the ionising source(s). The centre left image shows SCUBA 850 μm contours overlaid on a DSS image, infrared sources from the 2MASS Point Source Catalogue (Cutri et al. 2003) are shown as triangles. The centre right plot shows the J-H versus H-K$_s$ colours of the 2MASS sources associated with the cloud while the bottom image shows the SED plot of the object composed from a best fit to various observed fluxes. MSX contours start at 9σ for clarity. Peak and r.m.s. flux levels are as follows, MSX peak = 8.2 10^5 W m^{-2} sr^{-1}, MSX 3σ = 4.35 10^5 W m^{-2} sr^{-1}. NVSS peak = 1.80 mJy beam^{-1}, NVSS 3σ = 0.87 mJy beam^{-1}. SCUBA peak = 0.18 Jy beam^{-1}, SCUBA 3σ = 0.11 Jy beam^{-1}.

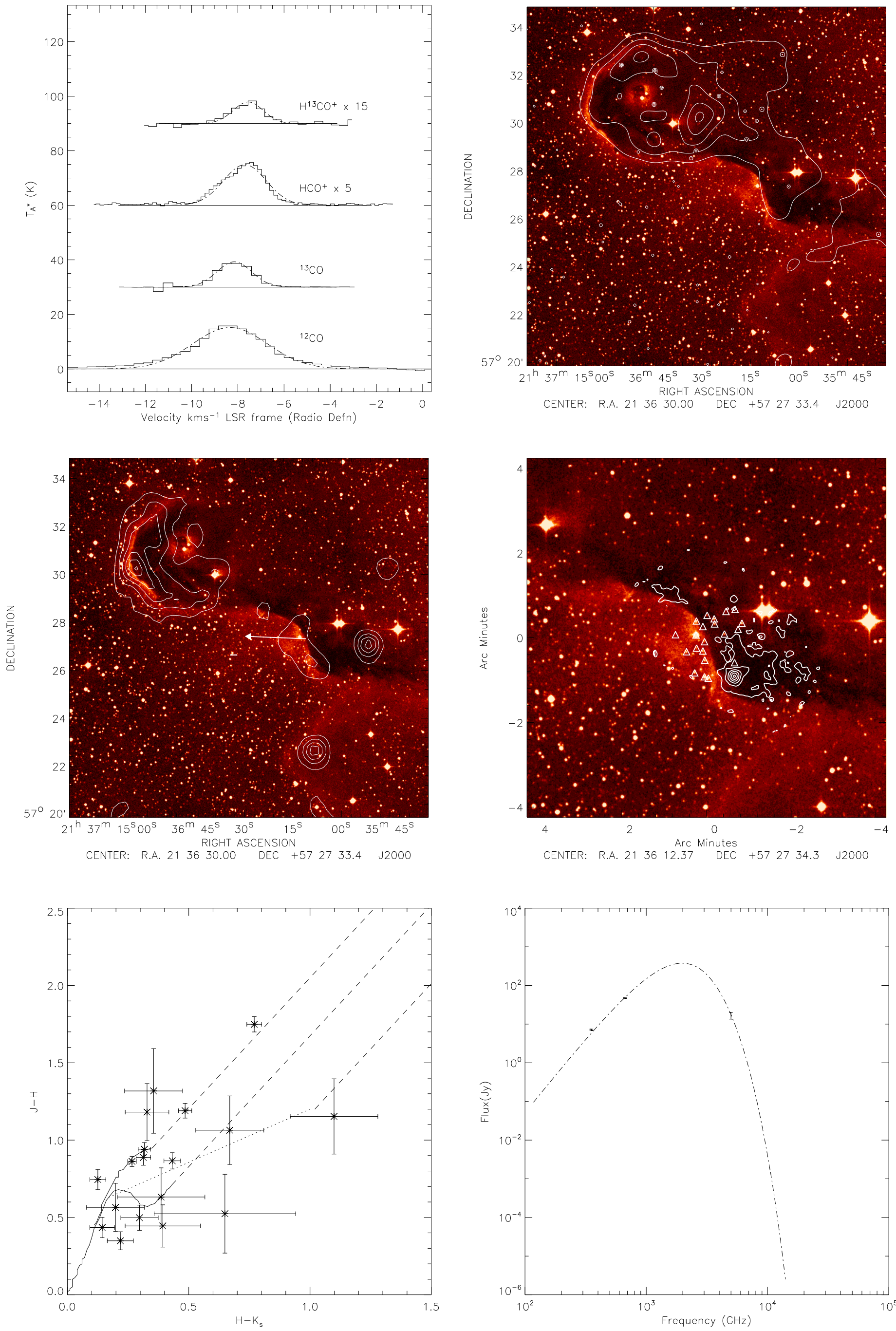

Figure 27: Plots and images associated with the object SFO 36. In the top left is a representation of all spectra observed for this object. The top right image shows MSX 8.3 μm emission contours overlaid on a DSS image. The centre left image is of NVSS 20 cm emission contours overlaid on a DSS image. Arrows show the direction of the ionising source(s). The centre right image shows SCUBA 850 μm contours overlaid on a DSS image, infrared sources from the 2MASS Point Source Catalogue (Cutri et al. 2003) are shown as triangles. The bottom left plot shows the J-H versus H-K$_s$ colours of the 2MASS sources associated with the cloud while the bottom right image shows the SED plot of the object composed from a best fit to various observed fluxes. Peak and r.m.s. flux levels are as follows, MSX peak = 22.9 10^5 W m^{-2} sr^{-1}, MSX 3σ = 1.15 10^5 W m^{-2} sr^{-1}. NVSS peak = 11.03 mJy beam^{-1}, NVSS 3σ = 1.41 mJy beam^{-1}. SCUBA peak = 1.44 Jy beam^{-1}, SCUBA 3σ = 0.17 Jy beam^{-1}.

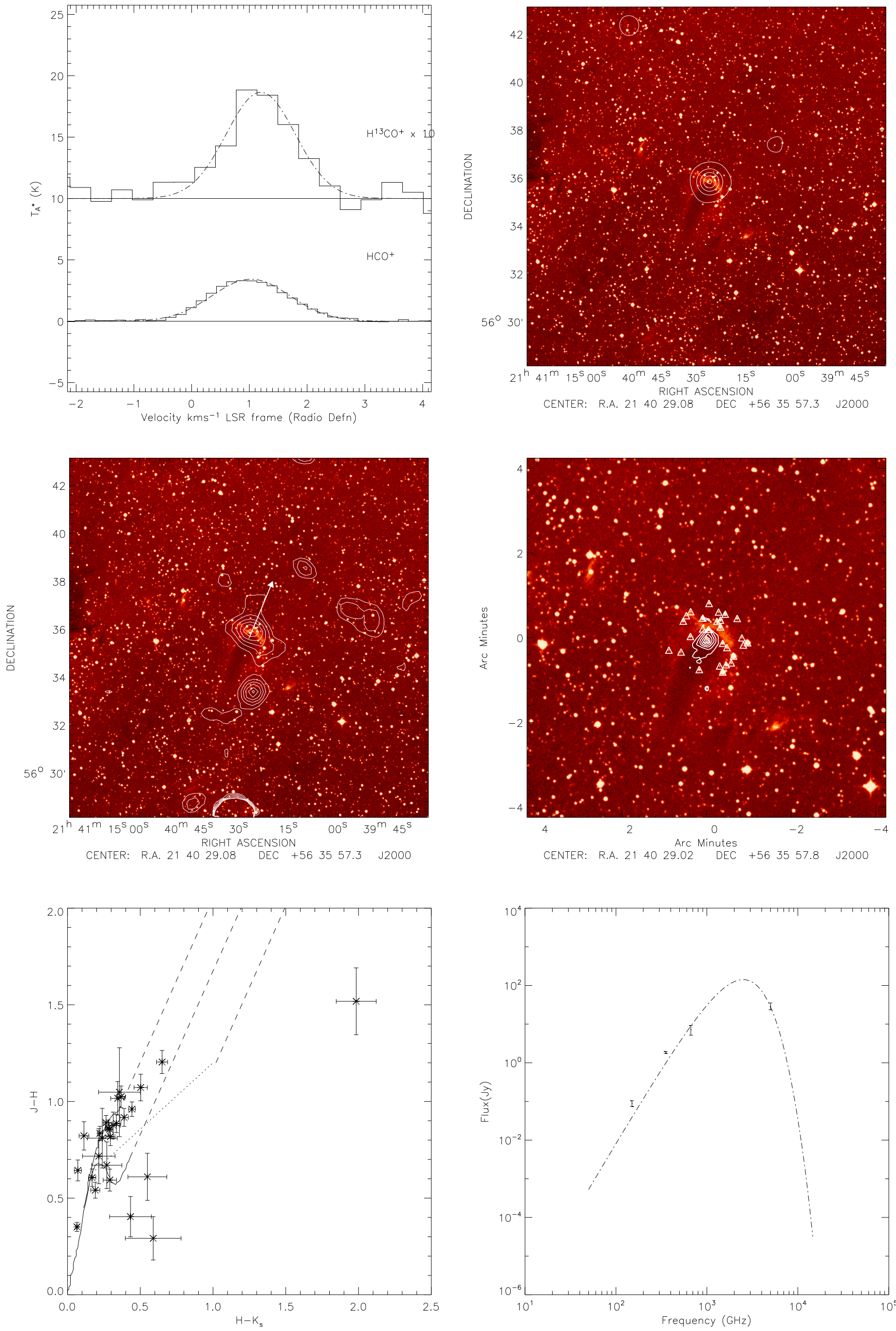

Figure 27: Plots and images associated with the object SFO 37. In the top left is a representation of all spectra observed for this object. The top right image shows MSX 8.3 μm emission contours overlaid on a DSS image. The centre left image is of NVSS 20 cm emission contours overlaid on a DSS image. Arrows show the direction of the ionising source(s). The centre right image shows SCUBA 850 μm contours overlaid on a DSS image, infrared sources from the 2MASS Point Source Catalogue (Cutri et al. 2003) are shown as triangles. The bottom left plot shows the J-H versus H-K$_s$ colours of the 2MASS sources associated with the cloud while the bottom right image shows the SED plot of the object composed from a best fit to various observed fluxes. Peak and r.m.s. flux levels are as follows, MSX peak = 19.7 10^5 W m^{-2} sr^{-1}, MSX 3σ = 0.88 10^5 W m^{-2} sr^{-1}. NVSS peak = 3.50 mJy beam^{-1}, NVSS 3σ = 1.14 mJy beam^{-1}. SCUBA peak = 0.81 Jy beam^{-1}, SCUBA 3σ = 0.14 Jy beam^{-1}.

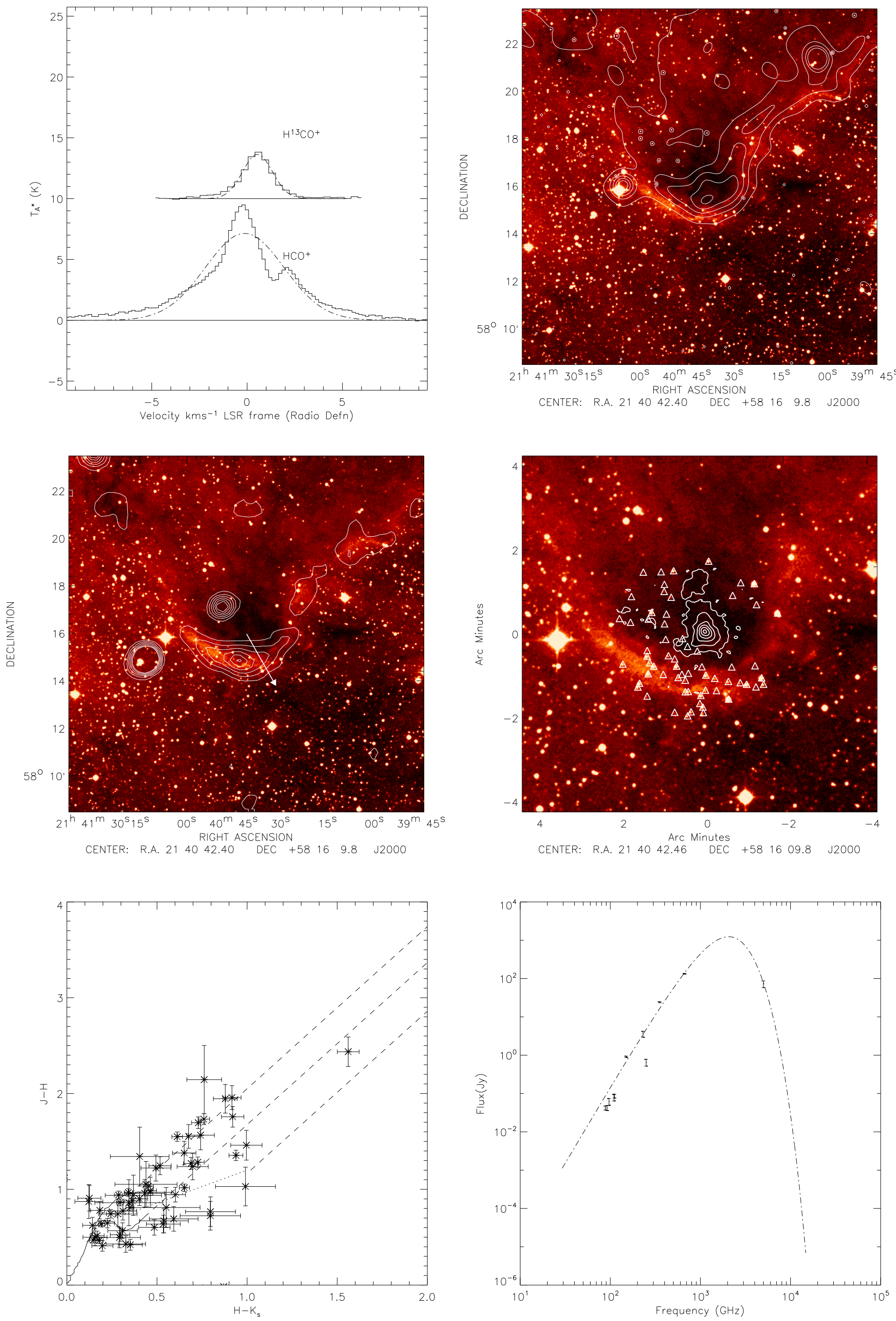

Figure 27: Plots and images associated with the object SFO 38. In the top left is a representation of all spectra observed for this object. The top right image shows MSX 8.3 μm emission contours overlaid on a DSS image. The centre left image is of NVSS 20 cm emission contours overlaid on a DSS image. Arrows show the direction of the ionising source(s). The centre right image shows SCUBA 850 μm contours overlaid on a DSS image, infrared sources from the 2MASS Point Source Catalogue (Cutri et al. 2003) are shown as triangles. The bottom left plot shows the J-H versus H-K$_s$ colours of the 2MASS sources associated with the cloud while the bottom right image shows the SED plot of the object composed from a best fit to various observed fluxes. Peak and r.m.s. flux levels are as follows, MSX peak = 14.7 10^5 W m^{-2} sr^{-1}, MSX 3σ = 1.20 10^5 W m^{-2} sr^{-1}. NVSS peak = 5.98 mJy beam^{-1}, NVSS 3σ = 1.16 mJy beam^{-1}. SCUBA peak = 3.90 Jy beam^{-1}, SCUBA 3σ = 0.39 Jy beam^{-1}.

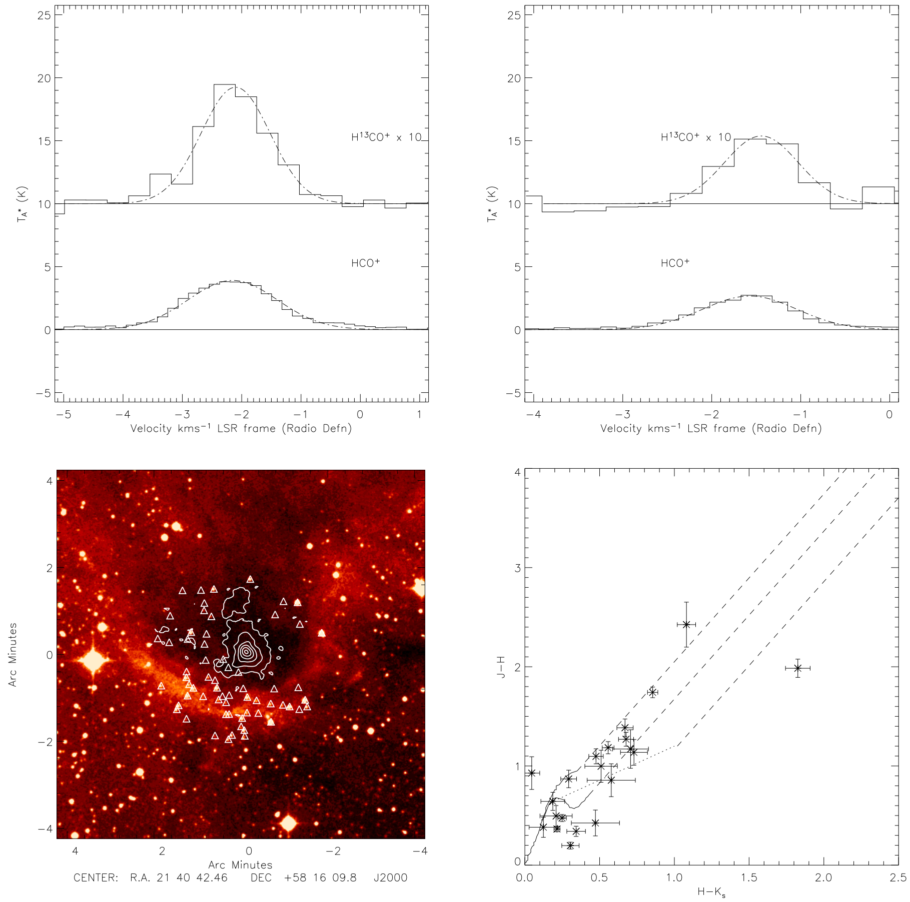

Figure 27: Plots and images associated with the object SFO 39. In the top two panels are representations of all spectra observed for the objects SFO 39 SMM1 and SMM2 on the left and right respectively. The bottom left image shows SCUBA 850 μm contours overlaid on a DSS image, infrared sources from the 2MASS Point Source Catalogue (Cutri et al. 2003) are shown as triangles. The bottom right figure shows the J-H versus H-K$_s$ colours of the 2MASS sources associated with the cloud. Peak and r.m.s. flux levels are as follows, SCUBA peak = 0.82 Jy beam^{-1}, SCUBA 3σ = 0.09 Jy beam^{-1}.

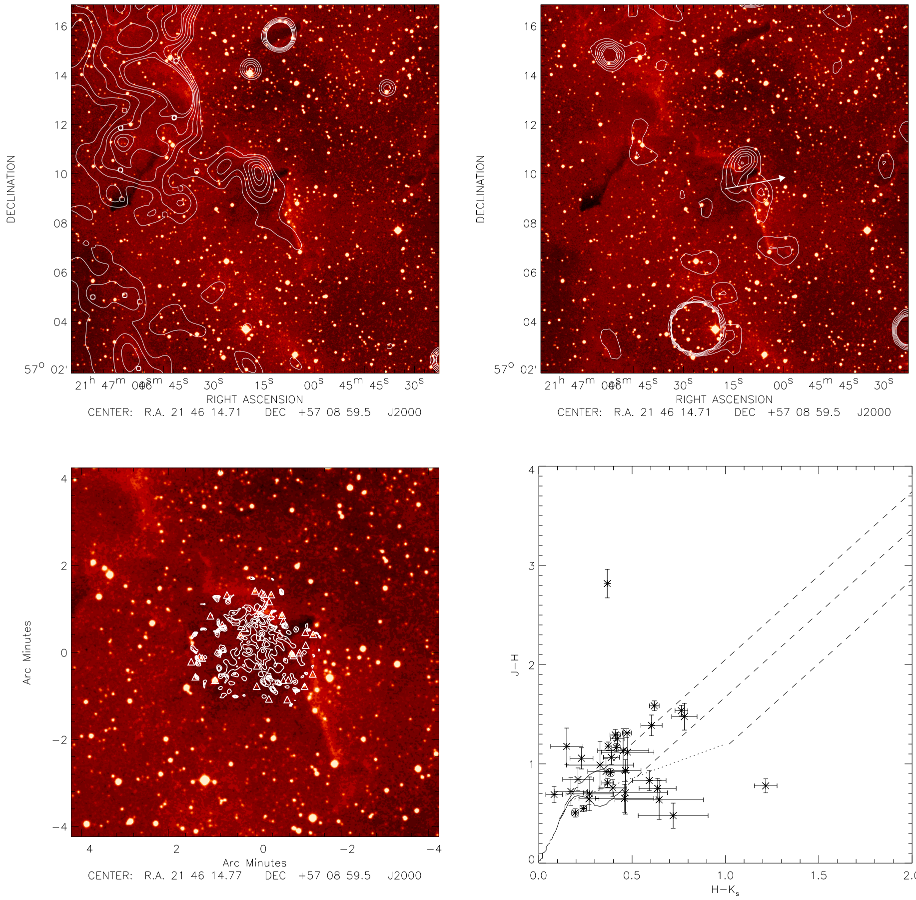

Figure 27: Plots and images associated with the object SFO 40. The top left image shows MSX 8.3 μm emission contours overlaid on a DSS image. The top right image is of NVSS 20 cm emission contours overlaid on a DSS image. Arrows show the direction of the ionising source(s). The bottom left image shows SCUBA 850 μm contours overlaid on a DSS image, infrared sources from the 2MASS Point Source Catalogue (Cutri et al. 2003) are shown as triangles. The bottom right plot shows the J-H versus H-K$_s$ colours of the 2MASS sources associated with the cloud. MSX contours start at 12σ for clarity. Peak and r.m.s. flux levels are as follows, MSX peak = 6.9 10^5 W m^{-2} sr^{-1}, MSX 3σ = 4.62 10^5 W m^{-2} sr^{-1}. NVSS peak = 4.93 mJy beam^{-1}, NVSS 3σ = 1.32 mJy beam^{-1}. SCUBA peak = 0.29 Jy beam^{-1}, SCUBA 3σ = 0.09 Jy beam^{-1}.

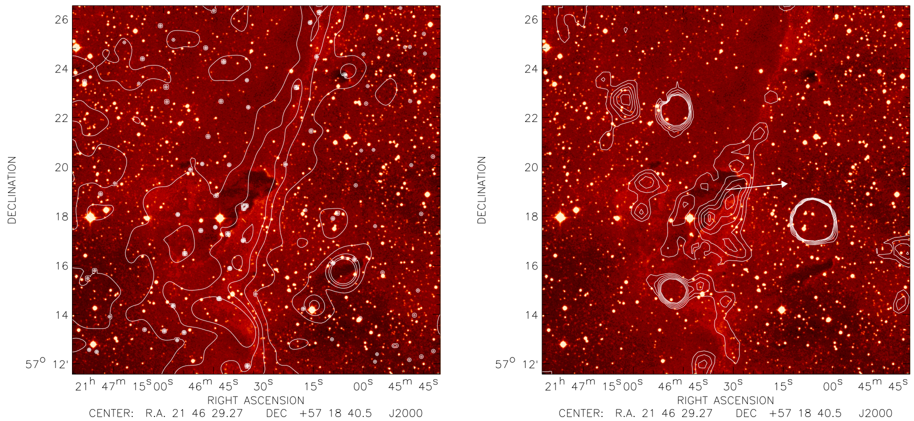

Figure 27: Plots and images associated with the object SFO 41. The left image shows MSX 8.3 μm emission contours overlaid on a DSS image and the right image is of NVSS 20 cm emission contours overlaid on a DSS image. Arrows show the direction of the ionising source(s). Peak and r.m.s. flux levels are as follows, MSX peak = 7.2 10^5 W m^{-2} sr^{-1}, MSX 3σ = 1.01 10^5 W m^{-2} sr^{-1}. NVSS peak = 2.73 mJy beam^{-1}, NVSS 3σ = 0.95 mJy beam^{-1}.

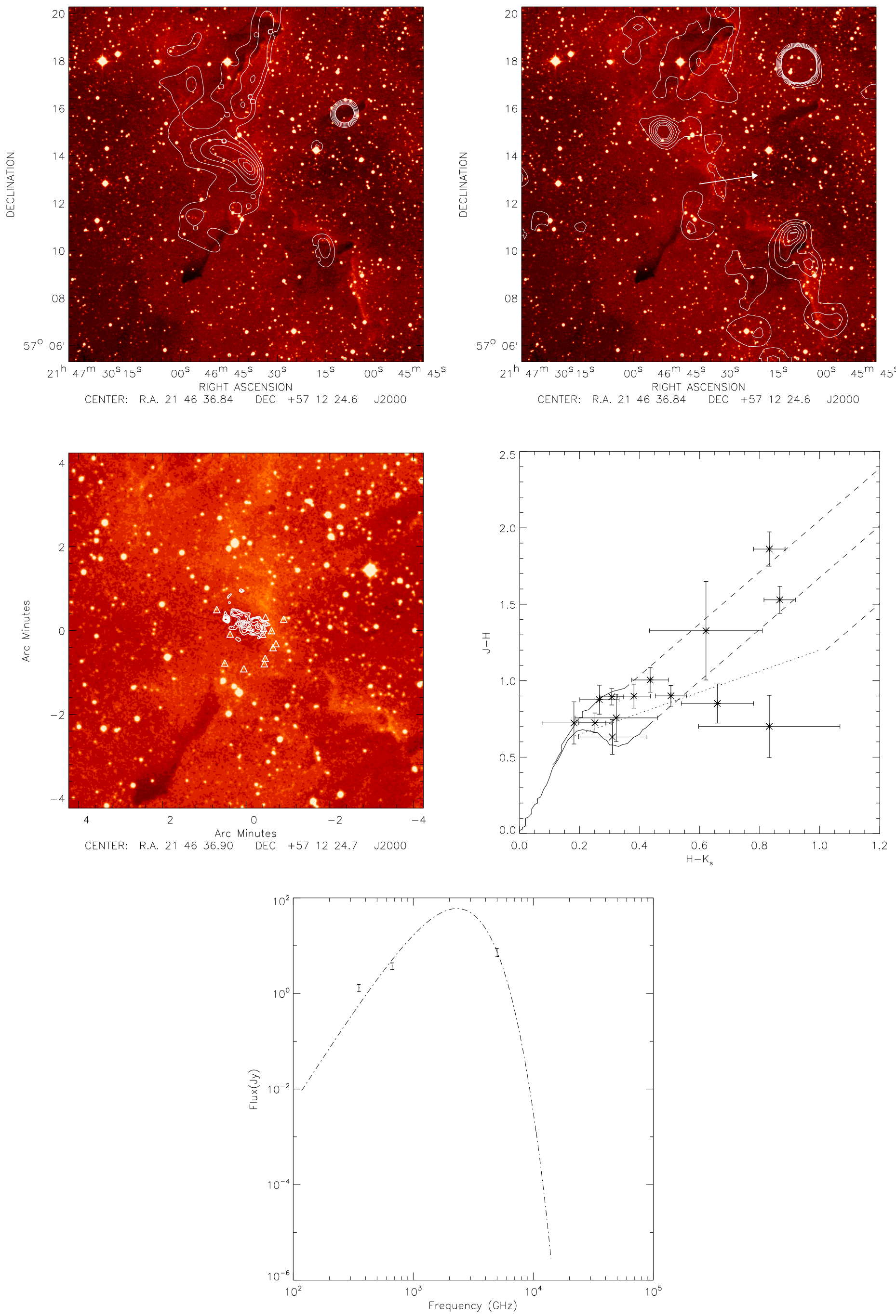

Figure 27: Plots and images associated with the object SFO 42. The top left image shows MSX 8.3 μm emission contours overlaid on a DSS image. The top right image is of NVSS 20 cm emission contours overlaid on a DSS image. Arrows show the direction of the ionising source(s). The centre left image shows SCUBA 850 μm contours overlaid on a DSS image, infrared sources from the 2MASS Point Source Catalogue (Cutri et al. 2003) are shown as triangles. The centre right plot shows the J-H versus H-K$_s$ colours of the 2MASS sources associated with the cloud while the bottom image shows the SED plot of the object composed from a best fit to various observed fluxes. MSX contours start at 15σ for clarity. Peak and r.m.s. flux levels are as follows, MSX peak = 9.2 10^5 W m^{-2} sr^{-1}, MSX 3σ = 5.76 10^5 W m^{-2} sr^{-1}. NVSS peak = 4.88 mJy beam^{-1}, NVSS 3σ = 1.05 mJy beam^{-1}. SCUBA peak = 0.23 Jy beam^{-1}, SCUBA 3σ = 0.13 Jy beam^{-1}.

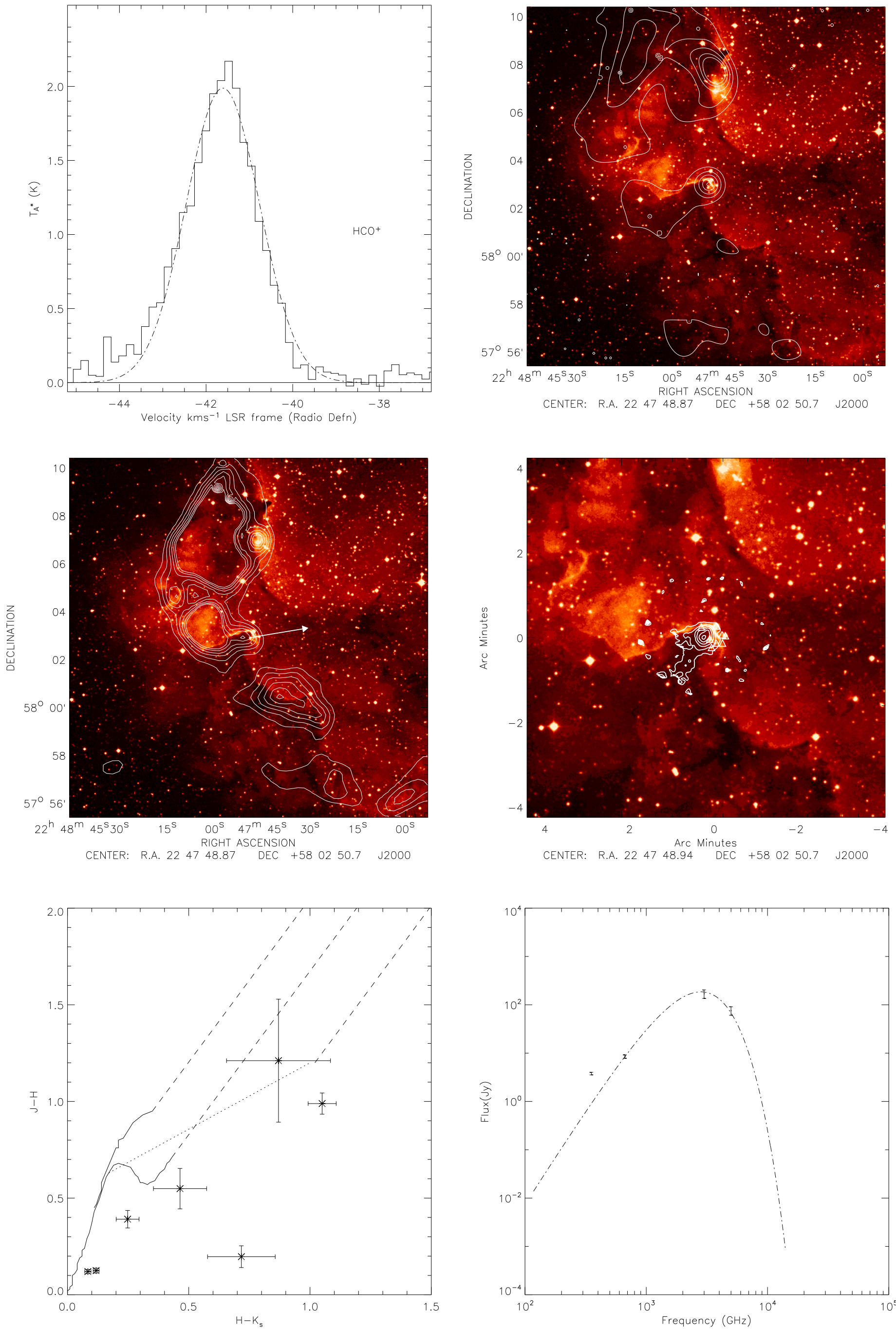

Figure 27: Plots and images associated with the object SFO 43. In the top left is a representation of all spectra observed for this object. The top right image shows MSX 8.3 μm emission contours overlaid on a DSS image. The centre left image is of NVSS 20 cm emission contours overlaid on a DSS image. Arrows show the direction of the ionising source(s). The centre right image shows SCUBA 850 μm contours overlaid on a DSS image, infrared sources from the 2MASS Point Source Catalogue (Cutri et al. 2003) are shown as triangles. The bottom left plot shows the J-H versus H-K$_s$ colours of the 2MASS sources associated with the cloud while the bottom right image shows the SED plot of the object composed from a best fit to various observed fluxes. Peak and r.m.s. flux levels are as follows, MSX peak = 69.0 10^5 W m^{-2} sr^{-1}, MSX 3σ = 1.18 10^5 W m^{-2} sr^{-1}. NVSS peak = 14.00 mJy beam^{-1}, NVSS 3σ = 2.45 mJy beam^{-1}. SCUBA peak = 0.67 Jy beam^{-1}, SCUBA 3σ = 0.11 Jy beam^{-1}.

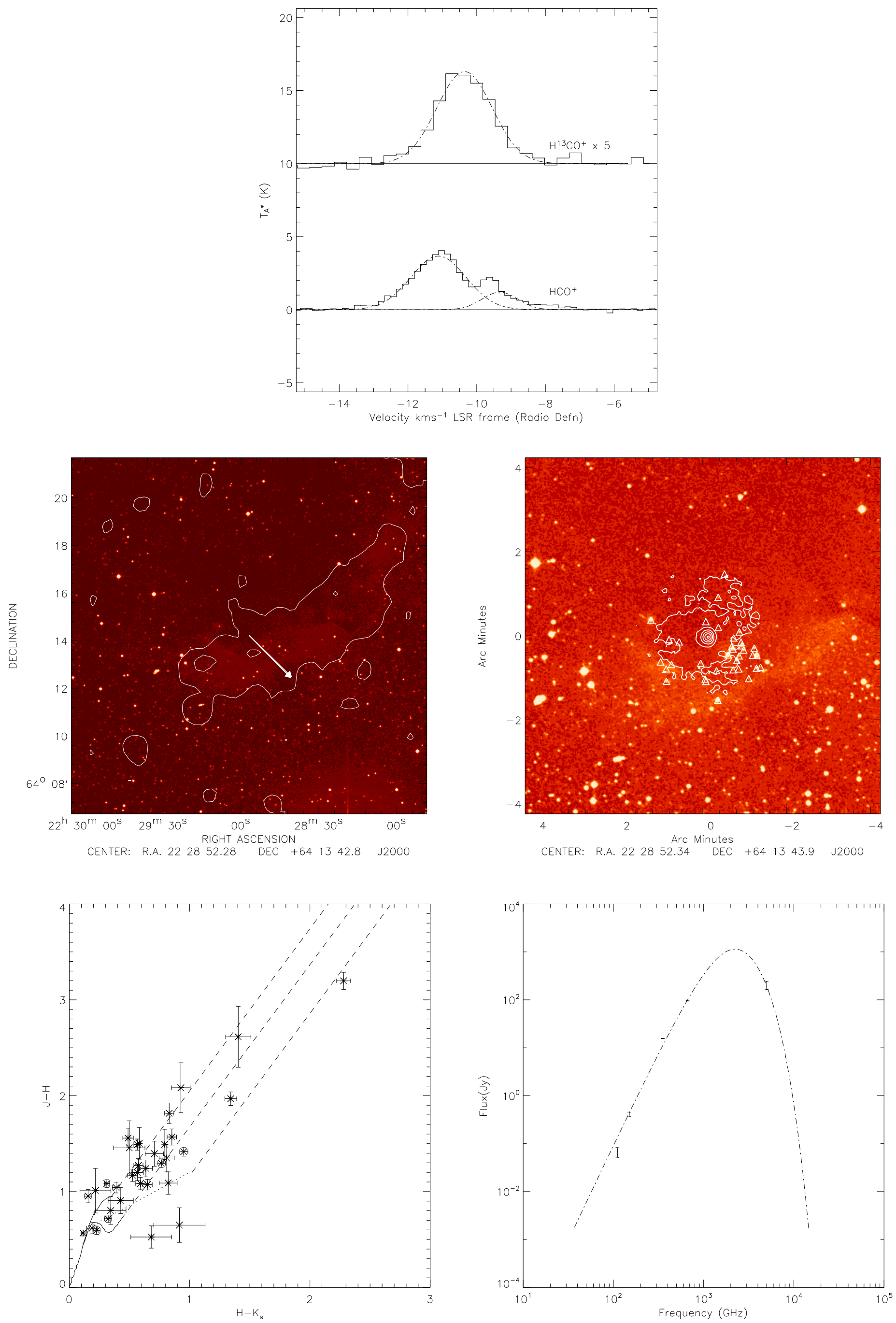

Figure 27: Plots and images associated with the object SFO 44. At the top is a representation of all spectra observed for this object. The centre left image is of NVSS 20 cm emission contours overlaid on a DSS image. Arrows show the direction of the ionising source(s). The centre right image shows SCUBA 850 μm contours overlaid on a DSS image, infrared sources from the 2MASS Point Source Catalogue (Cutri et al. 2003) are shown as triangles. The bottom left plot shows the J-H versus H-K$_s$ colours of the 2MASS sources associated with the cloud while the bottom right image shows the SED plot of the object composed from a best fit to various observed fluxes. Peak and r.m.s. flux levels are as follows, NVSS peak = 37.00 mJy beam^{-1}, NVSS 3σ = 0.90 mJy beam^{-1}. SCUBA peak = 3.48 Jy beam^{-1}, SCUBA 3σ = 0.10 Jy beam^{-1}.

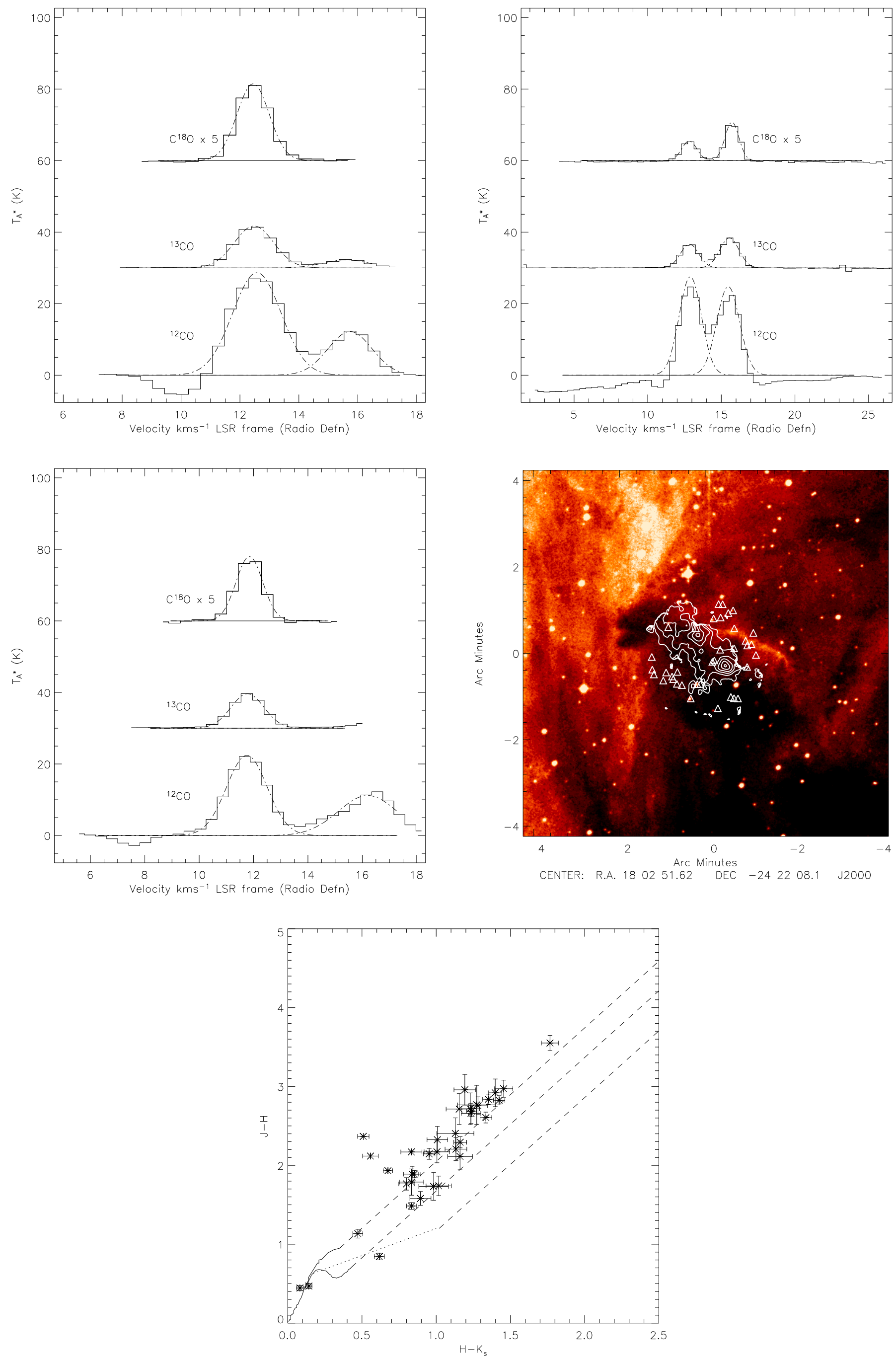

Figure 27: Plots and images associated with the object SFO 87. In the first three panels are representations of all spectra observed for the objects SFO 87 SMM1, SMM2 and SMM3 on the top left, top right and centre left respectively. The centre right image shows SCUBA 850 μm contours overlaid on a DSS image, infrared sources from the 2MASS Point Source Catalogue (Cutri et al. 2003) are shown as triangles. The bottom figure shows the J-H versus H-K$_s$ colours of the 2MASS sources associated with the cloud. Peak and r.m.s. flux levels are as follows, SCUBA peak = 0.66 Jy beam^{-1}, SCUBA 3σ = 0.17 Jy beam^{-1}.

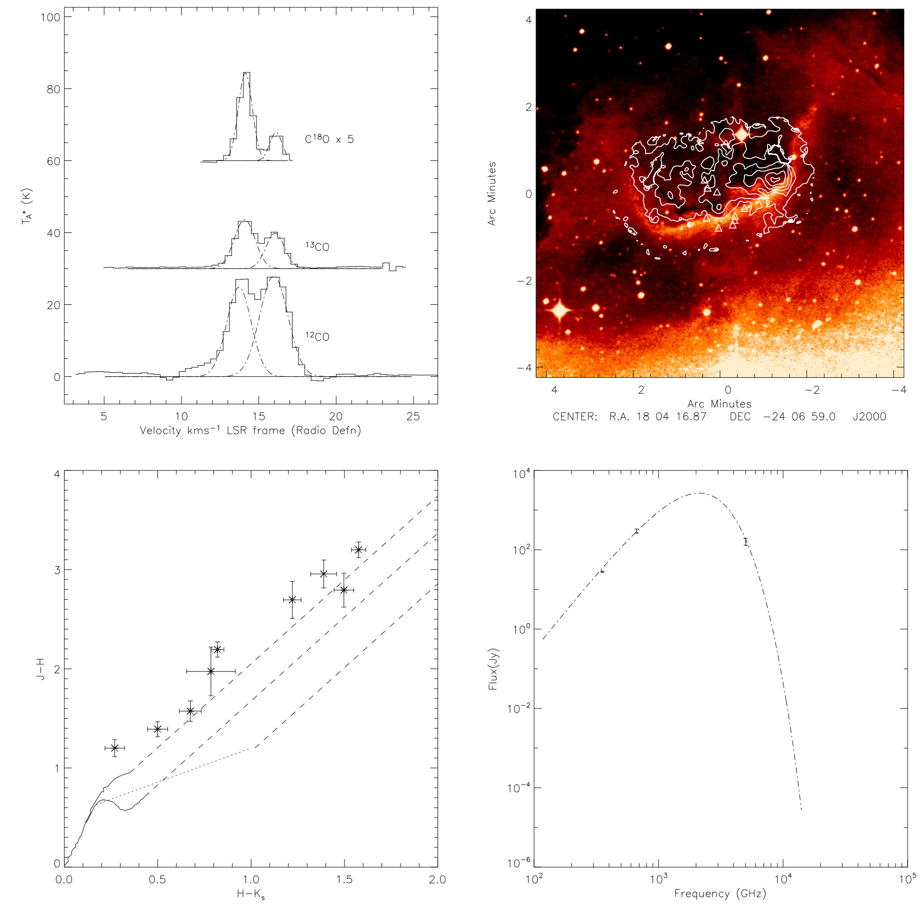

Figure 27: Plots and images associated with the object SFO 88. In the top left is a representation of all spectra observed for this object. The top right image shows SCUBA 850 μm contours overlaid on a DSS image, infrared sources from the 2MASS Point Source Catalogue (Cutri et al. 2003) are shown as triangles. The bottom left plot shows the J-H versus H-K$_s$ colours of the 2MASS sources associated with the cloud while the bottom right image shows the SED plot of the object composed from a best fit to various observed fluxes. Peak and r.m.s. flux levels are as follows, SCUBA peak = 0.83 Jy beam^{-1}, SCUBA 3σ = 0.10 Jy beam^{-1}.

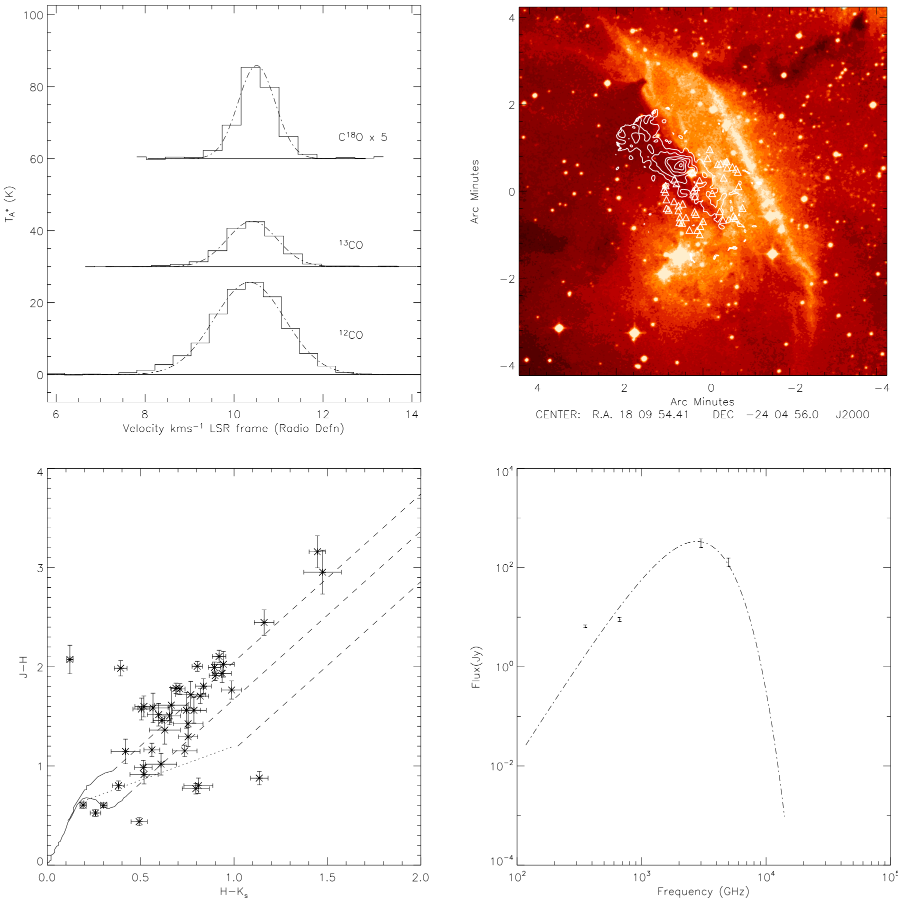

Figure 27: Plots and images associated with the object SFO 89. In the top left is a representation of all spectra observed for this object. The top right image shows SCUBA 850 μm contours overlaid on a DSS image, infrared sources from the 2MASS Point Source Catalogue (Cutri et al. 2003) are shown as triangles. The bottom left plot shows the J-H versus H-K$_s$ colours of the 2MASS sources associated with the cloud while the bottom right image shows the SED plot of the object composed from a best fit to various observed fluxes. Peak and r.m.s. flux levels are as follows, SCUBA peak = 0.48 Jy beam^{-1}, SCUBA 3σ = 0.11 Jy beam^{-1}.

Appendix B

Further Acknowledgements

I would like to thank all of the staff at the JCMT for their support and assistance during observing runs. This research has made extensive use of the SIMBAD astronomical database service operated at CDS, Strasbourg, France and the NASA Astrophysics Data System Bibliography Services. The Digitized Sky Surveys were produced at the Space Telescope Science Institute under U.S. Government grant NAG W-2166. The images of these surveys are based on photographic data obtained using the Oschin Schmidt Telescope on Palomar Mountain and the UK Schmidt Telescope. The plates were processed into the present compressed digital form with the permission of these institutions.

This research has made use of the NASA/ IPAC Infrared Science Archive, which is operated by the Jet Propulsion Laboratory, California Institute of Technology, under contract with the National Aeronautics and Space Administration.

This research has made use of data products from the Two Micron All Sky Survey, which is a joint project of the University of Massachusetts and the Infrared Processing and Analysis Center/California Institute of Technology, funded by the National Aeronautics and Space Administration on the National Science Foundation.

This research has also made use of data products from the Midcourse Space Experiment. Processing of the data was funded by the Ballistic Missile Defense Organization with additional support from the NASA Office of Space Science.

Bibliography

Andre, P., Ward-Thompson, D., & Barsony, M. 1993, ApJ, 406, 122

Arce, H. G. & Sargent, A. I. 2005, ApJ, 624, 232

Aumann, H. H., Fowler, J. W., & Melnyk, M. 1990, AJ, 99, 1674

Bachiller, R. 1996, ARA&A, 34, 111

Bacmann, A., Lefloch, B., Ceccarelli, C., et al. 2003, ApJ, 585, L55

Bally, J. & Scoville, N. Z. 1980, ApJ, 239, 121

Baudry, A. & Diamond, P. J. 1991, A&A, 247, 551

Beckwith, S. V. W., Sargent, A. I., Chini, R. S., & Guesten, R. 1990, AJ, 99, 924

Beltrán, M. T., Girart, J. M., Estalella, R., Ho, P. T. P., & Palau, A. 2002, ApJ, 573, 246

Bertoldi, F. 1989, ApJ, 346, 735

Blitz, L. 1993, in Protostars and Planets III, 125–161

Boulon, J. & Fehrenbach, C. 1958, Journal des Observateurs, 42, 149

Cao, Y., Terebey, S., Prince, T. A., & Beichman, C. A. 1997, ApJS, 111, 387

Carpenter, J. M., Heyer, M. H., & Snell, R. L. 2000, ApJS, 130, 381

Carpenter, J. M., Snell, R. L., & Schloerb, F. P. 1990, ApJ, 362, 147

Cernicharo, J., Bachiller, R., Duvert, G., Gonzalez-Alfonso, E., & Gomez-Gonzalez, J. 1992, A&A, 261, 589

Chandler, C. J. & Richer, J. S. 2000, ApJ, 530, 851

Chavarria-K., C., Moreno-Corral, M. A., Hernandez-Toledo, H., Terranegra, L., & de Lara, E. 1994, A&A, 283, 963

Chiar, J. E., Gerakines, P. A., Whittet, D. C. B., et al. 1998, ApJ, 498, 716

Claria, J. J. 1974, A&A, 37, 229

Codella, C., Bachiller, R., Nisini, B., Saraceno, P., & Testi, L. 2001, A&A, 376, 271

Condon, J. J., Cotton, W. D., Greisen, E. W., et al. 1998, AJ, 115, 1693

Conti, P. S. & Alschuler, W. R. 1971, ApJ, 170, 325

Crampton, D. & Fisher, W. A. 1974, Publications of the Dominion Astrophysical Observatory Victoria, 14, 283

Currie, M. J. & Berry, D. S. 2002, Starlink Project, CCLRC

Cutri, R. M., Skrutskie, M. F., van Dyk, S., et al. 2003, VizieR Online Data Catalog, 2246, 0

de Jager, C. & Nieuwenhuijzen, H. 1987, A&A, 177, 217

De Vries, C. H., Narayanan, G., & Snell, R. L. 2002, ApJ, 577, 798

Deharveng, L., Zavagno, A., Cruz-Gonzalez, I., et al. 1997, A&A, 317, 459

Dent, W. R. F., Matthews, H. E., & Ward-Thompson, D. 1998, MNRAS, 301, 1049

Desmurs, J. F. & Baudry, A. 1998, A&A, 340, 521

Draine, B. T. & Lee, H. M. 1984, ApJ, 285, 89

Duvert, G., Cernicharo, J., Bachiller, R., & Gomez-Gonzalez, J. 1990, A&A, 233, 190

Egan, M. P., Price, S. D., Moshir, M. M., Cohen, M., & Tedesco, E. 1999, NASA STI/Recon Technical Report N, 14854

Ehrenfreund, P. & Charnley, S. B. 2000, ARA&A, 38, 427

Evans, N. J. 1999, ARA&A, 37, 311

Fukui, Y., Iwata, T., Mizuno, A., Ogawa, H., & Takaba, H. 1989, Nature, 342, 161

Gallimore, J., Wolfe, C., & Beck, H. 2003, American Astronomical Society Meeting Abstracts, 203

Gibb, E. L., Whittet, D. C. B., Schutte, W. A., et al. 2000, ApJ, 536, 347

Gibson, D. J., Rudolph, A., & Barsony, M. 1997, Bulletin of the American Astronomical Society, 29, 1220

Gies, D. R., Mason, B. D., Bagnuolo, W. G., et al. 1997, ApJ, 475, L49+

Goldsmith, P. F., Bergin, E. A., & Lis, D. C. 1996, in IAU Symp. 170: CO: Twenty-Five Years of Millimeter-Wave Spectroscopy, 113

Goorvitch, D. 1994, ApJS, 95, 535

Gordon, M. A. 1995, A&A, 301, 853

Hardie, R. H., Seyfert, C. K., & Gulledge, I. S. 1960, ApJ, 132, 361

Hatchell, J. & van der Tak, F. F. S. 2003, A&A, 409, 589

Hawkins, I. & Jura, M. 1987, ApJ, 317, 926

Hildebrand, R. H. 1983, QJRAS, 24, 267

Holland, W. S., Robson, E. I., Gear, W. K., et al. 1999, MNRAS, 303, 659

Huard, T. L., Sandell, G., & Weintraub, D. A. 1999, ApJ, 526, 833

Hughes, V. A., Vallee, J. P., & Viner, M. R. 1978, BAAS, 10, 661

Humphreys, R. M. 1978, ApJS, 38, 309

Imai, H., Morris, M., Sahai, R., Hachisuka, K., & Azzollini F., J. R. 2004, A&A, 420, 265

Ishida, K. 1970, PASJ, 22, 277

Jansen, D. J., van Dishoeck, E. F., & Black, J. H. 1994, A&A, 282, 605

Jeans, J. H. 1928, Astronomy and cosmogony (Cambridge [Eng.] The University press, 1928.)

Jenness, T. & Lightfoot, J. F. 2000, Starlink Project, CCLRC

Kassim, N. E. 1988, ApJS, 68, 715

Keane, J. V., Tielens, A. G. G. M., Boogert, A. C. A., Schutte, W. A., & Whittet, D. C. B. 2001, A&A, 376, 254

Koornneef, J. 1983, A&A, 128, 84

Kroupa, P., Tout, C. A., & Gilmore, G. 1990, MNRAS, 244, 76

Kruegel, E. & Siebenmorgen, R. 1994, A&A, 288, 929

Kuiper, T. B. H. 1975, A&A, 42, 323

Lada, C. J. & Adams, F. C. 1992, ApJ, 393, 278

Lada, C. J. & Black, J. H. 1976, ApJ, 203, L75

Lada, C. J., Lada, E. A., Clemens, D. P., & Bally, J. 1994, in ASSL Vol. 190: Astronomy with Arrays, The Next Generation, 473

Lada, C. J., Thronson, H. A., Smith, H. A., et al. 1981, ApJ, 251, L91

Langer, W. D. & Penzias, A. A. 1990, ApJ, 357, 477

Langer, W. D., van Dishoeck, E. F., Bergin, E. A., et al. 2000, Protostars and Planets IV, 29

Larson, R. B. 2003, Reports on Progress in Physics, 66, 1652

Lefloch, B., Cernicharo, J., Rodríguez, L. F., et al. 2002, ApJ, 581, 335

Lefloch, B. & Lazareff, B. 1994, A&A, 289, 559

Lefloch, B. & Lazareff, B. 1995, A&A, 301, 522

Lefloch, B., Lazareff, B., & Castets, A. 1997, A&A, 324, 249

Leger, A. & Puget, J. L. 1984, A&A, 137, L5

Leung, C. M. & Brown, R. L. 1977, ApJ, 214, L73

Mardones, D., Myers, P. C., Tafalla, M., et al. 1997, ApJ, 489, 719

Margulis, M., Lada, C. J., & Young, E. T. 1989, ApJ, 345, 906

Mathis, J. S., Rumpl, W., & Nordsieck, K. H. 1977, ApJ, 217, 425

Matthews, H. I. 1979, A&A, 75, 345

Mcdonald, G. & Alvey, N. 2002, in ASP Conf. Ser. 267: Hot Star Workshop III: The Earliest Phases of Massive Star Birth, 387

Megeath, S. T. & Wilson, T. L. 1997, AJ, 114, 1106

Meyer, M. R., Calvet, N., & Hillenbrand, L. A. 1997, AJ, 114, 288

Minier, V., Burton, M. G., Hill, T., et al. 2005, A&A, 429, 945

Mitchell, G. F., Johnstone, D., Moriarty-Schieven, G., Fich, M., & Tothill, N. F. H. 2001, ApJ, 556, 215

Morgan, L. K., Thompson, M. A., Urquhart, J. S., White, G. J., & Miao, J. 2004, ArXiv Astrophysics e-prints

Morgan, W. W., Code, A. D., & Whitford, A. E. 1955, ApJS, 2, 41

Mueller, K. E., Shirley, Y. L., Evans, N. J., & Jacobson, H. R. 2002, ApJS, 143, 469

Myers, P. C., Heyer, M., Snell, R. L., & Goldsmith, P. F. 1988, ApJ, 324, 907

Myers, P. C., Linke, R. A., & Benson, P. J. 1983, ApJ, 264, 517

O'Dell, C. R. & Doi, T. 2003, AJ, 125, 277

Ogura, K. & Ishida, K. 1981, PASJ, 33, 149

Panagia, N. 1973, AJ, 78, 929

Patel, N. A., Greenhill, L. J., Ho, P. T. P., & Moran, J. M. 2001, Bulletin of the American Astronomical Society, 33, 1504

Pestalozzi, M., Booth, R., Humphreys, E. M. L., Conway, J., & Minier, V. 2003, in ASP Conf. Ser. 287: Galactic Star Formation Across the Stellar Mass Spectrum, 361–366

Pestalozzi, M. R. 2004, Ph.D. Thesis

Price, S. D., Egan, M. P., Carey, S. J., Mizuno, D. R., & Kuchar, T. A. 2001, AJ, 121, 2819

Privett, G., Jenness, T., & Lightfoot, J. F. 1998, Starlink Project, CCLRC

Racine, R. 1968, AJ, 73, 588

Reipurth, B. 1983, A&A, 117, 183

Reynolds, R. J. & Ogden, P. M. 1979, ApJ, 229, 942

Rieke, G. H. & Lebofsky, M. J. 1985, ApJ, 288, 618

Rovenskaya, N. I. 1994, Ap&SS, 211, 215

Salpeter, E. E. 1955, ApJ, 121, 161

Sartori, M. J. & Lepine, J. R. D. 1996, in Revista Mexicana de Astronomia y Astrofisica Conference Series, 87

Sault, R. J., Teuben, P. J., & Wright, M. C. H. 1995, in ASP Conf. Ser. 77: Astronomical Data Analysis Software and Systems IV, 433

Savage, B. D., Drake, J. F., Budich, W., & Bohlin, R. C. 1977, ApJ, 216, 291

Savage, B. D. & Mathis, J. S. 1979, ARA&A, 17, 73

Savage, C., Apponi, A. J., Ziurys, L. M., & Wyckoff, S. 2002, ApJ, 578, 211

Seth, A. C., Greenhill, L. J., & Holder, B. P. 2002, ApJ, 581, 325

Sharpless, S. 1959, ApJS, 4, 257

Sheffer, Y., Federman, S. R., Lambert, D. L., & Cardelli, J. A. 1992, ApJ, 397, 482

Shirley, Y. L., Evans, N. J., & Mundy, L. G. 2003, American Astronomical Society Meeting, 203

Snell, R. L., Huang, Y.-L., Dickman, R. L., & Claussen, M. J. 1988, ApJ, 325, 853

Stamatellos, D., Whitworth, A. P., André, P., & Ward-Thompson, D. 2004, A&A, 420, 1009

Steinacker, J., Lang, B., Burkert, A., Bacmann, A., & Henning, T. 2004, ApJ, 615, L157

Sugitani, K., Fukui, Y., Mizuni, A., & Ohashi, N. 1989, ApJ, 342, L87

Sugitani, K., Fukui, Y., & Ogura, K. 1991, ApJS, 77, 59

Sugitani, K., Matsuo, H., Nakano, M., Tamura, M., & Ogura, K. 2000, AJ, 119, 323

Sugitani, K. & Ogura, K. 1994, ApJS, 92, 163

Thompson, M. A., Urquhart, J. S., & White, G. J. 2004a, A&A, 415, 627

Thompson, M. A., White, G. J., Morgan, L. K., et al. 2004b, A&A, 414, 1017

Walker, C. K., Adams, F. C., & Lada, C. J. 1990, ApJ, 349, 515

Walmsley, C. M., Flower, D. R., & Pineau des Forêts, G. 2004, A&A, 418, 1035

Webber, W. R., Lukasiak, A., McDonald, F. B., & Ferrando, P. 1996, ApJ, 457, 435

White, G. J., Lefloch, B., Fridlund, C. V. M., et al. 1997, A&A, 323, 931

White, G. J., Nelson, R. P., Holland, W. S., et al. 1999, A&A, 342, 233

Wilking, B. A., Blackwell, J. H., Mundy, L. G., & Howe, J. E. 1989, ApJ, 345, 257

Wolf-Chase, G., Moriarty-Schieven, G., Fich, M., & Barsony, M. 2003, MNRAS, 344, 809

Wood, D. O. S. & Churchwell, E. 1989, ApJ, 340, 265

Wyrowski, F., Hofner, P., Schilke, P., et al. 1997, A&A, 320, L17

Yamaguchi, R., Saito, H., Mizuno, N., et al. 1999, PASJ, 51, 791

Zhou, S. & Evans, N. J. 1994, in ASP Conf. Ser. 65: Clouds, Cores, and Low Mass Stars, 183

Zinner, E. 1996, in Astronomical Society of the Pacific Conference Series, 147